

**Size evolution of laser-generated  
nanoparticles before and after cavitation  
bubble confinement**

**Inaugural Dissertation**

by

**Alexander Letzel, M.Sc.**

born in Dortmund

for the degree of

Doctor of Natural Science

- Dr. rer. nat. -

Faculty of Chemistry

University Duisburg-Essen

Germany

**Essen, 2019**

# DuEPublico

Duisburg-Essen Publications online

UNIVERSITÄT  
DUISBURG  
ESSEN

*Offen im Denken*

ub | universitäts  
bibliothek

Diese Dissertation wird über DuEPublico, dem Dokumenten- und Publikationsserver der Universität Duisburg-Essen, zur Verfügung gestellt und liegt auch als Print-Version vor.

**DOI:** 10.17185/duepublico/70224

**URN:** urn:nbn:de:hbz:464-20190628-111027-9

Alle Rechte vorbehalten.

The present thesis was conducted from May 2015 to October 2018 in the research group of Prof. Dr.-Ing. Stephan Barcikowski at the Institute for Technical Chemistry of the University of Duisburg-Essen.

Referees: Prof. habil. Dr.-Ing. Stephan Barcikowski  
University of Duisburg-Essen

PD habil. Dr. rer. nat. Anton Plech  
Karlsruhe Institute of Technology

Chairman: Prof. habil. Dr. rer. nat. Elke Sumfleth  
University of Duisburg-Essen

Day of the disputation: December 17, 2018

Für Carina,  
Christel, Hans-Günther  
und Philipp

*Man merkt nie, was schon  
getan wurde, man sieht immer  
nur, was noch zu tun bleibt.*

*Marie Curie*

## Danksagung

Diese Dissertation ist mit Hilfe der Unterstützung vieler Personen entstanden. Der Jahre dauernde naturwissenschaftliche Promotionsprozess ist eine aufregende Zeit voller spannender wissenschaftlicher Entdeckungen und der persönlichen Entwicklung. Er ist aber auch eine Zeit voller Entbehrungen und harter Arbeit. Wie immer im Leben gab es auch in der Zeit in der diese Dissertation entstanden ist Höhen und Tiefen. Glücklicherweise waren die Höhen sowohl häufiger als auch größer als die Tiefen.

### Vielen Dank an...

... **meinen Doktorvater Prof. Dr. Stephan Barcikowski** für die Möglichkeit in deiner Arbeitsgruppe zu promovieren, für das entgegengebrachte Vertrauen und die Wertschätzung, für die detaillierte Betreuung, viele anregende Diskussionen und die Vorbereitung auf die Zukunft.

... **PD Dr. Bilal Gökce** für die intensive Betreuung in deiner Forschungsgruppe, den ansteckenden Wunsch unsere Ergebnisse zu publizieren und das vertrauensvolle Verhältnis.

... **PD Dr. Anton Plech** für die fünf bis sechs gemeinsamen Strahlzeiten, je nachdem ob man die drei Tage in Karlsruhe mitzählen möchte. Außerdem für die Einarbeitung und Betreuung an den Stahlquellen in Karlsruhe, Villigen und Grenoble, die zahlreichen Diskussionen, sowie die stets aufrichtige und sachliche Kritik.

... **Dr. Andreas Menzel** für die Möglichkeit außerplanmäßig an deiner Beamline zu arbeiten und die Zeit, immerhin eine ganze Nacht, die du dafür geopfert hast. Natürlich auch vielen Danke dafür, dass du bei den geplanten Strahlzeiten immer ein verlässlicher und geduldiger Ansprechpartner warst.

... **die Deutsche Forschungsgemeinschaft** für die Bewilligung von Sachbeihilfe im Rahmen des Forschungsprogramms BA 3580/15-1.

... **Stefan Reich** für die gegenseitige Unterstützung bei unseren jeweiligen Projekten, deine ansteckende gute Laune und die sachlichen Diskussionen. Ich werde an unsere Zeit immer mit Freude zurückdenken und das liegt nicht nur an der Flasche Wein in Grenoble.

... **Marco Santoro** for visiting our group as a guest PhD student, for being as open as you are and of course for your help with the shadowgraphy setup. The moment when we first saw the cavitation bubble was the most exciting moment during my PhD studies. Thank you for having become a friend.

... **Alexander Kanitz und Jan Hoppius** für die Herstellung der Hartmann-Maske und die geopfert Zeit.

... **das Team der Technischen Chemie I** für die Zusammenarbeit, den Zusammenhalt und die vielen Gelegenheiten gemeinsam zu lachen. Einigen Kollegen möchte ich an dieser Stelle ganz besonders danken:

... **Jurij Jakobi** für unzählige TEM-Analysen.

... **René Streubel** für Hilfe bei allen technischen und optischen Fragestellungen.

... **Anna Ziefuß** für die Identifikation von Nanoclustern und die Begeisterung darüber.

... **Sebastian Kohsakowski** für die geteilte Expertise auf dem Gebiet der Laserablation.

... **Marc Kalus** für den Austausch über die optische Bildgebung während der Ablation.

... **Wolfgang Kranefoed** für die unbürokratische und professionelle Umformung von Gold- und Silbertargets in dünne Bänder.

... **Julia Frohleiks** für die Möglichkeit an eurem Nanofocus zu messen und die Zeit die dafür nötig war.

... **Roland Grzeschik** für den kurzen Draht in den Arbeitskreis von Prof. Schlücker.

... **meine Familie, vor allem meinen Eltern**, dafür, dass ihr immer für mich da wart und seid. Mein allergrößter Dank gilt meiner lieben Frau **Carina**.

# Table of contents

<b>Abbreviations.....</b>	<b>IX</b>
<b>Abstract .....</b>	<b>XI</b>
<b>1 Introduction.....</b>	<b>- 1 -</b>
<b>2 Objectives.....</b>	<b>- 4 -</b>
<b>3 State of the art.....</b>	<b>- 5 -</b>
3.1 Fundamentals of pulsed laser ablation in liquids.....	- 7 -
3.1.1 <i>Evolution of the cavitation bubble.....</i>	- 10 -
3.1.2 <i>Noble metal nanoparticles synthesized by laser ablation in liquids.....</i>	- 13 -
3.2 Stability of colloidal nanoparticles .....	- 16 -
3.2.1 <i>Ostwald ripening .....</i>	- 16 -
3.2.2 <i>Coagulation and coalescence .....</i>	- 17 -
3.2.3 <i>Electrostatic and steric stabilization.....</i>	- 18 -
3.3 Noble metal nanoparticles .....	- 26 -
3.4 Size control by additives in laser synthesis of noble metal nanoparticles .....	- 29 -
3.5 X-rays for the static and dynamic size analysis of nanoparticles .....	- 32 -
<b>4 Materials and methods .....</b>	<b>- 39 -</b>
4.1 Experimental design .....	- 42 -
4.1.1 <i>Experimental design for in situ investigations.....</i>	- 42 -
4.1.2 <i>Experimental design for pulsed laser ablation and fragmentation in liquids.....</i>	- 43 -
4.1.3 <i>Shadowgraphy setup .....</i>	- 44 -
<b>5 Results and discussion.....</b>	<b>- 46 -</b>
5.1 Suitability and interpretability of the high-speed X-ray setup and results .....	- 49 -
5.1.1 <i>Primary particle diameter differentiation and bimodality identification by five analytical methods using gold nanoparticle size distributions synthesized by pulsed laser ablation in liquids - 52 -</i>	
5.1.2 <i>How the re-irradiated of a single ablation spot affects cavitation bubble dynamics and nanoparticles properties in laser ablation in liquids.....</i>	- 69 -
5.2 <i>In situ</i> observation of nanoparticle size reduction by additives.....	- 88 -
5.2.1 <i>Size quenching during laser synthesis of colloids happens already in the vapor phase of the cavitation bubble.....</i>	- 91 -
5.2.2 <i>Time and mechanism of nanoparticle functionalization by macromolecular ligands during pulsed laser ablation in liquids.....</i>	- 109 -
<b>6 Summary and conclusion .....</b>	<b>- 127 -</b>
<b>7 Outlook .....</b>	<b>- 131 -</b>
<b>8 References.....</b>	<b>- 132 -</b>

<b>9</b>	<b>Appendix</b> .....	<b>- 154 -</b>
9.1	List of figures .....	- 179 -
9.2	List of tables.....	- 188 -
<b>10</b>	<b>Curriculum Vitae</b> .....	<b>- 189 -</b>
<b>11</b>	<b>Declaration</b> .....	<b>- 190 -</b>
11.1	Declaration of scientific contributions .....	- 191 -
<b>12</b>	<b>Publications and conference contributions</b> .....	<b>- 193 -</b>

## Abbreviations

ADC	Analytical disc centrifuge
AgNP	Silver nanoparticle
AGR	Additive-to-gold-ratio
AuNP	Gold nanoparticle
c.c.c.	critical coagulation concentration
CMOS	Complementary metal–oxide–semiconductor
DFT	Density functional theory
DLS	Dynamic light scattering
HR-TEM	High-resolution transmission electron microscope
IHL	inner Helmholtz layer
IHP	inner Helmholtz plane
MC	Monte Carlo method
MEEAA	2-[2-(2-Methoxyethoxy)ethoxy] acetic acid
mPEG-SH	Methoxypoly(ethylene glycol)
n.m.r.	Nominal mixing ratio
OHL	outer Helmholtz layer
OHP	outer Helmholtz plane
PLAL / LAL	Pulsed laser ablation in liquids
PLFL / LFL	Pulsed laser fragmentation in liquids
PPI	Primary particle index
PTFE	Polytetrafluoroethylene (Teflon)
PVA	poly(vinyl alcohol)
PVC	Polyvinyl chloride
PVP	Polyvinylpyrrolidone
RCF	Relative centrifugal force
S7 / S10 / S50	Gold nanoparticles of median diameter of 7 nm / 10 nm / 50 nm (volume-weighted).
SAXS	Small-angle X-ray scattering
SDS	Sodium dodecyl sulfate
SERS	Surface-enhanced Raman spectroscopy
SPR	Surface plasmon resonance
STEM	Scanning transmission electron microscope
TEM	Transmission electron microscopy

UF	Unified fit
UV/Vis	Ultraviolet-visible
vdW	van der Waals forces
XHI	X-ray Hartmann mask imaging
XPS	X-ray photoelectron spectroscopy
YAG	Yttrium aluminum garnet

## Abstract

Nanoparticle synthesis by pulsed laser ablation in liquids (PLAL) is a method to obtain particles with clean surfaces, free of any organic residuals. A drawback to this method is the particle size distribution, which exhibits an intrinsic bi- or multi-modality. One known strategy to narrow the particle size distribution in a single step is to use electrolytes or macromolecules as additives to the liquid phase. The laser impact on the ablation target is followed by a hemispherical cavitation bubble, which acts as a container for the ablated mass for the first tens to hundreds of microseconds, depending on the laser parameters, and significantly affects the genesis of the final particle sizes. Clarifying the role of this cavitation bubble and identifying the time and location of additive-particle interactions are the main objectives of this dissertation.

Laser percussion drilling was used to demonstrate that neither the shape nor the lifetime of the cavitation bubble significantly affects the size of the resulting silver nanoparticles due to the large amounts of nanoclusters (size  $\leq 3$  nm) that form during PLAL. These nanoclusters add to the final nanoparticle sizes by subsequent growth processes on a macroscopic time scale.

The interior of the gaseous cavitation bubble in the presence of micromolar concentrations of additives (sodium chloride and polyvinylpyrrolidone (PVP)) was probed by analytical X-ray methods that exploited the brilliant beams generated from synchrotrons.

Using spatio-temporally resolved small-angle X-ray scattering (SAXS), it was shown that dissolved NaCl does start to interact with the ablated species of a gold target already inside the gaseous phase of the cavitation bubble as both the size and abundance of large nanoparticles decreased with respect to the ablation in pure water.

X-ray Hartmann mask imaging (XHI) was used for the analysis of the macromolecular ligand PVP for reducing the size of gold nanoparticles. In contrast to SAXS, XHI allows one to record the entire cavitation bubble in a single-shot experiment. While an effect already inside the cavitation bubble was not excluded, PVP mostly affected the nanoparticles in the liquid phase, after the collapse of the bubble, by hindering the ripening of the nanoparticles.

The time and location of the interaction of different classes of size-reducing additives were identified as well as the vast generation of nanoclusters. These new findings present starting points for additional studies on the origin of the bimodal size distribution that is obvious before the evolution of the laser-induced cavitation bubble.



## **1 Introduction**

Regarding the unique properties of nanoparticles that are induced by their high surface-to-volume ratios, it is straightforward to exploit these in order to influence the macroscopic world. The number of preconditions a nanoparticulate colloid must fulfill to be considered for applications is vast and varies by the individual task. Among these conditions are the particle size distribution, the number, and type of surface defects, and the colloid's polydispersity, morphology, crystallinity, composition, state of oxidation, toxicity, biocompatibility, stability, and functionalization. Additionally, the productivity of nanoparticle mass per time is crucial. Large-scale nanoparticle production occurs by reduction of precursor salts or sol-gel processes in the liquid phase in bottom-up synthesis. Large-scale top-down synthesis is frequently conducted in the gas phase, starting from macroscopic or microscopic materials, by spray pyrolysis, arc discharge, or laser ablation in air. Still, none of these techniques can be used to produce nanoparticles of any desired composition if at the same time, the addition of large amounts of additives must be avoided or if the particles are required to be individually dispersed in a liquid phase instead of as aggregated powders.

A bottom-up technique that combines the flexibility of the nanoparticle material with ligand-free surfaces and a direct dispersion in a freely selectable liquid phase is pulsed laser ablation in liquids (PLAL). The principle is simple: a solid object, the target, is placed in a vessel and covered with a liquid. When a pulsed laser with a fluence exciting the ablation threshold of the target material is used, which is usually achieved by focusing the laser beam on the target surface, the macroscopic material is converted into nanoparticles. After laser irradiation and removal of the residual target, the system consists of only two components: the liquid phase and the dispersed nanoparticles. The addition of organic stabilizers to the dispersion is unnecessary as the particles are electrostatically stabilized by surface charges, an effect that is particularly pronounced if the water is used as the liquid phase. Despite the unique advantages of PLAL, some of PLAL's drawbacks are its limited productivity, the production of nanoparticles with varying stoichiometries, and the limited size control of the nanoparticles.

The latter point deserves a more thorough introduction as in this dissertation, the formation and interaction of nanoparticles with additives that are added to the liquid prior to laser ablation is investigated. Laser-generated nanoparticles inherently exhibit a size distribution that is at least bimodal, an effect that is even more pronounced if ultrashort laser pulses of some picoseconds or less are used. Nevertheless, the scope of the present work is PLAL with nanosecond pulses and as such no ultrashort pulses are employed. The mentioned bimodal particle size distribution cannot be avoided

without performing subsequent particle processing by, e.g., fractionation or laser fragmentation. However, the size distribution is significantly narrowed by adding micromolar concentrations of electrolytes to the liquid phase prior to PLAL. Some size reduction is further achieved by the addition of macromolecular ligands to the liquid, either prior to ablation or immediately after nanoparticle generation. While these phenomena are known, it is not clear at which delay after laser impact and in which location these size reductions take place. The question of whether the additives are present and active within the laser-induced cavitation bubble is still under debate. As the cavitation bubble exhibits a lifetime of up to some hundreds of microseconds and is limited in its extension to some millimeters, the investigation of its interior and possible occurring reactions demands analytical techniques with high temporal and spatial resolution as well as the ability to cross the curved interface between the liquid phase and the gaseous phase of the cavitation bubble. Therefore, it cannot be probed by methods that use optical light because optical light is scattered at the liquid-gas interface.

The experimental studies presented here explore ways to more efficiently control the size of PLAL colloids by clarifying the time of nanoparticle size reduction by additives using advanced X-ray techniques. At the interface of the laser-irradiated target, hot plasma forms in nanoseconds. Upon cooling, its energy is transferred to the surrounding liquid, which leads to evaporation and the formation of the hemispherical cavitation bubble attached to the target. That bubble acts as a container for a significant share of the ablated mass during its lifetime. Bubble lifetime and size, for PLAL with nanosecond pulses, in a large range are proportional to the applied fluence.

As X-rays are not restricted from crossing the liquid-gas interface because of the refractive index is close to 1 the advanced techniques small-angle X-ray scattering (SAXS) and X-ray Hartman mask imaging (XHI) are used here to clarify the interactions that occur inside the cavitation bubble. The collected data were combined with related *ex situ* investigations to connect the high-speed *in situ* data to the kinds of *ex situ* data available in a typical laboratory of colloidal chemistry.

The knowledge of the time and location of the additive-particle interaction provides input for the design of PLAL experiments that are aimed at other goals, including alloying and controlling the particle composition of alloys and reactive target materials (e.g., oxides in water). For instance, the formation of alloy nanoparticles may yield real alloy nanoparticles as well as core-shell particles. The shell material can be inverted under appropriate experimental conditions, which is often achieved by using alternative liquids. The formation of alloy nanoparticles is not fully understood yet and therefore control over the composition of the resulting nanoparticles is limited for many materials. Knowledge about the processes that occur inside the gaseous phase of the cavitation bubble might, therefore, add

to the picture of alloy particle formation in different liquids and to the final composition of nanoparticles generated from reactive target materials.

## 2 Objectives

The aim of this work is to clarify central questions related to additive-mediated particle size control during nanosecond pulsed laser ablation in liquids. The point in time after laser impact and the interaction between nascent nanoparticles and inorganic ions and organic macromolecules are addressed. This includes referencing of the central analytical technique, which is SAXS. In general, the first tens of microseconds after laser impact, when the cavitation bubble is oscillating, are investigated using the advanced X-ray techniques SAXS and XHI. Additionally, the overall impact of the cavitation bubble on the resulting particle sizes is evaluated. The central scientific questions for this thesis are:

- i. At which delay after laser impact do dissolved ions quench the size of nanoparticles? Does the size quenching start inside the confinement of the laser-induced cavitation bubble?
- ii. What is the impact of the cavitation bubble induced by the same laser parameters but varying bubble volumes and oscillation times on the final particles? What defines the final particle size, if not the cavitation bubble and how and when can it be tackled?
- iii. Is SAXS a suitable technique for the analysis of bimodal colloids if no time resolution is required? What are the limitations of this approach?
- iv. How do macromolecular ligands affect the ablated nanoparticles? Are the involved delays after laser impact the same as those of dissolved ions?

Points (i, iii-iv) are addressed using gold targets and water or aqueous solutions of additives. For the clarification of point (ii), silver targets are used instead.

### 3 State of the art

The European Commission defines a nanomaterial as a material consisting of an ensemble of individual particles in which at least 50 % of these particles are smaller than 100 nm, in at least one spatial direction, in the number-weighted particle size distribution [1]. Defining a nanomaterial by such strict conditions might, however, miss the point as the properties of the material change drastically with decreasing size. This change does not exhibit a constant cut-off value at 100 nm or any other fixed size limit. Among the size-dependent properties are such prominent examples like heterogeneous catalysis [2], magnetism [3], optical [4], and mechanical properties [5]. In nanoscience, it is, therefore, more convenient to define a nanomaterial according to its size-dependent properties rather than static geometric limits.

To obtain such nanomaterials in particulate forms, the chemical reduction of precursors to induce particle nucleation and growth (bottom-up synthesis) [6] and decreasing the size of bulk material (top-down synthesis) [7] is possible. It is often desirable for applications to synthesize nanoparticles dispersed in a liquid environment rather than in air. In the past decades, pulsed laser ablation in liquids (PLAL) has emerged as a technique for top-down production of nanoparticles. The methods offer the opportunity to obtain nanoparticles that are completely free of any organic residues at the particle surface and in the surrounding liquid phase [8]. No liquid or particle purification by centrifugation [9], ultra-filtration [10], dialysis [11], or ligand exchange [12] is required. The principle of PLAL is simple: a solid target (e.g., a metal plate) is placed at the bottom of a beaker (e.g., a cuvette) and overlaid with a liquid phase (e.g., water). In the next step, a pulsed laser is focused on the target surface, so that the threshold fluence (laser pulse energy per area) is reached or exceeded (see 3.3). The laser-material interaction will ultimately cause damage at the target and the formation of nanoparticles, which are immediately quenched in the surrounding liquid. After stopping laser irradiation and removal of the target from the beaker the system consists solely of the liquid and the colloidal stable, dispersed nanoparticles.

Despite the progress in the identification of the mechanisms involved in nanoparticle formation during PLAL some question remain open. This includes questions on the broadness of the final particle size distribution [13-15]. The laser-induced an oscillation cavitation bubble attached to the target surface during the first hundreds of microseconds after laser impact [16-18]. It was shown that this cavitation bubble acts as a container for the ablated particles [19, 20].

Size control of laser-generated nanoparticles can be achieved by the addition of surface-active substances to the liquid phase prior to laser ablation, among other things [21]. While the size

quenching effect of inorganic and organic additives is well-known from analysis after the synthesis (*ex situ*), it remains elusive whether the interaction between the additives and the particles starts in the liquid phase, after the final collapse of the laser-induced cavitation bubble, or already inside the gaseous environment of the bubble. This central question was addressed in this work. In order to provide a better understanding of the discussions in section 5, the principles of plasmonic nanoparticles, colloidal stability and particle growth, the fundamentals of PLAL, and the use of X-ray for nanoparticle analysis are introduced in the following. Note that X-rays were used to cross the interphase of the cavitation bubble as the refractive index for X-ray is close to one in many liquids [22, 23].

### 3.1 Fundamentals of pulsed laser ablation in liquids

One could assume that chemistry plays a minor role in pulsed laser ablation in liquids as it is a physical top-down method. To some extent, this is true, especially as nanoparticles are generated from the bulk material without the necessity of the addition of chemicals. Additionally, the process is very fast and already some hundreds of laser pulses on a target immersed in a small liquid volume (e.g., 1 ml) can result in the visible formation of nanoparticles. This effect is particularly pronounced if noble metal nanoparticles with plasmonic properties are produced (section 3.3). For the observers eye the entire synthesis process, taking some seconds under the described conditions, appears to take place almost instantaneously. Taking a closer look at the process of particle formation, with a temporal and spatial resolution of sub-milliseconds and -meters or less, leads to the observation that multiple processes are involved in particle genesis and growth until they are collected by the observer on the macroscopic scale. It is, therefore, reasonable to change the initial statement on chemistry and add that the physical processes and chemical reactions during particle formation are proceeding rapidly and cannot be observed without advanced analytical techniques.

The number of involved processes between laser impact on the target surface and collection of the final nanoparticle colloid is large, it involves:

- 1) Laser impact
  - a) Threshold fluence for ablation [24]
  - b) Electron-to-lattice energy exchange [25]
- 2) Plasma formation at the target surface
  - a) Laser-plasma interaction [26-28]
- 3) Shock- and soundwave formation [18]
- 4) Cavitation bubble evolution and nanoparticle confinement [16, 19]
  - a) Oscillation of the cavitation bubble [18, 29]
  - b) Particle release to the liquid phase [30]

#### *Laser-material interaction and plasma formation*

The process of laser interaction with the target (1) is best described for the process of laser ablation without a covering liquid layer, e.g., in a vacuum. The consideration is dominated by the pulse duration of the laser pulse and the resulting different mechanisms of interaction with the target material. As the ablated material species are initially in a high-energy state, the processes (1) and (2) are closely related.

One particular difference in ablation with ultrashort femtosecond pulses and long nanosecond pulses is the lifetime of the laser-induced plasma at the solid surface [31, 32]. In the case of femtosecond laser pulses, the pulse width  $\tau_p$  is much shorter than the electron cooling  $\tau_e$  ( $\tau_p \ll \tau_e$ ) time. Therefore the electron-lattice coupling time can be neglected [25]. As a result, ablation occurs before the lattice (phonons) are thermally heated up by the electrons. The ablation is thus considered to be caused by an almost instantaneous solid-vapor transition of the atoms of the target [25].

The opposite case is the use of nanosecond lasers which leads to significant heating of the target lattice [25, 33]. This is due to the pulse width being larger than the lattice cooling time  $\tau_p \gg \tau_L$ . Electron temperature and lattice temperature are equal and the lattice is in a first step heated to its melting point. The material is then vaporized in a second step. During the process, a proportion of the energy is lost because of heat transfer to the target. One important implication of this behavior is that the threshold fluence, the minimum fluence required for laser ablation of a given solid, scales with the square root of the pulse duration for long nanosecond pulses,  $F_{th} \sim \tau_p^{1/2}$  [24, 25, 34].

Picosecond ablation resides between the two extreme cases of femto- and nanosecond pulses and the ablation mechanisms depend on the exact duration of the laser pulses. Widths in the range of 10 ps, still in the stress-confined state, represent a case more closely related to the solid-vapor transition described for femtosecond pulse ablation (Figure 1a) [35-37].

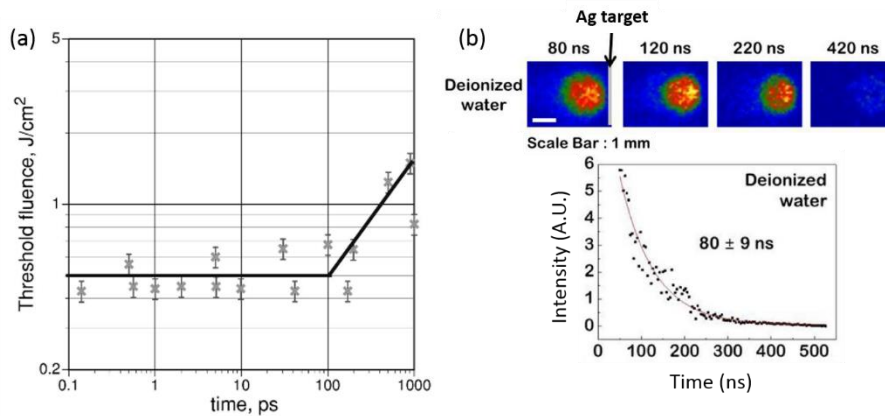


**Figure 1:** (a) Dependency of the threshold laser fluence for material ablation on the laser pulse duration. At about 100 ps pulse width the threshold fluence scales with  $F_{th} \sim \tau_p^{1/2}$  [24]. (b) Top: Time-resolved images of the plasma plume above a silver target during PLAL in pure water. The laser pulse width is 6 ns Red color indicates high emission intensity. Bottom: Decay of integrated plasma intensity of the same sample. The plasma lifetime is  $\sim 300$  ns [38].

Switching the focus back to laser ablation in liquids, it can be reasonably stated that the laser-induced plasma consists of atomized and ionized species delivered from the solid target, it can be considered

as the primary source of ablated matter [26, 39] (This holds of course also for ablation in air or in vacuum.). Yet, the plasma lifetime in liquids is at least some nanoseconds [28, 40, 41]. Considering PLAL with a pulse duration of e.g. 10 ps this means that the pulse duration is negligible with respect to the plasma lifetime. It is considered not to significantly increase its energy by additional pumping (Figure 1b) [28]. On the other hand ablation of the same system with the same parameters except for a pulse duration of e.g., 10 ns, the plasma lifetime is in the same order of magnitude as the laser pulse [38, 42]. This results in an additional energy transfer from the laser pulse to the plasma leading to a more extended plasma [27, 43]. More laser energy is transferred to the plasma and not to the target [44]. In consequence, the ablated material resides for a prolonged time in a heated state (>5000 K) and the increased plume size evaporates a larger liquid volume resulting in larger cavitation bubbles with longer lifetimes [18, 45]. This phenomenon is reported by the observations made by Gamaly et al. on the threshold fluence for laser ablation (in air) as a function of the pulse duration of the utilized laser [24]. They found that the threshold fluence is independent of the pulse duration up to  $\sim 100$  ps, from which a linear relationship starts (Figure 1a).[24] This is explained by the plasma expansion time that overlaps with the laser pulse if the pulse width is large enough [28, 40, 46]. Thereby, also the interaction with particles clusters, which are formed almost instantly after the laser impact on the target is altered [46, 47].

It was demonstrated by Shih et al. in sophisticated computational simulations [46, 48], partly in combination with experimental support [48], that for PLAL of silver films the treatment of laser pulses below the electron-phonon equilibration time  $\tau_{e-ph} < 8$  ps the particle formation mechanism differs from the case of longer laser pulses  $\tau_p$ . In particular, the different evolution of the final particle size distributions bimodality using picosecond and nanosecond lasers is explained [49]. In fact, a trimodal size distribution of nanoparticles was found already 3 ns after laser impact. The computational colloid contains atom clusters of some nanometers that grow to larger particles of about 10 nm. The ablation mechanism of the clusters was found to be the explosive decomposition of the superheated target [46]. A molten target layer is additionally disrupted by the hydrodynamic instabilities. Pressure differences in the molten layer and the surrounding supercritical water accelerate the melt in a nanojet-like fashion away from the target surface. After  $\sim 3$  ns hydrodynamic instabilities, especially Rayleigh-Taylor instabilities, rapidly decelerate the nanojet leading to the formation of large droplets of molten material [48]. These species form the secondary particles typical for PLAL colloids ( $d > 10$  nm) and are suspected to reveal themselves as small satellite bubble surrounding the laser-induced cavitation bubble [48]. Hence, not the entire fraction of secondary nanoparticles is confined within the cavitation bubble during picosecond PLAL [30].

### 3.1.1 Evolution of the cavitation bubble

Caused by the high energy of the species –clusters, atoms, and ions– forming the plasma on the target surface, its physical conditions are harsh with some 1,000 K and some 100 Pa [41]. During the rapid decay and cooling of the plasma, along with the energy transfer to the liquid phase, a hemispherical shockwave evolves at the target, moving away from its surface at the speed of 1500 m/s in water [18].

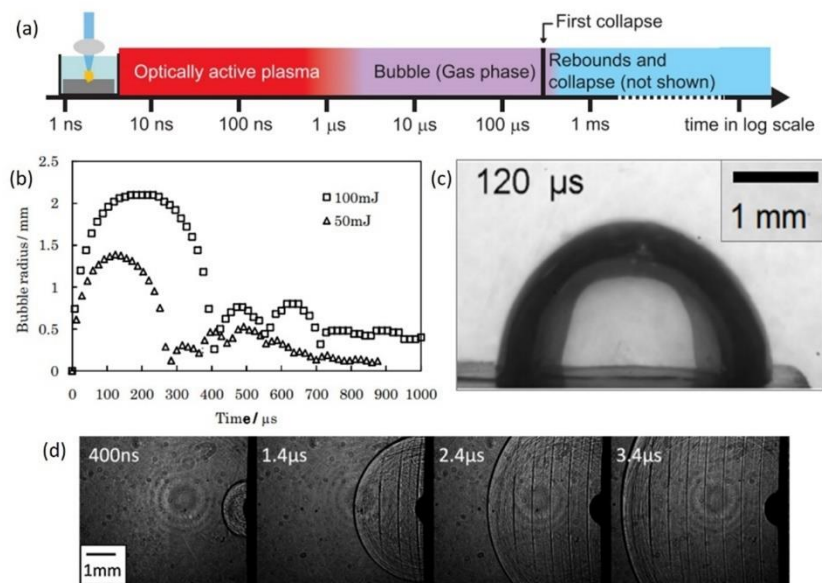


**Figure 2:** Collage of images that illustrate the fundamental processes occurring during the first millisecond after laser impact during PLAL with nanosecond lasers. (a) Scheme of the different processes and their time dependency [50]. The optically active plasma, which consists of excited species, transfers its energy to the liquid phase within a few microseconds. (b) Cavitation bubble radius as a function of time of laser pulses with 100 mJ and 50 mJ pulse energy. Derived from high-speed imaging of the bubble by shadowgraphy [18]. (c) Example of a laser-induced cavitation bubble at its maximum extension 120  $\mu\text{s}$  after laser impact. The center of the bubble is transparent due to diffusive illumination [29]. (d) High-speed image of the semispherical shockwave emerging away from the target (black vertical line) at different delays. After 1.4  $\mu\text{s}$  additional soundwaves that propagate parallel to the target are observed [18].

Reflections of the soundwave cause the evolution of soundwaves parallel to the target surface away from the target [18]. Some frames from optical shadowgraphy showing the shock- and the sound waves along the uprising cavitation bubble, black hemisphere, are presented in Figure 2d [18].

In general, Figure 2a gives an overview of the most important processes during PLAL on a time scale that is typical for the case of nanosecond PLAL [50]. Initially, the laser is absorbed in the target surface and ignites a plasma of the time scale of  $\leq 1$  ns. The plasma is experimentally accessible by plasma emission spectroscopy and has a lifetime of up to approximately 1  $\mu$ s [38, 51].

Upon energy-transfer to the liquid, it evaporated causing the evolution of the gaseous cavitation bubble shown at its maximum extension in Figure 2c. The bubble is hemispherical shaped and attached to the target surface. It was observed by Tamura et al. that the plasma and the cavitation bubble exist simultaneously during the first hundreds of nanoseconds, depending on laser pulse duration and energy [52]. This is considered in Figure 2a by the smooth transition from the plasma phase (red) to the bubble phase (purple). The cavitation bubble undergoes several shrinking or collapses and rebound phases. The cavitation bubble radius is shown in Figure 2b as a function of the time delay after the laser impact. As indicated the maximum bubble extension and total lifetime depending on the laser pulse energy [18] or more precisely the fluence [17, 44].

The cavitation bubble can be altered in shape and the corresponding bubble dynamics by variations of the target geometry. The results discussed so far were obtained from cavitation bubble created by laser ablation of flat targets. A prominent example of an alternative target geometry is a wire. It offers the advantage of continuous target transport by the motor to allow a reproducible and continuous ablation process [53]. The cavitation bubble wraps around the target if it is hit perpendicular by the laser, even tip ablation in this configuration was reported [29, 53]. Compared to PLAL of bulk targets with identical laser parameters, the maximum extension and lifetime of the bubble are reduced. Target wrapping was identified to be a result of symmetric breaking by the wire. Accordingly, the cavitation bubble was forced to similar dynamics as from bulk PLAL by grooved supporting of the wire to mimic bulk target geometry [29].

The following discussion focuses on the prominent case of nanosecond PLAL, as both plasma and cavitation bubble lifetime is increased compared to short laser pulses and its observation is facilitated. The laser-induced plasma was shown to effectively absorb light from the still incident laser [44]. Such behavior is relevant for pulse durations  $\tau_p \gg \tau_L$ . As shown in Figure 3, the maximum bubble volume of the first cavitation bubble scales linearly with the laser fluence above  $\sim 50$  J/cm<sup>2</sup>.

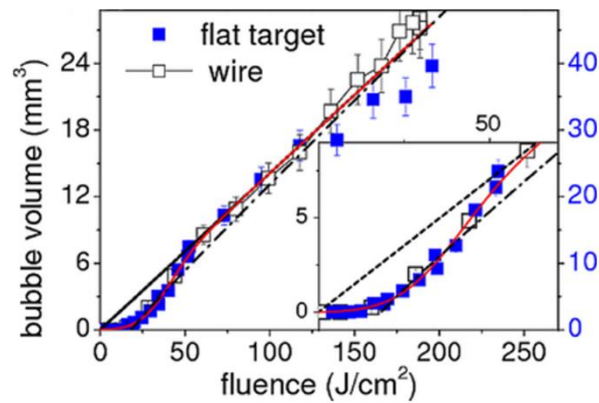


**Figure 3:** Maximum bubble volume as a function of laser fluence with nanosecond pulse duration for two target geometries, a flat target (blue squares) and a wire (white squares). The dashed line represents a linear relationship according to a thermal model, with full energy transfer into cavitation bubble formation ( $>50 \text{ J/cm}^2$ ). The dashed-dotted line represents a linear relationship assuming a pure threshold model for ablation and bubble evolution. In the inset, the typical threshold fluence  $F_{th}$  behavior is shown [44].

It was concluded that in the low-fluence regime conversion of laser energy is steeper as a function of fluence as compared to bubble expansion [44]. The threshold for the linear relationship (Figure 3) was explained by the occurrence of dielectric breakdown of the liquid phase at a threshold fluence. At this point, the plasma expands in the liquid rather than the solid. Consequently, the plasma is effectively pumped by the still active laser pulse and becomes more energetic [44]. This conclusion is in accordance with the observation of the ablated mass not scaling linearly with the laser fluence [44]. It is also supported by the proposed mechanism of layer-by-layer evaporation of the liquid phase upon cooling of the plasma and energy transfer to the surrounding [54].

Many attempts have been made to fit the cavitation bubble size as a function of time with hydrodynamic models to calculate the temperature and pressure dynamics inside the bubble and their implications for the confined nanoparticles [50, 55-57]. While the use of the Rayleigh-Plesset model for cavitation bubbles in liquids [58-60] is capable of fitting the first PLAL-induced cavitation bubble it fails after the first bubbles collapse due to the compressibility of the liquid. It further requires considering material constants like surface tension and viscosity as freely variable, the model predicts extreme pressure peaks upon bubble collapse [55-57, 61]. The initial hydrodynamic equation from Rayleigh [58] did not take into account the liquid parameters surface tension and viscosity but was later considered by Plesset [59, 60].

A model that is more capable to model the cavitation bubble dynamics in PLAL was developed by Gilmore [62]. The Gilmore model considers the compressibility of the liquid in addition to the Rayleigh-Plesset model [63], and a Van der Waals attraction with hard-core repulsion (named “Van der Waals hard core law”) was added [64]. Therefore, the pressure of the gas phase is not constant in the Gilmore model. It was demonstrated to fit the dynamics of a laser-induced cavitation bubble in a free liquid, not at a solid boundary, in good agreement [63, 65]. Fitting the bubble dynamics of a cavitation bubble by the Gilmore equation [63] allows determining the pressure conditions in the gaseous and the liquid phase. This accounts especially for the time between two cavitation bubbles (collapse and rebound), corresponding to the time delays of ~400, 550, and 700  $\mu\text{s}$  in Figure 2b (100 mJ). Yet, according to De Giacomo et al. the temperature inside the cavitation bubble is limited to some 100 K based on time-resolved measurements of bubble size and calculation using a core Van der Waals model [66]. The pressure and corresponding temperature peaks during bubble oscillation in PLAL might have a significant influence on the nanoparticles inside the bubble. Hence, calculations according to the Gilmore model can help to understand the influence of the cavitation bubble on particle formation and growth.

### **3.1.2 Nobel metal nanoparticles synthesized by laser ablation in liquids**

Plasmonic noble metal nanoparticles were among the first in the history of PLAL. In 1993, Fojtik and Henglein [67] discovered the possibility to synthesize nanoparticles by laser irradiation of a metal film covered by a liquid layer, which immediately quenches and disperses the particles. Precisely they laser ablated gold, nickel, and carbon dissolved in water, 2-propanol, and cyclohexane [67]. Some typical extinction spectra obtained from the analysis of gold, silver and copper nanoparticles synthesized by PLAL were reported by Amendola and Meneghetti [68]. They demonstrated the presence of spheroidal particles along with spherical particles in laser-generated gold colloids by TEM image analysis and additionally by fitting the respective extinction spectra by the Mie model for spheres and the Mie Gans model for ellipsoids [68, 69]. Most of the publications related to noble metal PLAL-nanoparticles investigate gold or silver nanoparticles but also platinum and palladium are frequently used.

Besides flexibility, the most important advantage of PLAL is the possibility to produce nanoparticles in the total absence of organic ligands that attach to the particle surface and partly remain in the liquid. Therefore, no ligand exchange and cleaning procedures are required, as no toxic organic ligands are present in the colloidal solutions [70, 71].

Some unique features of gold, silver, and their alloy nanoparticles are exploited in biomedical applications like drug delivery by functionalization of AuNP with small molecules for increased peptide binding affinity [72] and controlled AuNP functionalization for enhanced cellular uptake [73]. Alloying of Au and Ag was used to prevent Ag<sup>+</sup> induced damage to mammalian gametes [74] and controlled ion release from AgNP was used for antibacterial treatment [75, 76]. Furthermore, an *in vitro* study has demonstrated the non-toxicity of polyethylene glycol (PEG) coated PLAL-AuNP to human cells [77]. Controlled cell binding was achieved by gold nanoparticles functionalized with a thermoresponsive polymer [78]. *In vivo* therapy was performed by a coating of neural electrodes with ligand-free platinum nanoparticles for increased impedance stability along with increased viability of surrounding neurons [79].

Other applications for PLAL-synthesized plasmonic nanoparticles are based on the aim of increasing the signal-to-noise ratio of analytical techniques such as surface-enhanced infrared absorption spectroscopy (SEIRAS) [80], surface-enhanced Raman spectroscopy (SERS) [8], surface- [81] and matrix-assisted [82] laser desorption/ionization mass spectroscopy (SALDI- and MALDI-MS). The increased performance is based on the absence of additional signals from ligands attached to the nanoparticle surface. In addition, gold aggregates were trapped by optical tweezing [83] and SERS was applied to the trapped species to prove hot spot-formation in the prepared aggregates [84].

Plasmonic nanoparticles were also used in energy applications, e.g., heterogeneous catalysis, mainly as alloys or attached to support-particles. AuPt alloy particles from PLAL were supported on CeO<sub>2</sub> nanotubes for the hydrogenation of 4-nitrophenol, with the alloy increasing the catalytic activity by a factor up to 4 with respect to the same system used with the pure metals supported on CeO<sub>2</sub> [85]. The same group has demonstrated that ligand-free gold nanoparticles are adsorbed onto the support, whereas adsorption of citrate-capped gold nanoparticles synthesized by chemical reduction was much lower even after purification [86]. Therefore, the CO conversion in the CO oxidation reaction was significantly increased through PLAL-AuNP [86]. The adsorption of ligand-free AuNP to BaSO<sub>4</sub> microparticles was shown fit the Freundlich adsorption model, which was explained by the oppositely charged ions in the Stern layers of the nano- and microparticles [87].

While this list of applications of ligand-free plasmonic nanoparticles synthesized by PLAL is incomplete, it demonstrates the versatility of the approach with respect to applications in multiple disciplines. All the aforementioned applications suffer from the same drawback, which is the inherently bimodal particle size distribution of colloids obtained by PLAL. A single size fraction of nanoparticles is highly desirable because the particle size is the main variable that affects the physical and chemical properties of noble metal colloids. In addition, the presence of additional large or small particles, depending on

the respective point of view, increases the monetary costs of the synthesis as small/large particles must be sorted out by additional processing steps. This highlights the necessity of understanding the PLAL process in more detail with an emphasis on the possible control of the particle size distribution and, ideally, avoiding bimodal colloids in a single-step ablation process. Therefore, the results presented in this dissertation on the analysis of the size reduction and quenching reactions with spatio-temporal resolution in the microsecond regime add not only to the scientific understanding of the origin of the nanoparticles bimodality but also at introducing laser-generated nanoparticles to potential applications in an industrial scale.

## 3.2 Stability of colloidal nanoparticles

Colloidal particles are thermodynamically unstable. Their formation and existence either are due to the low speed of the kinetic processes forcing them into larger quantities, by adsorption onto macroscopic surfaces, growth processes, or by collision-based aggregation. Colloids are defined as, at least, two-phase systems, characterized by the homogenous distribution (dispersion) of one phase; the dispersed or discontinuous phase, in the other phase, designated as the dispersion medium or continuous phase. Both phases can exist in all three physical states (solid, liquid, gaseous), even in the same state, e.g., emulsions are colloidal systems of two non-miscible liquids. This chapter introduces the aging and stabilization of nanoparticles dispersed in liquids.

### 3.2.1 Ostwald ripening

Multiple processes contribute to the destruction of nanoparticle dispersions. Among the most important, especially related to PLAL, are Ostwald ripening and coalescence of particles as described by Jendrzej et al. [88]. Ostwald ripening is a phenomenon that expresses itself by the dissolution of small droplets or particles in the continuous liquid phase. As a result, larger particles/droplets increase in size at the expense of smaller ones. Accordingly, Ostwald ripening is a diffusion-controlled process that required at least a minimum solubility of the dispersed phase in the surrounding liquid phase. Assuming a solubility of the dispersed phase of absolutely zero in the continuous medium, Ostwald ripening cannot occur [89, 90]:

$$\frac{S(r)}{S(\infty)} = \exp\left(\frac{2\gamma V_m}{rRT}\right) \quad \text{Equation (1)}$$

$S(r)$ : solubility of a particle with radius  $r$

$S(\infty)$ : solubility of the bulk material

$\gamma$ : interfacial tension

$V_m$ : molar volume of the dispersed phase

$R$ : gas constant (8.314 J/mol\*K)

The equation is known as the Kelvin equation. It denotes that the solubility of small particles/droplets increases exponentially with decreasing size. An 8 nm (= 2r) particle, therefore, exhibits a 10-times higher solubility compared to 20 nm particles [91]. This dependency highlights the importance of Ostwald ripening in colloidal chemistry as it shows that Ostwald ripening is outmost impossible to prevent, even for crystalline particles [92].

The synthesis of monodisperse colloids is not exclusively desired due to more defined properties compared to polydisperse colloids but also a consequence of the implications derived from the Ostwald equation [91]:

$$\frac{RT}{V_m} \ln \left( \frac{S(r_1)}{S(r_2)} \right) = 2\gamma \left( \frac{1}{r_1} - \frac{1}{r_2} \right) \quad \text{Equation (2)}$$

$S(r_{1,2})$ : solubility of the particle with radii 1 and 2

$r_{1,2}$ : droplets/particles of radius 1 and 2

Accordingly, the rate of Ostwald ripening increases upon increasing difference of the particle sizes in the colloid [91]. Regarding PLAL the bi-, or more precisely trimodal, size distribution, made of nanoclusters, primary, and secondary nanoparticles, offers the possibility of fast particle growth caused by Ostwald ripening [88]. Still, Equation (2) also defines the limit of Ostwald ripening, because its rate decreases with increasing particle size. This prevents the formation of a single large droplet as the result of ripening.

Ostwald ripening has been demonstrated for nanoparticles obtained by PLAL for some noble metals (Cu [93], Pt [88], Au [88, 93]) and is thus an important contribution to the size of the nanoparticles. As Ostwald ripening is a time-consuming phenomenon it is irrelevant for studying the size evolution of nanoparticles trapped inside the oscillation cavitation bubble during PLAL (section 5.2.1 and 5.2.2). On the other hand, as soon as the laser-synthesized nanoparticles are analyzed by *ex situ* methods (e.g., electron microscopy and light scattering) the influence of ripening effects should be considered. Accordingly, analytical results may differ at different measurement delays after sample collection. This is demonstrated in section 5.1.2 using the example of nanoclusters that are smaller than 3 nm. While this particle species is usually not observed in PLAL colloids due to its consumption by Ostwald ripening, it can indeed be stabilized by using particle concentrations as low as some tens of milligram per liter. Considering the importance of particle ripening is further important for the interpretation of the *in situ* X-ray experiments performed in this dissertation and linking the results to the findings from *ex situ* particle analysis.

### 3.2.2 Coagulation and coalescence

Coagulation describes the phenomenon of two particles approaching each other until their surfaces are in direct contact. A coagulate can additionally grow if more particles attach to its surface. The resulting fractal object is either an agglomerate or aggregate. These structures differ in the reversibility

of the particle contact. Irreversibly coagulated nanoparticles are defined as aggregates, while agglomerates are re-dispersable by energy input [94].

Two types of coagulation are discriminated fast and slow coagulation. In fast coagulation, every collision between two particles results in coagulation. In terms of mathematics, it is possible to define a stability ratio  $W = \text{number of collisions} / \text{number of collisions resulting in coagulation}$ . While  $W$  is equal to 1 for fast coagulation, its rate  $R_f$  is hampered by the actual diffusion speed of the nanoparticles and the particle number concentration in the colloid [90]. An additional potential barrier between the approaching nanoparticles, resulting in a stability ratio  $W > 1$ , characterizes slow coagulation. In other words, some collisions do not induce coagulation. Accordingly,  $W$  reduces the rate of slow coagulation  $R_s = R_f / W$  [90]. The phenomena contributing to the responsible potential barrier are electrostatic repulsion of the particles and repulsion by van der Waals forces (3.2.3 DLVO theory). If polymers are linked to the particle surface, their interaction can also add to the repulsive force (3.2.3 Stabilization by polymers).

Coalescence is the fusion of two or more coagulated droplets to a single larger drop [95]. It primarily occurs in emulsions but is also relevant for the solid nanoparticles produced in PLAL [77, 88]. Besides the fusion of coagulated dimers to larger particles, coalescence is suspected to contribute to the formation of large spherical particles by fusion of coagulated small particles confined inside the laser-induced cavitation bubble [19, 20, 30]. When the oscillating bubble shrinks to its minimum volume the nanoparticles experience harsh conditions of up to  $\sim 400$  °C and  $\sim 10^5$  Pa [66]. Although, bubble collapse occurs within several microseconds not leaving much time for coalescence to proceed. The laser-induced cavitation bubble is described in detail in 3.3.1.

### 3.2.3 Electrostatic and steric stabilization

#### Electrostatic stabilization - DLVO theory

The theory describing the interactions between two approaching nanoparticles in a liquid was established in 1939-1945 by Derjaguin and Landau [96] and by Verwey and Overbeek [97]. The name DLVO theory stems from the first letters of its inventors' names. In DLVO theory, the repulsive force by surface charges of the nanoparticles and attractive forces by van der Waals forces (vdW) are used to calculate the stability of nanoparticles against aggregation. As the number of considered interparticle forces is reduced to two, DLVO theory accounts exclusively for charged nanoparticles, without polymers attached to the surface [96, 97]. The relevance of the implications for laser-

generated nanoparticles is clear, especially as such particles are stabilized exclusively by surface charges [98]. It is reasonable to assume that laser-generated nanoparticles are charged because of, e.g., hydrogen group formation at the surface [21, 99]. For the description of surface charges, the model of Graham, a modification of the Stern model, for the electrical double layer of ions detached to a nanoparticle is introduced [100]. In the following, the curved surface of a spherical particle is approximated by a flat surface.

For reasons of charge neutrality, a layer of counterions binds specifically to the particle surface. This fixed layer was first described by Helmholtz and is called the inner Helmholtz layer (IHL) in the Stern model. On top of the fixed ion layer, the outer Helmholtz layer (OHL) is connected. It is characterized by reduced charge density compared to the IHP as its ions exhibit a solvation shell. At larger distances from the surface a diffusive, non-specifically bound layer of solvated ions accumulates around the particle surface [101]. This diffusive ion cloud is the Gouy-Chapman layer. A graphical description of the influence of ions accumulated around the solid surface on its potential  $\Psi$  as a function of distance  $X$  from the surface ( $X = 0$ ) is given in Figure 4 [101].

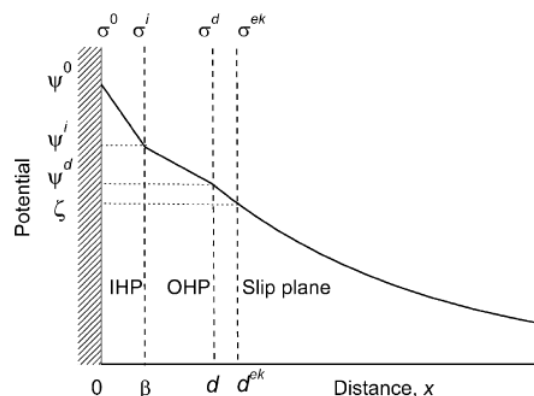


**Figure 4:** The electrostatic potential of a charged flat surface  $\Psi$  as a function distance  $X$  using the example of a positively charged surface [101]. The potential is a result of the charge density  $\sigma(X)$ . The surface potential is not experimentally accessible. The IHL of specifically adsorbed counterions ends at the IHP ( $\Psi_i$ ;  $X = \beta$ ). The OHL consist of solvated ions, starting at the IHP and ending at the OHP ( $\Psi_d$ ;  $X = d$ ). The OHP marks the beginning of the diffusive layer of counterions which results from the need of electroneutrality of the system. The extension of the diffusive layer can be calculated by linear approximation of the Poisson-Boltzmann differential equation (see Equation (4)).

The surface potential  $\Psi_0$  (charge density  $\sigma^0$ ) of a particle is not directly accessible. At a slightly larger distance from the surface, the inner Helmholtz plane (IHP) is located ( $X = \beta$ ;  $\sigma^i$ ;  $\Psi^i$ ), marking the edge of the IHL. Thereafter follows the outer Helmholtz plane (OHP) which ends at the outer Helmholtz

plane (OHP;  $x = d$ ;  $\sigma^d$ ;  $\Psi^d$ ). The OHP marks the locations of the diffusive ion layer around the particle. IHL and OHL are sublayers of the initially described Stern layer. While the ions in the IHL are directly bound to the particle surface, the ions of the OHL are solvated, which results in a reduced charge density. The overall charge of the system sums up to 0 ( $\sigma^0 + \sigma^i + \sigma^d = 0$ ) for reasons of electroneutrality [101]. Finally, the experimentally assessable potential is located at the slip plane ( $X = d^{ek}$ ). At this distance, the zeta potential  $\zeta = f(\kappa)$ ; see Equation (3)) is accessible. It is a measure for the stability of the nanoparticles against aggregation. If a higher electrolyte concentration is considered compared to the situation in Figure 4, the surface potential  $\Psi_0$  would be unaffected but the potential would approach the x-axis faster. This is because the double layer is compressed by the additional charges in the liquid [90]. The spatial extension of the double layer is described by the inverse Debye length  $\kappa$ , it has the dimension of an inverse distance [ $m^{-1}$ ] [90]:

$$\kappa = \left( \frac{e^2 \sum n_i^0 z_i^2}{\epsilon k_B T} \right)^{1/2} \quad \text{Equation (3)}$$

$e$ : elementary charge ( $1.602 \cdot 10^{-19}$  C)

$n_i$ : number of ions per unit volume

$z_i$ : valency of each type of ion

$k_B$ : Boltzmann constant ( $1.380 \cdot 10^{-23}$  J/K)

Accordingly, in a 1:1-electrolyte of given concentration the Debye length  $\kappa^{-1}$  only depends on the permittivity  $\epsilon$  of the liquid phase, and the actual temperature. The electrical double layer may extend from one to more than 100 nanometers in a typical nanoparticle colloid [90]. As the ion cloud, described by  $\kappa^{-1}$ , plays a central role in the DLVO theory of colloidal stability, the actual theory is now accessible. At a distance away from the charges surface equal to the Debye length, the potential is reduced by  $1/e$  because of the linear approximation of the Poisson-Boltzmann differential equation, for 1:1 an electrolyte and low potentials ( $\Psi_0 < 25$  mV;  $|ze\Psi| < k_B T$ ) [100, 102]:

$$\Psi \approx \Psi_0 \exp(-\kappa x) \quad \text{Equation (4)}$$

$\Psi_0$ : surface charge density

$x$ : distance from the surface

Equation (4) is the so-called Debye-Hückel equation [102]. In principle, the exponential decay of the surface potential as a function of the distance from the surface can be suspected from the curve progression in Figure 4, even though the actually presented curve is more detailed.

The sum all interaction energies considered in DLVO theory is  $W = W_A + W_R$ , with the attractive van der Waals energies  $W_A$  and the repulsive energies mediated by the electric double layer  $W_R$  [90]. As the treatment of the interaction of two approaching spherical particles complicates the ansatz, the calculations of  $W_{A,R}$  is limited to the case of two interacting plates. The mathematical correlations are [90]:

$$W = W_A + W_R = -\frac{A}{D^2} + B * \exp(-\kappa D) \quad \text{Equation (5)}$$

$A: = H_A/12\pi$  [Hamaker constant  $H_A$ : strength of vdW force between two particles]

$$B: = 64n_0kBTZ^2/\kappa$$

$n_0$ : number of ions per unit volume

$$Z: = \tanh(ze\Psi_0/4k_B T)$$

Obviously, the attractive forces exhibit a longer range and dominate the total interaction energy  $W$  when the plates approach each other close enough. An important difference of the plate approximation to the case of two spherical particles is that the exponent of the distance in the attractive term is 2 for parallel plates [102]. The implications of the DLVO theory are summarized in Figure 5 [102]. Plotting the interaction energy  $W$  as a function of the distance normalized to the Debye length  $\kappa D$  the attractive and repulsive contributions (dashed lines) become visible. The inset on the top right shows the assumed geometry of two parallel negatively charged plates at distance  $D$ . It is clear that the total interaction energy depends largely on the surface charge density  $\sigma$  because a non-charged surface does not exhibit electric double-layer repulsion and  $W = W_A + 0$  (low  $\sigma$  in Figure 5). Regarding the situation of high  $\sigma$  and starting at large normalized distances of the parallels plates, the attractive force by vdW interactions is never 0 but weak for high  $\kappa D$ . At shorter distance  $\kappa D \approx 5$  a local minimum of the total interaction energy  $W$  appears. This so-called secondary minimum marks the point of particle agglomeration. Remember that agglomerates are clusters of particles that are reversibly bound together. At even smaller separations of the plates, an energy barrier arises because of  $W_A \sim D^{-2}$ . The energy barrier prevents aggregation effectively if it exceeds the thermal energy significantly  $W \gg k_B T$ . If the barrier is, however, overcome and the parallel plates approach very short distance  $D$ , the vdW attraction becomes predominant and irreversible aggregation at the primary minimum occurs. Note, that additional repulsive forces by Born energy and solvation forces at smallest  $D$  values are neglected in Figure 5 as they are not part of the classical DLVO theory.

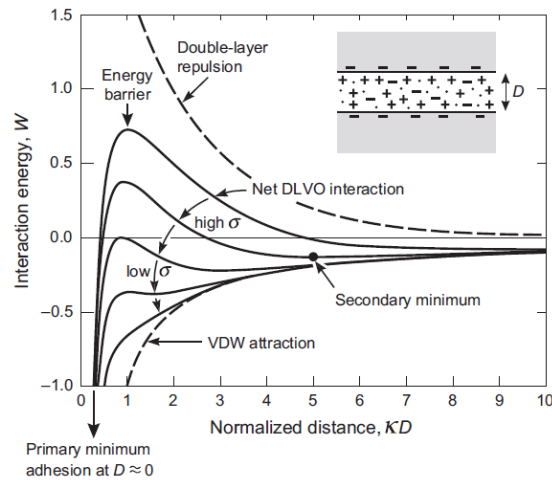


**Figure 5:** Total interaction energy  $W$  as a function of the normalized distance  $\kappa D$  of two charged parallel plates according to the DLVO theory [102]. The repulsive contribution by the electric double layers  $W_R$  and the attractive contribution  $W_A$  by vdW forces are shown as dashed lines. At high surface charge density  $\sigma$ , a secondary minimum at medium distances occurs. It marks reversible agglomeration. At low distances, an energy barrier evolves that hinders the plates from the aggregation if it exceeds the thermal energy  $k_B T$  significantly. At even shorter distances of the plates, the vdW attraction becomes superior resulting in irreversible aggregation of particles (primary minimum).

The DLVO theory fails for approaching particles closer than  $\sim 10$  nm [90]. This is because of neglecting of another interaction, the solvation force  $W_S$  [102, 103]. At short distances, these forces might dominate the total interaction energy. Solvation force is largely excluded here but it should be noted that it scales with  $\exp(-D/C)$ , with the interparticle distance  $D$ . Factor  $C$  depends on the particular form of solvation force [102].

Coming back to Equation (5), it can be calculated that if  $\kappa D = 2$  fast coagulation is initiated. At standard conditions and assuming water as the liquid phase this critical coagulation concentration (c.c.c.) is inversely proportional to the sixth power of the electrolytes valency  $z$  (c.c.c.  $\sim z^{-6}$ ). This is the so-called Schulze-Hardy rule [104, 105]. It explains why coagulation is disproportionately more effective by multivalent ions like  $\text{Fe}^{3+}$  than by monovalent ions like  $\text{Na}^+$ . Anticipating section 3.4 on nanoparticle size control during PLAL induced by electrolytes, the Schulz-Hardy rule points out why for size quenching during laser synthesis only monovalent ions are used.

*Steric stabilization by polymers*

Polymers can increase the stability of nanoparticles against aggregation. This most prominent effect is steric stabilization, which is most easily described by the model of a rigid wall mediating a repulsive force, but also stabilization by depletion forces is possible. In contrast to the long-range forces mediated by charged surfaces, the repulsive forces induced by polymers are short ranged. Similar to electrostatic stabilization the repulsive forces mediated by polymers must overcome particle attraction by vdW forces.

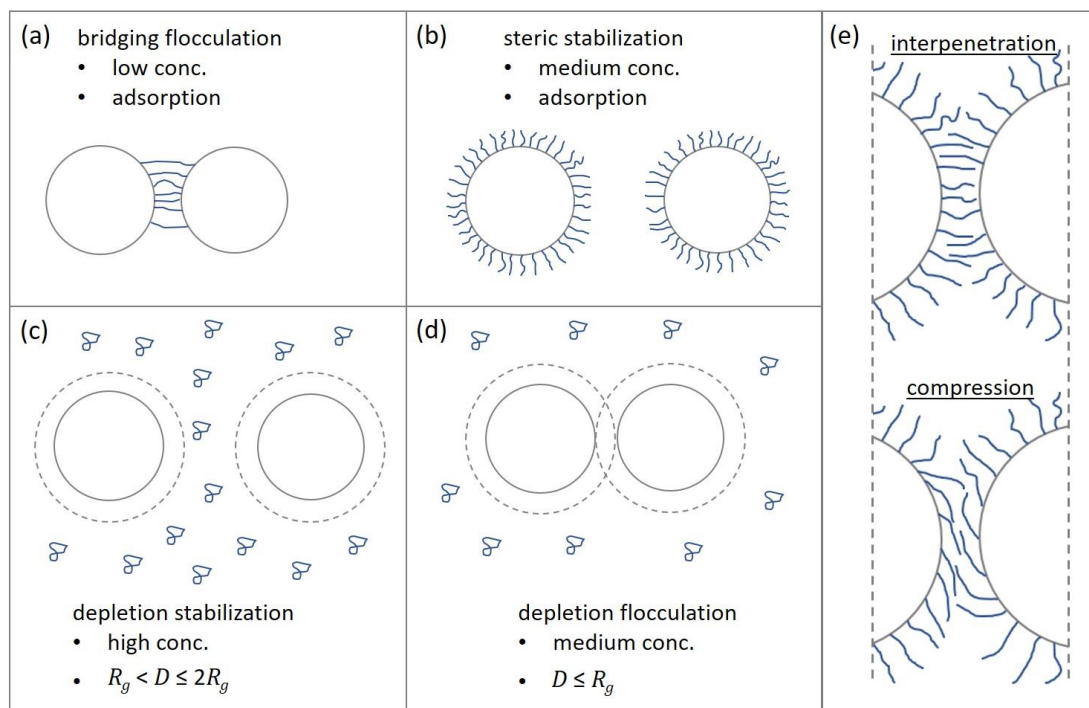


**Figure 6:** Schemes of possible polymer mediated interactions between two approaching colloidal particles. (a) Bridging flocculation occurs at low surface coverage of particles with polymers. The polymer must have two active sites to anchor to two particles. (b) Steric stabilization requires full surface coverage of the particles. The interpenetration of the polymer shell is energetically an entropic unfavored. If the shells interpenetrate each other, e.g., because the solvent is at the  $\Theta$ -point, flocculation occurs (e). If on the other hand polymer-polymer interaction is unfavored compression of the shells occurs when they spatially overlap. A restoring force results and flocculation is prevented (e). (c) Depletion stabilization is an effect of unbound free polymer in solution. At high concentrations, the approaching particles lead to polymer-solvent demixing in the gap. (d) Depletion flocculation occurs at medium concentrations of the free polymer. The excluded volume around the particles that is not accessible of the polymer is reduced if the particles are in direct contact. The osmotic pressure difference decreases.

Steric effects become significant at distances  $L \leq D \leq 2L$  [90]. Here,  $L$  is the extension of the polymer shell into the liquid and  $D$  is the distance between the surfaces of the two particles cores. The interactions of particles with adsorbed polymers are complex and can be attractive or repulsive [90]. The direction of the force field depends on polymer concentration and the polymers solvency. Polymer concentration effects are best described using the model in Figure 6a. As can be seen, if a polymer adsorbs to the surface of one particle and contains another functionality to bind to a free surface site of a second particle, bridging by polymers occurs between the particles. As the particle is not in direct contact, a difference to coagulation and coalescence (section 3.2.2), the destabilization of a colloid by bridging is referred to as flocculation [90].

Steric stabilization by polymers (Figure 6b) anchored to the surface of the particles is a process that can be dominated by enthalpy, entropy, or both effects. In order to explain this, it is worth noticing that several authors reported on the similarity of the temperature at which flocculation starts and the  $\theta$ -temperature [106-108]. The  $\theta$ -temperature was described by Flory [109]. The interactions between the polymer chains are equal to those with the solvent molecules at that temperature. The polymer chains behave therefore like molecules rather than colloids. In good solvents, the polymer chain exhibits maximum extension. At the same time, they do not sense each and the steric repulsion force drops to its minimum causing flocculation [109]. This is depicted in Figure 6e (top) by the interpenetrating polymer shell. If the  $\theta$ -point is not reached the shells of extended polymers attached to the nanoparticles of a dispersion will repel each other at the distance beginning of polymer shell interpenetration [90]. This is shown in Figure 6e by the lower sketch which shown the situation of polymer shell compression. As noted, steric stabilization has an enthalpy and an entropy contribution. The first one is based on the mixing of the polymer shells. In a good solvent, the interactions between the extended polymer chains and the solvent molecules are favored compared with polymer-polymer interactions. Therefore, polymer-shell intermixing increase the enthalpy of the system of mixing [90]. An alternative interpretation is based on the resulting osmotic pressure difference [95]. The entropy contribution to steric stabilization is based on the loss of degrees of freedom of the polymer chains upon interpenetration [95].

In addition to forces mediated between colloidal particles, unbound polymers in the solution can induce repulsive and attractive forces [102]. They are depletion stabilization and deletion flocculation (Figure 6c,d). Depletion stabilization occurs at high free-polymer concentrations. Depletion forces are based on the volume surrounding each particle that cannot be entered by the free polymer of size  $R_g$  (radius of gyration) because of decreasing entropy [102]. The excluded volume is highlighted in Figure 6c,d by the dashed lines around the particles. Considering a situation in which two particles approach

to a distance  $D \leq R_g$ , the total excluded volume decreases by the overlapping volume. The depletion of free polymer between the particles results in an osmotic pressure difference that sucks out the solvent from the gap, leading to flocculation of the particles [110]. On the other hand, depletion stabilization requires higher free polymer concentration and the involved particle-to-particle distance is different (Figure 6c). Two particles that approach to the distance of one or two  $R_g$ , the excluded volume is larger compared to depletion flocculation, in concentrated polymer solutions sense a repulsive force. This is because of polymer-solvent demixing in the gap between two particles, an energetically unfavored process [90].

In general, if the liquid phase represents a good solvent for the polymer dedicated for stabilization of the colloid a repulsive force between the nanoparticles is expected.

### 3.3 Noble metal nanoparticles

#### Bulk material approximation

Plasmonic material is defined by their optical properties given by the electronic structure of the material. Nanoparticles represent a special case of plasmonic materials, especially those made of the noble metals gold, silver, and copper which exhibit a strong plasmon resonance in the visible range of the optical spectrum [68, 111]. The evolution of surface plasmons at the interface between two media requires them having permittivities  $\epsilon$  of opposite sign. This is met for metal nanoparticles ( $\epsilon < 1$ ) dispersed in water ( $\epsilon_m > 1$ ) [112]. It is worth noting here that the permittivity is a complex quantity given by the sum of its real and imaginary part  $\epsilon(\omega) = \epsilon_r + i\epsilon_i$ . Obviously, the complex permittivity is additionally a function of the radial frequency of incident light  $\omega$ . The frequency dependent complex permittivity (here: dielectric function) of bulk gold is shown in Figure 7a [113]. While the imaginary part of the permittivity is almost independent of the incident light wavelength, its real part decreases with increasing wavelength, exhibiting mostly negative values. The electrons in the conduction band of a metal (particle) contribute to its free electron gas. Therefore, surface plasmons can be regarded as the collective oscillations of conduction electrons. An incident electromagnetic wave induces a dipole at the metal nanoparticle surface by excitation of the free electron gas to a damped oscillation [113]. Hence, the polarizability  $\alpha$  of a nanoparticle is of major importance for the evolution of surface plasmons as it is a measure for the difficulty of inducing a dipole by electron-atom core displacement. This is schematically illustrated in Figure 7b for the examples of a dipolar plasmon induced at a metal nanosphere [114].

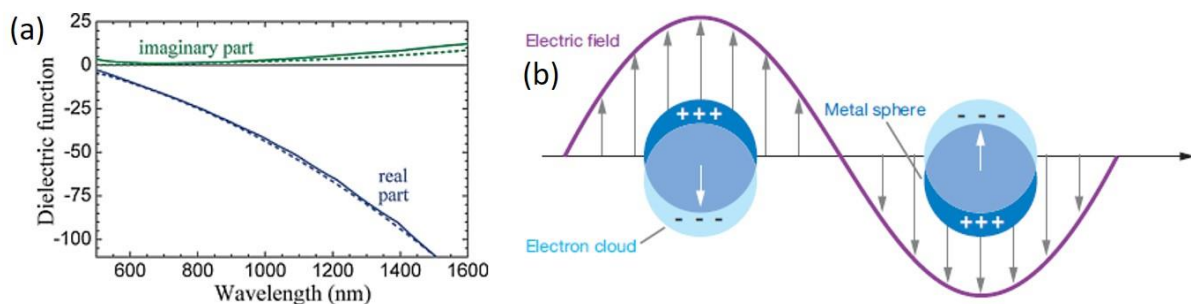


**Figure 7:** (a) Bulk dielectric function of gold as a function of the excitation wavelength. The solid curves represent experimental data for the real and imaginary part of the dielectric function taken from [115] by [113]. The dashed lines are derived from Equation (6) [113]. (b) Scheme of the effect of an incident electromagnetic wave on a spherical metal nanoparticle. The induced dipole, indicated by positive and negative signs, oscillates uniform across the nanosphere [114].

Regarding a perfectly spherical nanoparticle, its optical dispersion is a function of its extinction cross section  $C_{ext}$ . It reflects the loss of photons while crossing the nanoparticle. The losses are caused by absorption  $C_{abs}$  and scattering  $C_{sca}$  of photons [116]. If the spherical nanoparticle matches the condition of  $[2\pi(\varepsilon_m)^{1/2}/\lambda]R \ll 1$ , with  $\lambda$  being the wavelength of the incident light, its extinction cross section  $C_{ext}$  is given by [112, 116]:

$$C_{ext} = \frac{24\pi^2 R^3 \varepsilon_m^{3/2}}{\lambda} \left[ \frac{\varepsilon_i}{(\varepsilon_r + 2\varepsilon_m)^2 + \varepsilon_i^2} \right] \quad \text{Equation (6)}$$

$R$ : radius of a nanosphere

The origin of the absorption peak in the optical extinction spectrum is predicted by Equation (6) through the condition  $\varepsilon_r = -2\varepsilon_m$  if at the same time the imaginary part of the permittivity  $\varepsilon_i$  is small [112] (Figure 7a). The real part of the permittivity determines the actual wavelength of the surface plasmon resonance, and the imaginary part determines the bandwidth [117]. Finally, the optical response  $C_{ext}$  of a spherical nanoparticle depends on particle size  $R^3$ , at constant wavelength  $\lambda$ . Nevertheless, replacing the single particle size  $R$  by an entire particle size distribution requires adaptation of Equation (6) as demonstrated by Amendola and Meneghetti, who replaced  $R$  by the two parameters that are necessary for the characterization of a log-normal size distribution [118].

#### Large nanoparticles

Large spherical particles with sizes above  $d \approx 0.2\lambda_m = \lambda_0/(\varepsilon_m)^{1/2}$  require the introduction of retardation effects to describe their optical response to excitation. Here,  $\lambda_m$  is the mode wavelength in the liquid phase, and  $\lambda_0$  is the wavelength in vacuum. This was considered in the theory of Gustav Mie already in 1908 [116]. He found that the particles extinction cross-section is a function of electric and magnetic scattering coefficients, as well as of  $\lambda_m$ . For large spherical nanoparticles the polarizability  $\alpha$  is [119]:

$$\alpha = 3V\varepsilon_m \frac{1 - \frac{0.1(\varepsilon + \varepsilon_m)\theta^2}{4}}{\frac{\varepsilon + 2\varepsilon_m}{\varepsilon - \varepsilon_m} - \frac{(0.1\varepsilon + \varepsilon_m)\theta^2}{4} - i(2/3)\varepsilon_m^{3/2}\theta^3} \quad \text{Equation (6)}$$

$\theta$ : size parameter ( $= 2\pi R/\lambda$ )

$R$ : radius of a sphere

When the size parameter  $\theta$  becomes zero, Equation (7) becomes equal to the approximation of  $\alpha$  for smaller nanoparticles down to 10 nm, which do not show significant retardation effects [113].

### Small nanoparticles/-clusters

When the size of a nanoparticle approaches the penetration depth of a current, induced by an electromagnetic field, inside the conductive material  $\delta = 1/\sqrt{\pi f \mu \sigma}$  ( $f$ : current frequency,  $\mu$ : permeability,  $\sigma$ : conductivity) [120], the assumption of equality of the permittivity in bulk and nanomaterial is no longer valid [113]. The penetration depth for gold is about 10-15 nm depending on the incident wavelength. As a result, the permittivity  $\varepsilon(\omega)$  is modified to consider the increased conduction band electrons damping rate  $\tau^{-1}$  [121]:

$$\varepsilon(\omega)_{mod} = \varepsilon(\omega) + \frac{\omega_p^2}{\omega(\omega + i\tau^{-1})} - \frac{\omega_p^2}{\omega(\omega + i\tau^{-1} + \frac{iv_F}{R})} \quad \text{Equation (7)}$$

$v_F$ : Fermi velocity

Electrons with energies approaching the Fermi level additionally contribute to the damping rate  $\tau^{-1}$ . Comparison of the results from Equation (8) with experimental data showed reasonable agreement [113]. The plasma frequency  $\omega_p$  of a metal is a material constant and is proportional to the electron number density  $N^{1/2}$  and the electrons effective mass  $(1/m_{eff})^{1/2}$  [122]. At the plasma frequency, the permittivity of the material exhibits negative values, leading to the evolution of plasmons (Figure 7b).

### 3.4 Size control by additives in laser synthesis of noble metal nanoparticles

The strategy of size control during PLAL by size quenching using additives is based on the principals of colloidal chemistry that mediate the stability of particles against aggregation. For the investigation, the influence of additives on the size of the nanoparticles the laser parameters are kept constant. Nevertheless, in PLAL as well as in re-irradiation of colloids and particles fragmentation (PLFL) or melting (PLML) size control of particles is to some extent possible [123-125].

Particle aggregation and growth are prevented in PLAL by electrostatic and steric stabilization as described in 3.2. Steric stabilization and particle functionalization with specific molecules and chemical groups are often not distinguished but it is noted that functionalization often results in additional steric stabilization. A typical functionalization process is performed either by adding the ligand to the liquid phase, in which it is soluble, prior to laser ablation or to add the ligand to the final colloidal dispersion. The organic molecules used for size control by the introduction of steric repulsion can be subdivided into several groups:

- I. Surfactants
  - a. Ionic [17, 126, 127]
  - b. Non-ionic [128, 129]
- II. Polymers
  - a. Physisorption [130-132]
  - b. Chemisorption [78, 131, 133]
- III. Biomolecules [134-136]
- IV. Monomer solutions [137-139]

The synthesis of silver nanoparticles in the ionic surfactant sodium dodecyl sulfate (SDS) was first investigated by Mafuné et al [126]. Note that when comparing the results of different groups, it is also important to consider the experimental setup for data interpretation. Mafuné et al. performed batch ablation using a 532 nm laser wavelength, which is close enough to the SPR peak of silver nanoparticle at about 400 nm to allow significant absorption of light by nanoparticles from previous pulses. Therefore, the ablated particles might experience PLFL what additionally contributes to the size reduction of particles [51]. The effective size reduction that was observed in colloids containing SDS ( $c = 0.003\text{-}0.1\text{ M}$ ) is, therefore, the sum size reduction during PLAL and PLFL. As shown by Lau and Barcikowski PLFL of zinc oxide particles in a free liquid jet, containing no surfactants, into a 0.1 M SDS solution effectively prevents agglomeration, and thus ripening, of the fragmented particles [140]. Still, the size reduction effect of SDS is unquestionable and was supported by Tomko et al. by PLAL of gold in 8 mM SDS solution [17]. Compared to PLAL in pure water, the average particle size was reduced by

$\geq 5$  nm. While size reduction of ablated nanoparticles is effective using SDS it is difficult to attribute the effect solely to steric effects as SDS contains an ionic sulfate group. As discussed below size reduction of noble metal nanoparticles by micromolar amounts of monovalent ions is likewise possible and very effective. In addition to SDS, the surfactant 2-[2-(2-methoxyethoxy)ethoxy]acetic acid (MEEAA) was used for size reduction of the non-plasmonic material yttrium oxide [141]. The particles were reduced from  $\sim 6$  nm to 2 nm. Again, attributing the size reduction during PLAL is difficult as ablation in a batch process at a laser wavelength of 355 nm was performed, so that possible fragmented species were stabilized by MEEAA. Furthermore, MEEAA is a charged molecule and the effect of the decreased pH of the solvent is not clear until now but might induce size quenching similar to dissolved inorganic ions [142].

Polyvinylpyrrolidone (PVP) is a non-ionic polymer that is frequently used in the synthesis of silver nanoparticles by the reduction of precursor substances [143]. Millimolar solutions of PVP reduce the size of silver nanoparticles obtained from batch-PLAL at 1064 nm from 18 nm to 11-13 nm, depending on the respective concentration [51]. PVP was also used to reduce the size UV-region of the electromagnetic spectrum, of aluminum particles, exhibiting SPR in the and to minimize surface oxidation [130]. The size was reduced by up to 9 nm in average compared to PLAL in pure water. In contrast, PLAL in the presence of poly(vinyl alcohol) (PVA) reduced the average size by 6 nm.

When working with gold nanoparticles thiol terminated capping agents are frequently used due to the strong bond to the gold surface. Salmaso et al. performed batch-PLAL of gold in pure water at 1064 nm and added a thiol-terminated thermoresponsive polymer to the dispersion [78]. This *ex situ* addition of a functional polymer did however not result in size reduction of the gold nanoparticles but the colloidal stability against aggregation was significantly increased.

Sajti et al. though demonstrated the importance of time delay after laser-synthesis of gold nanoparticles and the addition of thiolate peptides [144]. Micromolar amounts of peptides were added seconds to minutes after PLAL in a flow chamber, to avoid re-irradiation of the synthesized nanoparticles. They have shown that both the hydrodynamic and Feret diameter of the final gold nanoparticles increases with an increasing delay of peptide addition. Accordingly, the introduced steric effect effectively suppressed particle growth and ripening [144]. The same group performed batch-PLAL of gold in the presence of thiolated oligonucleotides and found significant size reduction [145]. These results give rise to the question of whether size reduction by organic molecules happens inside of the laser-induced cavitation bubble or exclusively on a later stage or both. This question is addressed in section 5.2.2 of this work.

A very effective approach of the size reduction of noble metal nanoparticles is the used of monovalent anions in micromolar concentrations. If a concentration is employed small enough to not decrease the Debye length (Equation (3)) of the nanoparticles and thus destabilizing the colloid as predicted by DLVO theory (section 3.2.3), the size of e.g., gold nanoparticles is significantly reduced. At the same time, the ligand-free nature of the PLAL nanoparticles is conserved. The effect was first described by Rehbock et al. for the ablation of gold in concentrations of 1-2000  $\mu\text{M}$  NaCl, NaBr, NaF, and  $\text{Na}_2\text{SO}_4$  [21]. Due to the identity of the cation, the size reduction power of the anion was extracted. A follow-up study has demonstrated the importance of the anions compared to the cation [146]. The anions  $\text{F}^-$  and  $\text{SO}_4^{2-}$  did not result in size quenching of nanoparticles. A similar effect was observed for PLAL of gold and palladium nanoparticles in sodium phosphate buffer solution (NaPP) that reduced the average particle Feret diameter from  $>20$  nm down to 5 nm [21, 142]. The effectiveness of the different anions was found to correlate to the Hofmeister sequence  $\text{F}^- \approx \text{SO}_4^{2-} < \text{Cl}^- \approx \text{NO}_3^- < \text{I}^- \approx \text{Br}^- \approx \text{SCN}^-$  and to scale proportionally with the hydration of the anions but scale inversely proportional with the respective polarizability [146]. Using X-ray photoelectron spectroscopy (XPS) increased stability and reduced particle size was demonstrated to origin from additional surface oxidation of the particles. Additionally, ion adsorption contributed to the surface charge of nanoparticles [146].

In summary, organic macromolecules and monovalent anions are capable to reduce the size of nanoparticles during PLAL. Still, for both material classes, it remains elusive whether they interact with the nascent nanoparticles already inside the laser-induced cavitation bubble or in the liquid phase.

### 3.5 X-rays for the static and dynamic size analysis of nanoparticles

It is of utmost importance to note that the investigation of the cavitation bubble is highly relevant because it contains a large fraction of the total ablation mass during its existence. This was for the first time experimentally shown by direct probing of the cavitation bubble using small-angle X-ray scattering (SAXS) by Ibrahimkutty et al. [19]. It was found that the laser-induced cavitation bubble acts as a reservoir of the ablated gold species during the entire lifetime of the bubble, including all subsequent oscillations. Already after 80  $\mu\text{s}$  the existence of two distinct particle size fractions was demonstrated, the so-called primary and secondary particles (see Figure 8) [19]. Yet, the results could not distinguish if the secondary particles consist of large spherical nanoparticles, agglomerates, or a mixture of both.

In a subsequent study, the cavitation bubble induced by PLAL of a silver target was investigated [20]. While the same particle fractions, primary and secondary particles, were found, it was furthermore shown that the size and relative volume fraction depend on the delay after laser impact and the related bubble collapse and rebound phases. The size of small primary particles was hardly affected by the oscillations of the cavitation bubble. On the other hand, the secondary particles increased by up to 20 nm in diameter upon the collapse of the first cavitation bubble after  $\sim 100 \mu\text{s}$ . At the same time, the relative mass of the secondary particles compared to the primary particles increased [20]. All these findings pointed towards an agglomeration of particles induced by the cavitation bubble. This effect is most pronounced in the center of the bubble over the target surface. Yet, this can still not be considered as a proof for the absence of large spherical nanoparticles that are always found in *ex situ* particle characterization for PLAL colloids.

The effect of the dynamic cavitation bubble on the confined nanoparticle, measured by high-speed SAXS, is shown in Figure 8a for different heights above the target surface (0.17 mm; 0.5 mm center of the cavitation bubble; 1.0 mm; 1.2 mm above the maximumly extended bubble) [19]. The blue dots represent the size of small primary particles, the black squares the secondary particles, here accounted as agglomerates. For details of data analysis and independent consideration of two size fractions from a single X-ray scattering signal see Equation (11) and the associated text passage. The first vertical dashed line in Figure 8a marks the laser impact at zero delays. The second vertical at about 150  $\mu\text{s}$  marks the collapse of the first cavitation bubble [19]. At 0.17 mm above the target, the size of both particle fractions increased upon the collapse of the first and evolution of the second cavitation bubble, which is possibly caused by coalescence and growth due to high temperature and pressure conditions. Large secondary particles (black squares) were also found in the center of the bubble (0.5 mm height), at the top of the bubble (1.0 mm height), and above the bubble (1.2 mm height).

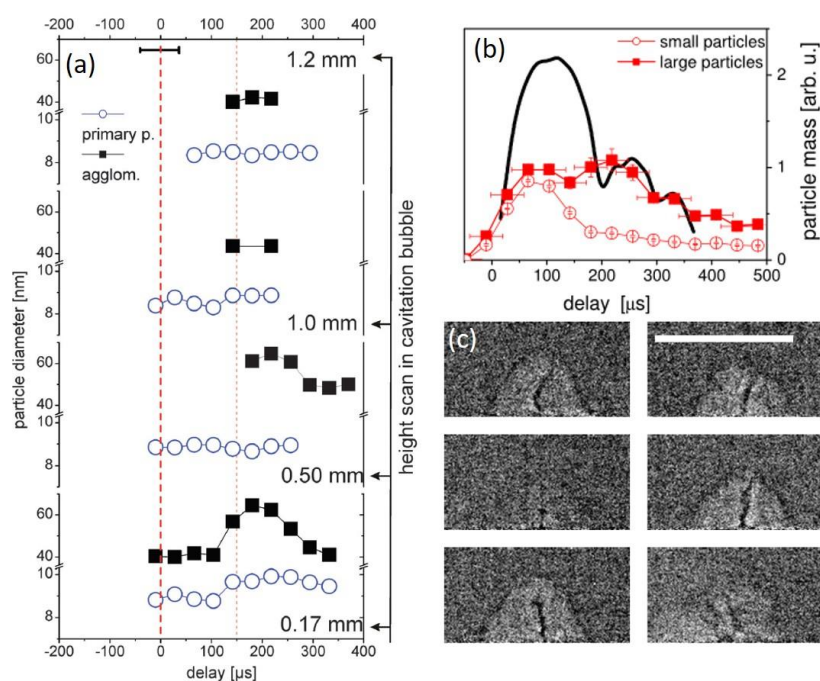


**Figure 8:** (a) Particle diameters obtained by time-resolved SAXS of primary (blue dots) and secondary (here agglomerates) (black squares) particles confined inside the laser-induced cavitation bubble during PLAL as a function of the delay after laser impact (red dashed vertical line). The cavitation bubble was scanned at different heights above the target surface (right ordinate). The dotted vertical line at 150  $\mu\text{s}$  marks the collapse of the first cavitation bubble. [20]. (b) Relative particle fraction mass from SAXS as a function of the delay. The black solid line is the X-ray transmission of the oscillating cavitation bubble [30]. (c) Six individual frames of the third cavitation bubble at 320  $\mu\text{s}$  obtained by X-ray radiography with absorption contrast. The black curved vertical line intersecting the bubbles consist of dense ablated material that is emitted across the gas-liquid interface in a jet-like fashion. The scale bar is 1 mm [30].

In the bubble center, no significant size increase of primary particles was observed but the secondary particle behavior was similar to a scan at 0.17 mm height above the target. At the bubble tip and above no agglomeration induced by the cavitation bubble was observed. Yet, the counting statistics at these points were much lower than for the data points at smaller distances to the target surface [19]. In Figure 8b a similar diagram is shown but instead of the particle size, the relative mass of the primary (small) and secondary (large) nanoparticles is shown on the ordinate [30]. The black solid line represents the cavitation bubble as observed by recording the X-ray transmission. Data acquisition was performed at 0.5 mm above the target surface, in the middle of the cavitation bubble. It is obvious that the relative mass of the two size fractions is equal until the collapse of the first bubble sets in at  $\sim 150 \mu\text{s}$ . After the evolution of the second cavitation bubble (first bubble rebound), the mass of

secondary particles is several times higher compared to the small primary particles. This was interpreted as an agglomeration of small particles in the extreme confinement of the minimum cavitation bubble volume [30]. This additionally allows the conclusion that the particles cannot cross the cavitation bubble interface. Afterward, the mass of both species decreased with increasing delay, indicating the redistribution of ablated material to the target. After the final collapse of all cavitation bubbles at delays  $>350 \mu\text{s}$ , the mass of the secondary particles is slightly higher than for the primary particles [30]. Yet, this is not surprising as the mass of a (spherical) nanoparticle scales with its radius to the power of six  $R^6$ .

It was shown by additional X-ray radiography with absorption contrast that the particles cross the interface between the cavitation bubble and the surrounding liquid phase after  $\sim 320 \mu\text{s}$  [30]. This delay represents the maximum extension of the third cavitation bubble. As shown in the six single frames of Figure 8c, the interface crossing happens in a jet-like fashion. The material jet is dense enough to reveal itself in the absorption contrast as a curved vertical line inside all shown cavitation bubbles. The results from X-ray radiography were additionally supported by time-resolved SAXS measurements.

Thus, already before this dissertation started SAXS was proven to be a powerful tool for the analysis of the confined species during PLAL, which makes it the method of choice for the time-resolved analysis of the size quenching by additives.

Recently, imaging the cavitation bubble by means of X-ray radiography with different contrast mechanisms attracted some attention. Initially, the exploited contrast mechanism was pure absorption, as already discussed, with some inherent phase contrast appearing on the bubble interface. While absorption contrast imaging provided important information about the material transfer from the gaseous phase of the cavitation bubble into the surrounding liquid phase, it lacks sensitivity towards the nanosized matter. Only in the case of very dense material, caused by reduced bubble volume, absorption contrast can map the ablated species. Yet, no information about the size and relative mass of the nanoparticle species can be derived. A more sophisticated approach of X-ray imaging is the implementation of dark-field or scattering contrast [147]. As this contrast mechanism has its origin in the scattering of X-ray [147], information about the ablated nanoparticle is accessible. In contrast to SAXS, X-ray imaging with scattering contrast is a real single-shot method that allows recording the entire bubble cross section in a single experiment. Using a compound array refractive lens for hard X-ray Reich et al. have demonstrated the utility of the approach [148]. By changing the sample-detector distance the sensitivity of the method as a function of the diameter of scattering objects is tunable. Thereby, distinguishing between the scattering signals from nanoparticles inside the cavitation bubble and from emerging microbubbles [148]. A similar approach, X-ray Hartmann mask

imaging, is used in section 5.2.2 of this dissertation. The section includes a detailed description of the method.

### *Small-angle X-ray scattering*

For the analysis of nanoparticle small-angle X-ray scattering is a powerful tool. It is widely used to characterize nanoparticles, especially when high time-resolution is mandatory [149-153]. Here, the considerations are limited to the analysis of nanoparticle size and especially the size distributions. Additionally, the nanoparticles are assumed to be surrounded by a liquid phase rather than a vacuum. This represents the relevant case of nanoparticles synthesized by PLAL sufficiently well, even if difficulties arise when analyzing the particles when they are still trapped inside the gaseous phase of the cavitation bubble as background removal by considering the liquid phase, prior to the evolution of the cavitation bubble, is somewhat misleading.

What are the principles of small-angle X-ray scattering? First, the contrast mechanism of SAXS is the same as in TEM. Variations of electron density cause bright and dark spots on the detector. Still, TEM provides information in real space, while SAXS provides reciprocal space data. Therefore, small spatial changes in the electron density will scatter X-ray to larger angles than larger changes in electron density [154].

If an X-ray beam interacts with a nanoparticle these are potentially absorption, inelastic scattering, and elastic scattering. Only elastic scattering of X-rays at electrons contributes to the small-angle intensity, while absorption and inelastic scattering are negligible [154]. Absorption and inelastic scattering are widely negligible for small scattering angles so that the background radiation is mainly formed by the solvent molecules. Elastic scattering, on the other hand, creates a typical 2D pattern of bright and dark circles on the scattering detector [155]. X-rays induce oscillations of the electrons in the sample material with the exact same energy as the X-rays as the signal is produced by elastic scattering, leading to the emission of secondary waves. The distance from the sample to the detector is large compared to the incident wavelength, because small scattering angles require large distances, so that constructive and destructive interference between the secondary waves from the same particle, at different spots of the particle, can occur [156]. This causes the bright and dark rings on the detector. As single electrons cannot be localized in the sample, it is common to use the quantity of electron density in SAXS [156]. The 2D scattering pattern is then reduced to a 1D graph of the scattering intensity  $I(q)$  as a function of the scattering vector  $q = (4\pi/\lambda) \cdot \sin(\theta)$ , with the X-ray wavelength  $\lambda$ , and the half scattering angle  $\theta$ . For particles that are randomly orientated in the samples, an isotropic scattering pattern is recorded and the pattern is azimuthally averaged [154].

For data analysis in the sections 5.1.1 and 5.2.1 of this dissertation spherical particle were assumed. Furthermore, dilute solutions were considered as in the present single laser pulse experiments this was a reasonable assumption. If the additional assumption of the identity of all particles  $l$  is applied, the scattering intensity of the particles  $I_l(q)$  can be expressed as the product of the form factor  $P(q)$  and the structure factor  $S(q)$  [154]:

$$I_l(q) = P(q) \cdot S(q) \quad \text{Equation (8)}$$

The form factor describes the shape of the particles and the underlying size distribution if the particles are not identical. It is thus highly desirable to calculate the form factor in order to fit a scattering pattern of a nanoparticle colloid. The structure factor, on the other hand, contains information on the organization of particle systems, or in other words the arrangement of particles to each other. In a dilute solution of particles that do not specifically interact with each other, the structure factor approaches unity. In the latter case, the scattering pattern is completely fitted by the form factor  $P(q)$ . The form factor is defined as [154, 157]:

$$P(q) = \int n(R) \langle |F(q, R)|^2 \rangle dR \quad \text{Equation (9)}$$

$n(R)$ : size distribution function

$F(q, R)$ : form factor oscillation

The form factor oscillation  $F(q, R)$  represents the characteristic damped oscillation of the scattering pattern that is produced by monodisperse spherical nanoparticles. Therefore, it contains information about the particle shape. Furthermore,  $F(q, R)$  is the Fourier transform of the electron density variation. It is hence a central quantity for understanding that origin of small-angle scattering and reciprocal space relation of SAXS [154]. To calculate the form factor  $P(q)$  it is necessary to know or assume either the size distribution function  $n(R)$  or the particle shape before performing the calculation. In the case of laser-generated nanoparticles, it is reasonable to assume spherical nanoparticles, even if some particles are rather ellipsoids than spheres [118]. It is then possible to calculate the size distribution without any precondition on its shape. Often the Schultz-Zimm distribution function is assumed [158-160]. Yet, for time-resolved analysis of nanoparticles inside the laser-generated cavitation bubble during PLAL the size distribution function  $n(R)$  is not known. At the same time, the particle shape is well known from TEM image analysis and it is unlikely that the mostly spherical particles exhibit different shapes inside the cavitation bubble as the spherical shape is a low-energy state.

As already stated, the scattering intensity of non-identical particles cannot be split into the product of form and structure factor as in Equation (9) without any further assumptions. Still, in a solution of

polydisperse nanoparticles with negligible structure factor, the scattering intensity can be calculated. In this dissertation, an empirical model called the Unified Fit model (UF) by Beaucage et al. [161-163] and a Monte Carlo model by Pauw et al. [164, 165] was used for the analysis of nanoparticle size distributions by SAXS. These models are therefore briefly introduced in the following.

The unified fit model by Beaucage et al. is based on the Guinier and Porod approximations for the small ( $q < 1/R_g$ ) and high  $q$  region ( $q \gg \pi/R_g$ ) [161]. The radius of gyration is  $R_g = R(3/5)^{1/2}$  for monodisperse spheres. These approximations are used in the unified fit approach as a Guinier law [156] and an associated Porod power-law regime [166] to fit each hierarchical structural level, e.g. primary and secondary particles in PLAL. For a single polydisperse structural level the scattering intensity is given by [162]:

$$I_{UF}(q) = G \cdot \exp\left(\frac{-q^2 R_g^2}{3}\right) + B \cdot (q^*)^{-4}; \quad q^* = \frac{q}{\left[\operatorname{erf}\left(\frac{q R_g}{6^{1/2}}\right)\right]^3} \quad \text{Equation (10)}$$

*G: prefactor,  $\sim$ particle V*

*B: prefactor,  $\sim S$*

*S, V: average surface area/volume of particles*

Using the unified fit, it is possible to fit every hierarchical level of scattering structures in a sample, starting with the smallest. The result is the average size of the scattering particles and their relative volume contribution to the total nanoparticle volume by integration of the respective graph section. Still, it is not possible to retrieve the size distribution without assuming an envelope using the unified fit model [161-163]. The unified fit has been used to determine the relative mass fractions of primary and secondary nanoparticles inside the gaseous environment of the cavitation bubble by Ibrahimkuty and Wagner et al. [19, 30, 167]. As this dissertation can be considered an extension of their work in part the unified fit is utilized in every SAXS data analysis for reasons of comparison and because it has proven to be a powerful tool for fitting SAXS scattering curves.

Using the Monte Carlo approach (MC) introduced by Pauw et al. it is furthermore possible to obtain the particle size distribution of nanoparticles in a given sample volume. This feature is highly desirable during high-speed SAXS experiments as performed in this work as it allows to conclude on the effect of size quenching agents, e.g. electrolytes, more precisely compared to the unified fit that is limited to the determination of averaged size fractions. The MC approach aims to minimize the reduced chi-square of the scattering function by accepting every iteration that reduced  $X^2_{red}$  and dismissing every contribution that increases  $X^2_{red}$ . In the MC model the scattering intensity is given by [164]:

$$I_{MC}(q) = b + A \sum_{b=1}^{n_s} |F_{sph,k}(qR_k)|^2 \left(\frac{4}{3}\pi\right)^2 R_k^{(6-p_c)} \quad \text{Equation (11)}$$

*b*: constant background term

*A*: scaling factor, related to the volume fraction of scattering structures

Obviously, the MC model requires the assumption of specific particle shape, spheres in the present case, but not a specific size distribution function (see Equation (12)). The number of contributions  $n_s$  that are considered do not influence the calculated results, but the time required for that task. Similar accounts for the adjustable parameter  $p_c$ . The MC model was successfully tested by Lak et al. for the analysis of bimodal iron oxide nanoparticles [168].

While numerous algorithms are available to determine the size or the size distribution of nanoparticles from SAXS data [154], the UF and MC approaches are particularly suitable for the data produced in this dissertation. The SAXS experiments are performed with a high temporal resolution some tens of microseconds and lack from a high signal-to-noise ratio as the ablated nanoparticulate species are very diluted inside the extended cavitation bubble. However, this drawback is overcome by averaging hundreds of individual scattering curves. Both of the presented fits have been tested in terms of their ability to determine the size and size fractions of defined nanoparticle colloids [169] (study is presented in section 5.1.1) and have proven excellent agreement with the expected results and in comparison to hydrodynamic techniques like dynamic light scattering or analytical disc centrifugation but also compared to electron microscopy with image analysis. The excellent performance of SAXS with the UF and the MC fit, without any temporal resolution, makes this combination the technique of choice for the analysis of nanoparticle sizes when a high temporal resolution is required.

## 4 Materials and methods

Depending on the respective scientific question the experimental equipment, the used laser system, the chemicals, and analytical technique were adopted. The following sub-sections describe the experimental setup of the *in situ* and *ex situ* studies, as well as the designed setup for shadowgraphy imaging of the laser-induced cavitation bubble. The used instruments and a brief description are presented in Table 1. Additional descriptions of the equipment and setups are given in the materials and methods sections of each sub-chapter of 5.

**Table 1:** Summary of the used lasers for nanoparticle synthesis and the applied analytical instruments.

Instrument	Manufacturer	Model	Specification	Application and description
Laser	Rofin-Sinar	RS-Marker D100	1064 nm, 40 ns, 15 W @ 3 kHz	PLAL of gold nanoparticles
	Innolas	Spitlight DPSS-250-100	1064 nm, 9 ns, 1 W @ 100 Hz, 4 mW @ 0.2 Hz	PLAL of gold nanoparticles during <i>in situ</i> SAXS analysis and PLAL of silver nanoparticles for shadowgraphy
	EdgeWave	HD-40I-E	1064 nm, 40 ns, 3 W and 13 W @ 2 kHz	PLFL of gold nanoparticles
	Spectra Physics	Spitfire Ace	800 nm, 100 fs, 196 mW @ 5 kHz	Preparation of the Hartmann mask by laser drilling
	Continuum	Minilite I	1064 nm, 7 ns, 110 mW @ 10 Hz	PLAL of gold nanoparticles during <i>in situ</i> XHI analysis
	Rofin	PowerLine E	1064 nm, 7 ns, 7 W @ 10 kHz	PLAL of gold nanoparticles
Analytical disc centrifuge	CPS instruments	DC 24,000 UHR	24,000 rpm, 405 nm	Determination of particle size distribution by fractionation in a centrifugal force field
Benchtop centrifuge	Hettich	Universal 32R	Rotor 1613, 6000 rpm	Fractionation of gold colloids by centrifugal force
Analytical ultracentrifuge	Beckmann Coulter	Proteomelab XL-I	An-50 Ti Rotor, 30000 rpm, SedFit	Determination of particle size distribution by

Instrument	Manufacturer	Model	Specification	Application and description
			(software), UV/Vis detector	analysis of sedimentation speed
Power and energy meter	Coherent	Field Max II-Top	EnergyMax Sensor	Direct measurement of laser pulse energy by a pyroelectric element.
Plunger pump	Ismatec	ISM 321C	5-50 ml/min	Liquid flow during PLAL and PLFL
Peristaltic pump	behr	WT600-2J	35 ml/min	Liquid flow during shadowgraphy. Flow rate reduced by additional pressure on tubes and reduced tube diameter.
Dynamic light scattering	Malvern	ZetaSizer ZS	4 mM, 633 nm	Determination of particle size distribution and zeta-potential
UV/Vis spectrometer	Thermo Scientific	Evolution 201	1 mm band width, 5 mm beam path	Determination of the extinction of colloids
Transmission electron microscope	Zeiss	EM 910	120 kV	Determination of number-weighted particle size distribution
High-resolution transmission electron microscope	Jeol	JEM-2200FS	200 kV	Determination of number-weighted particle size distribution
Pulse generator	Thurlby Thandar Instruments	TGP 110	10 MHz, 50 ns pulse delay, 50 $\mu$ s pulse width	Electric resistance preconnected to the camera
Camera	Basler	acA1600-60gm	10 $\mu$ s resolution	Optical shadowgraphy
Camera lens	Sill optics	correctal T/1,5	1.5-fold magnification	Magnification of the camera image
Flashlight	LED Lenser	L7	115 lm	Light source for optical shadowgraphy
3D printer	MakerBot	Replicator 2X	100 $\mu$ m layer resolution, 0.4 mm nozzle diameter	Printing of the ablation chamber for shadowgraphy
Confocal 3D microscope	NanoFocus	$\mu$ surf custom		Analysis of laser-induced damage on the target surface

The chemicals used during the experimental work of this thesis are summarized in Table 2, together with information on the suppliers, specifications, and applications.

**Table 2:** Specifications of the chemicals used in the experiments.

Chemical	Supplier	Specification	Application
Sodium chloride (NaCl)			Size control of laser-generated gold nanoparticles
Polyvinylpyrrolidone (PVP) (CAS: 9003-39-8)	Acros Organics	3500 g/mol (Lot: A0368382)	Size control of laser-generated gold nanoparticles
Sodium bromide (NaBr)			Size control of laser-generated gold nanoparticles
Gold target (plate)	Allgemeine Gold- und Silberscheideanstalt	99.9 %, 0.5 mm thickness	Target for PLAL
Gold target (ribbon)	ZierRat KG	99.9 %, 200 $\mu$ m thickness, 4mm width	Target for <i>in situ</i> experiments
Silver target (plate) (CAS: 7440-22-4)	Alfa Aesar	99.985 % (Premion), 1 mm thickness (Lot: M26B010)	The target for shadowgraphy of the cavitation bubble
Gold colloid	Nanopartz	Nominal particle size: 40 nm	Sample S50 for <i>ex situ</i> testing of SAXS
Methoxy polyethylene glycol thiol (mPEG-SH)	abcr	356.5 g/mol, > 95 % (Lot: 1335547)	Steric stabilization of gold colloids

## 4.1 Experimental design

### 4.1.1 Experimental design for *in situ* investigations

The setups of *in situ* X-ray probing of the laser-induced cavitation bubble was similar for both applied techniques, SAXS and XHI. The custom-made ablation chamber, made of steel in the SAXS setup and 3D printed for the XHI setup, consisted of scaffold building of a central hollow space. Here the continuous ablation target, a 4 mm wide and 200  $\mu\text{m}$  thick gold ribbon, was continuously transported upwards across the ablation chamber relative to the incoming laser beam. On top and below the laser-focusing lens there were two tubes connected to provide the water flow through the ablation chamber. The channels for the liquid were connected to the central hollow space and the water was pumped upwards to avoid the accumulation of persistent gas bubbles in the chamber. The laser entered the chamber through a lens, of 30 mm focal length in air, screwed in the chamber wall perpendicular to the target. At the same time, the lens acted as a seal to avoid leaking of the chamber.

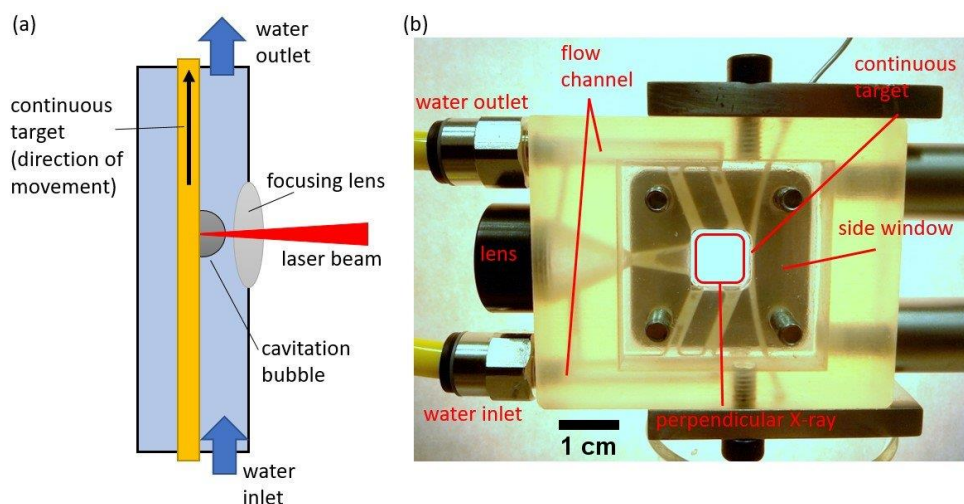


**Figure 9:** Graphical description of the experimental setup for *in situ* X-ray investigations. The structure of the ablation chamber and the role of the single pieces are described. A continuous gold target (ribbon) is transported upwards across the chamber, perpendicular to the incoming laser beam. The laser is focused on the target by a lens screwed in the outer wall of the chamber. The applied water flow is directed from the bottom to the top. (a) Simplified scheme of the setup. The framework of the chamber and the incoming X-ray beam are neglected. (b) Photograph of the 3D printed ablation chamber as designed and printed at the Karlsruhe Institute of Technology (KIT). The inner channels are visible due to decreased absorption of light at the thin structures.

Two removable side windows were positioned perpendicular to both the target and the incoming laser beam. The side windows were made of steel in all setups and pressed a layer of silicon seal and a subjacent layer of polyimide foil (Kapton) to the chamber framework. Thereby, the liquid layer height for the incoming X-ray beam to cross through the side windows was limited to 5 mm. A thicker layer of water would have absorbed a significant amount of beam energy. A scheme and photography of the setup are presented in Figure 9, while more detailed descriptions are given within the sections 5.1.2 and 5.2.2.

#### 4.1.2 Experimental design for pulsed laser ablation and fragmentation in liquids

Laser ablation of gold nanoparticles in water was always executed in a liquid flow setup. This was to mimic the parameters of the *in situ* setup. Through all experiments, custom-made ablation chambers made of polytetrafluoroethylene (PTFE, Teflon) were used to avoid contamination of the colloids. The chamber for PLAL consisted of several 4 x 4 mm quadratic parts that were put together in a layer-by-layer like fashion. These parts are listed in an order starting with the part that had the largest distance to the incoming laser beam below:

- i. Backside made of PTFE (thickness 5 mm) with a rectangular depression of 0.5 mm depth. This depression defined the location and dimension of the gold target.
- ii. Silicone seal of 1 mm thickness with a round hole in the middle of 12 mm in diameter. This allowed pressing the underlying rectangular target at its corners to the chamber's back side.
- iii. Central PTFE block (thickness 5 mm) with the dual cone-shaped channel for the liquid flow. Accordingly, the liquid layer height above the target was 5 mm.
- iv. Silicone seal of 1 mm thickness with a round hole in the middle of 12 mm in diameter.
- v. The window made of a cut microscopy slide as an entrance for the laser beam.
- vi. Silicone seal of 1 mm thickness with a round hole in the middle of 12 mm in diameter.
- vii. Front part made of PTFE (thickness 5 mm) with a round hole in the middle of 12 mm in diameter.

The used gold targets had a thickness of 0.5 mm and the ablation pattern on the target surface had a spiral-like pattern of 8 mm in diameter. Scanning across the surface was performed using an F-Theta lens. The liquid volume flow was adjusted by a plunger pump connected to the centerpiece of the chamber by polyvinyl chloride (PVC) tubes. The final colloids were collected in vessels made of either

polyethylene or polypropylene. The focus position was determined either by gravimetry of the target before and after ablation or by UV/Vis extinction spectroscopy at 380 nm. Hence, the focus position was the position of maximum material ablation and not the geometric focal position.

The chamber and setup for PLFL were similar. Instead of the PTFE-backside of the chamber, a second front part was mounted together with a second glass window to allow the attenuated laser beam to exit the chamber and to avoid subsequent ablation processes. Furthermore, the colloid was pumped in a circle for a given period.

#### 4.1.3 Shadowgraphy setup

The ablation chamber used for shadowgraphy was 3D printed to allow a liquid flow PLAL while observing the laser-induced cavitation bubble from the side. The liquid flow was necessary to remove residual nanoparticles and persistent gas bubbles between two laser pulses. As it was required to observe the edge of the target during imaging, the target was fixed to the backside of the chamber using double-sided tape. A sketch of the principal setup and the geometry of the central part of the ablation chamber are depicted in Figure 10.

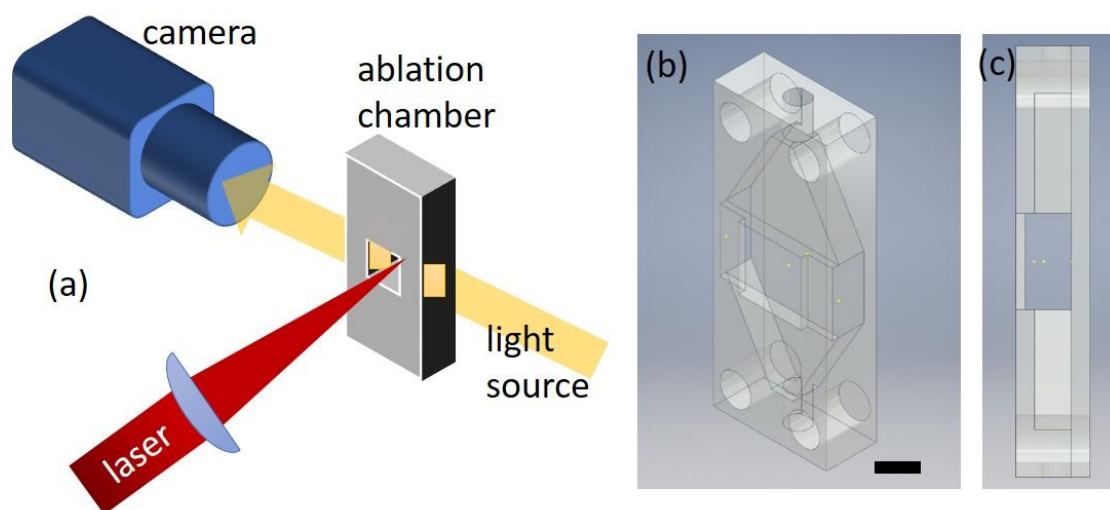


**Figure 10:** Sketch of the setup for imaging of the cavitation bubble by optical shadowgraphy. (a)

Scheme of the centerpiece of the ablation chamber with the laser entering from the front perpendicular to the target. The side windows allow the visible light to enter the target and the transmitted intensity is recorded by the camera. The liquid flow from the bottom to the top of the chamber, the remaining parts of the chamber, and other equipment are omitted. (b) CAD design of

*the centerpiece highlighting the geometry of the flow channel and the front and side windows. (c) CAD-view from the side through the chamber. Scale bar accounts for (b) and (c) and is 5 mm.*

While only a part of the ablation chamber is shown and the indication of the liquid flow direction (upwards through the chamber) is omitted, a good overview of the setup is clarified. A more detailed description is given in 5.1.2.

## 5 Results and discussion

This chapter is divided into four sections that deal with the different aspects of the laser-induced cavitation bubble and the experimental designs for the clarification of the underlying scientific questions. All experiments were performed using lasers with pulse widths of several nanoseconds. Therefore, the findings are not directly transferable to the process of PLAL with femto- or picosecond pulses. Still, the identification of the early processes that occur during nanosecond PLAL are an important piece of information for future studies of PLAL with ultrashort pulses.

Section 5.1 contains the preparatory work for the studies investigating the bubble's interior by means of SAXS [19, 20] and, partly, the interpretation of XHI data. Here (5.2.1), the analytical precision of the utilized SAXS method is compared to more frequently used techniques of colloidal analysis, e.g., ADC, DLS, and optical UV/Vis extinction spectroscopy (Figure 11, upper left). The latter one was possible as the comparative study is conducted using plasmonic gold nanoparticles. The results highlight the analytical accuracy of SAXS but also the limits of that technique. Consequently, the findings greatly contribute to the interpretation of the data derived in section 5.2.1.

The design for probing the laser-induced cavitation bubble with high temporal resolution using advanced X-ray methods differs significantly from that frequently used in quantitative nanoparticle synthesis by PLAL, especially the thickness of the ablation target. For the synthesis of high concentrations or large amounts of nanoparticles, the target thickness is usually in the range of 0.5 – 1.0 mm or thicker; in contrast, X-ray probing of the cavitation bubble requires a target thickness of  $\leq 200 \mu\text{m}$ . Therefore, another preparatory work in 5.1.2 determines the limits of a targets ability to absorb multiple pulses on the same spot without inducing changes to the cavitation bubble and possible influences on the synthesized nanoparticles (Figure 11, upper right). The ablation crater is found to largely influence the cavitation bubble shape, its maximum extension height and volume, and its overall dynamics. Consequently, reproducible analysis of particles confined inside the cavitation bubble with high-speed X-ray methods requires continuously moving targets; however, the stiffness of thick gold targets hinders their continuous transport relative to the laser beam.

The aforementioned section, 5.2.1, deals with the experimental design required for the detection of the nanoparticle size and size distribution on the microsecond time-scale by SAXS and includes an explanation of how the synchrotron X-ray beam is positioned relative to the laser-induced cavitation bubble and the temporal resolution is discussed. The observation of ablated species already inside the gas phase of the cavitation bubble is defined as *in situ* analysis throughout the entire experimental description within this dissertation.

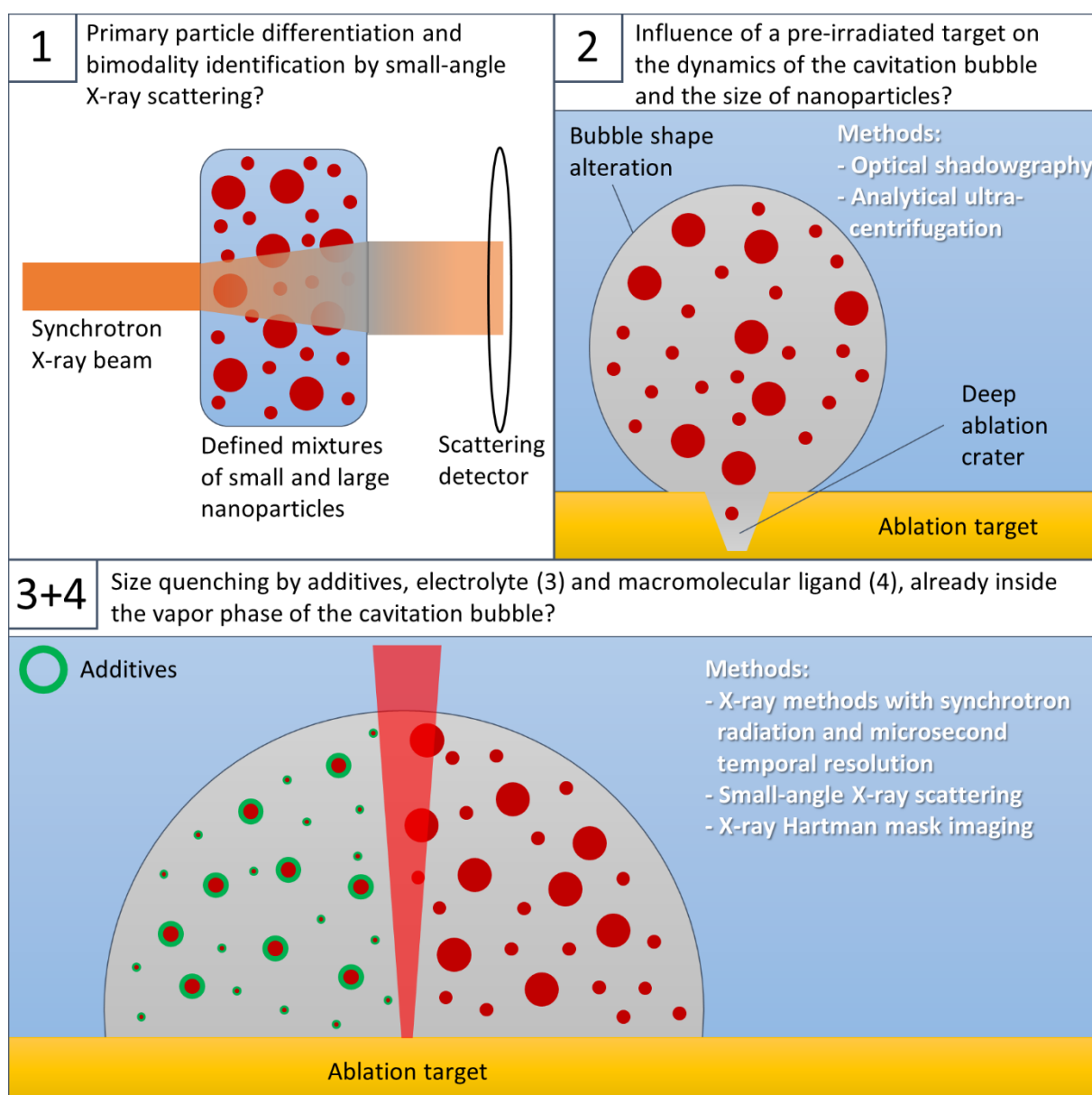


**Figure 11:** Schemes that illustrate the scientific questions and applied methods that were used to solve them. The upper row (1 and 2) represents the *ex situ* studies that are presented in the sections 5.1.1 and 5.1.2. The bottom row (3+4) represents the *in situ* studies that are presented in the sections 5.2.1 and 5.2.2.

In contrast, experiments and analyses performed on a final colloid on the time scale of minutes and more are referred to as *ex situ* experiments. Within the study presented in 5.2.1, the interior of the cavitation bubble is probed *in situ* during the laser ablation of a gold target in pure water and in a micromolar solution of NaCl (Figure 11, bottom). In combination with additional *ex situ* analysis of gold colloids, it is shown that the ions delivered by the electrolyte result in an effective size quenching of the ablated nanoparticles already inside the confinement of the cavitation bubble.

In addition to adding micromolar concentrations of monovalent electrolytes to the liquid phase prior to PLAL, another common way to control the size of the product nanoparticles is to add organic ligands and polymers to the solution. In section 5.2.2, the question of the time of impact of macromolecular ligands on the final nanoparticle size distribution is addressed (Figure 11, bottom). The exploited X-ray method is varied, in comparison to section 5.2.1, from SAXS to X-ray Hartmann mask imaging. In addition to the description of the operating principle and experimental design, the suitability of the method is demonstrated by reproducing the *in situ* finding from SAXS that micromolar concentrations of NaCl result in size quenching inside the gaseous phase of the cavitation bubble. The chosen macromolecular ligand is PVP and no effect on the nanoparticles is observed *in situ*. Since PVP reduces the final *ex situ* particle size distribution, it is concluded that the macromolecular ligand, in contrast to NaCl, acts as an *ex situ* growth quenching agent by suppressing particle growth by coalescence and Ostwald ripening.

The experimental results presented in this dissertation point toward the importance of the exploited experimental designs for *in situ* particle analysis and the different mechanisms of size control during PLAL by electrolytes and macromolecules. These differences lead to conclusions on the particle generation mechanism during nanosecond PLAL and the implications for the size control of laser-generated nanoparticles. These implications are summarized in section 6.

## 5.1 Suitability and interpretability of the high-speed X-ray setup and results

Laser ablation in liquids does not produce a single uniform nanoparticle fraction; instead, a bimodal colloid is usually obtained. The bimodality is increased with decreasing laser pulse width. Nevertheless, no combination of laser parameters is known that results in the formation of monodisperse colloids. As even single-pulse laser ablation leads to a combination of small and large nanoparticles, the bimodality is most likely an inherent output of PLAL. It is, therefore, mandatory to perform a reference study to elucidate the suitability of SAXS for the analysis of bimodal colloids without any temporal resolution. Depending on the outcome of this reference study, the interpretation of *in situ* SAXS data is facilitated and becomes more significant. The basic principle of the design experiment is presented in Figure 12.

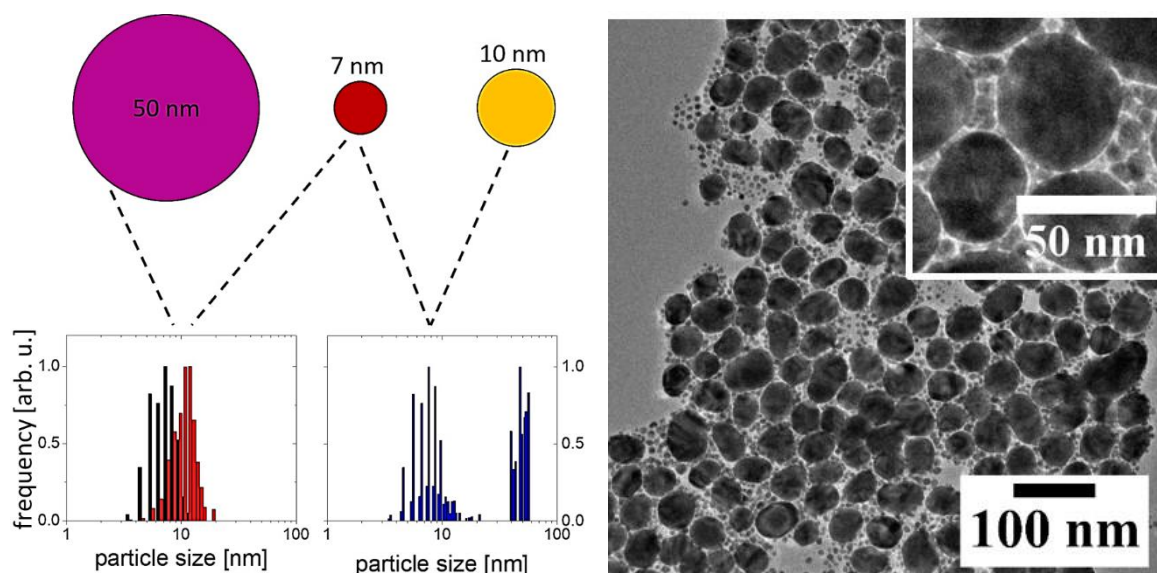


**Figure 12:** To reproduce the size distributions from PLAL, monomodal colloids of various sizes are synthesized and mixed in defined nominal mixing ratios (*n.m.r.*). Left: Scheme of the preparation path of defined bimodal colloids (adapted from reference [169]). In a first step, laser-generated particles are re-irradiated with a laser-wavelength close to the SPR peak of AuNP to fragment the particles and obtain monomodal colloids (top). The 50 nm-sample was obtained commercially. In a second step, the particles are mixed together in defined ratios according to the nanoparticle concentration of the initial colloids (bottom). One series of samples is made of colloids with overlapping size distributions, whereas another series is made of colloids with non-overlapping size distributions. Right: High-resolution TEM of a sample containing nanoparticles from the 7-nm and 50-nm samples in a *n.m.r.* of one. The inset shows an area of the image with higher magnification.

The bimodality of laser-generated colloids is mimicked by subsequent laser ablation and fragmentation so that two monomodal colloids with average sizes of 7 nm and 10 nm are obtained. A third colloid with an average size of 50 nm was obtained commercially. The overall gold concentration in the colloids is determined and the individual samples are mixed in defined ratios. Two series of samples are prepared this way: (i) mixtures of 7-nm and 50-nm colloids to mimic colloids obtained by PLAL, and (ii) mixtures of 7-nm and 10-nm colloids. The latter mixture is prepared to determine if SAXS can resolve these slight changes in the overall composition of a colloid. This knowledge boosts the interpretation of *in situ* SAXS data from PLAL of gold in pure water and the size quenching agent NaCl, as presented in section 5.2.1. In addition, for particle size distribution analysis by means of SAXS, the samples are further analyzed by more frequently used methods of colloidal chemistry. The initial samples are characterized by scanning electron microscopy, whereas all samples mixtures are analyzed by the fractionating technique of analytical disc centrifugation, dynamic light scattering, and UV/Vis spectroscopy with Mie-Gans analysis. This variety of analytical techniques allows one to not only judge the suitability of SAXS for the analysis of laser-generated nanoparticles, but also presents its relative accuracy compared to other techniques. Thus, the results presented in section 5.1.1 are a necessary groundwork for the *in situ* SAXS study that is presented in 5.2.1. This SAXS study is also an important reference for the interpretation of the *in situ* X-ray Hartman-Mask imaging experiments performed in section 5.2.2.

Afterwards, the influence of the cavitation bubble itself on the resulting nanoparticles is investigated (section 5.1.2). Regarding the cavitation bubble, its influence is hardly accessible as changing the cavitation bubble's lifetime or shape is usually not possible without changing at least one other parameter in the system. Hence, it is not unambiguously clear whether a possible change in particle size is attributed to the changes in the cavitation bubble or due to some other parameter.

The approach that was chosen in the investigation, presented in 5.1.2, is simple. A thick target (1 mm) was ablated in a liquid flow setup without any scanning strategies applied; the laser was not moved relative to the target nor vice versa. The evolving ablation crater on the target does indeed significantly change the shape and lifetime of the cavitation bubble at the same time, as schematically shown in Figure 13.

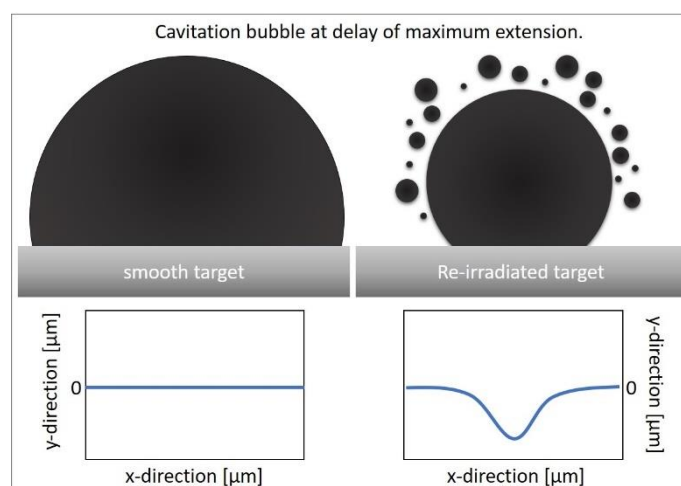


**Figure 13:** Scheme of the laser-induced cavitation bubble at the delay after laser impact of maximum bubble extension. In the top left, the semispherical bubble on a smooth (= undamaged) target spot is shown. In contrast, after multiple pulses on the same spot, the resulting crater changes the bubble shape to almost spherical, with additional small bubbles surrounding it in the liquid phase. The schematic diagrams in the bottom outline line scans across the target surface. In the case of a smooth surface, no indentations are observed. A re-irradiated target, in contrast, exhibits a distinct ablation crater.

Besides the cavitation bubble, the only other parameter that might undergo changes is the fluence; however, the fluence is constant throughout the major range of applied laser pulses. The induced spherical shape of the bubble (Figure 13, top right) is of great importance as damage to the target cannot be avoided in PLAL. Hence, the influence of the cavitation bubble on the final nanoparticles is crucial. Here, no additives are used. This way, the combined results of 5.1 and 5.2 can add to the overall aim of size control during PLAL, especially as in section 5.1.2, no time resolution is applied regarding the analysis of the size of the nanoparticles and the overall investigated time range is hence expanded from the microsecond time scale from *in situ* experiments (section 5.2) to the time scale of hours and days.

The cavitation bubble induced on a silver target is imaged using shadowgraphy and the observed bubble features are correlated to the measured particles' sizes. As the particle concentration in the as-prepared final colloids is on the order of  $10^{-4}$  g/l, particle analysis was challenging. Measurements by means of analytical ultracentrifugation identified many nanoclusters ( $\leq 3$  nm) that were produced along with primary and secondary nanoparticles. As will be discussed in 5.1.2, these nanoclusters can add to the size of larger particles by growth processes. These results may pave the way towards new methods of particle size control during laser synthesis in liquids.

### 5.1.1 Primary particle diameter differentiation and bimodality identification by five analytical methods using gold nanoparticle size distributions synthesized by pulsed laser ablation in liquids

Alexander Letzel, Bilal Gökce, Andreas Menzel, Anton Plech, and Stephan Barcikowski

Published in: "Primary particle diameter differentiation and bimodality identification by five analytical methods using gold nanoparticle size distributions synthesized by pulsed laser ablation in liquids, *Appl. Surf. Sci* 435 (2018) 743-751."

#### Abstract

For a known material, the size distribution of a nanoparticle colloid is a crucial parameter that defines its properties. However, measured size distributions are not easy to interpret as one has to consider weighting (e.g. by light absorption, scattering intensity, volume, surface, number) and the way size information was gained. The radius of a suspended nanoparticle can be given as e.g. sphere equivalent, hydrodynamic, Feret or radius of gyration. In this study, gold nanoparticles in water are synthesized by pulsed-laser ablation (LAL) and fragmentation (LFL) in liquids and characterized by various techniques (scanning transmission electron microscopy (STEM), small-angle X-ray scattering (SAXS), analytical disc centrifugation (ADC), dynamic light scattering (DLS) and UV/Vis spectroscopy with Mie-Gans Theory) to study the comparability of different analytical techniques and determine the method that is preferable for a given task related to laser-generated nanoparticles. In particular, laser-generated colloids are known to be bimodal and/or polydisperse, but bimodality is sometimes not analytically resolved in literature. In addition, frequently reported small size shifts of the primary particle mode around 10 nm needs evaluation of its statistical significance related to the analytical method. Closely related to earlier studies on SAXS, different colloids in defined proportions are mixed and their size as a function of the nominal mixing ratio is analyzed. It is found that the derived particle size is independent of the nominal mixing ratio if the colloid size fractions do not overlap considerably. Conversely, the obtained size for colloids with overlapping size fractions strongly depends on the nominal mixing ratio since most methods cannot distinguish between such fractions. Overall, SAXS and ADC are very accurate methods for particle size analysis. Further, the ability of different methods to determine the nominal mixing ratio of sizes fractions is studied experimentally.

## Introduction

Size distribution analysis of dispersed nanoparticles is a major challenge in colloidal chemistry and nanotechnology. The size of a nanoparticle defines physical and chemical properties such as optical [170, 171] electric [172, 173], magnetic [174, 175] and catalytic [176, 177] properties. Usually, nanoparticle dispersions are not comprised of particles of the exactly same size. Real samples – even those referred to as monodisperse – exhibit a certain variety of differently sized nanoparticles [178-180] leading to particle size distributions that have a certain width. Therefore, for real particle size analysis it is not sufficient to present a single average size value. As the special properties of nanoparticles are caused by their large surface to volume ratio, the particle surface is of particular importance of the interaction with incident radiation or mechanical sensors. Often nanoparticles are functionalized with organic ligands attached to the surface so that this additional shell adds to the signal from the core-particles. One route to ligand-free nanoparticles is the synthesis via pulsed laser ablation in liquids (LAL) [33]. For a number of applications nanoparticles with clean surfaces, in other words with no steric stabilizers or electrosteric surfactants attached, are required. These include biological [49, 181], medical [182, 183] and chemical application like heterogeneous catalysis [184, 185]. Pulsed laser ablation in liquids has first been described by Fojtik and Henglein [67, 186] and has developed into a competitive synthesis route that is green chemistry [98, 187]. Nowadays, many material classes are accessible through laser synthesis, including noble metals [68], base metals [188], oxides [189] and alloys [190, 191]. These materials obtain characteristic properties e.g., magnetism or, depending on the functionalization, biological functions. In recent work, we performed SAXS during the ablation of gold in a micromolar solution of sodium chloride [192], which is known to stabilize the resulting gold nanoparticles and decrease their size due to additional surface charges [146]. Interestingly, it was shown by SAXS that already inside the gas phase of the laser-induced gas filled cavitation bubble the ions start to reduce the size of gold nanoparticles [192]. One difficulty in the analysis of highly dynamic processes, such as LAL is that few methods are compatible to the *in situ*, high spatial and time resolution examination, as is SAXS. After cavitation bubble collapse and collection of the particles, *ex situ* analysis with imaging techniques like electron microscopy or further analytics is possible but as the particles still grow inside the bubble the results might not be directly comparable to the results obtained from *in situ* SAXS. Therefore, it is demanded to calibrate the utilized methods with respect to their comparability and the relation to *ex situ* changes. In general, for particle size analysis knowledge about the particles' physical properties and synthesis route are beneficial as these contain important information required for data interpretation [193]. For example, if a colloid made of gold is analyzed it is possible to extract size information from its ultraviolet–visible extinction

spectrum (UV/Vis) in particular due to the surface plasmon resonance (SPR) of gold nanoparticles (AuNP) [171, 194]. In many cases, particle size distributions are broad or exhibit multiple modes. For instance, particles prepared by LAL are known for their purity [195, 196], but are bimodal or of even higher polydispersity [13, 21, 142]. Avoiding or reducing the inherent polydispersity and relating it to the phenomena involved in LAL are subject to earlier work [20, 30, 192]. Ultimately, analytical techniques and evaluation methods suitable for complex size distributions are mandatory. As agglomeration and aggregation are common phenomena in colloidal chemistry, at least bimodal size distributions must be reliably resolved. Unfortunately, sizes derived from different methods will differ both because of sensitivity issues (such as weighting by number or volume) or because of the underlying physical detection phenomena. For example dynamic light scattering (DLS) is a non-fractionating method analyzing nanoparticles in their nascent hydrodynamic state and sensitive to intensity fluctuations of scattered laser light due to particle diffusion [197]. The hydrodynamic analysis also includes immobilized adsorbed species on the particles. Electromagnetic wave scattering (including SAXS), furthermore is sensitive to the volume of the particles rather than their number because of the cubic relation of the particle volume to the intensity in Rayleigh-Scattering. In contrast, transmission electron microscopy (TEM) does not image particles in their nascent environment since they undergo liquid evaporation during sample preparation. Apart from this, TEM directly provides the number-weighted particle size distribution due to counting of every single particle.

In the past years, there have been many studies comparing particle size analyses of a given colloid obtained from different methods [160, 163, 168, 193, 198-203]. Many of these studies focused on the case of monodisperse colloids or assumed monodisperse colloids [160, 163, 168, 198-203]. Some studies also take bi- and multimodal colloids into account but are neglecting the determination of the relative volume of the underlying fractions [193, 202, 204]. For instance, Lak et al. mixed colloids in defined ratios [168]. In more detail, Thünemann et al. characterized a bimodal iron oxide colloid through field-flow-fractionation with a SAXS detector [205]. Other groups focused on the implementation of data evaluation routines to optimize certain methods like DLS, SAXS or particle tracking without a comparison to a full set of other analytical methods [206-208]. Recently, Kestens et al. have tested silica particles as new reference material in an exhaustive ring-trial and have shown the difficulties of measuring the “size” of nanoparticles [209]. In the present work, we prepare gold colloids of varying sizes and mix them in defined mass ratios. The prepared bimodal gold colloids stabilized by thiolated mPEG are characterized by means of scanning transmission electron microscopy (STEM), UV/Vis spectroscopy with combined data analysis by Mie-Gans theory [118], DLS with cumulant analysis, analytical disc centrifugation (ADC) and small-angle X-ray scattering (SAXS) with data evaluation by a generalized fit approach and a reverse Monte Carlo fit [161, 162, 164, 210]. We show

that SAXS is a highly accurate method for the analysis of LAL colloids and thereby support the findings of our earlier work, dealing with the *in situ* analysis of embryonic LAL nanoparticles which are still trapped within the confinement of the laser induced cavitation bubble [19, 20, 192]. We further demonstrate the limits of the SAXS methods in terms of analysis of particles mixtures with over-lapping size distributions, minimum particle diameter and effect of the presence of large particles on the particle size distribution of a mixed colloid containing small ( $d < 10$  nm) and large particles ( $d > 40$  nm). In detail, primary particle size shifts from 10 nm to 7 nm cannot be statistically and significantly resolved by *in situ* SAXS during laser ablation in liquids, but can clearly be differentiated *ex situ* by the same analytical principle [192]. This explains that size shifts can be easily observed for the secondary (large or agglomerated) particles by *in situ* SAXS, but not for the primary (small) particles. Hence, complementary analytical methods are required to assess the same sample *ex situ* in detail, and provide statistical analysis of the significance of extracted size information.

## Experimental section

### *Gold nanoparticles*

The gold nanoparticles labeled “S7” and “S10” per their nominal sizes in Table 1 are prepared by LAL. During LAL, a solid gold target (99.99%, Allgemeine Gold- und Silberscheideanstalt AG) is ablated by a focused nanosecond laser (Rofin PowerLine E, 7 W, 10 kHz, 1064 nm, 7 ns). The beam is scanned in a spiral pattern to prevent fast perforation of the solid gold target. To avoid uncontrolled fragmentation of the as-synthesized AuNP a flow chamber made of Teflon (PTFE) is used and a constant volume flow of a 0.3 mM of a sodium bromide (NaBr) aqueous solution is adjusted (14 ml/min). As nanoparticles obtained from PLAL exhibit a characteristic bimodality [13, 21, 142] these colloids are further irradiated with laser pulses of a wavelength of 532 nm close to the SPR peak-maximum of AuNP. This process is referred to as pulsed laser fragmentation in liquids (LFL) [88, 140, 211]. The laser used for LFL is operated at a repetition rate of 2 kHz (Edgewave HD-40I-E) and exhibits a pulse width of 40 ns. No beam focusing is applied. The large area of the raw beam (6 mm<sup>2</sup>) ensures to treat all particles with the same average pulse energy. As it is well known that the minimum particle diameter accessible by means of LFL of AuNP is a function of the applied laser fluence [68] the pure colloidal solutions of S7 and S10 are irradiated with 25 mJ/cm<sup>2</sup> for 5 min and 108 mJ/cm<sup>2</sup> for 10 min respectively. The volume flow is adjusted to 30 ml/min. Throughout all experiments and particles preparations, we use exclusively demineralized Milli-Q water (18.2 MΩ/cm).

As it is difficult to fabricate a monomodal fraction of 50 nm particles by laser ablation, a chemically prepared, purified colloid was taken to represent that size range. The AuNP sample named as “S50”

per Table 3 is a commercial product obtained from Nanopartz. This sample was centrifuged five times at relative centrifugal force (RCF) of 675 for 7 min each to remove large aggregates. All AuNP colloids are capped with a final concentration of 10  $\mu$ M thiolated mPEG with average molecular weight of 356.5 g/mol obtained from ABCR (> 95 % oligomer purity). The capping agent is used without further purification. The functionalization increases the long-term stability of the colloids (as aliquots of the same sample had to be analyzed by five different, time-consuming methods) and further minimizes interactions between the sucrose, used in analytical disc centrifugation, and the gold nanoparticles.

**Table 3:** Number-weighted mode diameters ( $d_n$ ) and volume-weighted median ( $d_{50}$ ) obtained of the pure colloids analyzed by STEM. Median includes information on the entire size distribution and does not require an error bar.

Sample	$d_n$ (mode) (nm)	$d_{50}$ (STEM) (nm)
S7	$6.6 \pm 1.7$	7.3
S10	$8.9 \pm 2.6$	10.2
S50	$6.9 \pm 1.4$	47.6

As ligand-free gold nanoparticles from LAL might be covered with an undefined multilayer shell of physisorbed sucrose molecules when inserted to the density gradient of the analytical disc centrifuge, a defined molecular layer is applied. Furthermore, the chemisorbed mercapto-PEG coating of the nanoparticles provides a robust and comparable definition of nanoparticle stabilization for the different measurements, as for instance the remote SAXS experiments at the Swiss Light Source synchrotron.

#### *Determination of gold concentration*

As the present study requires the mixing of controlled amounts of different AuNP colloids the determination of the underlying gold concentrations is vital. Therefore, the linear relationship between the interband absorption of AuNP at 380 nm and the overall mass of AuNP is exploited [212]. For this purpose UV/Vis spectroscopy is used. The final gold concentration is obtained using the calibration curve determined by Rehbock et al. [21].

#### *Analytical methods*

We use five different analytical techniques to gain size information of the pure colloids (S7, S10, and S50) and their mixtures. Among these are STEM, which is primarily sensitive to particle number at given size. A JEOL JEM-2200FS with 200 kV acceleration voltage is used. Small amounts of colloids are drop

casted onto carbon coated copper grids and dried overnight. The resulting images are analyzed using ImageJ 1.50i. Diameters of spherical particles (samples S7 and S10) are obtained directly. Diameters of non-spherical particles (S50, Figure 14i) are calculated from the volume equivalent diameter. STEM is solely applied to the pure colloids, but not to the particle mixtures. Note that particles sizes are determined by the Feret diameter, as the image analysis was not performed automatically. This would have been necessary to specify the area-equivalent diameter of the nanoparticles. ADC is performed using a CPS Inc. 24,000 device. The detector measures the attenuation of an incident laser beam of 405 nm wavelength. The speed is set to 24,000 rpm for all samples, D(+)-Sucrose is used to build up a density gradient and prior to every measurement a reference standard colloid is injected (PVC, 0.237 nm) to increase the accuracy. This routine is well established in our group. The PVC standard is chosen as its' particle size is close to the samples particles sizes and also includes the size range of possible agglomerates and aggregates. If such structures can be excluded a priori of a measurement, an even small standard colloid can be used to improve the accuracy of the measurement. Calculation of volume-weighted size distributions is performed by the device's internal software. The diameters obtained from ADC represent spheres with equal sedimentation properties. DLS is performed with a Malvern ZetaSizer ZS operating at a wavelength of 633 nm in the backscattering mode. Particle size and size distribution by application of the cumulant method is performed by the device's internal software. The algorithm is chosen as it is available in many laboratories. Still, more accurate ones are available e.g., the CONTIN algorithm [213]. The hydrodynamic diameter of particles with organic ligands attached to their surface will appear larger in DLS. As AuNP exhibit a strong surface plasmon resonance around 520 nm [214], UV/Vis spectroscopy is performed and the mean particle size of the colloids determined by Mie-Gans-Theory [17, 118]. An algorithm written and provided by Amendola and Meneghetti is used. As the Mie-Gans model is insensitive to bimodality we limit our experiments to the pure colloids and mixtures of S7 and S10. Mixtures of S7 and S50 are excluded. The model was used without any prior calibration. Interactions between surface adsorbates and the particle surface might alter the plasmonic properties of the gold nanoparticles. To improve the accuracy of the Mie-Gans model such interaction can be taken into account. SAXS is performed with synchrotron radiation at the cSAXS beamline of the Swiss Light Source (Paul Scherrer Institute, CH). The X-ray photon energy is 11.2 keV. Pure water in the X-ray capillaries (Hilgenberg) is used as background. Data evaluation is performed in two ways. First, the commonly used so-called unified fit (UF) is applied [161-163]. It does not resolve detailed particle size distributions but gives information about average particle sizes of predefined size fractions in a colloidal solution. Furthermore, it provides the Porod invariant of these fractions, which gives information about the fractions' share of overall particle volume. The size information is given as radius of gyration and subsequently calculated into volume equivalent

diameters manually assuming spheres. Secondly, a fit to the scattering data based on a Monte Carlo Method (MC) is applied [164, 210]. Here, a distribution of spherical particles is varied freely for best fit of the scattering curve. For convenience, a visibility limit is given for the smallest particles that contribute significantly to the measured scattering. Particles below that limit are neglected [164]. This approach is able to resolve particle size distribution without prior knowledge and is therefore complementary to the unified fit. As the scattering vector range used for both ways of SAXS evaluation is  $0.07 - 3.0 \text{ nm}^{-1}$  the theoretically resolvable size range is approximately  $2 - 90 \text{ nm}$ . Prior to all measurements, the colloids are dispersed in an ultra-sonic bath for at least 10 min.

#### *Statistical errors of particle sizes*

Error bars are determined by repeating the measurements three times for DLS. The Mie-Gans Fit results in an error of 6 % [118] but is set to a minimum of  $\pm 1 \text{ nm}$  in the case of smaller deviations. The error bar of SAXS (UF) is calculated as described earlier, using the fit parameters  $R_g$ ,  $B$  and  $G$  [162]. All other size distributions obtained by STEM, SAXS (MC) and ADC are fitted and the standard deviations are calculated for each separate size fraction.

## **Results and discussion**

### *Analysis of pure colloids*

The pure colloids are, in a first step, analyzed by STEM, since electron microscopy provides direct information on particle shape and is often used as the method of choice for nanoparticle analysis [215]. Electron microscopy offers many benefits due to its wide accessibility, easy data interpretation and direct sensitivity to the number-weighted particle size distribution, due to individual particle counting. Still, if aggregates are present within the dispersed sample, they will not appear in the TEM-histogram. They can be identified by means of TEM but measuring their size is not beneficial as the aggregates may also be created during the drying process of the sample. Also, large particles do either not appear in the histogram due to insufficient counting statistics or they do appear but often the respective size bars are hardly visible next to a dominant fraction of smaller particles in TEM-histograms. Size fractions of less frequently appearing larger particles are visualized in TEM-histograms by converting the number-weighted data to e.g. volume-weighted data. As electron microscopy is the only method in this study that is directly sensitive to particle number it is transferred to such a volume-weighted distribution as shown in Figure 14. All other methods are based on electromagnetic wave absorption or scattering and are therefore sensitive to particle volume rather than particle number. As can be seen in Figure 14, the peak maxima of the particle size distributions of monomodal colloids are shifted

toward larger sizes when transformed to volume-weighted representation due to the cubic relation between radius and volume. Accordingly, large particles affect a volume-weighted size distribution much more than smaller ones. By STEM analysis of the commercial sample (Figure 14g-i) it is shown that indeed the nominal particle size of 40 nm is not representative. The mode diameter weighted by number obtained from Figure 14g is  $6.9 \pm 1.4$  nm.

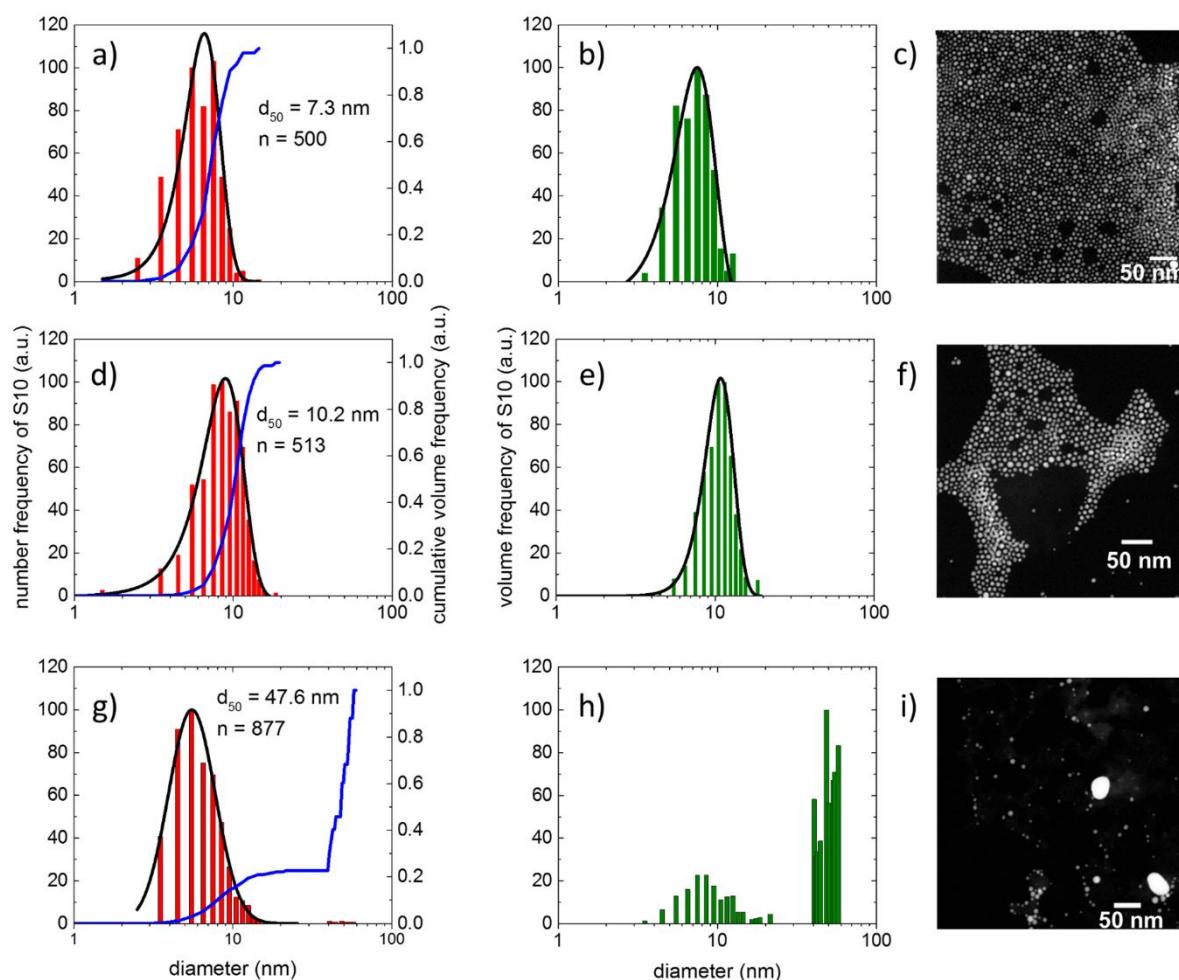


**Figure 14:** STEM images and resulting number- and volume-weighted size distributions of the pure gold colloids S7 (a–c), S10 (d–f) and S50 (g–i). The left column shows number-weighted size distributions with additional information of cumulative volume-weighted sizes (blue lines). The middle column shows the calculated volume-weighted size distributions. The right column shows representative STEM images of the pure AuNP. (For interpretation of the references to colour in this figure legend, the reader is referred to the web version of this article.)

On the other hand, the median diameter  $d_{50}$  obtained from the cumulative volume-weighted distribution is 47.6 nm which is sufficiently close to the nominal particle size, which is related to the native bimodal size distribution. The major difference between the number- and volume-weighted histograms in Figure 14g and Figure 14h shows that particle size analysis is complex and not necessarily reliable, when just a single analytical method is applied. As STEM is used as a reference method in this study and not applied to any of the particle mixture but exclusively to the pure colloids, the colloids are denoted per their STEM  $d_{50}$  (volume-weighted median diameter: S7, S10, and S50) below. This convention is summarized in Table 3. Accordingly, all methods described in the experimental section are applied to the pure samples S7, S10 and S50 to verify their monomodality (S7 and S10) and gain further information on the size fractions (S50). As more information about a colloidal sample can be drawn from size distributions rather than from average sizes the following discussion is focused on the additional techniques SAXS (MC), ADC and DLS in the first step. The statistic relevance of these techniques is high as their signals stem from millions of nanoparticles in contrast to STEM. The expectations for the laser-generated monomodal samples S7 and S10 are fully met. As the S7 and S10 particles have already been shown to be spherical and the input parameters to the MC calculation also assume spherical particles, no deviation between the SAXS (MC) and STEM size distribution is expected. As shown in Figure 15 and summarized in Table 4 this is experimentally verified. Additionally, the deviation of mode sizes is as small as 1 nm. ADC analysis further supports the monomodality of S7 and S10, but the size distributions are slightly shifted towards smaller sizes (Figure 15). This is explained by the shell of mPEG on the particle surfaces which results in both drag force against sedimentation and reduced average particle density and consequently to slower sedimentation inside the centrifuge. Thus, as expected, the particle size from ADC is slightly lower compared to STEM and SAXS. An opposite trend is predicted and shown for size distributions obtained from DLS. Obviously, the sizes found for S7 and S10 are larger compared to the other techniques (Figure 15). As ligand-functionalized particles exhibit a decreased average density, the Brownian motion is slowed down resulting in larger measured particle sizes. For the pure samples S7 and S10 a distinct monomodality is proven not only by methods resolving particle size distributions (Figure 15) but also by SAXS (UF) and Mie-Gans Theory, which are sensitive exclusively to mean particle sizes (Table 4). Regarding sample S50 the results from SAXS (MC), ADC and DLS are more complex. SAXS (MC) does support the bimodality of the sample, but both fractions appear several nanometers smaller compared to STEM as shown in Figure 15 and Table 4. The reason for the decreased size of the large fraction is considered the non-spherical shape of those particles. The MC algorithm assumed spheres, which might cause the observed deviation. Furthermore, the minimization of  $\chi^2$  in MC presumably results in a sharper distribution. The deviation in the small fraction size of 5 nm is probably caused by the resolution limit of the STEM. The images

show numerous structures appearing smaller than 5 nm. Still, in many cases, these cannot be certainly identified as nanoparticles and are hence not considered. Therefore, it is surprising not to detect the small particles in sample S50 using ADC. This is most probably related to the low mass concentration of gold in this specific sample, which is determined to be 20.6  $\mu\text{g/ml}$ . As shown in Figure 14g,h most of the gold mass is related to the large particles in sample S50. Accordingly, the mass concentration of small particles is significantly lower than 20.6  $\mu\text{g/ml}$ .

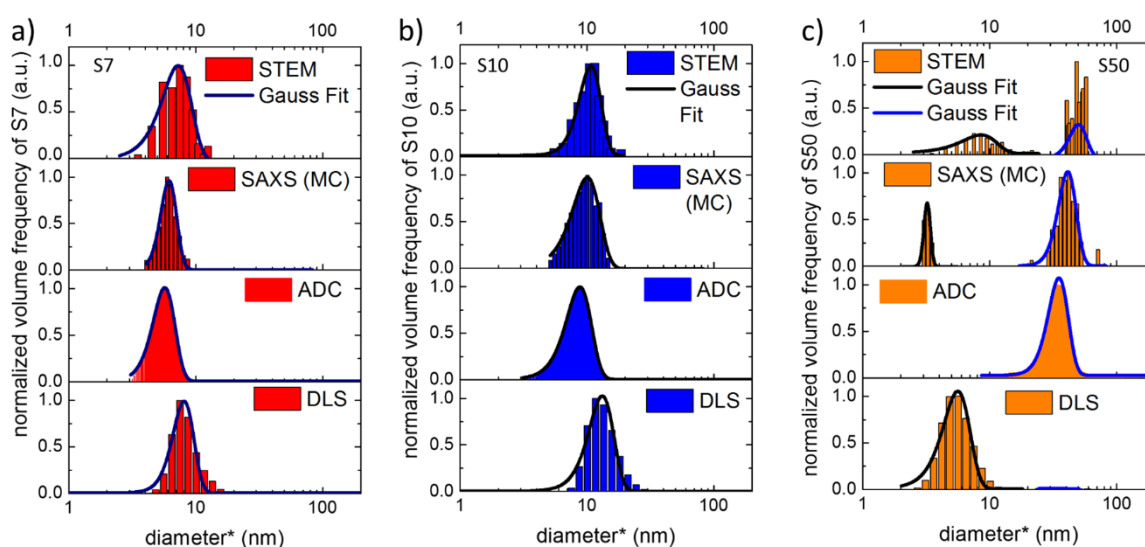


**Figure 15:** Volume-weighted particle size distributions of the pure gold colloids obtained with STEM, SAXS (MC), ADC and DLS. The asterisk indicated that the methods are sensitive to different physical properties of the particles (e. g. hydrodynamic or volume equivalent diameter). All size fractions are fitted with a Gaussian envelope.

As a consequence the amount of small nanoparticles arriving at the detector position of the ADC at any given time is too small to provide a sufficiently strong absorbance. The DLS result of S50 requires a detailed explanation. One would expect that DLS overestimates the large particle fraction due to the increased Rayleigh scattering intensity of large particles. Most likely this problem is related to the applied DLS analysis algorithm. The cumulant method results in a low match between the experimental and the calculated correlation function. Therefore, the DLS with cumulant analysis is believed to be unsuitable for the analysis of colloid S50. As indicated in Table 4 ADC, DLS, and Mie-Gans are not able to resolve the bimodality, hence the discussion of the relative amount of the fractions is based on SAXS (MC and UF) and STEM measurements. While STEM and SAXS (MC) give quite similar values for the fractions volume ratios (16/84 and 19/81), SAXS (UF) shows a larger deviation with a ratio of 30/70. Insufficient fitting of SAXS data with UF in the large scattering vector range representing the small particles most likely causes this. Accordingly, also the size of the small particle fraction of S50 is

21.4 ± 1.1 nm per SAXS (UF), which differs significantly from the size values obtained by SAXS (MC) and STEM.

**Table 4:** Summary of the volume-weighted size and volume/mass information obtained from the pure colloids S7, S10 and S50 with all applied methods. In the case of S50 also the volume ratio of the two size fractions was calculated.

sample	method	d (mode 1) (nm)	d (mode 2) (nm)	volume 1 (%)	volume 2 (%)
S7	STEM	7.3 ± 1.9	-	100	0
	SAXS (UF)	7.2 ± 3.8	-	100	0
	SAXS (MC)	6.2 ± 1.0	-	100	0
	ADC	5.7 ± 1.1	-	100	0
	DLS	8.1 ± 1.5	-	100	0
	Mie-Gans	6.8 ± 1.0	-	100	0
S10	STEM	11.7 ± 2.1	-	100	0
	SAXS (UF)	11.9 ± 1.6	-	100	0
	SAXS (MC)	10.1 ± 2.5	-	100	0
	ADC	8.8 ± 2.0	-	100	0
	DLS	13.2 ± 3.0	-	100	0
	Mie-Gans	9.8 ± 1.0	-	100	0
S50	STEM	8.5 ± 2.7	50.1 ± 7.8	16	84
	SAXS (UF)	21.4 ± 1.1	50.9 ± 1.7	30	70
	SAXS (MC)	3.2 ± 1.0	41.2 ± 6.7	19	81
	ADC	-	35.1 ± 6.4	-	100
	DLS	5.6 ± 1.4	31.7 ± 8.1	99	1
	Mie-Gans	16.0 ± 1.0	-	n/a	n/a

The additional free parameters of size dispersion of the respective fraction and particle smoothness (fractal dimension) add to this bias. It is therefore concluded that STEM and SAXS (MC) support each other sufficiently well to assume the small particle fraction in S50 to contribute to 16 % of the nanoparticle total volume. Every given nominal mixing ratios of S7-S50 are hence corrected by this factor.

#### *Size determination of particle mixtures*

The mixing of sample S7 and S50 is performed in a range of ratios from 0.033 to 100, whereby small values represent a high amount of S50 and large values represent a high amount of S7 in the mixture. As the size fractions of S7 and S50 do not overlap (except for the small fraction of S50 that directly contributes to S7 and is considered within the corrected nominal mixing ratio) the two fractions of the mixtures are analyzed individually. The results are shown in Figure 16a-b. Here the volume-weighted diameters determined by means of SAXS (MC and UF), ADC and DLS are plotted as a function of the nominal mixing ratio of S7-S50. Figure 16a shows the size evolution of the fraction S7. It is concluded that the determined size of S7 in mixtures of S7-S50 is independent of the mixing ratio except for the low fraction size (nominal mixing ratio  $\leq 1$ ), where the small particles from the S50 sample add considerably to the total fraction of small particles. Furthermore, the results from all methods except for ADC are within the range of STEM standard deviation (given by thin dashed horizontal lines). ADC results in 14% smaller particle sizes due to low sphericity of the large particles. The results for the sizes of the S50 fraction depicted in Figure 16b again show the independence of the determined diameter from the nominal mixing ratio of S7-S50. However, only sizes determined from SAXS (UF) match the sizes from STEM. Surprisingly, the fit quality for mixtures of S7-S50 is much better compared to the pure S50 sample when applying SAXS (UF). SAXS (UF) determines the radius of gyration which is subsequently transformed to volume equivalent diameters. The analysis algorithms of ADC, DLS and SAXS (MC) in contrast assume spherical particles a priori, which ultimately results in an underestimation of particle diameter. This effect is particularly pronounced in ADC because non-spherical particles are moving faster under the influence of the sedimentation force compared to their virtual spherical analogues. Analyzing trends of primary particle diameter shifts during colloid laser-synthesis is important to understand, e.g. size quenching mechanisms. But this understanding requires the analytical method to be robust for differentiation of particle sizes in often only some ten percent of the primary particle diameter. Hence, in a second experiment the effect of mixing the samples S7 and S10 whose size fraction strongly overlap as shown in Figure 14b,e. It should be noted that none of the investigated methods can distinguish between the size fractions except for ADC; the latter is achieved after manual peak deconvolution.

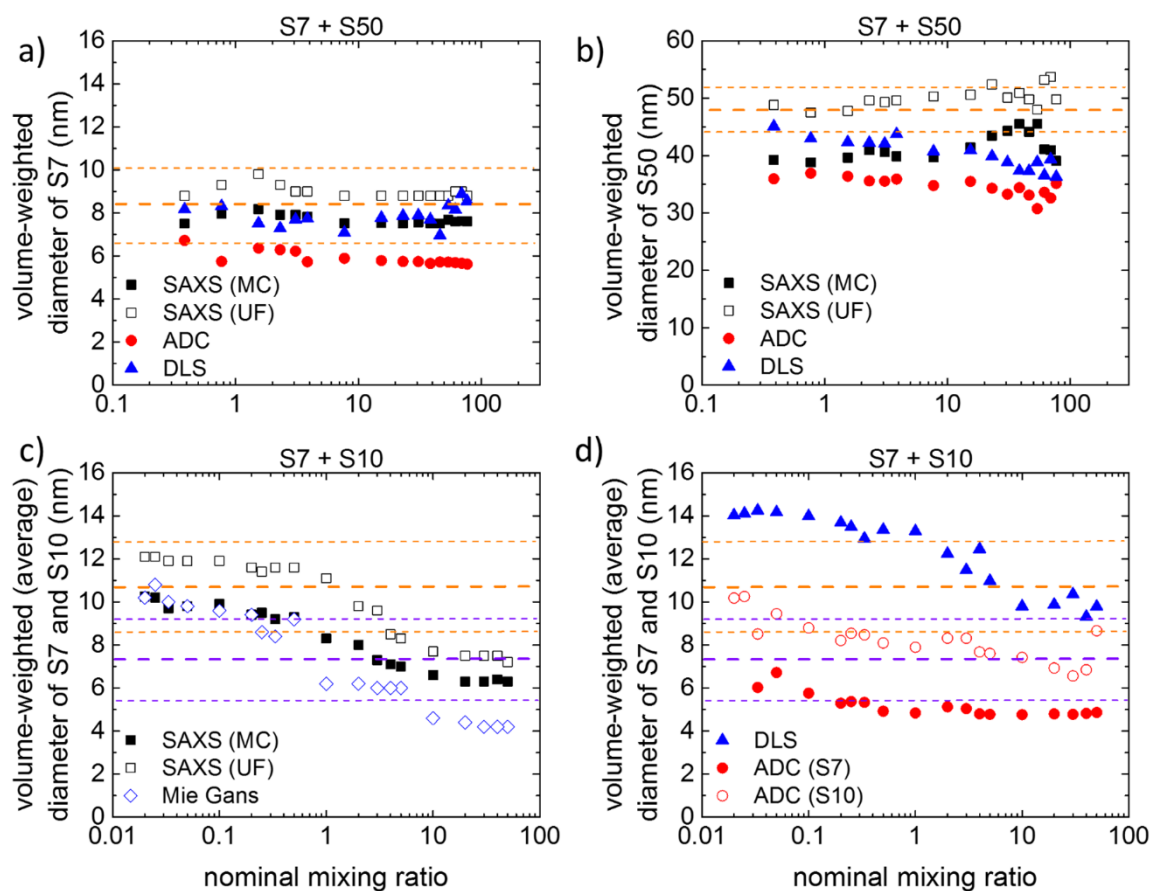


**Figure 16:** Volume-weighted sizes of the underlying fractions of mixtures of S7-S50 (a-b) and S7-S10 (c-d) as function of the nominal mixing ratio. (a) Size evolution of S7 in mixtures of S7-S50. (b) Size evolution of S50 in mixtures of S7-S50. (c) Size evolution of mean particle size in mixtures of S7-S10 (SAXS, Mie-Gans). (d) Size evolution of mean particle size and size fractions in case of ADC in mixtures of S7-S10 (DLS, ADC). The dashed yellow horizontal lines in a-b are guides to the eye and indicate the size obtained of the pure colloids by STEM and their standard deviations. The same accounts for the yellow and purple lines in c-d, which indicate the size of pure S10 (purple) and pure S7 (yellow), respectively. (For interpretation of the references to colour in this figure legend, the reader is referred to the web version of this article.)

This is attributed to the spatially fractionating nature of ADC, which makes it unique among (distinguishes it from) the compared methods in Figure 16c-d. Here the dashed orange lines represent the STEM diameter with given standard deviation of S7 and the purple dashed line represents the STEM size of S10. From Figure 16c it is obvious that the mean diameter of SAXS (UF and MC) is close to S7 at small and close to S10 at high nominal mixing ratios of S7-S10. Additionally, the turning point is given at mixing ratios of 1. Regarding DLS, a shift of about 3 nm to larger diameters is observed throughout all nominal mixing ratios of S7-S10 (Figure 16d). This may partly be attributed to the organic

ligand functionalization of particles. Apart from that, the curve progression of DLS is similar to SAXS and Mie-Gans modeling. As mentioned before ADC is able to discriminate the two size fractions which reveal themselves as shoulders in the size distributions at high and low nominal mixing ratios of S7-S10 (Figure 43 and Figure 44, chapter 9). Thus, peak deconvolution is applied, resulting in two distinct size fractions. As discussed before, the determined ADC sizes plotted in Figure 16d are smaller compared to the results of STEM due to ligand functionalization of the gold nanoparticles (reduced density) and the fact that Mie Theory (embedded in the data processing of the ADC) is of limited applicability for very small nanoparticles (< 5 – 10 nm), slightly overweighting small fractions [216]. These results clearly demonstrate the special features of size fractionating techniques in colloidal chemistry. Still, the effects of ligand functionalization and particle (non-)sphericity can only be considered if they are known. As SAXS or Mie-Gans are independent of this effect and fit the mean nominal diameters, it is recommendable to use several analytical techniques based on different physical phenomena for the characterization of a single colloidal sample.

#### *Determination of mixing ratios of S7-S50*

As the two size fractions of particle mixtures of S7-50 are reliably detected by SAXS, ADC and DLS information from the given size distributions is extracted to experimentally calculate the mixing ratios. The fraction sizes of a bimodal colloidal is important information for the experimentalist. Usually, additional information on the sample is required, namely the fraction volume e.g., during sample purification using centrifugation or for catalytic applications. The results of these experiments are summarized in Figure 17(top). The experimentally determined mixing ratios of S7-S50 are plotted as a function of the nominal mixing ratios obtained for the monodisperse samples from STEM combined with UV/Vis spectroscopy. The mixing ratio representing 100 % conformity between experimental and nominal mixing ratio is given by a dashed diagonal to guide the eye. Although DLS with cumulant analysis is suitable for size analysis (Figure 16a,b), it fails to give insight into the volume ratios of the fractions of S7 and S50, which is a serious drawback of the method. SAXS (UF and MC) and ADC show an almost linear relationship between experimental and nominal mixing ratio of S7-S50 (Figure 17, top). Obviously, the deviation of ADC increases at high mixing ratios. For SAXS (MC) the deviation is low except for three data points between nominal mixing ratios of 12 and 30, which represent a situation of marginal contribution of large particles, in particular in the low-q range of the scattering curve. The deviation is even smaller when SAXS is evaluated with the UF algorithm, which is expected as it relies on the Porod invariant, which is a shape and size independent quantity. (To support this finding the modulus average deviation of all data points obtained by one technique is calculated and plotted in Figure 17 (bottom). Again, it is obvious that DLS is not suitable for this analysis (deviation

103)). Whereas the difference between the SAXS algorithms is minor (32 for MC and 24 for UF) the deviation obtained from ADC is almost twice as large compared to SAXS. This finding is quite surprising as ADC is the only size fractionating technique applied to all particle mixtures and has proven valuable for the analysis of particle mixture with overlapping size fractions (Figure 16d). Obviously, results obtained from SAXS, which is based on electromagnetic wave scattering, are hardly affected by bimodality of a size distribution with non-overlapping size fractions.

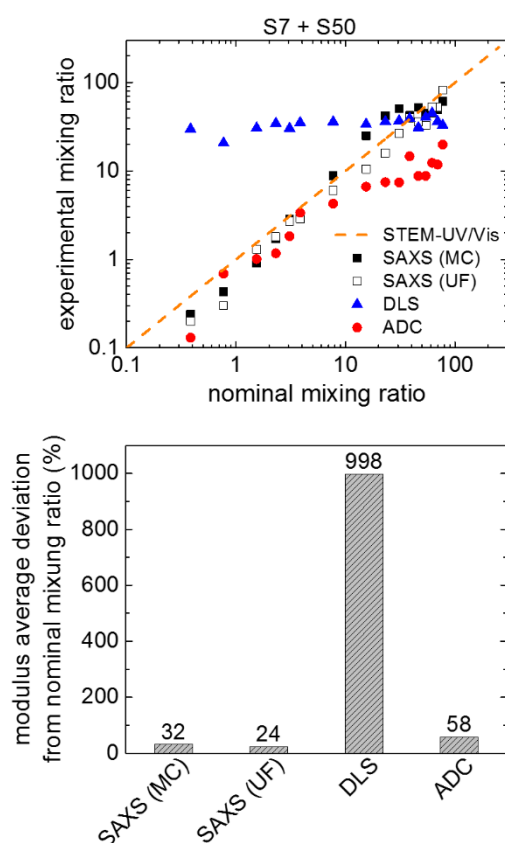


**Figure 17:** Experimentally obtained mixing ratios of S7-S50 and deviation from nominal mixing ratios. (top) Experimental mixing ratio as function of nominal mining ratio. The dashed diagonal indicates 1 to 1 conformity and serves as guide to the eye. (bottom) Modulus average deviation from nominal mixing ratios as function of applied analytical technique.

## Conclusions

Using the example of laser-generated gold nanoparticle size distributions, the complexity of nanoparticle size determination is demonstrated. The comparison of the results obtained from five analytical techniques (STEM, ADC, SAXS, UV/Vis with Mie-Gans Theory, DLS) demonstrates the challenges involved in particle characterization. Concerning laser-generated nanoparticles SAXS has been shown to be a unique method, as the sizes and volume ratios of particle fractions in bimodal

suspensions are analyzed with high accuracy and it furthermore allows for a spatially and temporally selective *in situ* characterization. For the size determination of non-overlapping particle size fractions in a colloidal suspension it is concluded that (i) size determination is independent of the mixing ratio of the individual size fractions when using SAXS and ADC and that (ii) particle non-sphericity and ligand functionalization must be considered carefully for data evaluation, in particular when using STEM, ADC and DLS. This effect is less pronounced for particles analysis with SAXS. Size differentiation of particle mixtures with strongly overlapping size fractions has been shown to be far more difficult. Such fractions could only be reliably resolved using the size fractionating method ADC combined with manual peak deconvolution. For all other four investigated methods, the results exhibit a smooth transition of an effective size from one fraction to the other, depending on the mixing ratio. Interestingly, the results reveal a distinct turning point at a nominal mixing ratio of 1 for SAXS, DLS and Mie-Gans Theory. Regarding the analysis of the pure sample S50, which is bimodal by default, ADC fails as the mass concentration of small particles is too low. This drawback does not apply to SAXS with synchrotron radiation, where the bimodality is easily demonstrated. The analysis of the relative volume of a size fraction in bimodal colloids is performed with samples exhibiting non-overlapping fractions. We find that (i) DLS with cumulant analysis is unsuitable for this purpose and (ii) nominal mixing ratios determined by SAXS are of a similar level of accuracy as those obtained from ADC. Obviously, even though SAXS is a scattering-integrating and non-fractionating method, it is well suited for the determination of mixing ratios of nanoparticles synthesized by pulsed laser ablation in liquids even at low concentrations. The method is powerful in analyzing laser generated bimodal gold colloids in terms of mean fraction diameter and nominal fraction volume ratio. Still, the method is at its limit when analyzing a bimodal colloid with strongly overlapping size fraction and mean diameters that differ by just a few nanometers, where analytical disc centrifugation presents the optimal analytical support. Finally, as an outlook for a possible follow-up study several points can be mentioned. First of all, a large particle sample (e.g., S50 in our study) would benefit from a real monodispersity. Not having to correct one of the initial samples using a correction factor would increase the accuracy of the determination of particle mixing ratios. It would be further interesting to analyze laser synthesized nanoparticles without any further steric stabilization. A comparison between the analytical results for ligand-free and unligated colloids would allow for a more sophisticated discussion on the influence of the ligand-shell. Especially, when using analytical methods like DLS or SAXS that analyze the nanoparticles in their natural dispersed environment. These two methods would further benefit from an even more detailed comparison of analytical soft-ware, of which in both cases a large variety exists. Such a study can quantify the influence of the evaluation methods on the finally obtained particle sizes. Ultimately, the routine for sample preparation can be adopted to improve the analytical results.

Therefore, the samples can be cleaned by filtration or dialysis to remove excess salts from the liquid and filtered prior to each individual measurement to remove possible agglomerates or even dust particles from the colloids.

### 5.1.2 How the re-irradiated of a single ablation spot affects cavitation bubble dynamics and nanoparticles properties in laser ablation in liquids

Alexander Letzel, Marco Santoro, Julia Frohleiks, Anna Rosa Ziefuß, Stefan Reich, Anton Plech, Enza Fazio, Fortunato Neri, Stephan Barcikowski, and Bilal Gökce

Published in: "How a re-irradiated ablation target affects cavitation bubble dynamics and nanoparticles properties in laser ablation in liquids, *Appl. Surf. Sci.* 473 (2018) 828-837"

#### Abstract

Fundamental theoretical and experimental studies on the formation of nanoparticles and cavitation during laser synthesis of colloids usually employ single-pulse conditions, whereas studies of the properties of nanoparticles naturally require prolonged ablation. We explored how a defined series of pulse number changes a silver target's surface geometry and thereby the dynamics of the laser-induced cavitation bubble and the resulting properties of the nanoparticles. The shape of the cavitation bubble transforms from hemispherical to almost spherical. The mass concentration inside the cavitation bubble follows an exponential decay with the number of laser pulses. Surprisingly, the ablated mass does not set the volume of the extended cavitation bubble, as one would expect, because of the linear dependency of both the volume of the bubble and the ablation mass per pulse on the laser fluence. No influence of the altered cavitation bubble on the nanoparticles was identified. Instead, clear evidence of a high share of silver nanoclusters ( $d < 3$  nm) was found in all samples at our low concentration conditions. The influence of these reactive species on the final particle size was found to be much greater than the cavitation bubble variations caused by prolonged surface ablation. In addition, no correlation was observed between the size of the primary particles ( $\sim 8$  nm) and the mass concentration in the cavitation bubble. Primary particles already must be pre-defined on a sub-microsecond time scale.

#### Introduction

Over the past decades, laser ablation in liquids (LAL) has developed into a competitive synthesis route to obtain nanoparticles. Since the pioneering work published in 1993 by Fojtik and Henglein [67], the method has become a vast field of research [33, 217]. Driven by the inherent purity of colloids produced by LAL, they have been and continue to be the subject of applied studies in various areas, such as disease research [72], biomedicine [218], analytical chemistry (e.g., surface-enhanced Raman

scattering [219], mass spectroscopy [82], and nanoparticle analysis [118, 169]), heritage science [80], heterogeneous catalysis [176], and many others as summarized in the comprehensive review by Zhang et al. [33]. The use of LAL-nanoparticles in this diversity of applications is driven by the purity of the particles' surfaces and the liquid dispersion medium. Only laser light, the desired pure liquid, and the desired target material are necessary, which excludes the need for organic ligands, surfactants, or chemical reagents. If noble metals are chosen as the target material, the process is facilitated further because of the easily-controllable compositions of the colloids that are produced.

Among the research in LAL that does not directly aim at defined applications, laser-induced cavitation bubbles and controlling the particle size distribution are of utmost relevance. The cavitation bubble follows the laser impact on the target. Almost instantaneously after laser impact, a plasma at the surface of the target is ignited for several tens of nanoseconds [41, 66, 220], which subsequently evaporates the surrounding liquid and forms the characteristic quasi-hemispherical cavitation bubble attached to the flat target [16, 54]. The cavitation bubble exhibits important implications for the LAL process and the produced nanoparticles. When using single nanosecond laser pulses with pulse energies of several millijoules, the bubble's lifetime is as long as several hundreds of microseconds, and its radius can be up to a few millimeters [221]. While the cavitation bubble is still active and undergoes its characteristic oscillations of collapse and rebound, additional laser pulses focused on the shielded target position lose energy by scattering at the liquid-gas interface [222]. This drawback can be avoided by moving either the laser beam relative to the target surface (scanning) [223] or vice versa [224, 225]. Also, the cavitation bubble acts as a reservoir of the ablated species in the early phase of LAL [19, 20, 40, 46, 226]. After its final collapse, the cavitation bubble leaves nanoparticles and persistent microbubbles behind, both of which add to the laser energy losses by shielding [227-229]. Thus, to achieve constant ablation rates, the use of a liquid flow setup is advantageous to take away these shielding species [230, 231].

The desire to control the particle size distributions obtained by LAL at will extensively is assumed to be closely related to the cavitation bubble phenomenon. First, a size distribution that exhibits at least a distinct bimodality or even a multimodality is characteristic for LAL, especially if high-intensity, ultra-short pulses are used [49, 232, 233], even though this effect is not caused by the cavitation. Microsecond-resolved small-angle X-ray scattering studies during nanosecond LAL identified the bimodality of nanoparticles already inside the laser-induced cavitation bubble, but they could not clarify the origin of that bimodality [19, 20, 29]. Numerical simulations have demonstrated that, indeed, two different ablation mechanisms are involved in particle formation for LAL with ultrashort pulses [46, 48]. Due to computational limitations, currently, such calculations do not exist for the more

common case of nanosecond LAL. However, even though the dominant mass of nascent nanoparticles is confined within the cavitation bubble (except some particle droplets jetted through the phase boundary of the bubble [48]), their size distribution already can be narrowed significantly in this gaseous phase by adding micromolar amounts of electrolytes to the liquid prior to laser ablation [192]. These ions also are present within the plasma [54] and the cavitation bubble, and they quench the size and increase the colloidal stability by electrostatic repulsive forces through adsorption on the surfaces of the particles [146, 192]. This points towards a ripening process inside the expanded bubble.

However, ideal conditions only apply if the target and the water are continuously refreshed during the ablation process. Several researchers have investigated the continuous production of nanoparticles using a moving, wire-shaped target in different configurations [53, 225, 234] and demonstrated the different cavitation bubble dynamics compared to a flat plate-shaped target [44]. However, the influence of individual changes in the cavitation bubbles on the size of the nanoparticles has not been determined. Scaramuzza et al. used targets with confined geometries and investigated their impact on the particle sizes with a focus on the temperature gradient inside the target induced by the interaction with the nanosecond laser [14]. Using a rotating cylindrical target, the particle size was found to be tunable by the target rotation speed [235], which causes different hydrodynamic regimes in close proximity to the surface of the target [236]. Lam et al. calculated the concentration ratio of ablated inorganic species and liquid molecules (by considering bubble volume and pressure) and found that the bubble consists mostly of vaporized molecules of the liquid [50]. Looking at sub-microsecond timescales when the volume of the bubble is minimal, highly concentrated atoms of the ablated species still undergo coalescence on a sub-nanometer time scale and form solid nanoclusters. Note that the gas phase theory of coalescence indicates that the condensation is proportional to the squared value of the particle concentration [237]. This points to the importance of knowing the intra-bubble concentration. To date, it is unknown whether this concentration is affected by the size of the bubble or if it changes under multiple-pulse conditions.

We performed LAL with an increasing pulse number while simultaneously imaging the cavitation bubble in order to close the gap between the single-pulse LAL results of spectroscopy and theoretical studies and the multi-pulse LAL results of nanoparticle property studies. Shielding species, such as residual nanoparticles and persistent bubbles, were removed by a liquid flow configuration [227, 238]. The size distribution of the silver particles in water was analyzed as a function of the number of laser pulses applied, and the influences of changes in the surface geometry of the target and changes in the volume of the cavitation bubble were determined.

## Materials and methods

### *Shadowgraphy setup for imaging of the cavitation bubble*

A custom-designed shadowgraphy system was developed by using an ablation flow chamber. A peristaltic pump provided a liquid flow rate of 35 ml/min, which avoided the screening effect of already-existing nanoparticles and persistent microbubbles due to the scattering and absorption of the laser beam (Figure 53, chapter 9). The pump stroke was removed by coupling a sealed glass bottle for pressure equilibration between the pump and the ablation chamber. A flat silver plate that was 1 mm thick was used as a target, and it was placed inside the ablation chamber and fixed perpendicular to the incoming, horizontal laser beam using double-sided tape. The height of the liquid layer above the target was 5 mm. MilliQ (18.2 M $\Omega$ ·cm) water was used in all of the experiments. The chamber was custom-made by the 3D-printing of an ABS (acrylonitrile butadiene styrene) filament (Renkforce, white). An Nd:YAG laser source (Innolas, SpitLight DPSS250-100) with a pulse duration of 9 ns and a wavelength of 1064 nm was focused by a lens that had a focal length of 75 mm and was located 65 mm from the target. The repetition rate was set at 0.2 Hz, and the pulse energy was set at 20 mJ, which was measured by the average energy of 1,000 laser pulses using a power meter. The calculated laser fluence was 14.5 J/cm<sup>2</sup>. The ablation spot size was determined by microscopy of the ablation spot and determination of its diameter after 100 pulses, the result was 420  $\mu$ m. A light source (flashlight, Led Lenser P7, 450 lm) and a camera (Basler acA1600-60, lens: Sill optics correctal T/1,5) were placed perpendicular to the laser beam and to the direction of liquid flow (Figure 18) to acquire images of the bubble and to record individual frames of the cavitation bubble. The gating time was 10  $\mu$ s and the intrinsic delay of the system was 43  $\mu$ s, which resulted in a fixed delay of 53  $\mu$ s. This is inherent since the laser was operated as the master, and the camera was a slave. The images are collected 1) by changing the delay time of the camera to study the dynamics of the bubbles and 2) by keeping the delay time of the camera constant at 83  $\mu$ s with the variation of the pulse number applied to the same spot on the target.

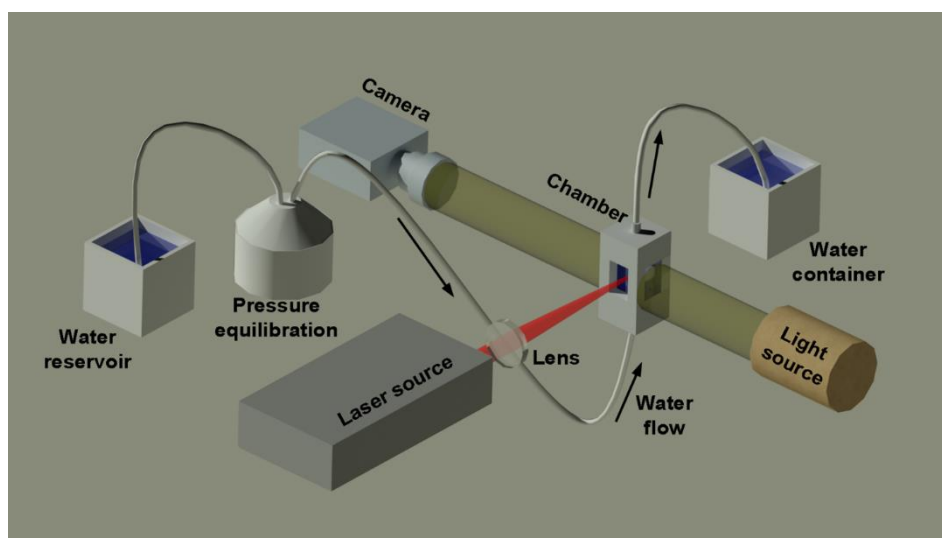


**Figure 18:** Experimental setup used for simultaneous LAL and imaging by shadowgraphy in liquid flow: The self-printed ablation chamber was made of ABS, and it had three glass windows, one perpendicular to the incoming laser beam and two parallel windows that were perpendicular to the optical light source and the camera. MilliQ water was pumped upwards across the ablation chamber by a peristaltic pump to remove persistent gas bubbles and nanoparticles. The pump stroke was removed by coupling a sealed bottle between the pump and ablation chamber. The silver target was fixed by double-sided tape on the back of the chamber, and the laser beam was focused by a 75-mm lens perpendicular to the surface of the target.

In this setup, each frame that was recorded represented a single laser pulse ablation event. Therefore, several pulses were fired while the camera delay was changed manually to acquire movies of the bubble during its entire lifetime. To calculate the volume of the cavitation bubble, we assumed hemispherical geometry. The processing and analysis of the images were performed using ImageJ (version 1.51s). The accumulation of persistent gas bubbles was minimized by a vertical, upward flow of the liquid with the laser beam coupled into the ablation chamber so that it was horizontal to the direction the liquid was flowing.

#### *Ablation configuration for collecting nanoparticles and conducting the target analysis*

Nanoparticles were collected after several defined numbers of laser shots. For this purpose, the liquid flow was stopped, and a fresh syringe was connected by a tube to the lower inlet of the chamber. The chamber was filled from the top with 0.5 ml of MilliQ water. An additional 10 laser pulses were used for ablation inside the crater that previously had been drilled by laser percussion at a repetition rate of 0.2 Hz, which was necessary to achieve the minimum concentration of particles. However, Figure

54 (chapter 9) shows that this did not induce significant fragmentation of the nanoparticles by the laser. A syringe was used to collect the particles at the lower inlet. The volume of the silver nanoparticles in the samples was in the range of 38  $\mu\text{l}$  to 3.8  $\text{nl}$ , depending on the number of previous pulses and the respective volumes of the ablation craters. Calculation of the mass concentrations of silver in the samples, done by measuring the ablated mass using confocal 3D microscopy, indicated that they were in the range of 0.8 to 80  $\mu\text{g/ml}$ .

The 0.5-ml inner volume of the flow chamber resulted in a theoretical residence time of 0.86 s, and the experimentally-determined residence time of the observable persistent bubbles was 0.1 s (Figure 53, chapter 9), which was less than 12 % of the residence time of the liquid. Accordingly, a laser repetition rate of 0.2 Hz ensured unaltered ablation conditions for each successive pulse.

The target surfaces and laser percussion-drilled craters were characterized using a confocal 3D microscope (NanoFocus,  $\mu\text{surf}$  custom) with a spatial resolution of several nanometers in the z-direction (vertical). It allowed the direct determination of the volume of the ablation crater, and, thereby, the ablated mass.

#### *Analysis of the silver colloids that were prepared*

The collected silver nanoparticles were analyzed in a dried state by scanning high-resolution transmission electron microscopy (HR-TEM) and in the hydrodynamic state using analytical ultracentrifugation (AUC). For the scanning HR-TEM (JEOL JEM-220FS, 200 kV), three drops of the colloid were drop-coated on a carbon-coated copper grid. The scanning mode was chosen because of the improved contrast that facilitated the identification of the small nanoparticles and the nanoclusters that were less than 5 nm in size.

AUC was performed using a Beckmann Coulter Proteomelab XL-I (An-50 Ti rotor) equipped with an absorption detector that operated at 280 nm and 20 °C using a 12-mm path length, double-sector EPON centerpiece equipped with a sapphire window. AUC is known to be an ideal method for sizing ultra-small nanoparticles, with its statistical resolution better than that of TEM [49, 50]. Two rotation speeds were used to record both nanoclusters with sizes of 1-7 nm (30,000 rpm, equivalent to 63,500 g), and also large, secondary, spherical nanoparticles with sizes in the range of 5-25 nm (3,000 rpm, equivalent to 365 g). The data were evaluated using SedFit (version 15.01b), with 500 data points used for measurements at low g-forces and 1,000 data points used at high g-forces. All samples are characterized the same day they were synthesized to minimize the ripening processes in the colloids.

## Results and discussion

### *Alteration of cavitation bubble by changing the number of laser pulses*

The evolution of the microscopic crater on the surface that was induced by subsequent laser pulses is a model case for the investigation of differences between single-pulse studies, engraving, and microstructuring of the surface of the target that occurs during continuous LAL. We examined the morphology of each cavitation bubble that occurred after each new laser pulse on the exact same position on the target. For each laser pulse that hit the target, a single camera frame was recorded using a constant delay of 83  $\mu\text{s}$ . This was to ensure that the bubble always was recorded at its maximum extension. Figure 19 shows representative frames of this single-pulse bubble observation after drilling a crater. After the first pulse, the cavitation bubble exhibited a characteristic quasi-hemispherical shape with a sharp interface with the water phase. The height of the bubble was in the order of 2-3 mm as was expected for high-energy, nanosecond LAL [18, 44]. As many as approximately 50 drilling shots preceded the single pulse, and the bubble basically was unaffected by the surface microstructure that was induced on the silver target. Here, we did not focus on incubation during the first few shots.

Already after 100 laser shots on the same target position, the shape of the bubble was changed significantly, indicating that the crater that was drilled into the silver target was beginning to break the symmetry of the target-bubble interface. This might further have affected the hydrodynamics of the liquid droplets as they lifted off from the surface of the solid target. While the absolute height of the cavitation bubble after 100 laser pulses was still the same as after a single pulse, the shape was no longer hemispherical because the outer areas of the bubble that contacted the target were closer to the center of the bubble. The interface between the gas-filled cavitation bubble and the surrounding liquid phase had multiple indentations, and there were some persistent, bubble-like gases that were very close to the interface. Shih et al. [48] recently described similar bubbles as satellite microbubbles. They attributed these microbubbles to the large, spherical nanoparticles that were ejected from the target in front of the expanding outer layer of the cavitation bubble. Still, the process of formation of persistent microbubbles by large nanoparticles remains elusive. The experimental conditions used by Shih et al. deviated from the current conditions ( $\leq 10$  ps in [48]), where the authors convincingly pointed out the different ablation mechanisms involved in pico-second and nano-second laser ablation [48]. Thus, it is interesting to see that similar adjacent microbubbles formed under nanosecond laser ablation as a function of the pulse number as well.

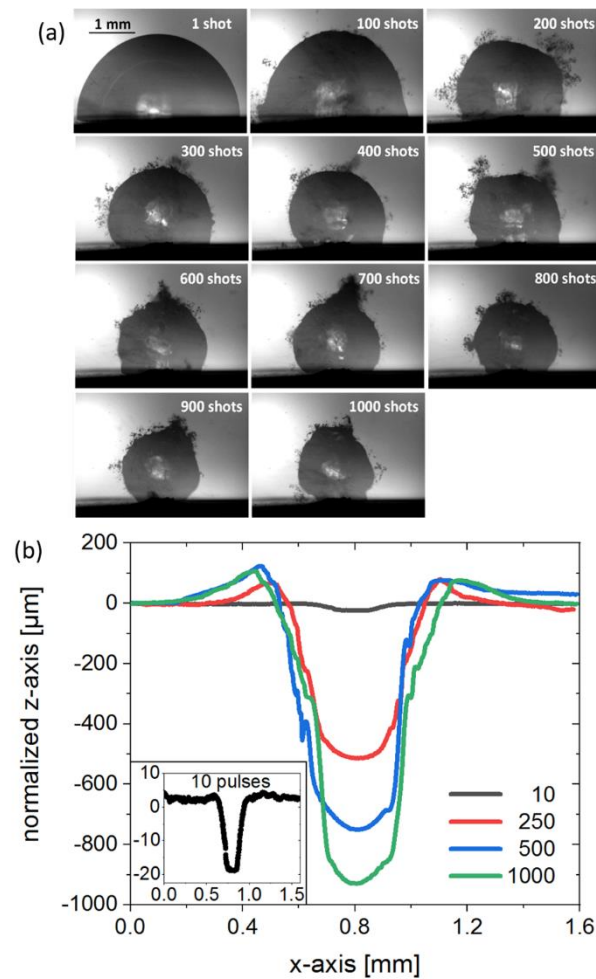


**Figure 19:** (a) Frames of the single laser pulse-induced cavitation bubbles on a 1.0 mm-thick silver target deposited after 1-1,000 preceding pulses on the same spot. Each frame was recorded at a constant delay of  $83 \mu\text{s}$  after laser impact with a camera gating time of  $10 \mu\text{s}$ . After a single laser pulse, the cavitation bubble was almost hemispherical (sphericity = 1.01), and it exhibited a sharp boundary with the surrounding liquid phase. With the increasing number of pulses on the same target position (0.2 Hz, 20 mJ), the boundary became rougher, exhibited daughter microbubbles, and, finally, the shape of the bubble was transformed to an approximately spherical shape (sphericity = 0.94); (b) Line scans of the craters on the silver target recorded by confocal 3D microscopy. All of the datasets were normalized to the zero position. As the number of laser pulses increased, the crater became deeper and wider. The latter accounts especially for the first 250 pulses. After 1,000 pulses, the crater approached the target thickness.

With the increasing number of laser shots, the induced cavitation bubble became more and more spherical instead of hemispherical (Figure 19a, 200-1000 shots) with the satellite microbubbles always present. At the same time, the height and volume of the bubble were shrinking as the number of pulses increased, i.e., the sphericity (vertical radius divided by the lateral radius [40, 41]) increased from 1.01

(hemisphere after single pulse) to 0.94 (quasi-sphere after 1,000 previous pulses). The decreased extension of the cavitation bubble indicated that its overall lifetime was changed [51]. To assure that the trigger delay of 83  $\mu\text{s}$  that was used was sufficient to hit the time point of maximum bubble extension even after a large number of previously fired laser shots, the cavitation bubble was imaged using different delays, i.e., from 53  $\mu\text{s}$  to 1053  $\mu\text{s}$ , and a total of 37 pulses to create an image sequence. The rather low number of pulses was necessary to avoid significant changes in the dynamics of the bubble due to the formation of the crater during the imaging runs. Figure 20a shows the results of the volume of the bubble as a function of the adjusted delay; the grey vertical bar indicates the gating time of the camera (10  $\mu\text{s}$ ).

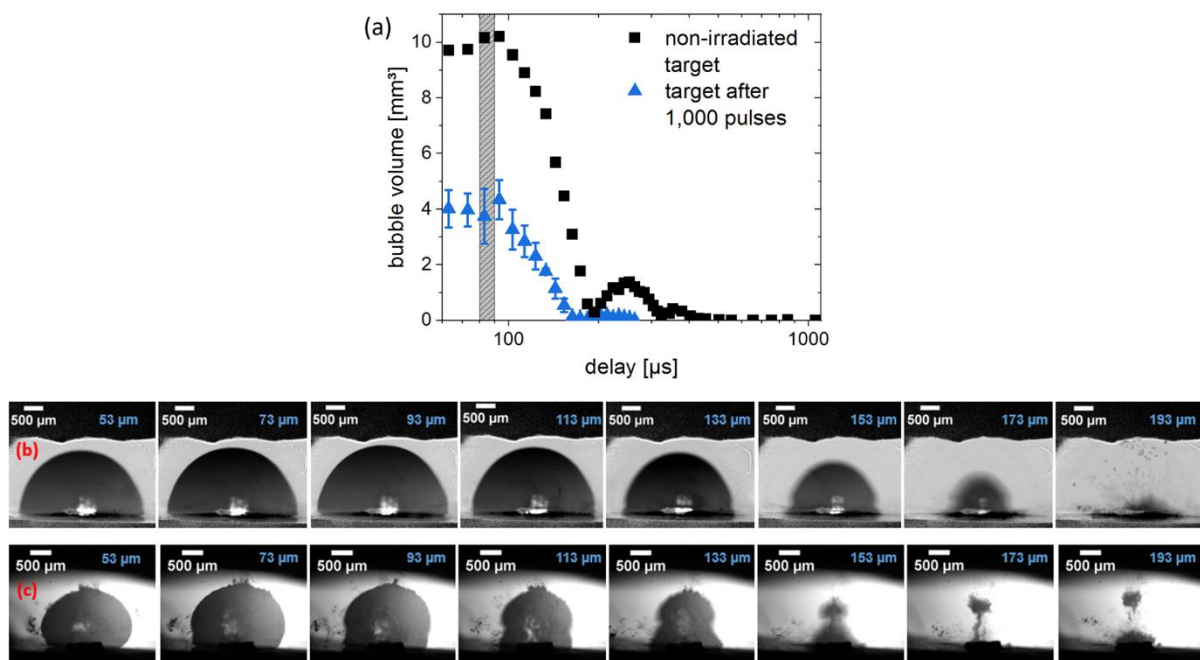


**Figure 20:** Evolution of the volume of the cavitation bubble as a function of the delay time after laser impact on the silver target: (a) The grey bar highlights the gating time of the camera (10  $\mu\text{s}$ ). The maximum size and the total lifetime of the bubble decreased as the number of laser pulses increased because of the damage to the surface of the target, while the lifetime of the first bubble remains unaffected. When comparing the two datasets, it is apparent that the delay in the maximum extension of the bubble remained unaffected; (b) Selected frames of the first cavitation bubble induced on a non-irradiated target surface; (c) Selected frames of the first cavitation bubble induced on a target that experienced 1,000 pulses in advance.

Both the delay of the maximum extension and the lifetime of the first cavitation bubble, which is the time until the bubble collapses for the first time, were equal on a non-irradiated target and on a target with a crater that was drilled by 1,000 laser pulses. However, the maximum volume of the bubble at

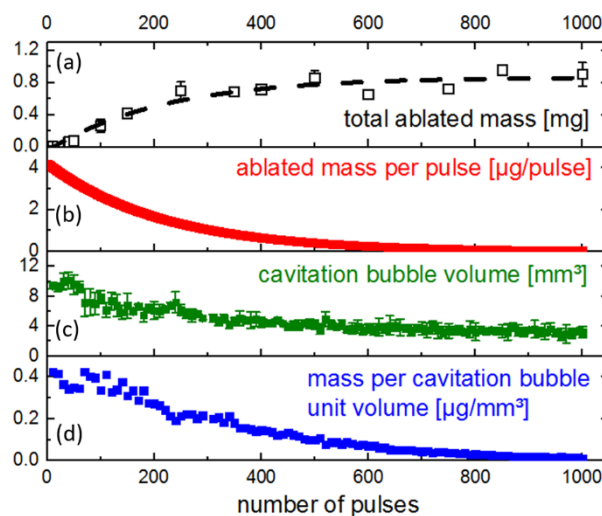
83  $\mu\text{s}$  delay decreased to approximately half of the volume of the bubble on a non-irradiated target. Also, the rebound of the second bubble lacked the energy required to induce a visible third bubble. The lifetime of the entire cavitation and rebound event was reduced significantly from 1,000  $\mu\text{s}$  to 250  $\mu\text{s}$ . Figure 20b and 20c show the changes in the dynamics of the cavitation bubble. On a virgin target, the collapse of the bubble evolves towards the target, as was known from the literature. But the situation changes drastically in the case of single-pulse ablation on a target that already had been ablated 1,000 times. The lift-off of the bubble during the first collapse phase was similar to the LAL of a wire-shaped target [53], probably caused by the symmetry being broken on the surface of the target [29]. Changes in the hydrodynamics of lifting the metal droplets caused by the microstructures of the surface were expected, similar to the altered hydrodynamics of the bubble. Figure 20 shows the feasibility of using a constant camera delay for observing a cavitation bubble during different stages of laser drilling. Previously, a correlation of the bubble sizes with the fluence showed a threshold regime for plasma ignition, followed by a linear volume increase with the fluence [44]. For a bubble with a volume of 10 mm<sup>3</sup>, a fluence of approximately 75 J/cm<sup>2</sup> is expected, which does, at first glance, not match the fluence of about 15 J/cm<sup>2</sup> applied in the present work. Still, as the observed bubble volumes in [44] and our work are similar, the effective fluence that reached the target must have been similar as well. This is explained by the fact that in this work the spot size was large compared to [44] and that, thereby, the pumping of the plasma by the long-lasting laser pulse was less but at the same time a larger area was affected by the laser leading to similar effective fluences and volumes of the cavitation bubbles. This effective fluence is thus high enough to ensure that the linear regime is reached, because that is where the volume of the bubble increases linearly with increasing laser fluence [44].

Figure 55a-e (chapter 9) show that the ablation volume and the volume of the cavitation bubble are the same for the experimental conditions that were described. They also are the same if the focal point is shifted 1 mm (= target thickness) away from the target surface. The ablated mass was therefore not sensitive to the exact focus position, keeping in mind the increasing crater depths. Still, the distribution of the local laser fluence may undergo changes based on what is known from nanosecond laser drilling in a gas atmosphere [239, 240]. The laser beam undergoes scattering inside the crater, which is partially compensated by light reflection from the walls of the crater [239]. These effects explain the increasing diameter and aspect ratio (depth  $L$  divided by diameter  $D$ ) of the crater as shown in Figure 22a, which also shows raw images from the target analysis by confocal 3D microscopy. However, the expansion of plasma inside the crater (= curved surface) is not equal to the expansion of the plasma on the non-irradiated surface (= flat surface) of the target, since the plasma cannot expand freely in all spatial directions [239]. It was shown that the absorption of laser energy in the plasma plume induced by the nanosecond pulses reduced the pulse energy absorbed by the target material to about 30 %

during laser drilling in air [241]. Overall, changes in the volume of the bubble cannot be attributed to changes in effective fluence, so they must be linked only to the geometry of the surface.

#### *Correlation of the ablated mass with the properties of the cavitation bubble*

The decrease in the maximum volume of the cavitation bubbles as the number of pulses increases as already was indicated qualitatively in Figure 19 is quantified in Figure 21c. Initially, the volume of the bubble on a non-irradiated to slightly-irradiated target is almost constant for the first 100 pulses with volumes of  $9.5 \text{ mm}^3$ . Even so, after about 50 pulses, the shape of the bubble already had started to change, which seemed to affect the volume of the bubble only slightly in the beginning. Afterward, the bubble shrinks exponentially with the number of pulses, and it becomes as small as  $3.3 \text{ mm}^3$  after 1,000 pulses. This reduction was independent of the volume of the ablation crater, which was 1-2 orders of magnitude less than the volume of the cavitation bubble (Figure 55f, chapter 9). Simultaneously, the ablated mass starts to approximately reach a saturation level after 200-300 pulses (Figure 21a).



**Figure 21:** (a) Total ablation mass; (b) ablated mass per pulse (ablation rate); (c) volume of the cavitation bubble; (d) silver mass concentration per cavitation bubble volume (mass concentration). The total ablation mass increases quickly within the first 100 to 200 pulses, after which it increases slower. This is highlighted by the ablation mass per pulse, which follows an exponential decay, which is calculated from the first derivative of the exponential fit (black dashed line in (a)) to the total ablation mass.

A more detailed view can be achieved by calculating the ablated mass per pulse (Figure 21b) by the first derivative of the exponential fit to the total ablation mass (dashed black line). The ablation rate

decreased with the number of pulses and no saturation was observed, indicating that, at some point, no ablation would occur. Regarding the decrease in the volume of the bubble, note that laser-induced cavitation bubbles frequently are described using the Rayleigh-Plesset equation (RPE) [58], although it is not suitable for describing the collapse of the bubble or the rebound phases in LAL [29, 44]. The interfacial tension of water and the kinematic viscosity were introduced as adjustable parameters to improve the usability of the Rayleigh-Plesset equation in LAL [55]. Even though the Gilmore model introduced the compressibility of the liquid [62, 63] and described LAL-induced cavitation bubbles sufficiently well.

From the data presented in Figure 21b and 21c, we calculated the single-pulse ablated nanoparticle mass per unit volume of the cavitation bubble, which is equivalent to the mass concentration inside the bubble (Figure 21d). Therefore, we assumed that most of the ablated mass initially was trapped inside the cavitation bubble. For a significant fraction of the ablated mass, this is a reasonable assumption, because nanosecond LAL structures with sizes between 3 and 100 nm have been identified inside the bubble before its final collapse [192], while no structures have been identified outside the bubble [30]. In our previous work, we reported that the minimum detectable size with high time resolution inside the cavitation bubble was 3-5 nm [192], and, therefore, smaller particles, clusters, and atoms might enter the liquid phase without being detected even before the collapse of the cavitation bubble. In addition, it is unclear whether the satellite bubbles documented in Figure 19 contained ablated matter, as reported for picosecond LAL [48]. Nevertheless, assuming complete confinement of the ablation mass inside the bubble, our calculations indicated that the mass concentration inside the cavitation bubble decreased exponentially as the number of pulses increased or the volume of the ablation crater increased, respectively (Figure 21d).

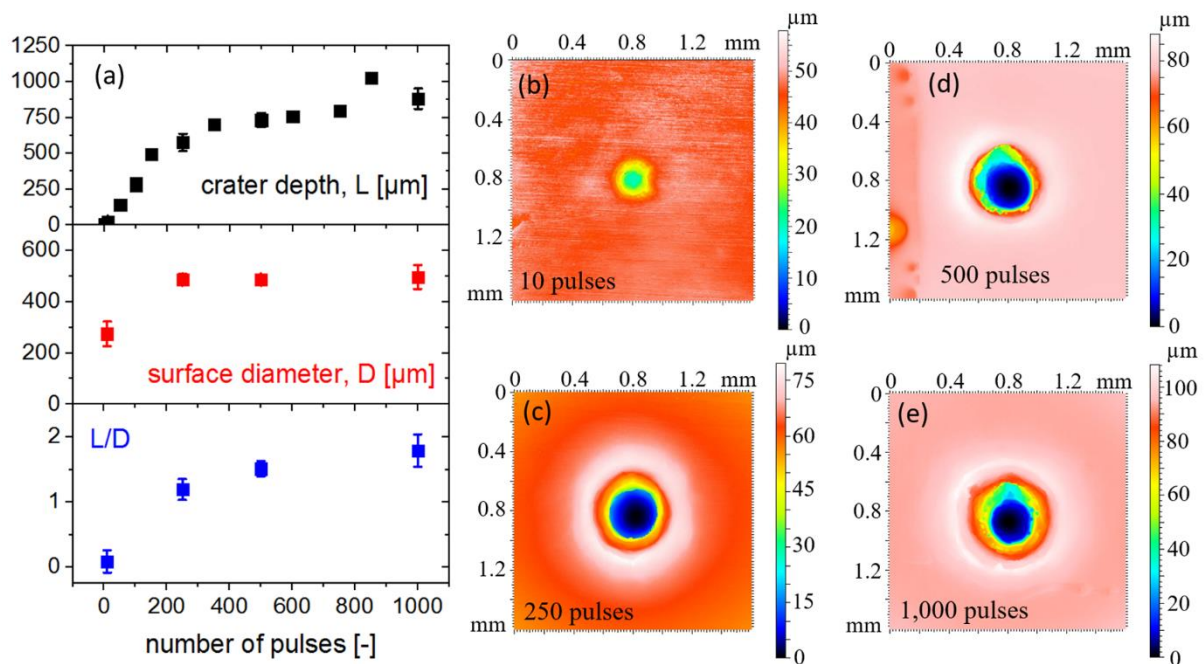


**Figure 22:** (a) Crater depth,  $L$ , crater surface diameter,  $D$ , and aspect ratio,  $L/D$ , as functions of the number of laser pulses. The increase of  $D$  and  $L/D$  shows the ablation of the crater wall with increasing depth of the crater. The target is not eroded all the way through even after 1,000 pulses; (b-e) Selected images obtained from confocal 3D microscopy that were used to analyze the target.

The hemispherical cavitation bubbles that were induced on a non-irradiated target had an internal silver concentration of  $0.4 \mu\text{g}/\text{mm}^3$ . However, after the application of 1,000 pulses and a crater as deep as  $900 \mu\text{m}$  and  $500 \mu\text{m}$  in diameter at the target surface (Figure 22), the mass concentration decreased by an order of magnitude, i.e., down to  $0.01 \mu\text{g}/\text{mm}^3$ . However, this was inconsistent with the observation of increasing ablation mass per pulse [242] and the volume of the bubble [44, 243] with increasing fluence. It is generally accepted that the ablated mass per pulse and the size of the cavitation bubble increase linearly with the laser fluence [17, 44] over a large range of fluences, but only above the respective threshold fluence. Hence, dividing both functions, i.e., the volume of the bubble and the ablated mass per pulse, is expected to result in either a new linear function or a constant value. To the contrary, we found a clearly exponential relationship between the mass concentration per bubble and the number of pulses. This clearly indicated that the mass concentration of the cavitation bubble was not correlated directly with the laser fluence, which means that changing the laser fluence provided no significant, direct control over the mass concentration of the silver inside the bubble. In turn, laser fluence is not the parameter that sets the mass concentration of the cavitation bubble, and it was more likely the confinement of the plasma inside the ablation crater and the alterations of the laser beam caused by partial refraction. Similar observations have not been reported because most

studies have focused on the analysis of the cavitation bubble [44], on the bubble and the resulting, concentrated nanoparticles [17], or focusing exclusively on the induced microstructure of the target surface [244]. Yet, the mass concentration inside the extended cavitation was affected significantly by the presence of the pre-existing craters on the surface of the target.

The cavitation bubble that are anticipated to significantly add to the growth of nascent nanoparticles by (barrier-less) coagulation and coalescence, we expected to find further influence of the particle concentration inside the extended bubble on the rate of particle growth and the final size of the nanoparticles. Assuming monodispersed particles and barrier-less sintering of two particles (coalescence), the rate of change of the concentration of the particles would be  $dN/dt = -K_0N^2$ , where  $K_0$  is the coagulation coefficient, and  $N$  is the concentration of the particles [237]. The final size of a respective nanoparticle  $d(t)$  is given by  $d(t) = d_0(1+N_0K_0t)^{2/3}$ , where  $d_0$  and  $N_0$  are the initial particle size and the number concentration, respectively, at time zero [237].

#### *Identification of nanoparticles and nanoclusters*

The concentration of particles in the samples that were prepared was extremely low (0.8-80 mg/l) because only 10 laser pulses (used for ablation in the craters) in a liquid volume of 0.5 ml were used for synthesis. However, analytical ultracentrifugation can detect such low concentrations of nanoclusters. Even though it is reported that AUC requires concentrations of at least 125 mg/l for plasmonic nanoparticles [229], nanoclusters require much lower concentrations due to their high molar extinction in the ultraviolet part of the light spectrum. This enables the use of concentrations of <10 mg/l. The normalized, number-weighted particle size distributions obtained from slow runs at 3,000 rpm are summarized in Figure 23b for 10, 250, 500, and 1,000 previous laser pulses. The size distributions were similar in that they have a large peak at 8 nm and a pronounced shoulder at about 11-13 nm, independent of the number of pulses. Regarding the same results, but weighted by particle mass, the size resolution of AUC allows the identification of five peaks in the size regime between 5 and 27 nm (Figure 23a). All four mass-weighted, normalized particle size distributions were similar, with dominating peaks at 8 nm and four additional peaks around 12, 16, 20, and 24 nm. This is summarized in Figure 23e in which the colors of the data points are identical with the colors of the bars in the background of Figure 23a, which mark the rough peak positions in the AUC size distributions. The dominance of the peak around 8 nm matched the results from *in situ*, small-angle X-ray scattering size determination inside the nanosecond LAL-induced cavitation bubble [192]. Even though the peak at 12 nm was absent after 500 pulses, the distributions were quite similar in terms of the positions of the

peaks. However, this did not account for the relative amounts of each particle fraction (i.e., peak integral). The additional normalized distributions shown in Figure 56b (chapter 9) show that the peak integrals varied significantly from synthesis to synthesis, which makes it impossible to conclude on trends regarding possible higher shares of large secondary spheres induced by satellite microbubbles surrounding the cavitation bubbles induced in deep ablation craters. In turn, what is constant is the fact that we observed no effect of the volume of the extended cavitation bubbles on particles  $\leq 25$  nm. No changes were identified in the aggregation behavior induced by fastened bubble dynamics or decreased silver mass concentration inside the bubble as a function of the number of preceding laser pulses. We hypothesized two possible reasons for this, i.e., (1) aggregation might be statistically meaningless and (2) the collapse of the bubble might change the share of large particles that cannot be resolved by AUC, even at angular velocities as low as 3,000 rpm. However, the main point is that a significant size alteration of the produced nanoparticles was not observed for changing the confinement conditions inside the bubbles. The particle production was rather defined by secondary processes, e.g., interaction with the plasma as well as laser fragmentation. The growth dynamics may have come to a halt at a time delay where the confinement due to the collapsing bubble sets in. This agrees with earlier findings that there is only minor growth observable during the lifetime of the bubble in an ideal (fresh substrate) condition [20]. Such a correlation was not observed for the silver mass inside the extended cavitation bubble (Figure 21d) and the size of primary particles, around 8 nm, (Figure 23c,e). Obviously, the primary particles were pre-defined even before the evolution of the cavitation bubble, in accordance with recent theoretical simulations [46, 48]. Our results are supported by a study by Dell'Aglio et al. in which LAL was performed under high pressure [245]. Although the maximum size and the lifetime of the bubble were decreased by increasing pressure, no influence on the final particle size distribution was identified [245]. We concluded that the mass concentration inside the extended bubble was not linked in a simple way to the initial mass concentration on a sub-microsecond time scale.

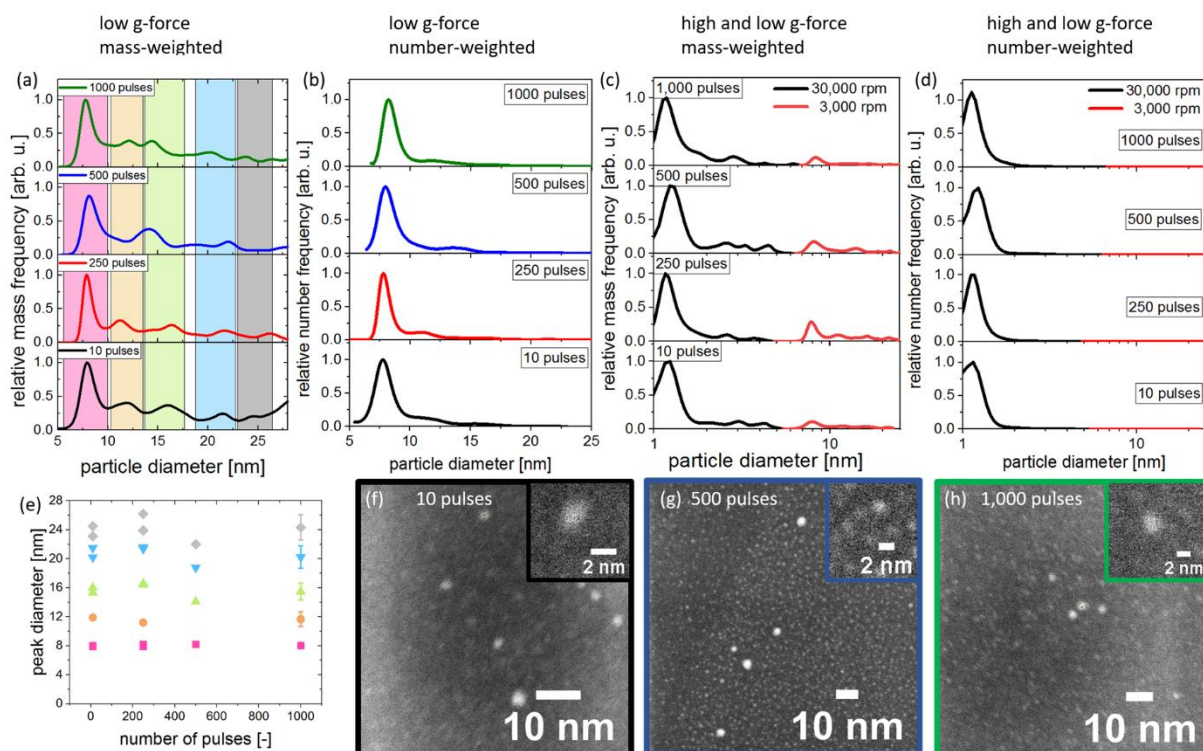


**Figure 23:** Analysis of the silver nanoparticles by AUC (a-c) and scanning HR-TEM (d,e): The AUC size distributions are normalized to the respective minimum peak diameter. (a) Mass-weighted nanoparticle size distributions of colloids obtained from craters drilled by 10, 250, 500, and 1,000 previous pulses. The AUC was operated at 3,000 rpm to detect particles up to several tens of nanometers in diameter. In (e), the colored background highlights the different peaks with the peak diameters plotted versus the number of pulses; (b) Number-weighted frequency of nanoparticles when operating the AUC at 3,000 rpm; (c) Combined normalized size distributions achieved from measurements at high (30,000 rpm, black lines) and low angular speed (3,000 rpm, red lines). High-g-force AUC analysis indicated the presence of small nanoclusters < 3 nm as the dominant particle species in all samples; (d) Same data as shown in (c) but weighted by particle number instead of mass. The images from scanning HR-TEM confirmed the presence of nanoclusters (10 pulses in (f), 500 pulses in (g), and 1,000 pulses in (h)).

Performing AUC at the high angular velocity of 30,000 rpm (Figure 23c, d) indicated that there was a dominant particle size fraction below 3 nm. Such small nanoparticles are referred to as nanoclusters [246, 247] because they have different physical properties than ordinary nanoparticles, such as the lack of surface plasmon resonance and increased fluorescence [248]. The presence of nanoclusters was verified by the scanning HR-TEM images presented in Figure 23f-h. Such ultra-small clusters have been reported as products of intensive laser fragmentation [88, 249] but we only used 10 pulses. Similar silver clusters were observed earlier during a laser fragmentation process using the second

harmonic of an Nd:YAG laser system [250]. It may be speculated that the ultra-small Ag particles resulted from the dissolution of silver in water. Hence, a reference experiment using a gold target and a single laser pulse confirmed the presence of nanoclusters even for this more inert material and with the full exclusion of laser fragmentation effects (Figure 54, chapter 9). Thus, the results from LAL of gold excluded the formation of cluster-like structures in the silver samples by dissolution of the silver particles on the TEM grid [251]. Note that, although the reproducibility of the size distributions from different syntheses was low even for the fast AUC runs, nanoclusters ( $d < 3$  nm) were identified in every run that was performed (Figure 56a, chapter 9). Also, it is important to understand why the dominant presence of nanoclusters usually has not been observed in the literature. First, nanoparticle-size histograms from single-pulse experiments or experiments that minimize the effects of laser fragmentation are rare. Second, it has been demonstrated that these clusters are consumed rapidly within days by growth processes, and the growth rate depends on the mass concentration in the sample because the probability of collision between two clusters or particles depends on their interparticle distance [88]. If the concentration of particles is extremely low, as it was in our case, nanoclusters are inherently stabilized and become detectable in significant amounts. Shih et al. [46, 48] predicted atom clusters ( $\sim 1$  nm) as the starting point for the formation of nanoclusters ( $< 3$  nm) inside the bubble, but (i) to date, only for picosecond laser pulses and (ii) not indicated their mass ratio contribution to the total mass of nanoparticles.

The presence of nanoclusters during nanosecond LAL, in the absence of laser fragmentation in liquids (LFL), has important implications for the particle-formation mechanism involved in and the experimental routines of LAL. Since nanoclusters obviously are the dominant species (Figure 23c, d) that initially form during LAL, and since the peak positions of the secondary large spheres are unaffected by the presence and depth of a crater, we concluded that (1) particle growth by ripening and coalescence [88] has a major role in the definition of the colloids after the final collapse of the cavitation bubble, which is even more significant than the shape, volume, and total lifetime of the bubble; (2) during continuous LAL, even when applying a scanning strategy the advancing surface microstructure induced on the target strongly affects the cavitation bubble, but, interestingly, it does not affect the resulting nanoparticles; hence, it is further confirmed that continuous, liquid-flow LAL is a stable synthesis process [187]; (3) manipulating the particle size is not limited to the early stage of ablation, e.g., inside the cavitation bubble, but expands to the minutes-to-days regime.

Regarding the satellite bubbles that were observed (Figure 19a), alternative explanations are (1) the (partially) ablated walls of the crater as shown by the non-linearly increasing crater aspect ratio  $L/D$  (Figure 22a); (2) hydrodynamic effects induced by additional confinement of the cavitation bubble

inside the craters, which led to higher acceleration of parts of the cavitation bubble. The latter hypothesis is supported by the frame recorded after 700 shots in Figure 19, in which a tail is visible on the top of the cavitation bubble; and (3) droplet jetting [48] may have benefited from the geometry of the crater or sub-surface voids [252] created by the preceding pulses.

## **Conclusions**

When synthesizing nanoparticles by laser ablation of solid metal targets in liquid, it is inevitable to induce microstructures on the surface of the target, but it has been unknown how pre-existing craters influenced subsequent phenomena caused by single pulses, e.g., the cavitation bubble and the properties of the particles. The cavitation bubbles usually are investigated on a non-irradiated, flat target. However, this contrasts with the synthesis of reasonable amounts or concentrations of nanoparticles by LAL because it requires several thousands of laser pulses. Even if scanning strategies were applied, the surface microstructure would still be significant.

We showed by single-pulse nanosecond laser percussion drilling in liquid flow that the volume of the cavitation bubble and the resulting depth of the crater due to ablation decrease exponentially as the number of preceding laser pulses increases. At the same time, satellite microbubbles were observed (only for pre-machined substrate) in close vicinity of the cavitation bubble, which might indicate the increased formation of large spherical particles with diameters in the tens of nanometers. In addition, the shape of the bubble at its maximum extension undergoes a transition from hemispherical to approximately spherical, combined with a decrease of rebound intensity. We found that the ablation rate decreased exponentially, comparable to the volume of the bubble, which may be caused by plasma confinement in the deep crater and by partial ablation of the wall of the crater, as indicated by increasing diameter of the crater. Interestingly, the mass concentration of silver inside the extended cavitation bubble did not decrease linearly with the number of preceding pulses. This behavior was expected because the volume of the extended bubble and the ablation mass per pulse are linear functions of the laser fluence for LAL on a flat target, and, hence, their ratio also should result in a linear function. Still, the silver mass concentration inside the bubble decreased exponentially from  $0.4 \mu\text{g}/\text{mm}^3$  after a single pulse on a flat target to  $0.01 \mu\text{g}/\text{mm}^3$  after the target was microstructured by 1,000 preceding pulses. As reported in literature, the ratio of ablated species to liquid molecules in the gas phase of the cavitation bubble is around 0.07 for ablation in water [50], and this is the reason that the ablated species must be considered to be very dilute inside the extended bubble. We showed that no direct (linear) link exists between the ablation mass and the volume of the extended bubble. The volume of the cavitation bubble was determined almost exclusively by the liquid molecules that

were vaporized to form a gas. Therefore, the vaporization of the liquid is not a process driven significantly by classical heat transfer from the ablated mass to the liquid. In addition to the influence of the microstructure of the surface on the volume of the extended cavitation bubble, the intensity of the vaporization that occurred in the process was altered significantly. While classical heat transfer from species ablated from the target was excluded as the reason for the vaporization of the liquid, the phenomenological origin of the gaseous cavitation bubble remains elusive. Still, we cannot exclude that the distribution of the fluence inside the laser-percussion drilled crater was affected by refraction at the crater wall or that plasma confinement influences the early phase of LAL.

The combined effects of plasma confinement, alteration of the cavitation bubble, and mass concentration per unit volume of the cavitation bubble could raise expectations for changes in the sizes of the nanoparticles. Surprisingly, the detailed analysis of the properties of the particles by means of analytical ultracentrifugation and scanning HR-TEM did not reveal systematic changes, either as a function of the depth of the crater or the shape of the cavitation bubble. Hence, the effect of altering the volume or shape of the cavitation bubble on particle size was found to be minor or even non-existent. Indeed, the sizes of the particle fractions within the size range between 5 and 27 nm were constant, with a distinct size peak at  $\sim 8$  nm. In all of the samples, we found a large relative amount of silver nanoclusters with diameters of  $< 3$  nm. These reactive species were stable in our study because of the very low concentration of particles per sample.

Long-time nanocluster-induced growth processes and primary plasma/ablation effects seem to be more important for the final colloids obtained by LAL as the shape change of the bubble. Nevertheless, particle yield is drastically reduced by the corrugated substrate.

## 5.2 *In situ* observation of nanoparticle size reduction by additives

Even though pulsed laser ablation in liquids produces clean nanoparticles with no organic molecules attached to the particle surface or residues in the liquid phase, the process suffers from a major drawback, which is the poor controllability of the size of the final nanoparticles. As along with the reduced size of a nanoobject, the expression of size-dependent properties increases; the need for size control of any synthesized nanomaterial is crucial. A typical laser-generated colloid consists of several species: (i) nanoclusters ( $d \leq 3$  nm) that are formed in an earlier stage of PLAL and dissolve over time by adding to the size of larger particles by coalescence and Ostwald ripening [88], though due to the speed of growth processes in concentrated colloids, nanoclusters are usually not observed; (ii) primary particles or small solid spheres with sizes of  $d \leq 10$  nm; and (iii) secondary particles that consist of two sub-fractions, namely large solid spheres ( $d > 10$  nm) and aggregates ( $d > 100$  nm). The definition of size fraction in PLAL-generated colloids is schematically depicted in Figure 24a with the fraction of nanoclusters excluded.

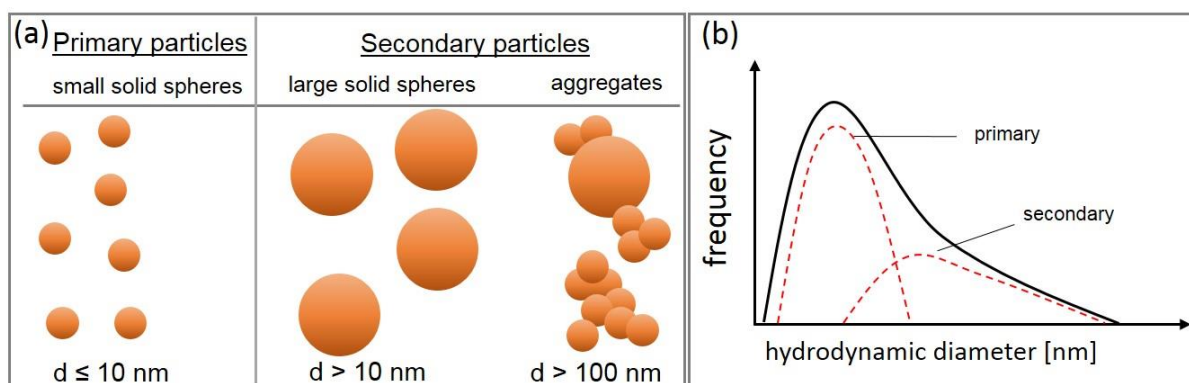


**Figure 24:** Principles of bimodality of particle size distributions obtained by PLAL. (a) Laser-generated colloids are made of several size fractions. The smallest fraction, defined as primary particles, consists of small solid spheres ( $d \leq 10$  nm). Larger particles are defined as secondary particles. These can be split into large solid spheres ( $d > 10$  nm) and aggregates ( $d > 100$  nm). (b) Sketch of a typical particle size distribution of gold nanoparticles synthesized by PLAL and obtained from analytical disc centrifugation. The dashed lines show the contribution of primary and secondary nanoparticles to the overall size distribution.

While this dissertation explores the fundamentals of nanosecond PLAL, the bimodality of colloids is best explained using the example of picosecond laser pulses for ablation as the particle size distributions of such colloids exhibit a more pronounced bimodality than those derived from nanosecond PLAL. An example of a typical size distribution of gold nanoparticles synthesized by PLAL

is presented in Figure 24b. As shown, the size distribution is best fitted using two sub-fits or is described by a lognormal envelope. Both cases indicate the presence of two or more size fractions of nanoparticles. The presented hydrodynamic analysis also clarifies the difficulties in distinguishing the sub-fractions of the secondary particles.

The formation of secondary particles cannot be avoided completely; however, it is likewise possible to re-irradiate a colloid to fragment the particles and homogenize the size fractions [235, 253, 254]. For gold nanoparticles, green lasers are preferred due to the high absorbance of AuNP, at about 523 nm, induced by SPR [123]. Another possible route towards the size control of PLAL nanoparticles is the addition of micromolar amounts of monovalent salts to the ablation medium prior to the ablation process [99, 146]. The clarification of the mechanism of the latter route by temporally and spatially resolved SAXS using synchrotron radiation is described in the following section (5.2.1). Data interpretation is enabled by the results of the previous section 5.1.1. Using the findings from the *ex situ* SAXS calibration, it is possible to calculate the ratio of secondary to primary particles. Further, the size distributions calculated using the MC method are precise. In combination with the finding that both SAXS algorithms – UF and MC – give equal results allows one to test the data from *in situ* measurements in terms of reliability.

Beside electrolytes, macromolecular ligands are used in PLAL to control the size of the synthesized nanoparticles. After the clarification of the time and location of nascent gold nanoparticles and ions delivered by NaCl in section 5.2.1, the next step is to identify the same for the interaction of particles and macromolecular ligands. As observed in the previously, the employed high-speed SAXS is unable to resolve the differences in the size of primary particles, independent of the presence of a size-quenching electrolyte. Therefore, an alternative X-ray method is used to probe the gaseous phase of the laser-induced cavitation bubble. For higher sensitivity towards the large secondary particles, XHI is chosen. The sensitivity of XHI towards the recorded scattering intensity of the nanoobject is not a linear function, but instead the sensitivity curve undergoes a global maximum. Depending on the design of an individual XHI setup, this maximum sensitivity can be shifted, as schematically shown in Figure 25 (red curves) [255]. The green curve illustrates the size distribution of gold nanoparticles obtained in water by PLAL. Still, XHI, in contrast to SAXS, does not allow one to calculate particle size distributions; instead, the recorded scattering intensity originates from all the probe species.

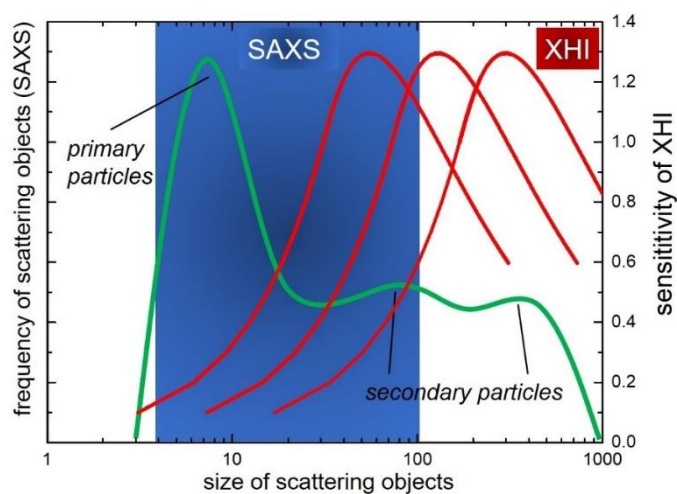


**Figure 25:** Scheme of the size ranges of scattering objects (nanoparticles) that are accessible by SAXS (blue rectangular area) and XHI (three red curves). The size distribution of a laser-generated colloid is illustrated by the green curve. XHI shows the advantage of easy tunability of the sensitivity maximum to various particle sizes. Sensitivity of XHI is adapted from [255].

The tunable sensitivity is exploited to focus on secondary particles. In contrast to XHI, in SAXS, tuning the accessible size range is challenging as the detection of smaller scattering vectors requires a large sample to detect distances in a range up to meters as well as higher X-ray flux to compensate for the loss of flux among the increased beam path. The size range that could be analyzed in the *in situ* SAXS study in 5.2.1 is marked as the blue background in Figure 25.

Accordingly, in 5.2, three related *in situ* experiments are carried out to determine whether the macromolecular ligand polyvinylpyrrolidone (PVP) acts as a size-quenching agent like the inorganic NaCl or if the macromolecule affects the ablated nanoparticles on a later time scale. Hence, the ablation of gold is performed in pure water as a reference. Besides PVP, NaCl is again used as an additive to the liquid phase prior to laser ablation. The ablation in NaCl is to test the method itself. According to the results from section 5.2.1, a low scattering signal is expected to be recorded by the XHI for the ablation in NaCl solution.

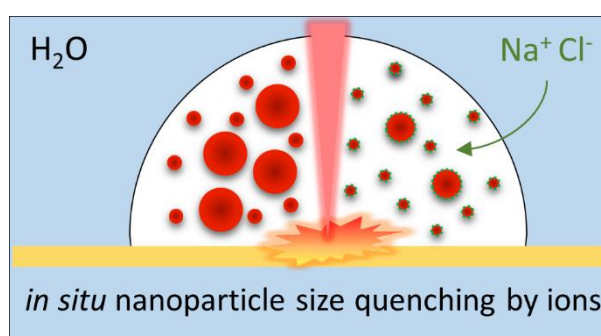
### 5.2.1 Size quenching during laser synthesis of colloids happens already in the vapor phase of the cavitation bubble

Alexander Letzel, Bilal Gökce, Philipp Wagener, Shyjumon Ibrahimkutty, Andreas Menzel, Anton Plech, and Stephan Barcikowski

Published in: "Size quenching during laser synthesis of colloids happens already in the vapor phase of the cavitation bubble, *J. Phys. Chem. C* 121 (2017) 5356-5365."

#### Abstract

Although nanoparticle synthesis by pulsed laser ablation in liquids (PLAL) is gaining wide applicability, the mechanism of particle formation, in particular size-quenching effects by dissolved anions, is not fully understood yet. It is well-known that the size of small primary particles ( $d \leq 10$  nm), secondary particles



(spherical particles  $d > 10$  nm), and agglomerates observed *ex situ* is effectively reduced by the addition of small amounts of monovalent electrolyte to the liquid prior to laser ablation. In this study, we focus on the particle formation and evolution inside the vapor filled cavitation bubble. This vapor phase is enriched with ions from the afore added electrolyte. By probing the cavitation bubbles' interior by means of small-angle X-ray scattering (SAXS), we are able to examine whether the size quenching reaction between nanoparticles and ions starts already during cavitation bubble confinement or if these reactions are subjected to the liquid phase. We find that particle size quenching occurs already within the first bubble oscillation (approximately 100  $\mu$ s after laser impact), still inside the vapor phase. Thereby we demonstrate that nanoparticle-ion interactions during PLAL are in fact a gas phase phenomenon. These interactions include size reduction of both primary and secondary particles and a decreased abundance of the latter as shown by *in situ* SAXS and confirmed by *ex situ* particle analysis (e.g., static SAXS and TEM).

#### Introduction

Nanoparticle synthesis by pulsed laser ablation in liquids (PLAL) is gaining wide applicability as a general method to produce surfactant-free, electrostatically stabilized colloidal nanoparticles from a broad range of material classes [33, 98, 231, 256-260]. Recently, nanoparticle productivity of several

materials surpassed the limit of 1 g/h up to about 4 g/h for gold nanoparticles [187, 238], making it competitive to classical chemical synthesis by reduction of gold salts. Functionalization and size quenching of those building blocks can be achieved simultaneously by binding of ligands *in situ* [134, 144].

There are contradicting results in reports within the recent years, which studied *in situ* functionalization during laser ablation in surfactant or organic ligand solution. Adding organic ligands or surfactants to the solution generally results in size quenching due to steric or electrosteric stabilization of primary particles ( $d \leq 10$  nm), no matter if they are added before or immediately after laser ablation. In the literature, there are several examples of size quenching effects using surfactants and polymers [126, 261, 262], biomolecules [263, 264] or even solid supports [265-267]. For instance, growth quenching by covalent binding to the gold nanoparticle surface is efficiently achieved by thiolated biomolecules [262]. At the same time, biomolecule degradation under appropriate focusing condition is below the detection limit, as proven by their preserved functionality [134, 268]. Thus, quantitative particle–biomolecule chemisorption is likely to happen after cavitation, as it is improbable that biomolecules would enter and survive the possible temperature and pressure conditions inside the cavitation bubble without significant degradation. One must consider the important difference between laser ablation by nanosecond lasers and ultrashort-pulsed lasers in terms of heating the solid target and the surrounding liquid and further heating of the laser-induced plasma plume by nanosecond laser pulses [14, 27, 43]. Possibly the same molecules degrade when nanosecond lasers instead of e.g. picosecond lasers are used. Additionally, liquid flow experiments present a further way for size quenching [134] and minimizing of biomolecule degradation [144]. Thus, there is indication for both modification of particle growth inside and outside of the bubble, depending on liquid, ligands, and flow conditions. However, the control of particle size by quenching is likewise possible ligand-free by inorganic salts [21]. Such inorganic salts are known to react with laser-ablated species leading to interesting single-crystalline morphologies of Si- and C-nanoparticles [269, 270]. Lam et al. have shown by means of *in situ* plasma emission spectroscopy and density functional theory (DFT) calculations on the laser ablation of  $\text{Al}_2\text{O}_3$  in water that oxidation may indeed start already several tens of nanoseconds after laser impact, still inside the laser-induced plasma [226]. This ligand-free size quenching is achieved during PLAL by the addition of micromolar concentrations of anions to the liquid before the laser ablation process, effectively delivering charges to the particle surface [146] and resulting in monodisperse, monomodal nanoparticle colloids [21]. Although this method is frequently used (electrostatic and electrosteric particle stabilization) [38, 128, 261, 271], the particle formation mechanism is only partly understood yet. In particular, the question arises of when (during which

phase in the bubble lifetime) and where (inside or outside the bubble) the stabilization of nanoparticles by ions takes place. With respect to the observation that nanoparticles obtained from laser ablation in pure water detected (*in situ*) inside the cavitation bubble's vapor phase [19, 20] are larger than nanoparticles obtained (*ex situ*) from liquids containing a size quenching agent [21, 146], an early phase of ion-particle interaction is implied, possibly already during cavitation. For reasons of reproducibility, performing *in situ* experiments during PLAL under continuous flow conditions is of major importance. Attempts to ablate gold in pure water in an optical cell results in simultaneous size reduction and deagglomeration by laser fragmentation [68]. Accordingly, *ex situ* analysis of thus prepared colloids provides only limited insight into the processes involved in particle formation at early stages [17]. Relying on *ex situ* analysis solely can, of course, provide new mechanistic findings but ripening must be carefully considered, reported to happen for platinum, gold, and palladium nanoparticles laser-fragmented in both water and micromolar saline solution [88]. As mentioned before, size quenching by ligands does at least partially take place outside the cavitation bubble [134]; otherwise, Matsumoto et al. have shown by means of plasma emission spectroscopy that electrolytes are present within the cavitation bubble, even in the same ratio as initially added to the liquid [54]. Even if these results contributed greatly to the understanding of ion interaction with the cavitation bubble, the mechanism of particle formation during PLAL could not be explained yet due to the lack of time-resolved nanoparticle size measurements [54].

The difficulties during exploration of the mechanism of size quenching of particles by anions originate from the manifold of temporally and spatially interrelated elementary processes during PLAL. For instance, the oscillating laser-induced cavitation bubble scatters light at the liquid-gas interface and obstructs the view on the bubble interior [16, 55, 272, 273]; hence, monitoring of particle formation using conventional optical methods remains problematic. At the same time, this laser ablation-induced bubble itself determines particle formation conditions due to confinement of the ablated matter [66, 238]. It has been debated to which extent nanoparticle growth and coalescence are happening already inside the bubble or during its collapse and the dispersion into the liquid.

In recent works, it was demonstrated by spatiotemporally resolved small-angle X-ray scattering (SAXS) that during the initial stage of laser ablation of gold and silver in pure water two fractions of nanostructures are formed: small primary particles ( $d \leq 10$  nm) and agglomerates or spheres in the regime of 30–70 nm [19, 20]. This typical bimodality may limit application prospects where monomodal, monodisperse colloids are demanded. The understanding of the origin of the two size fractions and control approaches could contribute to further advancement of PLAL. It could be shown that nanoparticles are already present within the bubble and, at least partially, may cross the bubble

interface at some time prior to collapse and finally end up being quantitatively dispersed in the liquid [19, 20]. This, however, requires an interface crossing of particles either during the expansion phase or the collapse of the bubble. As an alternative route, seeds could also be injected into the liquid prior to bubble formation. According to this, Hu et al. performed laser ablation of cobalt in solutions of  $K_2PtCl_4$  and demonstrated the formation of PtCo nanoalloys [274, 275]. The reaction of Co nanoparticles and  $PtCl_4^{2-}$  was hypothesized to occur outside the cavitation bubble, near the bubble–liquid interface [274, 275]. Regarding the interface crossing of small nanoparticles during cavitation bubble lifetime this is a plausible explanation. On the other hand, ions are present within the cavitation bubble as well [50, 54]. For an absolute statement time-resolved observations of nanoparticle–ion reactions are essential. Such measurements would allow distinguishing between (a) a thermodynamically driven redox reaction mechanism in the surrounding fluid and (b) a kinetically triggered reaction inside the bubble’s vapor phase. Furthermore, Shih et al. recently performed atomistic modeling of the ablated material during PLAL for the first 3 ns after laser impact on a solid target [46]. They showed that silver nanoparticles are present in the liquid already after 1 ns. Also, the computational model reveals a trimodality of the particle size distribution composed of atom clusters ( $\sim 1$  nm), primary particles of about 10 nm, and larger secondary particles in the order of tens of nanometers [46]. Although the model confirms *in situ* SAXS size measurements [19, 20], it cannot confirm the experimental results in the prediction of large solid particles since the model only covers a time range until 3 ns after laser impact (when the secondary particle fraction is still a liquid metal droplet) [46]. It is worth mentioning that Shih et al. modeled ablation with picosecond pulses [46][47] whereas in the present study nanosecond pulses have been used to increase cavitation bubble size to allow X-ray probing. Still, recently Scaramuzza et al. have shown by laser ablation of gold targets with varying confinements in lateral and transversal direction (as well as beam spot size) that such confinements alter both particle size and polydispersity of the resulting nanoparticles [14]. This effect must be taken into account when interpreting results from size quenching experiments with nanosecond laser pulses, as the plasma plume from laser impact interacts with the (still present) laser beam. This leads to further heating of the plasma and the surrounding environment in contrast to picosecond ablation [14, 27, 43, 68]. Furthermore, monovalent ions in micromolar concentration are known to strongly affect the entire particle size distribution of PLAL colloids, which is why we study the dynamics of nanoparticles within cavitation bubble confinement by pulsed laser ablation of gold in water and saline solution (0.5 mM NaCl) in this paper. NaCl is chosen due to its frequent use, compatibility to biological environment, and the observation of high size quenching efficiency at moderate concentrations of 0.5 mM [146]. Inorganic ions are expected to be resistant against high temperature and pressure at the expansion and collapse phase of the laser-induced cavitation bubble,

so degradation is less problematic during PLAL. We are able to show by means of *in situ* high spatial and temporal resolution SAXS with synchrotron radiation that interactions of nanoparticles and ions take place already within the laser-induced cavitation bubble's vapor phase as indicated in reference [54] and postulated to happen outside the bubble in references [274] and [275]. Reference [46] suggests theoretically that large droplets are starting to condense in the early phase of the bubble. Experimentally, we find an *in situ* influence of salts on the bimodality of laser-generated colloids, as they affect both small and large solid nanoparticles (hence, not only the aggregates) within the cavitation bubble. Therefore, our study extends the view of the mechanisms involved in PLAL by closing the time gap between the atomistic modeling [46] and *ex situ* experimental studies.

## Experimental section

### *Laser ablation setup and particle characterization*

SAXS usually requires data accumulation for a large number of pulses for sufficient signal-to-noise ratio. Laser ablation in a simple liquid batch chamber (or a beaker) is not a stationary process but highly dynamic due to the changing concentration of nanoparticles, unequal flow conditions (convection), progressing target erosion, and postirradiation of nanoparticles by subsequent laser pulses. Therefore, a stationary and reproducible process has to be provided for a sufficient long time interval. These requirements are met by a custom-made ablation chamber that is schematically illustrated in Figure 26. A nanosecond laser with 10 mJ pulse energy and a Gaussian beam profile (1064 nm, 9 ns, 100 Hz, Innolas Spitlight DPSS-250-100) is focused onto a spot size of about 100  $\mu\text{m}$  by a plano-convex lens. The target (a 4 mm wide gold ribbon fed by a continuous transport unit) and the liquid (either distilled deionized water or sodium chloride solution of 0.5 mM, Sigma-Aldrich) are continuously refreshed during ablation. Accumulation of persistent gas bubbles is minimized by a vertical, upward flow of the liquid and upward transport of the ribbon, while the laser beam is coupled horizontally from the side through the lens, which also acts as a container wall (35 mm effective focal length). The X-ray transmission through the liquid (on a photodiode) and SAXS (on a two-dimensional detector) are measured *in situ* perpendicular to both the ribbon and laser direction by entering the chamber through thin Kapton (DuPont) windows.

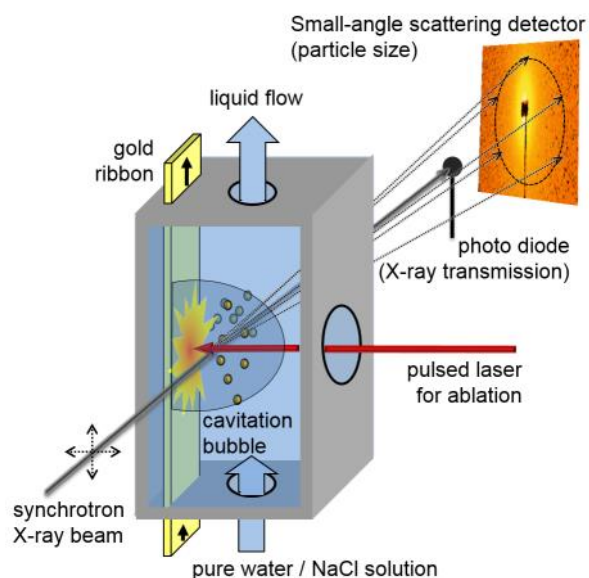


**Figure 26:** Scheme of the experimental setup of the time-resolved SAXS experiment with a continuously moving gold ribbon target, the supply and exhaust of the water (respectively NaCl solution) from the bottom to the top, and the laser beam entering the chamber from the side through a sealed lens. The X-ray path intersects the interaction area and is recorded by a photodiode (direct beam) and 2D detector (scattering).

For *ex situ* particle characterization, gold nanoparticles are laser-generated in pure water and saline solution using a flow chamber setup similar to Figure 26. Analysis is performed by transmission electron microscopy (TEM), ultraviolet–visible extinction spectroscopy (UV/Vis), analytical disc centrifugation (ADC), and SAXS. The hydrodynamic diameter  $d_H$  and agglomeration state of the colloidal nanoparticles are determined by ADC using a DC 24,000 from CPS instruments. A volume of 0.1 ml is injected against a saccharose gradient and an external standard (237 nm PVC particles) while the disc is operated at 24,000 rpm. For TEM, the colloidal solution is drop-coated onto a carbon-coated copper grid and examined using 200 keV acceleration voltage (Jeol JEM-2200FS). UV/vis extinction spectroscopy is performed using a benchtop spectrophotometer (Thermo Scientific Evolution 201). *Ex situ* SAXS measurements are performed at the same beamline as the *in situ* experiments (see next section), with the colloids filled in glass capillaries and sealed with wax. Further aggregation of Au colloids in pure water is prevented by adding bovine serum albumin several minutes after ablation.

### *Small-angle X-ray scattering and data analysis*

SAXS is performed at the beamline cSAXS at the Swiss Light Source (PSI Villigen, CH) with a collimated, thin X-ray beam. The spot size of  $6 \times 24 \mu\text{m}^2$  is much smaller than the maximum bubble size. Temporal resolution is obtained by switching a pixelated detector (Pilatus 2M) active during a short gate time (60  $\mu\text{s}$ ) relative to the arrival of the laser pulses at the target. This is repeated at 100 Hz for typically 2500 shots in order to accumulate enough statistics for scattering pattern analysis, which is subsequently performed with standard steps [16, 66]. This is repeated for both pure water and electrolyte about 50 times. *Ex situ* measurements are done at the same beamline with the colloids from batch ablation (flow chamber) filled in capillaries, while water-filled capillaries were used as background. Data evaluation is performed with the same tools as described above.

For spatial resolution of *in situ* measurements, the chamber and laser path are moved equally relative to the X-rays. Scattering background is removed by subtracting at each time delay and height above target a similar measurement that only differs by using a negative time delay (i.e., the scattering recorded before arrival of the laser). This procedure also suppressed signals from pre-existing particles in the liquid between two cavitation events [16, 276]. The scattered intensity at scattering vector  $q$ , given by the X-ray wavelength  $\lambda$  ( $=0.912 \text{ \AA}$ ) and scattering angle  $2\Theta$ , is basically a Fourier transform of the particle shape with rotational average. Characteristic X-ray intensity is recorded around  $q$  positions that scale to the inverse particle size  $2\pi/d$ . Particle geometry can be retrieved either by fitting with shape-dependent model functions or by shape-independent approaches [276]. One approach is the assumption of several hierarchies of particle sizes and degrees of agglomeration [161], which allows for a generalized fit of the main parameters of the particle distribution, such as average radius of gyration, agglomerate size, and dimensionality of the agglomerate. This approach is referred to as unified fit within the literature and this article [161, 162]. Please note that the application of two hierarchical levels in the unified fit is not arbitrary but is necessity for good fitting of the entire scattering curves. Additionally, the integral over the intensity  $I(q) \cdot q^2$  (Porod invariant) can be used as a measure of the probed scattering mass. This was successfully applied to nanoparticle formation by laser ablation in the gas phase [277]. Recently, a method was established to calculate particle size distributions from SAXS scattering curves without prior knowledge of the resulting distribution envelope (e.g., Gaussian or lognormal) [164, 165]. Instead, the scattering curves are fitted for a given particle shape by freely varying the distribution function by reverse Monte Carlo simulation. We chose spherical particles as they are also observed *ex situ* (Figure 31b-d). Using two independent methods of size data extraction from SAXS allows us to confirm our results independently of a single algorithm,

thus allowing general conclusions on particle evolution inside the cavitation bubble during pulsed laser ablation in liquids and the size quenching effect of low concentrations of electrolytes.

For better comparison of SAXS and TEM, all gyration radii  $R_g$  obtained in the following by the generalized SAXS data analysis are transformed into particle diameters of spheres and designated as particle size throughout the article. A typical scattering signal (see Figure 28a) consists of a high  $q$  ( $0.038\text{--}0.2 \text{ \AA}^{-1}$ ) and low  $q$  region ( $0\text{--}0.038 \text{ \AA}^{-1}$ ) divided by the underlying fits of hierarchical levels [162]. The high  $q$  particles species is defined as small particles ( $d \leq 10 \text{ nm}$ ) while low  $q$  species are defined as large secondary particles and agglomerates ( $d > 10 \text{ nm}$ ); for more information see reference [20]. Please note that SAXS is sensitive to particle volume rather than particle number. Therefore, it is more sensitive to larger particles. For better comparison of the presented data all average sizes and size distribution are presented in volume-weighted histograms.

## Results and discussion

Cavitation bubble dynamics are measured by the time-dependent X-ray transmission changes of the laser-induced vapor bubble with a photodiode in front of the 2D detector. The change of detected amplitude is considered as being proportional to the change in water thickness along X-ray beam projection volume, i.e., the bubble size. After absorption of the laser pulse a hemispherical cavitation bubble forms at the ablation spot and oscillates until its final collapse. Figure 27 shows representative traces of the transient. Note that gate time of the detector smooths the signal so that no sharp collapse time point can be visualized by this technique. It can be seen that the cavitation bubble follows a damped oscillation for laser-induced cavitation bubbles in liquid [30, 55].

Maximum bubble extension is observed after  $100 \mu\text{s}$ . Afterward, the bubble shrinks and collapses at  $220 \mu\text{s}$ . The second bubble reaches its maximal extension at  $300 \mu\text{s}$ , and after  $500 \mu\text{s}$  the bubble is finally collapsed. Nevertheless, there is still an offset in transient absorption after  $500 \mu\text{s}$ , indicating the presence of small persistent gas bubbles as observed before [16, 227].

Lateral analysis of the cavitation bubble shape implies a nearly spherical collapse with some flattening from the top [30]. The transients were recorded at different heights above the target ( $1 \text{ mm} =$  bubble top,  $0.5 \text{ mm} =$  bubble center) which show the same dynamics but with different amplitude. Additionally, the second bubble is found to be smaller ( $0.8 \text{ mm}$  radius) than the first one ( $1.5 \text{ mm}$  radius).

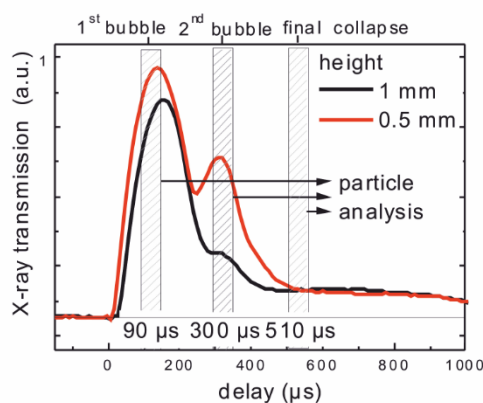


**Figure 27:** Relative cavitation bubble radius at 1 mm (black line, bubble top) and 0.5 mm (red line, bubble center) height above the gold target recorded via X-ray transmission. Hatched areas mark the region of interest for particle species analysis at the maximal extension of first bubble, second bubble, and after the final collapse.

A selected set of SAXS curves is shown in Figure 28 (top). Particle size analysis by SAXS is performed by applying the unified and MC fit approach to this data, leading to two hierarchical levels within the given  $q$ -range corresponding to primary particles and secondary particles and agglomerates. Primary particles of about 10 nm diameter are seen around  $0.07 \text{ \AA}^{-1}$  and spherical secondary particles (and agglomerates) with sizes in the range of  $d > 10 \text{ nm}$  at lower  $q$  values, which is in good agreement with prior work [19, 20]. The effect of the electrolyte is readily seen as a reduction of scattering intensity in the low  $q$ -range corresponding to a lower abundance of large particles and agglomerates. Data are given in Kratky representation ( $I(q) \cdot q^2$  vs  $q$ ). The fits obtained from reverse Monte Carlo simulations (green and pink lines) match the experimental data (filled squares and hollow circles) just as well as the unified fits (blue and red lines). Resulting volume-weighted size distributions (Figure 57, chapter 9) differ significantly from each other, especially above 10 nm as quantified by calculation of the relative amount of particles  $\leq 10 \text{ nm}$  (Figure 57, chapter 9). A significantly higher particle fraction with sizes smaller than 10 nm (67 % with salt versus 50 % without) is found *in situ* if NaCl is added to the solution. Figure 28 (bottom) reveals a higher abundance of particles in the regime between 10 and 100 nm in histograms of particles pure water inside the cavitation bubble. Obviously, the evolution of large secondary particles and agglomerates is quenched by the addition of anions within the first cavitation bubble and therefore in the gas phase. The further temporal evolution of particle sizes is shown in Figure 29 at heights above target of 0.5 and 1.0 mm. Primary particles slightly increase their size from the first bubble to after final collapse (Figure 29, left top, 100–500  $\mu\text{s}$ ), from  $10 \pm 2$  to  $14 \pm 2 \text{ nm}$ . After 2000  $\mu\text{s}$  the primary particle size again slightly decreases ( $12 \pm 2 \text{ nm}$ ).

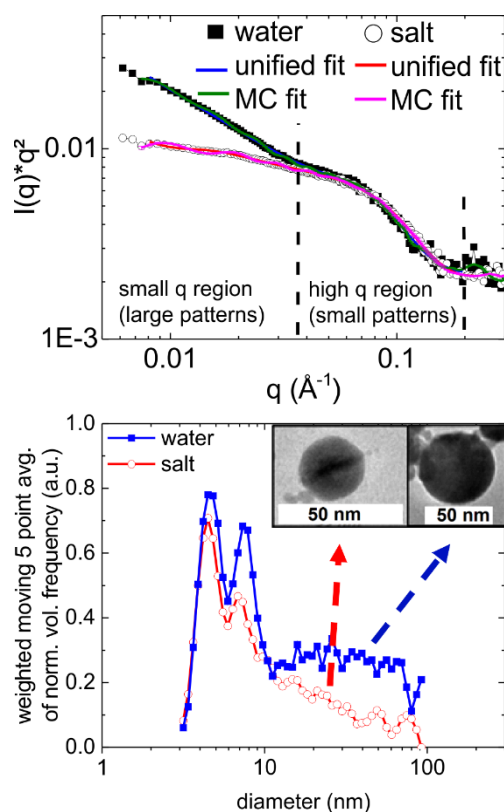


**Figure 28:** (top) SAXS curves from *in situ* measurements in Kratky representation ( $I(q) \cdot q^2$ ) as a function of scattering vector  $q$  at a height of  $0.5 \text{ mm}$  above target and a delay of  $100 \mu\text{s}$  after laser impact and corresponding unified and MC fits. Both fit the experimental data equally well. (bottom) The 5 point weighted moving average of the MC histogram data is plotted vs the corresponding particle diameter. Insets show large solid spheres appearing in *ex situ* TEM images.

These findings indicate that primary particle formation is within the time resolution of the experiment after laser pulse absorption and not significantly affected in the microsecond scale by cavitation bubble dynamics (at least for the size discrimination that can be probed by SAXS *in situ*) [20].

The detected change in the large particle fraction is more pronounced in *in situ* SAXS. It is in good agreement with prior measurements [19], with sizes of  $40\text{--}60 \text{ nm}$  during maximal bubble extension. In all measurements, the effect of salt addition is clearly seen for large structures. It is most pronounced at the first bubble maximal extension ( $100 \mu\text{s}$ ) and after final bubble collapse ( $2000 \mu\text{s}$ ). After the first bubble collapse ( $300 \mu\text{s}$ ) and right after the collapse of the second bubble ( $500 \mu\text{s}$ ) only minor effects of salt addition are observed. This supports our previous observations of forced particle agglomeration or growth due to bubble collapse [20].

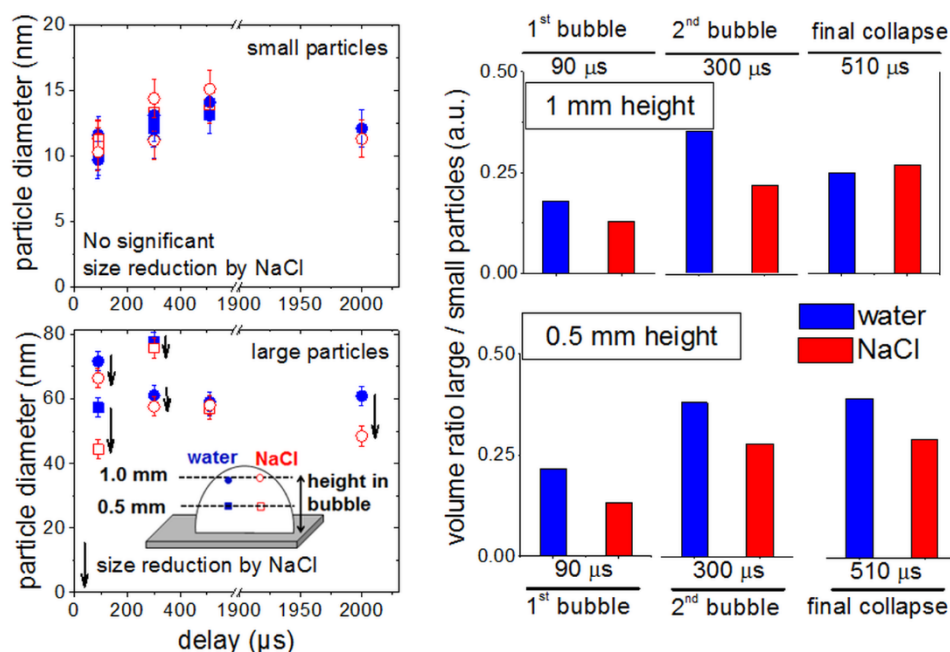


**Figure 29:** Left: particle size evolution (*in situ* SAXS) of small/primary and large secondary particles and agglomerates in pure water (full blue symbols) and NaCl solution (open red symbols) as a function of delay after laser impact for two different heights (0.5 mm: squares; 1 mm: circles) above the target. The arrows indicate trends of size change with NaCl addition. The spatial positions are illustrated by an inset scheme. Right: volume ratio between large and primary particle fraction as a function of delay and height above target in pure water (blue bars) and NaCl solution (red bars).

The similarity between large structure sizes at delays between 300 and 500  $\mu\text{s}$  might be due to strong drag forces confining particular matter on a limited space, thus forcing agglomerates to grow to a specific size, which is defined by the confining volume rather than the size of its building blocks (large particles) and particle interactions. The addition of NaCl results in a significant size quenching effect of both the large secondary particle (solid spheres) and agglomerate fraction already during cavitation bubble confinement as confirmed by *in situ* SAXS measurements. Within the first bubble, this size is reduced by 15 nm under saline conditions. Furthermore, the addition of salt reduces the abundance of this fraction. Figure 29 (right) shows the volume ratio of detected large particles in comparison to the primary particle fraction as a function of time and position inside the cavitation bubble. By the addition of NaCl, the share of large particles is significantly reduced by 30–50 % for different positions within the cavitation bubble. This effect is strongest for the first bubble and decreases a little until the final collapse of the bubble. The difference between top and center of the bubble is negligible. The time- and space-dependent size reduction shown in Figure 29 is in line with discussion of the data shown in Figure 28. Dissolved anions must be effective already inside the vapor phase of the cavitation bubble, as indicated by Matsumoto et al. [54] while Lam et al. quantify the total amount of molecules

in the bubble [50], and result in a reduction of secondary particle and agglomerate size and their abundance.

The observation of salts affecting the final particle size already inside the cavitation bubble is indeed surprising regarding the time scale. The anions inside the cavitation bubble can interact with particles crystallizing inside the cavitation bubble. The evident size reduction of large spheres as well as small primary particles (Figure 28, bottom) by NaCl already inside the first cavitation bubble (100  $\mu$ s) indicates that salts might not only hinder the formation of agglomerates or aggregates but also significantly decrease the size of secondary nanoparticles. This is discussed in more detail during the description of Figure 30. Obviously, agglomeration starts from the smaller primary particles and possible secondary particles as well; this coalescence competes with electrostatic stabilization of these seeds by anions via charge delivery. Note that this electrostatic effect by charge delivery has already been described based on *ex situ* measurement (XPS, UV/vis spectroscopy) [146], but seen here in the vapor phase (bubble). Compared to liquid state, electrostatic effects are even more pronounced in the vapor phase and a well-known phenomenon in gas-phase nanoparticle synthesis [278]. During maximal extension of the first bubble, the abundance of primary particles is highest and leads to collision-controlled agglomeration and particle size increase (Figure 29). The agglomeration is promoted by the collapse of the bubble [20]. Although the electrolyte quenching effect seems to be small within the second bubble and after, the ion stabilization effect still acts during dispersion in the liquid phase. As indicated in Figure 29 nanoparticle formation, agglomeration and chemical reactions are not finished after the collapse of the cavitation bubble (delay > 500  $\mu$ s). For time-resolved experiments on the microsecond to second time scale, the concept of a flow reactor as used here is very useful since it allows converting a selectable spatial delay into a temporal delay [49, 144]. Therefore, we map the size quenching efficiency downstream in the free liquid from the point of laser impact. In this experiment, the liquid flow rate and the distance of the X-ray beam to the initial laser position define the time after final bubble collapse. We observe that quenching is weakened downstream but is still measurable. Still, quenching efficiency is highest inside the vapor phase of the cavitation bubble. For further details on the downstream experiment, we refer to the Supporting Information (Figure 58, chapter 9).

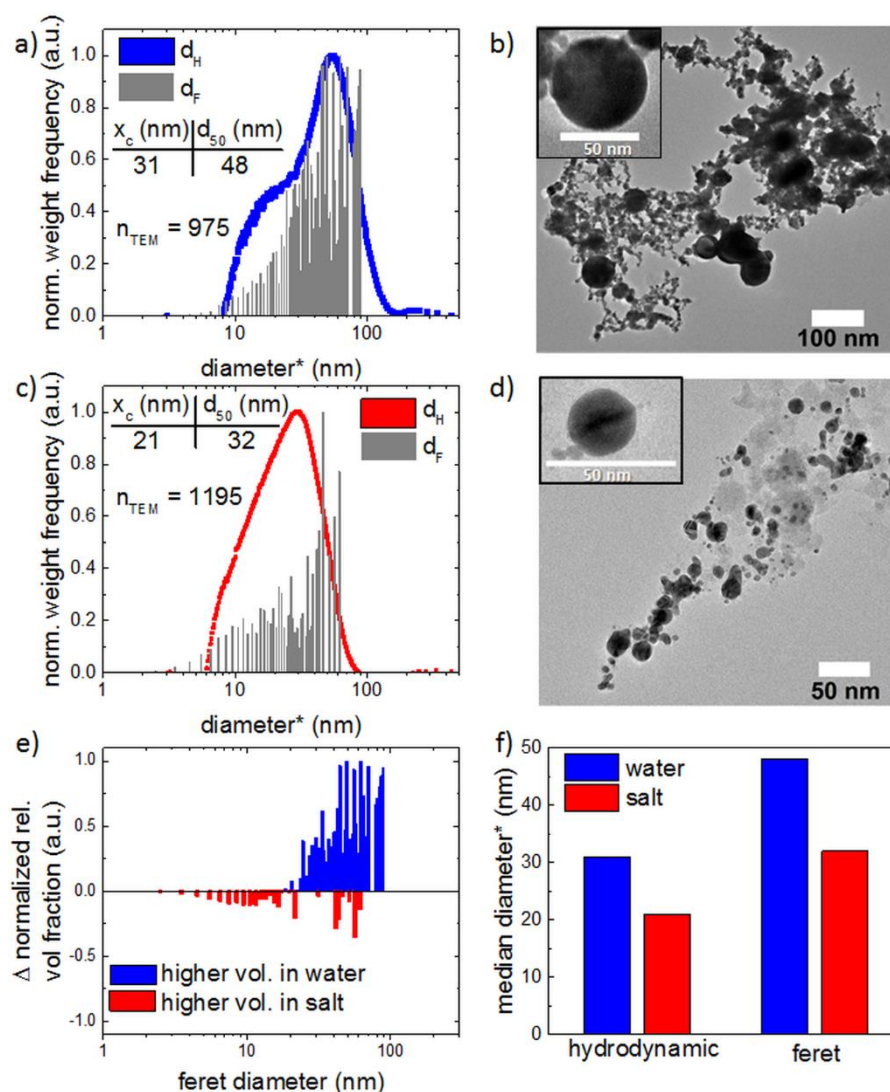


**Figure 30:** Ex situ histograms of transmission electron microscopy (gray bars) combined with results from analytical disc centrifugation (water: blue dots; NaCl: red dots) of gold nanoparticles laser-generated in pure water (a) and NaCl solution (c). The asterisk indicates the difference of hydrodynamic  $d_H$  and Feret diameter  $d_F$ . All size distributions are volume-weighted for direct comparison with results from small-angle X-ray scattering. Representative electron microscopic pictures show agglomerated structures for water (b) and stable particles for NaCl (d). Result of subtraction of the TEM histogram of particles in water from that of particles in NaCl (e). The insets exemplify the size reduction of large spherical particles when using NaCl. Comparison of hydrodynamic ( $x_c$  from ADC) and Feret ( $d_{50}$  from TEM) diameter in pure water and NaCl reveals drastic particle size reduction by salt ions of both the hydrodynamic agglomerates and Feret diameter of solid particles (f).

Nevertheless, the initial steps of particle formation observed in this work are (100–2000  $\mu\text{s}$ ) of importance for a detailed understanding of the process in its embryonic state. The initial ion stabilization reduces the strength of particle's electrostatic repulsion so that a deagglomeration in the free liquid downstream is facilitated. Furthermore, salts are found to reduce the size within the first cavitation bubble where agglomeration is at its minimum, indicating a quenching of formation of small primary and larger secondary particles as well. The importance of second-scale processes was previously verified using studies in batch systems and is confirmed here for the stationary case [279, 280].

In order to bridge the gap between *in situ* and *ex situ* particle properties, we prepare gold nanoparticles under similar conditions and analyze the final nanoparticle products using a variety of analytical techniques (Figure 30-32). Figure 30 shows the results of the TEM analysis and the ADC measurements of aqueous and electrolyte suspensions. The TEM images, in general, display the small primary particles as well as agglomerates or networks forming larger units (Figure 30b,d). Interestingly, a few, but prominent, compact larger spheres can be found. The size histograms are converted to volume-weighting in order to be compliant with the SAXS results and the ADC. Size analysis has been done by manual image analysis (ImageJ 1.50b) at about 1000 particles each. Because of the different particle states in ADC (still suspended, measurement of hydrodynamic size  $d_H$ ) to TEM (deposited and concentrated, determination of Feret diameter  $d_F$ ), a discussion of the full size distribution is difficult. Hydrodynamic diameter refers to the diffusional properties of a particle, while Feret diameter is defined by the distance between two parallel planes. Regarding the median values for size distributions obtained from ADC and TEM as indicated in the Figure 30a,c (summarized in Figure 30f), both are reduced significantly by 10 nm (ADC) and 16 nm (TEM) when NaCl is added to the liquid before laser ablation. Additionally, smaller particles appear with higher relative frequency. By subtracting the salt from the (TEM) water histogram, significant differences in the size distributions become apparent (Figure 30e). Hence, it is concluded that size reduction of primary particles also happens inside the vapor phase. Even if this size reduction by ions is not detectable *in situ* by SAXS, the effect is confirmed by complementary *ex situ* TEM. The relative amount of large spherical particles (agglomerates are not resolved in TEM) is more pronounced in pure water while particles < 20 nm appear more frequently in saline solution (Figure 28, bottom, and Figure 30e).

Furthermore, the UV/Vis spectra of colloids shown in Figure 31 also indicate larger particle sizes or stronger agglomeration for nanoparticles synthesized in pure water. This is seen from the elevated extinction of colloids prepared in water at wavelengths above 600 nm. A more quantitative method to obtain a measure for primary particle stabilization against agglomeration state from optical spectra is

the calculation of primary particle index (PPI) [37]. Here, a PPI of 1.3 for water and 1.6 for NaCl solution are found, indicating more efficient particle dispersion in NaCl solution, which is supported by a  $\zeta$ -potential of  $-28.3$  mV in pure water with increased negative charge toward  $-37.2$  mV in NaCl solution. Quantitatively the volume-weighted histograms clearly show a reduction of frequency at the large side of the size distribution, possibly a shift toward smaller sizes by adding salt.

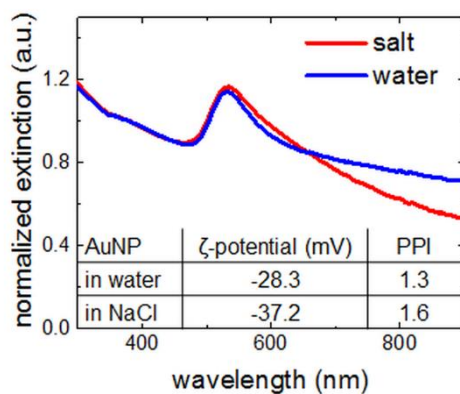


**Figure 31:** UV/Vis spectra of gold nanoparticles in water and NaCl solution. The primary particle index (PPI) and  $\zeta$ -potential are given in the table.

To verify the *in situ* SAXS data, we perform static *ex situ* SAXS with higher signal-to-noise ratio as well (Figure 32). Results from the Monte Carlo analysis show a high abundance of small primary particles with sizes  $\sim 8$  nm in saline solution and large particles of  $\sim 40$  nm in pure water. This is shown in Figure 32 (bottom) by subtraction of the salt from the pure water histogram comparable to the processing of TEM histograms. Compared to *ex situ* analysis with TEM and ADC the match is good, confirming a significant size quenching effect on both primary and secondary particles. Besides, the match to time-resolved *in situ* SAXS shown in Figure 29 (left) is good as well. In contrast, *ex situ* SAXS performed on gold nanoparticles in NaCl solution does not resolve the large fraction but show mainly a single fraction of primary particles of 8 nm as shown in Figure 32. Similar results are found by application of the unified fit (not shown). In conclusion, the particles analyzed with static *ex situ* SAXS after extended time confirm the size quenching effect as well as the change in the ratio between primary and secondary particles very clearly. From the compliance between dynamic *in situ* and static *ex situ* SAXS we conclude that secondary processes on the time scale of seconds are of minor importance when ablation is performed in pure water. On the other hand, addition of NaCl makes the system even more dynamic, leading to non-negligible processes like Ostwald ripening and collision growth on the time scale of seconds (and longer) [88].

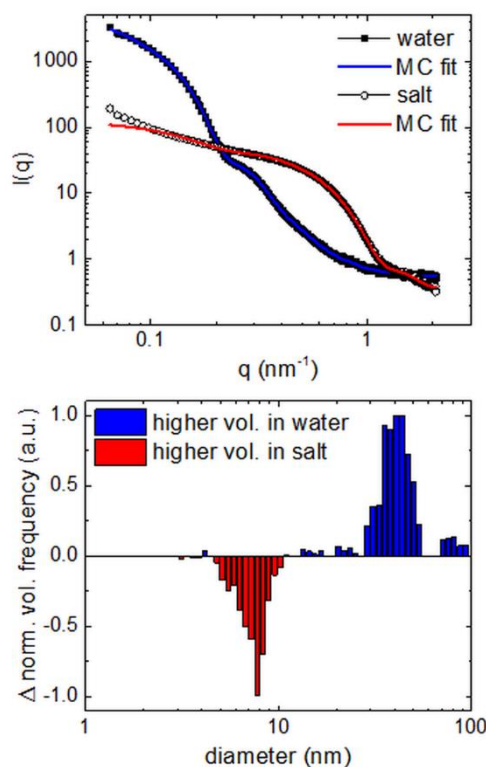


**Figure 32:** Ex situ SAXS curves and MC fits from gold nanoparticles prepared in water and NaCl solution (top). Subtraction of resulting volume weighted size distributions support that in NaCl solution the fraction of small primary particles ( $\sim 9$  nm) is more pronounced compared to water as liquid (bottom). According to this, a larger fraction of large particles (secondary particles and agglomerates  $\sim 40$  nm) are found in water solutions.

The observation at  $2000 \mu\text{s}$  (Figure 29) and *ex situ* studies indicate that formation dynamics of laser-generated nanoparticles are not completed after bubble collapse or dispersion into the liquid away from the ablation spot. Still, nanoparticle stabilization definitely occurs already within the cavitation bubble. One should bear in mind that particle concentration is still high in the spatial confinement promoting agglomeration or coalescence. Later, upon dilution, there must be a new equilibrium by dissolution of weakly stabilized agglomerates and formation of the final solid particles that can be observed by *ex situ* analysis like electron microscopy. In addition to deagglomeration, the early anion stabilization is also seen by a significant reduction of the size of secondary particles (see insets in Figure 30b-d). Such solid spheres  $\sim 50$  nm appear after laser ablation in pure water but are significantly reduced in size and abundance in a saline solution which is shown by Figure 28 (bottom), Figure 30, and Figure 32. The TEM-imaged volume-weighted median particles sizes show a strong shift from 48 nm (water) to 32 nm (NaCl) as a consequence of the appearance of less big solid spheres in saline solution. This reduction is probably linked to the size reduction of large spheres and not caused by

deagglomeration. TEM combined with image analysis is not sensitive to agglomerated structures but only to single particles. The almost perfect spherical shape of secondary particles indicates that formation occurs at high temperatures either during first submicrosecond phase after laser impact or bubble collapse via coalescence and not by agglomeration. Anion stabilization during bubble collapse reduces further growth by coalescence and agglomeration as well as the relative frequency of large solid spheres. This finding is supported by *ex situ* TEM and *in situ* SAXS data shown in Figure 28 (bottom) and Figure 30e, which also verifies size quenching of small primary particles. As the size reduction of primary and secondary particles as well as the abundance of the latter in NaCl solution is proven *ex situ* by TEM analysis (Figure 30), the size reduction of large species *in situ* is probably true for both the agglomerates and large spheres. The differential histograms of nanoparticles in water subtracted by particles in saline solution presented in Figure 30e show a relatively higher appearance of large secondary particles in pure water whereas in NaCl more primary particles are observed. It is therefore likely that electrolyte addition reduced the size and appearance of secondary spheres ( $10 \text{ nm} < d < 100 \text{ nm}$ ) already inside the laser-induced cavitation bubble. A possible mechanism includes explosive decomposition of the target as source of primary particles and breakup of superheated molten metal at the plasma–water interface as source of secondary particles as suggested by recent atomistic simulations [46]. We believe that the early action of electrolytes within the bubble as observed here is in agreement with the early appearance of particles as observed in reference [46]. The findings link evidence of early interaction of laser-ablated mass with electrolytes in the vapor phase of the bubble (*in situ*), on the one hand, and subsequent electrostatic nanoparticle stabilization, on the other. In addition, primary particles or atom clusters ( $< 2 \text{ nm}$ ) possibly originating from laser ablation as well have to be taken into account when thinking about the particle formation mechanism. Such atom clusters are not detectable by dynamic *in situ* SAXS as their scattering intensity is low relative to primary particles and are difficult to isolate in TEM but might play an important role during coalescence and growth of primary particles or (re)formation of nanoparticles after bubble collapse as demonstrated by Jendrzek et al. [88].

## Conclusions

Bimodality may compromise the application of laser-generated nanoparticles. Hence, an understanding of the fundamental reasons behind this bimodality is highly demanded for developing methods that allow narrower size distributions. We show that dissolved salts significantly influence the nanoparticle formation during pulsed laser ablation synthesis in liquid. Proven by spatiotemporally resolved SAXS, this effect is already active during an early stage of the process. In fact, it is evident that particle size reduction and stabilization against agglomeration and growth happens inside the laser-induced cavitation bubble. That means that (1) nanoparticle–ion interaction starts within the first microseconds after laser impact on the metal target and (2) size quenching by ions during PLAL is based on a gas phase reaction. Our results are in agreement with works showing that the ion composition in surrounding liquid is the same as inside the bubbles vapor phase [54] and an atomistic model predicting the existence of three particle size fractions (atom clusters, primary and secondary particles) already a few nanoseconds after laser impact [46]. We further show that stabilizing ions may enter the cavitation bubble and affect particle formation hypothesized to happen by delivering additional surface charges to early particles and reduce the degree of agglomeration, allowing to harvest a higher share of small and stable nanoparticles. By *ex situ* analysis (static SAXS and TEM), also the primary particles are shown to be significantly smaller and higher in mass fraction. The abundance of large solid spheres (part of secondary particle fraction) is reduced by 30–50 %. We assume that this size quenching happens inside the cavitation bubble but cannot be distinguished from deagglomeration by dynamic *in situ* SAXS. Consequently, the crucial findings of our study are that size reduction of both primary and secondary particles by ions is a gas phase reaction and that the typical bimodality of laser-synthesized nanoparticles is significantly reduced already inside the vapor phase of the laser-induced cavitation bubble.

### 5.2.2 Time and mechanism of nanoparticle functionalization by macromolecular ligands during pulsed laser ablation in liquids

Alexander Letzel, Stefan Reich, Tomy dos Santos Rolo, Alexander Kanitz, Jan Hoppius, Alexander Rack, Margie Olbinado, Andreas Ostendorf, Bilal Gökce, Anton Plech, and Stephan Barcikowski

Published in: "On the time and mechanism of nanoparticle functionalization by macromolecular ligand during pulsed laser ablation in liquids, *Langmuir* 35 (2019) 3038-3047."

#### Abstract

Laser ablation of gold in liquids with nanosecond laser pulses in aqueous solutions of inorganic electrolytes and macromolecular ligands for gold nanoparticle size quenching is probed inside the laser-induced cavitation bubble by *in situ* X-ray multi-contrast imaging with a Hartmann mask (XHI). It is found that (i) the *in situ* size quenching power of sodium chloride (NaCl) in comparison to the ablation in pure water can be observed by the scattering contrast from XHI already inside the cavitation bubble, while (ii) for polyvinylpyrrolidone (PVP) as a macromolecular model ligand an *in situ* size quenching cannot be observed. Complementary *ex situ* characterization confirms the overall size quenching ability of both additive types NaCl and PVP. The macromolecular ligand as well as its monomer N-vinylpyrrolidone (NVP) are mainly effective for growth quenching of larger nanoparticles on later time scales, leading to the conclusion of an alternative interaction mechanism with ablated nanoparticles compared to the electrolyte NaCl, probably outside of the cavitation bubble, in the surrounding liquid phase. While monomer and polymer have similar effects on the particle properties, with the polymer being slightly more efficient, only the polymer is effective against hydrodynamic aggregation.

#### Introduction

Since the discovery of pulsed laser ablation in liquids (LAL) as a tool for the synthesis of nanoparticles in 1993 [67] researchers still face major challenges that hinder LAL from being established as a competitive synthesis route towards nanomaterials [33]. Two of these are the control of mean size, and size distribution width. The challenge of gaining control over the final nanoparticle size in a single-step approach and without using surfactants or ligands was accelerated by the discovery that micromolar concentrations of monovalent salts like sodium chloride (NaCl) result in a size quenching of gold nanoparticles by adsorption to the particle surface and stronger electrostatic stabilization [21, 146]. This approach was extended to other noble metals like palladium [142] and platinum [196]. It was

found recently that size reduction by ions already happens inside the gas phase [192] of the laser-induced cavitation bubble [50, 221, 281] some tens of microseconds after a laser pulse hits the target [192]. Ions present in the electrolyte get in contact very early to the plasma emitted from the target and are thus able to interact with the material even before bubble expansion [282]. Note that Sakka et al. [54] demonstrated the presence of dissolved ions already in the laser-induced plasma. However, they used 100 ns laser pulse width, we used only 10 ns, and it cannot be excluded that ions are present inside the bubble because of solution vaporization at the plasma edge during its lifetime. Trapping of the early nanoparticles inside the confinement of the cavitation bubble had been observed first by means of time-resolved scanning small-angle X-ray scattering (SAXS) [19]. In the last years, a trend towards imaging of the entire bubble cross section by optical [283, 284] and *in situ* X-ray methods was followed. In this context X-ray radiography and multi-contrast imaging [285, 286] was introduced as a complement to *in situ* SAXS [30, 44]. Thereby, the distribution of nanoparticles and the ejection time of nanoparticles from the gaseous phase into the surrounding liquid were determined exploiting X-ray absorption contrast [30].

Alternative to anions, organic molecules can be employed for size quenching *in situ* [131, 135, 287], in particular, if the ligand's functional group has high affinity to the inorganic nanoparticle surface [78, 288, 289]. But less is known on the size quenching mechanism with macromolecules having no specific anchor group.

In this work, we address the controversy of the actual temporal and spatial distribution of LAL nanoparticles in the presence of macromolecular ligands to interact during *in situ* conjugation. This question was addressed by other groups by adding ligands like sodium dodecyl sulfate (SDS) [17] or 2-[2-(2-methoxyethoxy)ethoxy] acetic acid (MEEAA) [141] to the water phase. While these studies provides indication for particle-ligand interaction during an early stage, the size quenching cannot be solely attributed to the presence of the organic backbone as both SDS and MEEAA introduce additional electrolytes or change the pH of the liquid [142]. Steric stabilization and size reduction by polymers added to the liquid prior to laser ablation was observed for ,e.g., aluminum nanoparticles prepared in poly(vinyl alcohol) (PVA) solution [130], gold nanoparticles in poly(ethylene oxide) (PEG) solution [131] and silver nanoparticles in polyvinylpyrrolidone (PVP) solution [51]. The present study focuses on the functionalization of LAL nanoparticles by PVP. Tsuji et al. have demonstrated that PVP acts as a size quenching ligand in LAL using silver as a target material [51]. In chemical reduction synthesis of silver and gold nanoparticles PVP acts as a shape directing agent in some formulations [290, 291]. Yet the chemical synthesis of gold nanoparticles with PVP is reported frequently, while spherical morphologies are found [292-295]. Requejo et al. have even reported a route in which PVP leads to spherical gold

particles and the omission of PVP results in gold nanorods [296]. Non-spherical nanoparticles were also found during laser processing of nanoparticles when using a 355 nm laser source and performing laser fragmentation [132], these parameters and the setup are, however, not completely transferrable to those applied in this work.

As a matter of fact, it is possible to control the size of gold nanoparticles to some extent by a controlled delayed addition of oligonucleotides to the colloidal solution [144, 145]. This indicates that quenching by organic ligands can occur *ex situ*, i.e. outside of the cavitation bubble, by suppressing growth processes like Ostwald ripening and coagulation by steric stabilization of the nanoparticles [88]. Accordingly, there is indication for both possible quenching mechanisms, inside and outside of the cavitation bubble, occurring during LAL in the presence of macromolecular ligands. Therefore, it is mandatory to study nanoparticle formation during an early phase as well, when particles are still trapped inside the cavitation bubble. Due to the complexity of the problem a complementary approach to our earlier *in situ* SAXS studies is chosen [19, 20, 30, 192]. X-ray Hartmann mask imaging (XHI) was utilized to access multicontrast X-ray imaging, including scattering contrast [297, 298]. As described earlier in literature [297, 299-301] Hartmann-mask imaging exploits a laterally structured X-ray beam, whose attenuation, pattern shift and structure broadening allows to decompose absorption, differential phase and scattering contrast on a 2D detector. Here, the Hartmann mask consists of a platinum foil with a 2D periodic pattern of holes as shown in Figure 33a-d. The sensitivity maximum of targeted size intervals can be set by variation of the mask pitch and the sample to detector distance [299]. We have chosen a XHI setup with sensitivity maximum at 55 nm structure size. Hence, secondary particles like large spherical nanoparticles and agglomerates are preferably detected over smaller (primary) particles.

### Experimental section

The experimental details of the liquid-flow *in situ* LAL setup are described elsewhere in more detail [20, 44, 192]. In brief, laser ablation for *in situ* experiments was performed by focusing a nanosecond laser (Continuum Minilite I, 1064 nm, 7 ns, 10 Hz) with an average pulse energy of 11 mJ onto the target [44]. The effective fluence, taking the attenuation of the liquid layer at the laser wavelength into account [302], was 33 J/cm<sup>2</sup>. A gold ribbon (99.9 %) having a width of 4 mm and a thickness of 200 μm was used as a target material and continuously transported upwards through the chamber in the same direction as the liquid flow. Ablation was performed in a liquid flow configuration to remove residual nanoparticles for subsequent laser shots. Doubly-distilled water solutions of NaCl and PVP (Acros Organics, 3,500 g/mol, K12, Lot: A0368382) were prepared to a final concentration of 0.5 mM. *Ex situ*

LAL was performed using a liquid-flow ablation chamber with a liquid height of 5 mm above the target. A fixed gold plate of 0.5 mm thickness was used. *Ex situ* experiments were additionally conducted in N-vinylpyrrolidone (NVP), the monomer of PVP. The chemical was obtained from Acros Organics (99 %, stabilized with NaOH) and used without further purification. Measurements of the pH value of 1  $\mu\text{M}$  and 1000  $\mu\text{M}$  solutions of NVP revealed that it was almost constant from 5.9 at 1  $\mu\text{M}$  and 5.9-6.0 at 1000  $\mu\text{M}$ . Furthermore, the electrolytic conductivity was constant at 0.7-0.8  $\mu\text{S}/\text{cm}$ . The liquid volume flow was 50 ml/min, which is three times lower compared to the *in situ* experiments. For *ex situ* experiments Milli-Q water was used (18.2  $\text{M}\Omega/\text{cm}$ ). The laser (Rofin Sinar RS-Marker 100D, 1064 nm, 10 ns) was operated at 5 mJ pulse energy and 3 kHz and was scanned across the target surface in a spiral pattern using a galvanometric scanner. The effective fluence was 27  $\text{J}/\text{cm}^2$  which is 18 % less as compared to the *in situ* ablation experiments. To prove that this slight deviation does not affect the particle size distributions significantly additional size distributions obtained by *ex situ* LAL using an effective fluence of 36  $\text{J}/\text{cm}^2$  are compared with those obtained at 27  $\text{J}/\text{cm}^2$  in Figure 59 (chapter 9). The ablation chamber was made out of polytetrafluorethylene (PTFE) to avoid contamination of the product colloids by ions that might otherwise be dissolved of chambers made of e.g., steel or aluminum. For transmission electron microscopy (TEM) (Zeiss EM 910, 120 kV) the colloids were drop-casted onto a carbon-coated copper grid. Automatic image analysis was performed by the ImageJ (Version 1.51s) plugin ParticleSizer [303]. Analytical disc centrifugation (ADC, CPS instruments) was performed in a sugar density gradient and constantly operated at maximum speed of 24,000 rpm. Gold nanoparticles of 6 nm hydrodynamic diameter were used as calibration standard. In ADC the integral intensity of the entire injected sample mass is calculated by Mie theory and from the derived cumulative surface-weighted size distribution the specific surface area is accessible. Hence, for each data point the additive concentration per nanoparticle surface area or mass in  $\mu\text{mol}/\text{cm}^2$  or  $\mu\text{mol}/\text{mg}$  is derived, respectively. Note that the specific surface area and the median diameter are mutually linked quantities. Still, the specific surface area integrates every size fraction within the size distribution of the gold colloids as every particle contributes to the overall specific surface area. UV/Vis extinction spectroscopy was performed using a spectrophotometer (Thermo Scientific Evolution 201). Spectroscopy was used to calculate the ablated gold mass from the concentration of the *ex situ* synthesized colloids. Representative spectra from gold nanoparticles produced in pure water, 0.5 mM NaCl and PVP solutions and the calibration of the UV/Vis spectra by gravimetric analysis of the ablated gold mass are given in Figure 60 (chapter 9). Viscosities were measured using a rheometer (Anton Paar, Physica MCR 301).

Time-resolved visible-light shadowgraph of the cavitation bubbles in water and PVP solution were performed in a self-designed 3D-printed ablation chamber made of acrylonitrile butadiene styrene. A liquid flow rate of 35 ml/min was applied to remove residual nanoparticles and persistent bubbles between two laser pulses. The laser repetition rate was set to 0.2 Hz. Additional information on the used shadowgraphy setup is presented in the Supporting Information, including the recorded image sequences (Figure 61-64).

The platinum-based Hartmann mask used for multi-contrast X-ray imaging consists of a 25  $\mu\text{m}$  thick foil (Chempur, 99.9%) with regular holes of about 10  $\mu\text{m}$  in diameter, drilled by pulsed fs-laser micromachining (Spectra Physics Spitfire Ace, 800 nm, 100 fs) using a fluence of 2 J/cm<sup>2</sup> at a repetition rate of 5 kHz. The holes cover the rectangular pattern (7x5 mm) with a pitch of 65  $\mu\text{m}$ . Micrographs of the Hartmann mask are shown in Figure 33 from the front and back side. Light microscopy allows to visualize the funnel shape of the holes on the front side, perpendicular to the incident transmitted fs-laser (Figure 33a,b). The back side of the mask does not exhibit any funnels but a regular pattern of micron sized holes (Figure 33c,d). A scheme depicting the basics of the exploited imaging technique for *in situ* measurements during LAL is given in Figure 33e. Absorption of X-rays occurs whenever a beamlet, shaped by the shadow mask, interacts with matter e.g., after transmission through water. Transmission increases at the occurrence of the cavitation bubble in LAL with respect to the surrounding liquid.

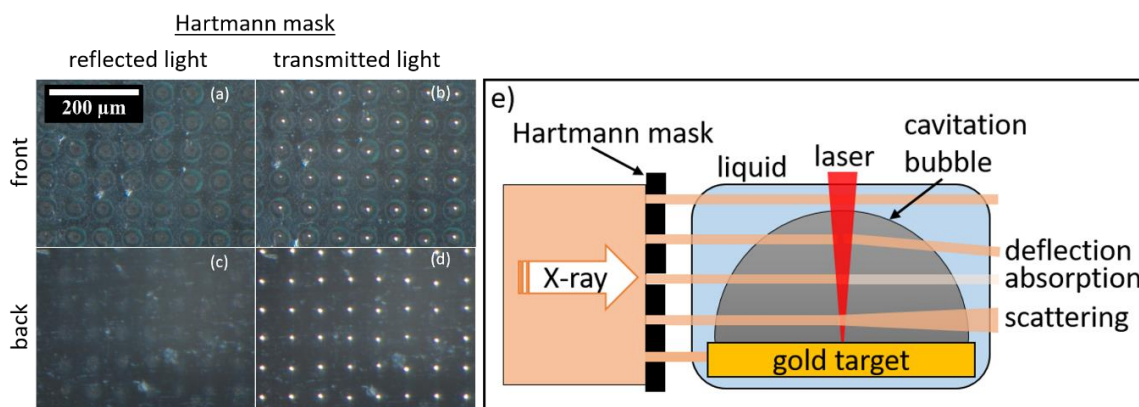


**Figure 33:** Images of the Pt foil acting as a Hartmann mask for *in situ* experiments obtained by optical microscopy. Front of the mask in reflected (a) and transmitted light mode (b). The laser-drilled holes are funnel-shaped on the front side (side at which the laser beam impinges). Back of the mask in reflected (c) and transmitted light mode (d). Sketch of the XHI approach with the incoming X-ray beam being split into multiple beamlets by the Hartmann mask, and undergoing absorption, differential phase shift (deflection) and diffuse scattering (broadening) when crossing the cavitation bubble and the confined nanoparticles (e).

XHI experiments were performed at the ID19 beamline of the European Synchrotron Radiation Facility (ESRF, Grenoble, France) using a quasi-monochromatic beam from a single-line undulator with an energy of 17.9 keV. The X-ray beam was restricted to an area of 7x5 mm by slits to illuminate only the Hartmann mask. The array of beamlets formed by the Hartmann mask passes the sample cell of 5 mm water to be converted to visible light by a YAG scintillator of 100  $\mu\text{m}$  thickness. The distance between the ablation point and the scintillator was 30 mm. A fast CMOS camera (PCO dimax) recorded the intensity distribution with 40  $\mu\text{s}$  exposure time, a sequence of images around the ablation event spaced 100  $\mu\text{s}$  was taken. An interleaving of several films with shifted delay time between acquisition and the laser impact allowed to construct a movie with 40 kHz (25  $\mu\text{s}$  spacing) image rate. A repetition of the image acquisition for a total of at least 3,000 laser shots was performed for every liquid in order to increase the signal-to-noise ratio. XHI is a multi-contrast X-ray imaging technique. Details on image formation and reconstruction are described in detail in [148, 285, 297, 298, 304]. Therefore, here only a short description shall be given. By usage of a Hartmann mask the intensity, position and broadening of the beamlets reveals three different contrast modes (absorption, differential phase, and scattering, respectively). In this publication the scattering contrast is of central interest as this stems from nanoscale inhomogeneities. The image reconstruction was performed identically to a previous publication by Reich et al. [148]. Instead of individual beamlet analysis a Fourier transform of the beamlet pattern allows to separate the different contrasts. Therefore, the Fourier transform of the pattern is followed by a back transform of the specific harmonics of the Fourier spectrum. Particularly, the cavitation bubble creates absorption contrast, which imprints on the scattering channel [304]. As reported earlier, this crosstalk from the absorption contrast to the scattering contrast can be removed by a decorrelation procedure [148, 305].

## **Results and discussion**

The goal of the present study is to clarify the mechanism of nanoparticle-macromolecular ligand interaction during LAL. Here, we use (i) pure water as a negative (null effect) reference liquid, (ii) NaCl (aq.) as positive reference. NaCl has the ability to quench the size of nanoparticles already inside the gaseous phase of the cavitation bubble, as shown before by scanning SAXS [7]. The additive (iii) that is employed is the macromolecular ligand PVP. It is utilized in the exact same molar concentration as NaCl to ensure direct comparability of the molar size quenching efficiencies. As PVP does not contain mercapto groups (-SH), no covalent bond (chemisorption) to the gold nanoparticle surface is expected. Yet, the N-C=O groups of the PVP backbone bind to the gold surface by physisorption [306-308]. Although PVP is frequently used as a stabilizing ligand for silver [51, 290, 309] rather than gold [294]

nanoparticles, a gold target is used here. This is motivated by gold nanoparticles proving to be effectively quenched by NaCl [192]. It is shown that NaCl exhibits the ability to quench the size of gold nanoparticles already inside the cavitation bubble (i.e. *in situ*).

Using absorption contrast, it is possible to record the cavitation bubble as shown in the inset of Figure 34b. Scattering contrast is a result of diffuse scattering of X-rays and originates from scattering at inhomogeneities of the probed specimen [299]. The angular width of scattering scales inversely to the object size according to the principles of small-angle X-ray scattering [147, 300]. In the present setup the sensitivity ranges from 20-230 nm in sizes (at 50 %, with a maximum at 55 nm). The calculated sensitivity curve is shown in Figure 34a, which was calculated from our setup parameters according to the equation derived by Lynch et al. (equation (68)) [299]. The detection of small primary particles ( $d < 15$  nm) by using XHI is negligible, and primary particle size shifts by the addition of NaCl are also not detected by SAXS [192] because SAXS is limited in differentiation of overlapping size fractions [169]. Hence, for the scope of the present study, the secondary size fraction is the main region of interest, as it is known to be connected to the product colloids' bimodality. The shifted sensitivity towards particles even larger than 100 nm adds complementary information on earlier works. In general, imaging offers prospects to map spatial distributions as opposed to localized SAXS. Within our sensitivity limit we see a homogenous scattering distribution across the bubble. At the same time size information in the classical sense in XHI is lost, therefore size quenching (of large particles) is translated to intensity changes. Anyway, also *in situ* SAXS does not reveal changes in the size of small primary particles induced by NaCl inside the cavitation bubble (Figure 65). By using negative delays (before laser impact) for the flat field correction, it is possible to remove signal from residual nanoparticles inside the ablation chamber volume that may not be transported off by the water flow. As visible from the black squares in Figure 34b the scattering signal of gold nanoparticles as ablated in pure water observed at the center of the cavitation bubble (inset) follows the growth and shrinking of the first and second cavitation bubble, the latter frequently referred to as bubble rebound. The relation of the cavitation bubble and the confined particles ablated in pure water further confirms (i) that the observed secondary nanoparticles are confined within the gaseous phase of the cavitation bubble and (ii) are retracted towards the target surface upon bubble shrinkage. Therefore, the first reference measurement of gold nanoparticles in pure water proves the validity of XHI for nanoparticle detection during LAL by reproducing the bubble-nanoparticle SAXS-behavior which is known from the literature [19, 20, 192].

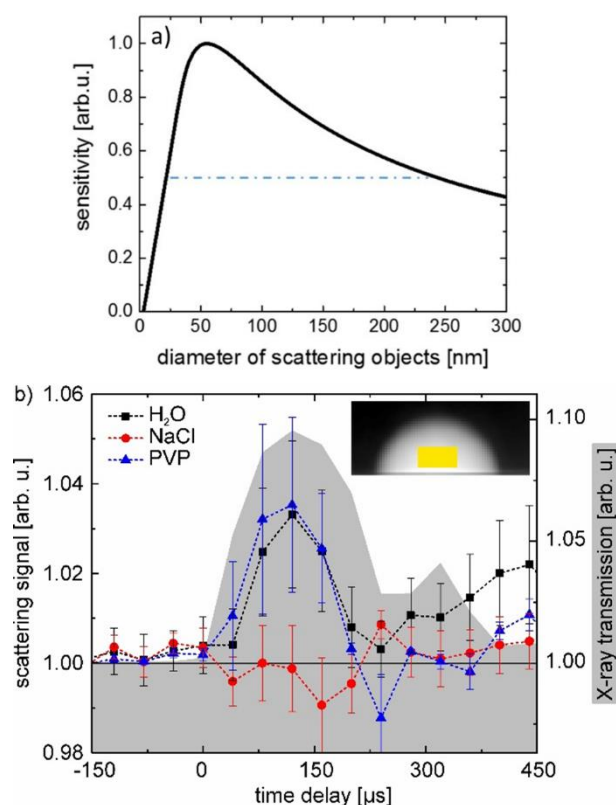


**Figure 34:** Scattering sensitivity on nanoparticles as function of the scattering object size for the given setup. The blue dashed-dotted line indicates the size interval above 50 % relative sensitivity (a). Scattering signal as function of the delay after laser impact obtained at the center of the cavitation bubble (inset shows the transmission signal together with the region of interest) (b). Scattering signals of gold nanoparticles in pure water (black squares), NaCl- (red circles) and PVP-solution (blue triangle) (both 0.5 mM). The shaded curve represents the change in X-ray transmission starting from 1 (0 % intensity change) before laser arrival. Error bars are the standard deviation between several runs.

The second reference experiment is the laser ablation of gold nanoparticles in a 0.5 mM NaCl solution. The temporal distribution is given by the red circles in Figure 34b representing the scattering signal from the nanoparticles. The scattering signal of nanoparticles ablated in a micromolar electrolyte solution is, at almost any delay after laser impact, as low as for the reference measurements at negative delays. It was shown before by means of *in situ* SAXS that the size and the amount of secondary particles is reduced inside the cavitation bubble already 90  $\mu\text{s}$  after laser impact [192]. As XHI is mostly sensitive to secondary particles (Figure 34a) it is concluded that the size reduction decreases the scattering signal intensity below the detection limit. Consequently, less to no signal is recorded.

Just like the NaCl solution the PVP solution is prepared prior to LAL so that PVP molecules are present in the liquid phase at any time during the ablation process. The blue triangles in Figure 34b show the scattering signal of nanoparticles ablated in presence of PVP as a function of the time delay after laser impact. Obviously, the curve progression is similar to the one in pure water. The results obtained from direct measurement of the particle X-ray scattering *in situ* (i.e. inside the cavitation bubble) show that the macromolecular ligand PVP does not affect the abundance of large gold nanoparticles (or aggregates) within the first 210  $\mu\text{s}$  after laser impact. This result is somewhat surprising, as it has been shown by several groups that size quenching of nanoparticles synthesized by LAL is possible by adding macromolecular ligands to the liquid phase before performing LAL [17, 131, 310]. Still, none of the references include direct *in situ* observation of the processes inside the gaseous phase of the cavitation bubble. Our data indicates the ineffectiveness of macromolecular ligand functionalization during cavitation bubble confinement.

Regarding the *in situ* XHI measurements it is concluded that PVP does not act as a size quenching agent for the secondary particles on the observed time scale during cavitation. This might be due to slow reaction kinetics, low diffusion constant or by the partial disintegration of PVP molecules by the harsh conditions induced by the laser impact. In principle, also a too low concentration could cause the observed ineffectiveness of PVP. This is excluded in the following section, addressing the *ex situ* analysis of size quenched nanoparticles. The size quenching efficiency of micromolar solutions of NaCl has been proven before *in situ* and *ex situ*. In contrast to NaCl, the macromolecular ligand PVP is less frequently used in combination with gold nanoparticle for size control during LAL. It is therefore mandatory to prove the size quenching ability of PVP with well-established *ex situ* methods to support the results from the *in situ* XHI. As the scattering contrast of the XHI method is based on scattering of X-rays it is sensitive to particle volume (mass). We will therefore compare the volume-weighted particle sizes when comparing the *ex situ* to the *in situ* results. To discriminate the influence of PVP on the size of the ablated gold nanoparticles, either by chemical functionality or molecular size, additional ablation in N-vinylpyrrolidone (NVP), which is the monomer of PVP, was performed.

The volume-weighted median diameters  $D_{50}$  of gold nanoparticle synthesized in NaCl, PVP and NVP are plotted in Figure 35a as a function of the additive-to-gold-ratio (AGR). These median diameters are derived from ADC while the ablated gold mass is calculated from the UV/Vis extinction spectra of the gold colloids. The two quantities allow for the calculation of the specific surface area. The absolute additive concentrations are varied between 1  $\mu\text{M}$  and 1,000  $\mu\text{M}$ . As shown in Figure 35a using solutions of NaCl with a concentration as low as 0.2  $\mu\text{mol}/\text{mg}$  is sufficient to start size quenching and a size reduction from 40 nm (pure water) to 12 nm in the volume-weighted average. As colloids produced in

1  $\mu\text{M}$  (0.02  $\mu\text{mol}/\text{mg}$ ) solutions of NaCl were unstable after minutes to hours independent of the AGR these results are excluded.

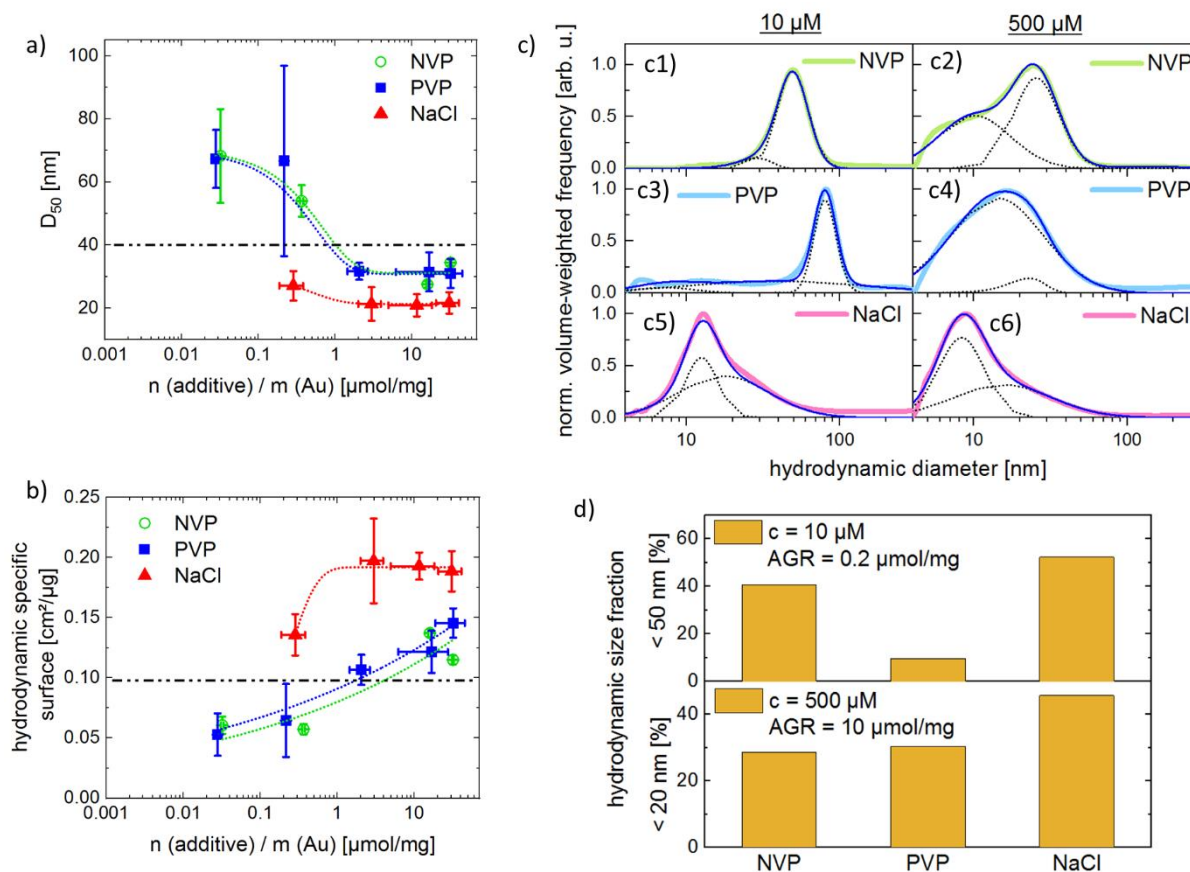


**Figure 35:** (a) Volume-weighted hydrodynamic median diameter obtained by analytical disc centrifugation and (b) related specific surface area of gold nanoparticles in PVP and NaCl as function of the additive-to-gold ratio (AGR). The dashed-dotted horizontal lines mark the reference experiments from LAL in pure water. Nanoparticle mass concentrations are obtained by optical UV/Vis extinction spectroscopy. (c) Volume-weighted particle size distributions of colloids in low and high additive concentrations derived from ADC analysis. (d) Hydrodynamic size fractions of particles < 20 nm and < 50 nm. The data is derived from the ADC size distributions in (c). The results display the properties of the particles in their nascent hydrodynamic environment.

The function is saturated already at AGR of 2  $\mu\text{mol}/\text{mg}$  resulting in hydrodynamic nanoparticle diameters of 20 nm. As these values are volume-weighted they prove the absence of considerable amounts of large secondary nanoparticles or aggregates. This finding corresponds well with the absence of *in situ* XHI scattering signal for NaCl in Figure 34b. PVP is suitable for size control of laser generated gold nanoparticles, if high concentrations are used. Still, the trend differs significantly from NaCl. While the relative concentration at saturation is similar for NaCl and PVP (1-2  $\mu\text{mol}/\text{mg}$ ) the size

reducing effect is lower for PVP (minimum size only 30 nm). At low concentrations ( $< 0.5 \mu\text{mol}/\text{mg}$ ) even a destabilization of particles seems to take place. The specific surface dose of additives per nanoparticle surface is plotted in Figure 35b. The ordinate shows the specific surface derived from ADC. The electrolyte NaCl shows a step-like behavior as a function of the AGR with a saturation at  $2 \mu\text{mol}/\text{mg}$ . Regarding PVP, this plot shows that the specific surface area is increasing as a function of the AGR while no saturation is reached within the investigated range (Figure 35b). In sum, the volume-weighted and surface related dependencies derived from the hydrodynamic analysis indicate a size quenching efficiency that is expected to correlate to the *in situ* XHI measurements (Figure 34b) when the amount of PVP per gold mass exceeds  $\sim 10 \mu\text{mol}/\text{mg}$ . Note that the absolute concentration of PVP in XHI of  $500 \mu\text{M}$  (equivalent to  $\sim 10 \mu\text{mol}/\text{mg}$  *ex situ*) is even higher in terms of AGR, but difficult to quantify in the dynamic environment due to the unknown time-averaged ablation yield. Apart from that, an effect of the PVP concentration on the laser transmission and LAL-cavitation can be excluded by measuring the extinction spectrum of the pure solution and bubble dynamics (as discussed later). It is concluded that PVP mainly acts as a growth quencher *ex situ* and that the effect is therefore not observable *in situ*. Note that the data in Figure 35 display the hydrodynamic sizes of the colloids. Keeping this in mind it is obvious that the large particles observed in PVP solutions with  $\text{AGR} \leq 0.1 \mu\text{mol}/\text{mg}$  are not individual nanoparticles but rather large agglomerates (Figure 69). These are formed, just as in pure water, by insufficient repulsive forces between the individual nanoparticles. While PVP binds to the gold surface the respective concentrations are just too low to induce steric stabilization of the many small particles because the overall surface in the system is high if the number of small particles is high as well. Therefore, the amount of PVP is just enough to stabilize the reduced (total) surface of the forming agglomerates. This behavior of agglomerate stabilization supports the conclusion that PVP acts as an *ex situ* growth quencher rather than already *in situ* inside the cavitation bubble.

To clarify the influence of the organic ligand PVP in terms of the size of the molecules and their functionality we performed additional *ex situ* experiments in different concentrations of solutions of the PVP's monomer N-vinylpyrrolidone (NVP). The chemical was obtained from Acros Organics (99 %, stabilized with NaOH) and used without further purification. Measurements of the pH value of  $1 \mu\text{M}$  and  $1000 \mu\text{M}$  solutions of NVP revealed that it was almost unaffected, with 5.9 at  $1 \mu\text{M}$  and 5.9-6.0 at  $1000 \mu\text{M}$ . Furthermore, the electrolytic conductivity was constant at  $0.7\text{-}0.8 \mu\text{S}/\text{cm}$ . The volume-weighted median diameter and the specific surface area of the gold nanoparticles was derived from combined ADC and UV/Vis analysis. The graphs in the Figure 35a,b reveal an almost identical curve progression of samples produced in NVP compared with those obtained in PVP but quite different to NaCl. This result points toward a major influence of the additives' functionality rather than the size of

the molecule. Hence, NVP and PVP of the same molarity have quite similar effect on the final size of the gold nanoparticles although NVP's molecular weight is only 1/35 of PVP (and roughly twice as large as that of NaCl). Both organic additives, NVP and PVP, do not bear functional groups capable to chemisorb on the gold surface obviously affect the size of the nanoparticles on a later time scale, probably after the final collapse of the cavitation bubble.

The similarity of the curve progression of NVP and PVP samples in Figure 35a,b requires further clarification. Therefore, in Figure 35c the size distributions (ADC, volume-weighted) of low and high concentrations of NVP and PVP are compared. Additional surface-weighted size distributions are presented in Figure 66. While at concentrations of 1  $\mu\text{M}$  the size distributions are quite similar, at 1000  $\mu\text{M}$  the entire PVP distribution is shifted to smaller hydrodynamic particle sizes whereas the NVP distribution shows only the evolution of a weaker primary mode at small particle sizes. Both additives are less effective in terms of their size quenching efficiency compared to NaCl (red line). The reason why the distinct differences in the size distributions of NVP and PVP are not displayed in Figure 35 are that (i) the median diameter does not describe all details of a size distribution and (ii) there are variations of abundance of particles larger than 100 nm in NVP and PVP (Figure 35c). Accordingly, while organic ligand's the functional group seems more important to size quenching compared to the molecular weight, the latter influence is not negligible with regard to the hydrodynamic diameter. The reduced abundance of hydrodynamically large (> 20 nm) particles in PVP is a proof for steric stabilization which is important for the colloid's long term stability against aggregation. This is clarified in Figure 35d by plotting the relative hydrodynamic size fraction of particles < 50 nm and < 20 nm as a function of the respective additive.

To summarize the hydrodynamic *ex situ* particle analysis, it is demonstrated that both additives result in smaller nanoparticles. Yet, while the addition of the electrolyte NaCl results in a plateau of the specific surface area already at a low AGR of 1  $\mu\text{mol}/\text{mg}$ , the macromolecular ligand does not saturate even at 20  $\mu\text{mol}/\text{mg}$ . This indicates that NaCl results in an additional energy barrier against ripening or coalescence of the nanoparticles (or their atom cluster seeds) by increasing the surface charges. On the other hand, PVP stabilizes nanoparticles sterically, building up a short-ranged steric barrier between the particles. With increasing amount of PVP molecules that barrier becomes more bulky and provides quenching of subsequent ripening processes. Hence, the hydrodynamic analysis indicates that the differing colloidal stabilizing mechanisms of NaCl and PVP also results in different size reductive effects in LAL.

To complement the *ex situ* particle analysis additional particle characterization by TEM has been performed. This is to provide additional information compared to a sole hydrodynamic analysis, as TEM

is sensitive to individual nanoparticles. The results are collected in Figure 36 (with TEM pictures shown in the Supporting Information, Figure 67-70). The left column (black bars) shows the number-weighted histograms of gold nanoparticles ablated in pure water, low (0.2  $\mu\text{mol}/\text{mg}$ , corresponds to 10  $\mu\text{M}$ ) and high (10  $\mu\text{mol}/\text{mg}$ , corresponds to 500  $\mu\text{M}$ ) AGRs of NaCl and PVP. It is visible that both additives reduce the size of the individual, number-weighted, nanoparticles with respect to pure water from 19 nm down to 6-8 nm with increasing AGR. As visible from the number-weighted TEM histogram in the left column of Figure 36, the nanoparticles synthesized in pure water exhibit a distinct, broad, and bimodal size distribution with an average size of 17 nm and a significant share of large solid spheres of 40-70 nm in diameter. If NaCl is used in a small AGR of 0.2  $\mu\text{mol}/\text{mg}$  the small particles (size reduction by 2 nm) are less affected than the large solid spheres. The size of the latter (maximum diameter 40 nm) and relative amount decrease drastically. This effect is enhanced by LAL with a high AGR of 10  $\mu\text{mol}/\text{mg}$ , which reduces the maximum size of large solid spheres to 20 nm and halves the size of the primary particles. Regarding LAL in PVP the situation is slightly different, especially at high AGR. Even an AGR of 10  $\mu\text{mol}/\text{mg}$  of PVP leaves a significant share of 40 nm-particles behind. Regarding the number-weighted-histogram of gold nanoparticles in high AGR of NVA, the similarity to the size distribution in PVP is obvious. Still, the distribution is broader in NVA, while in PVP a mode at diameters as small as 6 nm is dominant which is accompanied by a shoulder in the distribution. For reasons of comparability to the *in situ* XHI analysis the histograms are also converted from number- to volume-weighted distributions. By this statistics large particles are amplified. The corresponding histograms (Figure 36, middle column, red bars) show that NaCl indeed reduces the size and abundance of large particles, as the median diameter  $D_{50}$  is significantly reduced from 52 nm in pure water down to 10 nm at 10  $\mu\text{mol}/\text{mg}$  AGR.

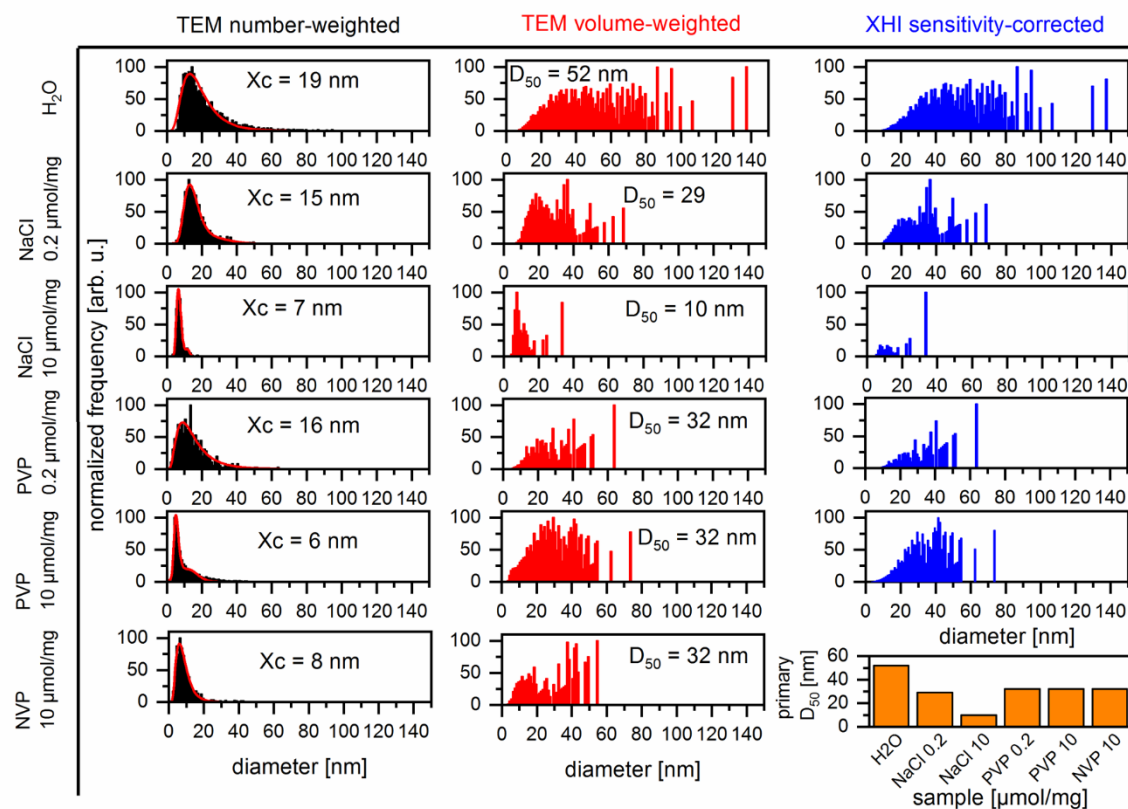


**Figure 36:** Representative TEM histograms of AuNP in pure water, NaCl and PVP at AGRs of 0.2 and 10  $\mu\text{mol/mg}$  (left column). The envelopes shown as solid red lines are obtained by lognormal fitting and the center of gravity  $X_c$  is displayed. The middle column shows the calculated volume-weighted histograms of the same samples with corresponding median diameters  $D_{50}$ . In the right column the volume-weighted histograms are further weighted by the XHI sensitivity curve shown in Figure 34a. The plot in the lower right corner sums up the volume-weighted primary particle median diameters as a function of the type and AGR of additive.

However, in the case of the macromolecule PVP the situation is different. While already small amounts of PVP (AGR of 0.2  $\mu\text{mol/mg}$ ) significantly reduce the median particle size from 52 nm to 32 nm, no further reduction is observed with increasing AGR. The volume-weighted distribution in high AGR of NVA is quite similar to that in low AGR of PVP (the lack of particles < 60 nm is due to the low number of large particles). It is concluded that the monomer and the polymer affect the primary particles in the same way but PVP is much more effective due to its higher chain-length and the resulting improved resistance against hydrodynamic ripening of the nanoparticles. The primary median diameters (volume-weighted) are displayed in Figure 36 (lower right) as a function of additive and concentration. All used additives and concentrations reduce the median particle size by at least  $\sim 20$  nm. Still, high

AGRs of NaCl are the only sample that quenches the particle size even down to 10 nm, which is therefore not detectable inside the cavitation bubble by XHI.

As discussed before the *in situ* XHI is sensitive to the ablated particle volume, but the overall size-dependent sensitivity is not a linear function. Therefore, the sensitivity curve (Figure 34a) is applied to the volume-weighted TEM histograms, resulting in histograms mapped onto the XHI sensitivity shown in the right column of Figure 36 (blue bars). Significant differences in the histograms are observable as function of the liquid composition. The sensitivity-weighted histogram of the colloid produced in pure water peaks at 90 nm and exhibits an overall broad distribution. The finding fits to the *in situ* XHI analysis (Figure 34b) as the expected strong scattering signal is indeed observed. Additionally, the high AGR of NaCl, as used for the *in situ* analysis, shows a scattering sensitivity maximum at about 35 nm, with all other particle species in the size range of  $\leq 25$  nm. Therefore, assuming that NaCl already quenches the size of nanoparticles *in situ* inside the cavitation bubble, no XHI scattering signal is expected. It is therefore plausible that the electrolyte NaCl not solely reduces aggregation inside the cavitation bubble, but also the size and abundance of individual large nanoparticles. The sensitivity-weighted TEM-histogram at 10  $\mu\text{mol/mg}$  AGR PVP peaks at 45 nm and the scattering signal remains high up to 75 nm, because of the higher sensitivity of the XHI setup towards larger particles (Figure 34a). Again, assuming PVP would affect the size of ablated nanoparticles already inside the cavitation bubble a reduced scattering signal in XHI would result, compared to the ablation in pure water. As this is not the case the conclusion is that PVP does not induce size quenching to individual nanoparticles already inside the cavitation bubble, but acts as a growth and ripening quencher on a later time-scale, thereby reducing the final particle size of both small primary and large secondary particles.

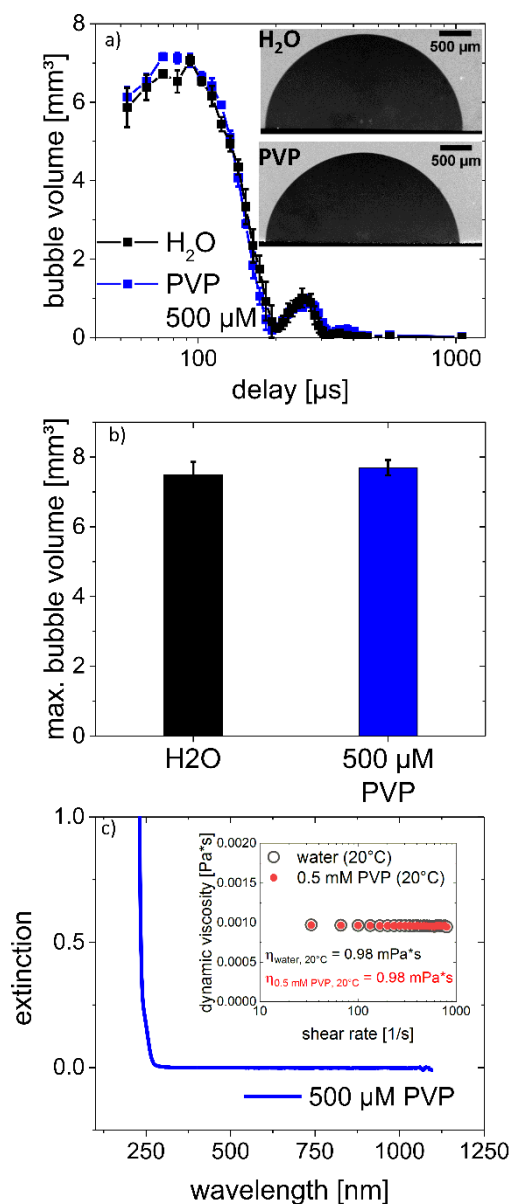


**Figure 37:** (a) Cavitation bubble dynamics as function of the delay from the laser impact. The PVP molecules do not affect the dynamics of the bubble. (b) Results of image analysis of the cavitation bubble at its maximum extension at 93 μs after laser impact on the target showing no difference between pure water and 500 μM PVP solution. (c) UV/Vis extinction spectrum of a 500 μM PVP solution. The solution is transparent at the laser wavelength of 1064 nm. Inset: Dynamic viscosity of pure water and a 0.5 mM PVP solution.

As both the *in situ* and the *ex situ* (hydrodynamic and structural analysis) point towards a growth quenching mechanism of the macromolecular ligand PVP at a time-scale after the lifetime of the cavitation bubble, we need to exclude processes related to the laser ablation and cavitation itself that

might cause this behavior. For example, Tsuji et al. have found a size quenching effect of PVP on silver nanoparticles during LAL [51]. They attributed this effect at least partially to the reduced size and lifetime of the laser-induced cavitation bubble, when PVP was used instead of pure water. Still, in our case the situation is different. The molecular weight of the PVP used in the present study is almost three times lower compared to Tsuji et al. [51], additionally the concentration we used for the *in situ* analysis (500  $\mu\text{M}$ ) is 36 times lower here. Overall this sums up to a negligible (factor of 108) influence of the PVP on the hydrodynamics. This is verified by performing shadowgraphic imaging of the cavitation bubble produced during LAL of gold in water with 500  $\mu\text{M}$  PVP. As shown in Figure 37b the maximum bubble volume (93  $\mu\text{s}$  after laser impact) is independent of the presence of PVP molecules. Therefore, it is underlined that the effective laser fluence on the gold target surface is the same for both liquids, as it is known that the cavitation bubble volume scales with the laser fluence [44]. The overall dynamics of the cavitation bubble (e.g. the volume and peak time of the bubble rebound) are also not significantly affected by the PVP molecules as shown in Figure 37a. The effective laser fluence on the target surface due to absorption in the solution is not expected to be affected by the low concentration of the used PVP (3,500 g/mol). The UV/Vis extinction spectrum of the pure PVP solution is given in Figure 37c, with the measured viscosity of water and the PVP solution given in the inset. Obviously, there is no measurable extinction at the laser wavelength of 1064 nm.

## Conclusions

Improvement of size dispersion of laser-generated colloids is often achieved *in situ* by anion-based charge transfer or organic ligands with high-affinity functional groups. Less is known about the quenching mechanism of macromolecular ligands, in particular non-thiolated polymers. To differentiate between the mechanisms of nanoparticle growth quenching by anions and macromolecules, we performed *in situ* X-ray multi-contrast imaging (with scattering contrast from a Hartmann mask) during pulsed laser ablation in liquids of gold combined with thorough *ex situ* evaluation. By using pure water and micromolar solutions of NaCl and PVP we have shown, that while NaCl reduces the size of primary and secondary nanoparticles already inside the gas phase of the laser-induced cavitation bubble, PVP does not change the nanoparticle size with respect to the sizes found in pure water. The maximum of size sensitivity in XHI is at 55 nm, which allows for the conclusion that the organic ligand PVP does not significantly alter the size of secondary nanoparticles, composed of large solid spheres and aggregates, inside the cavitation bubble. By studying the influences of the electrolyte NaCl and the macromolecular ligand PVP on the size and size distributions obtained *ex situ*, i.e., after final collapse of the cavitation bubble, it is found that PVP does reduce the size of small

primary nanoparticles ( $d < 10$  nm) and also the degree of aggregation. In general, the concentration of PVP must exceed a threshold to effectively reduce the size of aggregates compared to pure water. The used concentration of 0.5 mM is well above that threshold. One major difference between the additives NaCl and PVP is their impact on large secondary spheres. The combined results point towards the conclusion that PVP interacts with nanoparticles produced by LAL by a different mechanism as NaCl (as large particle size quenching is not observed). It is also indicated that primary and secondary particles are formed by different ablation mechanisms as large spheres can be affected by PVP *ex situ* more efficiently than small particles, possibly via coalescence quenching in colloidal state.

## 6 Summary and conclusion

Among the issues of pulsed laser ablation in liquids for the synthesis of colloidal nanoparticles is the lack of particle size control without further particle processing by laser re-irradiation or centrifugation. As a consequence of the bimodal particle size distribution of colloids, consisting of small primary particles ( $d \leq 10$  nm) and large solid spheres ( $d > 10$  nm), applications that demand monomodal or monodisperse colloids are inaccessible when using laser-generated nanoparticles. A possible solution to that problem is the addition of additives to the liquid phase prior to PLAL that are known to quench the size of the resulting nanoparticles and narrow the particle size distribution. Two types of additives are known for the ablation of noble metals dispersed in water, monovalent electrolytes and organic ligands. In this work, the focus was put on the model system of gold targets as the solid phase and aqueous solutions of NaCl, an inorganic salt, and PVP, a macromolecular ligand, as the liquid phase.

The aim of this dissertation was to elucidate the size-quenching mechanisms of different types of additives. Though chemical reactions proceed quickly in PLAL, less than minutes after laser impact on the target, the approach chosen here was to probe the interior of the laser-induced cavitation bubble by means of the size-sensitive X-ray techniques SAXS and XHI, both of which are based on the scattering of X-rays at nanoparticles. All X-ray-based experiments were performed using intense synchrotron radiation to optimize the signal-to-noise ratio.

A known exception to fast reactions during PLAL is nanocluster-induced ripening processes that take place on the scale of hours to days. The investigation of nanoclusters was hence also included in the performed experiments.

The time of interaction of the dissolved additives and the ablated species was, for a long time, under debate, with the question of whether size quenching starts after final cavitation bubble collapse and release of nanoparticles into the surrounding liquid phase or already inside the vapor phase of the cavitation bubble where the particles are initially trapped, an observation that further boosted the discussion.

As the most efficient size quenching is observed *ex situ* using inorganic electrolytes as additives, the initial experiment was performed using spatiotemporally resolved SAXS to probe the cavitation bubble induced on a gold target dispersed in an aqueous solution of 0.5 mM NaCl. Regarding the applied method, namely pulsed laser ablation in liquids, it was surprising to find that the salt-induced size quenching happens inside the gas phase of the cavitation bubble. While *ex situ* studies have revealed that the ablation in micromolar solutions of salts reduced all particle size fractions, primary and secondary, the *in situ* SAXS data pointed towards an exclusive size quenching of the larger secondary

nanoparticles; the primary particles were totally unaffected. The *in situ* results were independent of the oscillation cycles of the cavitation bubble. A fragmentation of the primary particles induced by the dissolved ions after final bubble collapse cannot be explained, especially as in this case the delayed addition of salts just after the collapse should result in the same particle size distribution as for the salt addition prior to laser ablation; it was likely that the resolution of the SAXS method was overextended for the analysis of small primary particles.

The resolution limit of SAXS was tested in terms of specific manifestations of the colloidal bimodality and in terms of the routine used for data analysis, i.e., two different algorithms for data fitting were applied. Accordingly, two monomodal colloids (7 nm and 10 nm on average) were prepared by subsequent PLAL and PLFL. A third colloid (approximately 50 nm) was prepared by chemical reduction synthesis and obtained commercially. In the next step, the model colloids were mixed together in defined ratios to ensure that the mass ratio of small and large particle size fractions was controllable. Particle mixtures of 7-nm and 50-nm particles were prepared in ratios from 0.4 (high amount of small nanoparticles) to 80 (high amount of large nanoparticles). The second series of samples consisted of 7-nm and 10-nm particles in ratios from 0.02 to 50. The first series was designed to mimic the overall bimodality of laser-generated colloids and the different ratios reflected the size quenching of large particles by the addition of dissolved electrolytes like NaCl. In contrast, the second series aimed at the broadness of the size distribution of particles obtained from PLAL. These are continuous, with the different size fractions merging with each other, and so were the size fractions of the 7-nm and 10-nm colloids. The results from SAXS analysis with two different algorithms and the comparison of the data to ADC, DLS, and UV/vis extinction spectroscopy with Mie Gans fitting have demonstrated that:

- i. The two SAXS algorithms are equivalent, with one resolving the average size of the underlying size fractions (UF) and the other one giving access to the entire particle size distribution (MC) of the colloid.
- ii. SAXS is highly accurate when it comes to the analysis of bimodal colloids consisting of small 7-nm particles and large 50-nm particles without any overlap of the size distributions. This applies for both the analysis of fraction sizes and of mass ratios.
- iii. The overlapping size distributions of colloids consisting of 7-nm and 10-nm colloids cannot be distinguished. The outcome is an average particle size that depends on the mass ratio of the mixed size fraction.

Hence, the *ex situ* study referencing the limits of the resolution of SAXS led to the conclusion that the finding of *in situ* SAXS, those small primary particles are not quenched while large secondary particles

are, is a measurement artifact caused by the broad and continuous size distributions produced by PLAL with and without the addition of salts. However, a high relative share of the secondary particles is significantly reduced already by *in situ* size quenching using NaCl.

Despite the identification of salt-induced size quenching inside the cavitation bubble, no route towards monomodal colloids was identified. The large spherical secondary particles are probably formed on a sub-microsecond time-scale, perhaps inside the plasma phase that exists at the target interface for approximately the first microsecond after laser impact. This time-resolution was, however, out of the scope of this work.

Investigations on the time of interaction between nanoparticles still confined within the cavitation bubble and the macromolecular ligand PVP were performed using XHI, instead of the previously exploited SAXS method. XHI is a single-shot imaging technique to record the entire cavitation bubble cross-section. The images are formed by three contrast mechanisms: absorption, differential phase, and scattering contrast. By decorrelation of the three contrast channels, the scattering contrast becomes accessible. Hence, spatiotemporally resolved imaging with sensitivity to nanoparticles was possible. For the experiments, three systems were used: ablation of gold in pure water, in NaCl solution just as during the previous SAXS study, and in PVP solution. While the water sample showed significant scattering during the lifetime of the cavitation bubble's first oscillation, the NaCl sample did not give signals beyond the average noise level. In other words, no secondary particles were observed in the NaCl sample in accordance with the SAXS data. The main sample of this study was the PVP sample. No significant differences, compared to the water sample, were found. Together with the results from *ex situ* particle analysis, it was concluded that the macromolecular ligand affects the particles in the liquid phase and not in the gas phase of the cavitation bubble because of the finding that both particle species' primary and secondary particles were reduced in size. Apparently, PVP is a growth-quenching agent that limits particle growth by coalescence and Ostwald ripening by steric stabilization of the nanoparticles.

The *ex situ* study correlating the shape and lifetime of the cavitation bubble with the resulting particle size of silver nanoparticles was conducted by optical imaging of the bubble by means of shadowgraphy. As no laser scanning was applied, every laser pulse contributed to the drilling depth of the ablated crater. This surface damage was ultimately the reason for the reduced lifetime of the cavitation bubble with an increasing number of laser pulses and the altered shape of the maximum extended bubble from semispherical to almost spherical. As the cavitation bubble confines, it was surprising that the bubble did not affect the resulting nanoparticle size significantly. Still, the produced colloids were highly diluted and it was observed that a high share of nanoclusters ( $d \leq 3\text{nm}$ ) was produced and

stabilized due to the high interparticle distance in the liquid. A significant influence of the cavitation bubble as a reservoir for the nanoparticles is certain, but it is not the only parameter that defines the final particle size. The produced nanocluster will be consumed by larger particles, with increasing time, by colloidal growth processes.

In brief, it was found that a micromolar solution of dissolved NaCl quenches the size of primary and secondary nanoparticles during PLAL that are already inside the laser-induced cavitation bubble. In contrast, the macromolecular ligand PVP does not. Instead, PVP quenches subsequent particle growth in the liquid phase. This is supported by the finding that a large amount of nanoclusters is produced during nanosecond PLAL. Accordingly, no route towards monodisperse colloids by single-shot PLAL was discovered; instead, it was found that the resulting colloids are not bimodal but trimodal as the fraction of nanoclusters must be considered. This latter finding highlights the importance of size and growth quenching in the liquid phase to prevent an increasing bi- and multimodality of the final particle size distribution of laser-generated colloids.

## 7 Outlook

This dissertation adds to the knowledge on particle formation during nanosecond PLAL, particularly on the control of the nanoparticle size. The earliest interaction between additives, specifically dissolved electrolytes, were observed inside the cavitation bubble at a delay of 90  $\mu\text{s}$  after laser impact. While there is no direct proof for the presence of large spherical nanoparticles already inside the cavitation bubble (because the observed large particles might also be agglomerates), all findings from *ex situ* experiments point towards the presence of large particles in the bubble. It is therefore likely that the nanoparticles obtained by PLAL are formed on an even earlier time scale, possibly during the plasma phase prior to the evolution of the cavitation bubble. Avoiding the formation of, e.g., the fraction of large secondary nanoparticles to obtain monodisperse colloids, would require that one understands particle formation during the first few nanoseconds after laser impact.

If a minor share of secondary nanoparticles in the colloid is, however, acceptable for the desired application, the combined addition of electrolyte and macromolecular ligand to the liquid phase might be an option. Possible competitive interactions of the additives might be investigated in future studies.

Nanocluster formation might further add to the bimodality in the colloid by the unequal growth of primary and secondary nanoparticles. Exploring the origin of nanoclusters is, therefore, crucial to gain further mechanistic insights into PLAL. This accounts strongly for the question of whether nanoclusters are trapped inside the cavitation bubble along with primary and secondary nanoparticles or if they are instantly injected into the liquid. Stabilization of nanoclusters, in low concentrations, with only minor subsequent growth processes could be achieved by using thiol ligands during the PLAL of gold targets.

As the plasma phase is decisive in the formation chain of nanoparticles during PLAL, the investigation of the processes occurring inside the cavitation bubble during picosecond PLAL can possibly reveal routes towards monodisperse colloids. In picosecond PLAL, in contrast to nanosecond laser pulses, the pulse duration is in the domain of the electron-phonon coupling time. Hence, the plasma is much less pronounced when ultrashort pulses are used, which can also affect the share of nanoclusters and subsequent ripening processes.

## 8 References

- [1] E. Commission, *Definition of a nanomaterial*, in, [http://ec.europa.eu/environment/chemicals/nanotech/faq/definition\\_en.htm](http://ec.europa.eu/environment/chemicals/nanotech/faq/definition_en.htm), 2017, pp. European Commission > Environment > Chemicals > Nanomaterials > Definition.
- [2] S. Guo, S. Zhang, S. Sun, *Tuning Nanoparticle Catalysis for the Oxygen Reduction Reaction*, *Angewandte Chemie International Edition* 52 (2013) 8526-8544.
- [3] A. Figuerola, R. Di Corato, L. Manna, T. Pellegrino, *From iron oxide nanoparticles towards advanced iron-based inorganic materials designed for biomedical applications*, *Pharmacological Research* 62 (2010) 126-143.
- [4] M. Pelton, J. Aizpurua, G. Bryant, *Metal-nanoparticle plasmonics*, *Laser & Photonics Reviews* 2 (2008) 136-159.
- [5] D. Golberg, Y. Bando, Y. Huang, T. Terao, M. Mitome, C. Tang, C. Zhi, *Boron Nitride Nanotubes and Nanosheets*, *ACS Nano* 4 (2010) 2979-2993.
- [6] M. Rycenga, C.M. Cobley, J. Zeng, W. Li, C.H. Moran, Q. Zhang, D. Qin, Y. Xia, *Controlling the Synthesis and Assembly of Silver Nanostructures for Plasmonic Applications*, *Chemical Reviews* 111 (2011) 3669-3712.
- [7] A. Biswas, I.S. Bayer, A.S. Biris, T. Wang, E. Dervishi, F. Faupel, *Advances in top-down and bottom-up surface nanofabrication: Techniques, applications & future prospects*, *Advances in Colloid and Interface Science* 170 (2012) 2-27.
- [8] R. Intartaglia, G. Das, K. Bagga, A. Gopalakrishnan, A. Genovese, M. Povia, E. Di Fabrizio, R. Cingolani, A. Diaspro, F. Brandi, *Laser synthesis of ligand-free bimetallic nanoparticles for plasmonic applications*, *Phys. Chem. Chem. Phys.* 15 (2013) 3075-3082.
- [9] J.D. Robertson, L. Rizzello, M. Avila-Olias, J. Gaitzsch, C. Contini, M.S. Magoń, S.A. Renshaw, G. Battaglia, *Purification of Nanoparticles by Size and Shape*, *Scientific Reports* 6 (2016) 27494.
- [10] I. Limayem, C. Charcosset, H. Fessi, *Purification of nanoparticle suspensions by a concentration/diafiltration process*, *Separation and Purification Technology* 38 (2004) 1-9.
- [11] R. Zsigmondy, R. Heyer, *Über die Reinigung von Kolloiden durch Dialyse*, *Zeitschrift für anorganische Chemie* 68 (1910) 169-187.
- [12] L.G. AbdulHalim, N. Kothalawala, L. Sinatra, A. Dass, O.M. Bakr, *Neat and Complete: Thiolate-Ligand Exchange on a Silver Molecular Nanoparticle*, *Journal of the American Chemical Society* 136 (2014) 15865-15868.
- [13] J.-P. Sylvestre, A.V. Kabashin, E. Sacher, M. Meunier, *Femtosecond laser ablation of gold in water: influence of the laser-produced plasma on the nanoparticle size distribution*, *Appl. Phys. A* 80 (2005) 753-758.
- [14] S. Scaramuzza, M. Zerbetto, V. Amendola, *Synthesis of Gold Nanoparticles in Liquid Environment by Laser Ablation with Geometrically Confined Configurations: Insights To Improve Size Control and Productivity*, *J. Phys. Chem. C* 120 (2016) 9453-9463.

- [15] G. Marzun, A. Levis, V. Mackert, T. Kallio, S. Barcikowski, P. Wagener, *Laser synthesis, structure and chemical properties of colloidal nickel-molybdenum nanoparticles for the substitution of noble metals in heterogeneous catalysis*, *Journal of Colloid and Interface Science* 489 (2017) 57-67.
- [16] T. Tsuji, Y. Okazaki, Y. Tsuboi, M. Tsuji, *Nanosecond Time-Resolved Observations of Laser Ablation of Silver in Water*, *Jpn. J. Appl. Phys.* 46 (2007) 1533-1535.
- [17] J. Tomko, J.J. Naddeo, R. Jimenez, Y. Tan, M. Steiner, J.M. Fitz-Gerald, D.M. Bubb, S.M. O'Malley, *Size and polydispersity trends found in gold nanoparticles synthesized by laser ablation in liquids*, *Phys. Chem. Chem. Phys.* 17 (2015) 16327-16333.
- [18] R. Tanabe, T.T.P. Nguyen, T. Sugiura, Y. Ito, *Bubble dynamics in metal nanoparticle formation by laser ablation in liquid studied through high-speed laser stroboscopic videography*, *Appl. Surf. Sci.* 351 (2015) 327-331.
- [19] S. Ibrahimkuty, P. Wagener, A. Menzel, A. Plech, S. Barcikowski, *Nanoparticle formation in a cavitation bubble after pulsed laser ablation in liquid studied with high time resolution small angle x-ray scattering*, *Appl. Phys. Lett.* 101 (2012) 103104.
- [20] P. Wagener, S. Ibrahimkuty, A. Menzel, A. Plech, S. Barcikowski, *Dynamics of silver nanoparticle formation and agglomeration inside the cavitation bubble after pulsed laser ablation in liquid*, *Phys. Chem. Chem. Phys.* 15 (2013) 3068-3074.
- [21] C. Rehbock, V. Merk, L. Gamrad, R. Streubel, S. Barcikowski, *Size control of laser-fabricated surfactant-free gold nanoparticles with highly diluted electrolytes and their subsequent bioconjugation*, *Phys. Chem. Chem. Phys.* 15 (2013) 3057-3067.
- [22] S.W. Smith, *The Refractive Index of Liquids for X-rays*, *Phys. Rev.* 40 (1932) 156-164.
- [23] U. Bonse, H. Hellkötter, *Interferometrische Messung des Brechungsindex für Röntgenstrahlen*, *Zeitschrift für Physik A Hadrons and nuclei* 223 (1969) 345-352.
- [24] E.G. Gamaly, A.V. Rode, B. Luther-Davies, V.T. Tikhonchuk, *Ablation of solids by femtosecond lasers: Ablation mechanism and ablation thresholds for metals and dielectrics*, *Phys. Plasmas* 9 (2002) 949-957.
- [25] B.N. Chichkov, C. Momma, S. Nolte, F. von Alvensleben, A. Tünnermann, *Femtosecond, Picosecond and Nanosecond Laser Ablation of Solids*, *Appl. Phys. A* 63 (1996) 109-115.
- [26] T. Sakka, S. Iwanaga, Y.H. Ogata, A. Matsunawa, T. Takemoto, *Laser Ablation at Solid-Liquid Interfaces: an Approach from Optical Emission Spectra*, *J. Chem. Phys.* 112 (2000) 8645-8653.
- [27] H. Oguchi, T. Sakka, Y.H. Ogata, *Effects of pulse duration upon the plume formation by the laser ablation of Cu in water*, *J. Appl. Phys.* 102 (2007) 023306.
- [28] J. Lam, D. Amans, F. Chaput, M. Diouf, G. Ledoux, N. Mary, K. Masenelli-Varlot, V. Motto-Ros, C. Dujardin,  *$\gamma$ -Al<sub>2</sub>O<sub>3</sub> nanoparticles synthesised by pulsed laser ablation in liquids: a plasma analysis*, *Phys. Chem. Chem. Phys.* 16 (2014) 963-973.
- [29] S. Reich, P. Schönfeld, P. Wagener, A. Letzel, S. Ibrahimkuty, B. Gökce, S. Barcikowski, A. Menzel, T. dos Santos Rolo, A. Plech, *Pulsed laser ablation in liquids: Impact of the bubble dynamics on particle formation*, *J. Colloid. Interface Sci.* 489 (2017) 106-113.

- [30] S. Ibrahimkuty, P. Wagener, T. dos Santos Rolo, D. Karpov, A. Menzel, T. Baumbach, S. Barcikowski, A. Plech, *A hierarchical view on material formation during pulsed-laser synthesis of nanoparticles in liquid*, *Sci. Rep.* (2015) 5:16313.
- [31] C. Momma, B.N. Chichkov, S. Nolte, F. von Alvensleben, A. Tünnermann, H. Welling, B. Wellegehausen, *Short-pulse laser ablation of solid targets*, *Opt. Commun.* 129 (1996) 134-142.
- [32] J.H. Yoo, S.H. Jeong, X.L. Mao, R. Greif, R.E. Russo, *Evidence for phase-explosion and generation of large particles during high power nanosecond laser ablation of silicon*, *Appl. Phys. Lett.* 76 (2000) 783-785.
- [33] D. Zhang, B. Gökce, S. Barcikowski, *Laser Synthesis and Processing of Colloids: Fundamentals and Applications*, *Chem. Rev.* 117 (2017) 3990-4103.
- [34] D. Du, X. Liu, G. Korn, J. Squier, G. Mourou, *Laser-induced breakdown by impact ionization in SiO<sub>2</sub> with pulse widths from 7 ns to 150 fs*, *Appl. Phys. Lett.* 64 (1994) 3071-3073.
- [35] L.J. Lewis, D. Perez, *Laser Ablation with Short and Ultrashort Laser Pulses: Basic Mechanisms from Molecular-Dynamics Simulations*, *Appl. Surf. Sci.* 255 (2009) 5101-5106.
- [36] P. Lorazo, L.J. Lewis, M. Meunier, *Short-Pulse Ablation of Solids: from Phase Explosion to Fragmentation*, *Phys. Rev. Lett.* 91 (2003) 225502.
- [37] D. Perez, L.J. Lewis, *Thermodynamic Evolution of Materials during Laser Ablation under Pico and Femtosecond Pulses*, *Appl. Phys. A* 79 (2004) 987-990.
- [38] K.K. Kim, M. Roy, H. Kwon, J.K. Song, S.M. Park, *Laser ablation dynamics in liquid phase: The effects of magnetic field and electrolyte*, *J. Appl. Phys.* 117 (2015) 074302.
- [39] T. Sakka, K. Takatani, Y.H. Ogata, M. Mabuchi, *Laser Ablation at the Solid-Liquid Interface: Transient Absorption of Continuous Spectral Emission by Ablated Aluminum Atoms*, *J. Phys. D: Appl. Phys.* 35 (2002) 65-73.
- [40] J. Lam, D. Amans, C. Dujardin, G. Ledoux, A.-R. Allouche, *Atomistic Mechanisms for the Nucleation of Aluminum Oxide Nanoparticles*, *J. Phys. Chem. A* 119 (2015) 8944-8949.
- [41] M. Dell'Aglio, R. Gaudio, O. De Pascale, A. De Giacomo, *Mechanisms and processes of pulsed laser ablation in liquids during nanoparticle production*, *Appl. Surf. Sci.* 348 (2015) 4-9.
- [42] V. Lazic, J.J. Laserna, S. Jovicevic, *Insights in the laser-induced breakdown spectroscopy signal generation underwater using dual excitation - Part I: Vapor bubble, shockwaves and plasma*, *Spectrochim. Acta B* 82 (2013) 42-49.
- [43] T. Sakka, A. Tamura, A. Matsumoto, K. Fukami, N. Nishi, B. Thornton, *Effects of pulse width on nascent laser-induced bubbles for underwater laser-induced breakdown spectroscopy*, *Spectrochim. Acta B* 97 (2014) 94-98.
- [44] S. Reich, P. Schönfeld, A. Letzel, S. Kohsackowski, M. Olbinado, B. Gökce, S. Barcikowski, A. Plech, *Fluence Threshold Behaviour on Ablation and Bubble Formation in Pulsed Laser Ablation in Liquids*, *ChemPhysChem* 18 (2017) 1084-1090.

- [45] A. Matsumoto, A. Tamura, A. Kawasaki, T. Honda, P. Gregorcic, N. Nishi, K. Amano, K. Fukami, T. Sakka, *Comparison of the overall temporal behavior of the bubbles produced by short- and long-pulse nanosecond laser ablations in water using a laser-beam-transmission probe*, Appl. Phys. A 122 (2016) 234.
- [46] C.-Y. Shih, C. Wu, M.V. Shugaev, L.V. Zhigilei, *Atomistic modeling of nanoparticle generation in short pulse laser ablation of thin metal films in water*, J. Coll. Interf. Sci. 489 (2017) 3-17.
- [47] C.-Y. Shih, M.V. Shugaev, C. Wu, L.V. Zhigilei, *Generation of Subsurface Voids, Incubation Effects and Formation of Nanoparticles in Short Pulse Laser Interactions with Bulk Metal Targets in Liquid: Molecular Dynamics Study*, J. Phys. Chem. C 121 (2017) 16549-16567.
- [48] C.-Y. Shih, R. Streubel, J. Heberle, A. Letzel, M.V. Shugaev, C. Wu, M. Schmidt, B. Gökce, S. Barcikowski, L.V. Zhigilei, *Two mechanisms of nanoparticle generation in picosecond laser ablation in liquids: the origin of the bimodal size distribution*, Nanoscale 10 (2018) 6900-6910.
- [49] C. Rehbock, J. Jakobi, L. Gamrad, S. van der Meer, D. Tiedemann, U. Taylor, W. Kues, D. Rath, S. Barcikowski, *Current state of laser synthesis of metal and alloy nanoparticles as ligand-free reference materials for nano-toxicological assays*, Beilstein J. Nanotechnol. 5 (2014) 1523-1541.
- [50] J. Lam, J. Lombard, C. Dujardin, G. Ledoux, S. Merabia, D. Amans, *Dynamical study of bubble expansion following laser ablation in liquids*, Appl. Phys. Lett. 108 (2016) 074104.
- [51] T. Tsuji, D.-H. Thang, Y. Okazaki, M. Nakanishi, Y. Tsuboi, M. Tsuji, *Preparation of silver nanoparticles by laser ablation in polyvinylpyrrolidone solutions*, Appl. Surf. Sci. 254 (2008) 5224-5230.
- [52] A. Tamura, A. Matsumoto, K. Fukami, N. Nishi, T. Sakka, *Simultaneous observation of nascent plasma and bubble induced by laser ablation in water with various pulse durations*, J. Appl. Phys. 117 (2015) 173304.
- [53] S. Kohsakowski, B. Gökce, R. Tanabe, P. Wagener, A. Plech, Y. Ito, S. Barcikowski, *Target geometry and rigidity determines laser-induced cavitation bubble transport and nanoparticle productivity – a high-speed videography study*, Phys. Chem. Chem. Phys. 18 (2016) 16585-16593.
- [54] A. Matsumoto, A. Tamura, T. Honda, T. Hirota, K. Kobayashi, S. Katakura, N. Nishi, K.-i. Amano, K. Fukami, T. Sakka, *Transfer of the Species Dissolved in a Liquid into Laser Ablation Plasma: An Approach Using Emission Spectroscopy*, J. Phys. Chem. C 119 (2015) 26506-26511.
- [55] W. Soliman, T. Nakano, N. Takada, K. Sasaki, *Modification of Rayleigh–Plesset Theory for Reproducing Dynamics of Cavitation Bubbles in Liquid-Phase Laser Ablation*, Jpn. J. Appl. Phys. 49 (2010) 116202.
- [56] W. Soliman, *Pseudo line tension in pressurized liquid-phase laser ablation*, Optics & Laser Technology 91 (2017) 40-45.
- [57] A. Casavola, A. De Giacomo, M. Dell'Aglio, F. Taccogna, G. Colonna, O. De Pascale, S. Longo, *Experimental investigation and modelling of double pulse laser induced plasma spectroscopy under water*, Spectrochimica Acta Part B: Atomic Spectroscopy 60 (2005) 975-985.
- [58] L. Rayleigh, *VIII. On the pressure developed in a liquid during the collapse of a spherical cavity*, The London, Edinburgh, and Dublin Philosophical Magazine and Journal of Science 34 (1917) 94-98.

- [59] a. M S Plesset, A. Prosperetti, *Bubble Dynamics and Cavitation*, Annual Review of Fluid Mechanics 9 (1977) 145-185.
- [60] M.S. Plesset, *THE DYNAMICS OF CAVITATION BUBBLES*, J. Appl. Mech.-Trans. ASME 16 (1949) 277-282.
- [61] J. Tomko, S.M. O'Malley, C. Trout, J.J. Naddeo, R. Jimenez, J.C. Gripenburg, W. Soliman, D.M. Bubb, *Cavitation bubble dynamics and nanoparticle size distributions in laser ablation in liquids*, Colloids and Surfaces A: Physicochemical and Engineering Aspects 522 (2017) 368-372.
- [62] F. R. Gilmore, *The Collapse and Growth of a Spherical Bubble in a Viscous Compressible Liquid*, in, Hydrodynamics Laboratory, California Institute of Technology, Pasadena, California, USA, 1952.
- [63] W. Lauterborn, T. Kurz, *Physics of bubble oscillations*, Rep. Prog. Phys. 73 (2010) 106501.
- [64] R. Löfstedt, B.P. Barber, S.J. Putterman, *Toward a hydrodynamic theory of sonoluminescence*, Physics of Fluids A: Fluid Dynamics 5 (1993) 2911-2928.
- [65] N. Dabir-Moghaddam, Z. Liu, B. Wu, *Modeling of the shrinking process of a bubble induced by laser metal ablation in water and experimental verification*, J. Appl. Phys. 121 (2017) 044908.
- [66] A. De Giacomo, M. Dell'Aglio, A. Santagata, R. Gaudio, O. De Pascale, P. Wagener, G.C. Messina, G. Compagnini, S. Barcikowski, *Cavitation dynamics of laser ablation of bulk and wire-shaped metals in water during nanoparticles production*, Phys. Chem. Chem. Phys. 15 (2013) 3083-3092.
- [67] A. Fojtik, A. Henglein, *Laser Ablation of Films and Suspended Particles in a Solvent: Formation of Clusters and Colloid Solutions*, Ber. Bunsen-Ges. Phys. Chem. 97 (1993) 252-254.
- [68] V. Amendola, M. Meneghetti, *Laser ablation synthesis in solution and size manipulation of noble metal nanoparticles*, Phys. Chem. Chem. Phys. 11 (2009) 3805-3821.
- [69] R. Gans, *Über die Form ultramikroskopischer Goldteilchen*, Annalen der Physik 342 (1912) 881-900.
- [70] C.M. Goodman, C.D. McCusker, T. Yilmaz, V.M. Rotello, *Toxicity of Gold Nanoparticles Functionalized with Cationic and Anionic Side Chains*, Bioconjugate Chemistry 15 (2004) 897-900.
- [71] C. Uboldi, D. Bonacchi, G. Lorenzi, M.I. Hermanns, C. Pohl, G. Baldi, R.E. Unger, C.J. Kirkpatrick, *Gold nanoparticles induce cytotoxicity in the alveolar type-II cell lines A549 and NCIH441*, Particle and Fibre Toxicology 6 (2009) 18-18.
- [72] C. Streich, L. Akkari, C. Decker, J. Bormann, C. Rehbock, A. Müller-Schiffmann, F.C. Niemeyer, L. Nagel-Steger, D. Willbold, B. Sacca, C. Korth, T. Schrader, S. Barcikowski, *Characterizing the Effect of Multivalent Conjugates Composed of A $\beta$ -Specific Ligands and Metal Nanoparticles on Neurotoxic Fibrillar Aggregation*, ACS Nano 10 (2016) 7582-7597.
- [73] J. Krawinkel, U. Richter, M.L. Torres-Mapa, M. Westermann, L. Gamrad, C. Rehbock, S. Barcikowski, A. Heisterkamp, *Optical and electron microscopy study of laser-based intracellular molecule delivery using peptide-conjugated photodispersible gold nanoparticle agglomerates*, Journal of Nanobiotechnology 14 (2016) 2.

- [74] D. Tiedemann, U. Taylor, C. Rehbock, J. Jakobi, S. Klein, W.A. Kues, S. Barcikowski, D. Rath, *Reprotoxicity of gold, silver, and gold-silver alloy nanoparticles on mammalian gametes*, *Analyst* 139 (2014) 931-942.
- [75] J.K. Pandey, R.K. Swarnkar, K.K. Soumya, P. Dwivedi, M.K. Singh, S. Sundaram, R. Gopal, *Silver Nanoparticles Synthesized by Pulsed Laser Ablation: as a Potent Antibacterial Agent for Human Enteropathogenic Gram-Positive and Gram-Negative Bacterial Strains*, *Applied Biochemistry and Biotechnology* 174 (2014) 1021-1031.
- [76] A. Schwenke, P. Wagener, A. Weiß, K. Klimenta, H. Wiegel, L. Sajti, S. Barcikowski, *Laser-Based Generation of Nanocomposites without Matrix-Coupling Agents for Bioactive Medical Devices*, *Chemie Ingenieur Technik* 85 (2013) 740-746.
- [77] A. Poletti, G. Fracasso, G. Conti, R. Pilot, V. Amendola, *Laser generated gold nanocorals with broadband plasmon absorption for photothermal applications*, *Nanoscale* 7 (2015) 13702-13714.
- [78] S. Salmaso, P. Caliceti, V. Amendola, M. Meneghetti, J.P. Magnusson, G. Pasparakis, C. Alexander, *Cell up-take control of gold nanoparticles functionalized with a thermoresponsive polymer*, *J. Mater. Chem.* 19 (2009) 1608-1615.
- [79] S.D. Angelov, S. Koenen, J. Jakobi, H.E. Heissler, M. Alam, K. Schwabe, S. Barcikowski, J.K. Krauss, *Electrophoretic deposition of ligand-free platinum nanoparticles on neural electrodes affects their impedance in vitro and in vivo with no negative effect on reactive gliosis*, *Journal of Nanobiotechnology* 14 (2016) 3.
- [80] S. Prati, M. Quaranta, G. Sciutto, I. Bonacini, L. Litti, M. Meneghetti, R. Mazzeo, *Use of nano gold obtained by laser ablation for SEIRA analyses of colorants*, *Heritage Sci.* 2 (2014) 28.
- [81] T. Yonezawa, H. Kawasaki, A. Tarui, T. Watanabe, R. Arakawa, T. Shimada, F. Mafune, *Detailed Investigation on the Possibility of Nanoparticles of Various Metal Elements for Surface-Assisted Laser Desorption/Ionization Mass Spectrometry*, *Analytical Sciences* 25 (2009) 339-346.
- [82] V. Amendola, L. Litti, M. Meneghetti, *LDI-MS Assisted by Chemical-Free Gold Nanoparticles: Enhanced Sensitivity and Reduced Background in the Low-Mass Region*, *Analytical Chemistry* 85 (2013) 11747-11754.
- [83] E. Messina, E. Cavallaro, A. Cacciola, M.A. Iatì, P.G. Gucciardi, F. Borghese, P. Denti, R. Saija, G. Compagnini, M. Meneghetti, V. Amendola, O.M. Maragò, *Plasmon-Enhanced Optical Trapping of Gold Nanoaggregates with Selected Optical Properties*, *ACS Nano* 5 (2011) 905-913.
- [84] E. Messina, E. Cavallaro, A. Cacciola, R. Saija, F. Borghese, P. Denti, B. Fazio, C. D'Andrea, P.G. Gucciardi, M.A. Iatì, M. Meneghetti, G. Compagnini, V. Amendola, O.M. Maragò, *Manipulation and Raman Spectroscopy with Optically Trapped Metal Nanoparticles Obtained by Pulsed Laser Ablation in Liquids*, *The Journal of Physical Chemistry C* 115 (2011) 5115-5122.
- [85] J. Zhang, G. Chen, D. Guay, M. Chaker, D. Ma, *Highly active PtAu alloy nanoparticle catalysts for the reduction of 4-nitrophenol*, *Nanoscale* 6 (2014) 2125-2130.
- [86] J. Zhang, G. Chen, M. Chaker, F. Rosei, D. Ma, *Gold nanoparticle decorated ceria nanotubes with significantly high catalytic activity for the reduction of nitrophenol and mechanism study*, *Applied Catalysis B: Environmental* 132-133 (2013) 107-115.

- [87] P. Wagener, A. Schwenke, S. Barcikowski, *How Citrate Ligands Affect Nanoparticle Adsorption to Microparticle Supports*, *Langmuir* 28 (2012) 6132-6140.
- [88] S. Jendrzej, B. Gökce, V. Amendola, S. Barcikowski, *Barrierless growth of precursor-free, ultrafast laser-fragmented noble metal nanoparticles by colloidal atom clusters - A kinetic in situ study*, *J. Colloid Interf. Sci.* 463 (2016) 299-307.
- [89] W. Thomson, *On the equilibrium of vapour at a curved surface of liquid*, *The London, Edinburgh, and Dublin Philosophical Magazine and Journal of Science* 42 (1871) 448-452.
- [90] R.J. Hunter, *Foundations of colloid science*, 2. ed. H1 - E31 URG1365(2)+1 ed., Oxford Univ. Press, Oxford [u.a.], 2001.
- [91] F. Tadros Tharwat, *Interfacial Phenomena and Colloid Stability, Basic Principles*, De Gruyter, Berlin/Boston, 2015.
- [92] M. Kahlweit, *Ostwald ripening of precipitates*, *Advances in Colloid and Interface Science* 5 (1975) 1-35.
- [93] B. Gökce, D.D. van't Zand, A. Menendez-Manjon, *Ripening kinetics of laser-generated plasmonic nanoparticles in different solvents*, *Chem. Phys. Lett.* 626 (2015) 96-101.
- [94] S.V. Sokolov, K. Tschulik, C. Batchelor-McAuley, K. Jurkschat, R.G. Compton, *Reversible or Not? Distinguishing Agglomeration and Aggregation at the Nanoscale*, *Analytical Chemistry* 87 (2015) 10033-10039.
- [95] T.F. Tadros, *Emulsions: Formation, Stability, Industrial Applications*, De Gruyter, 2016.
- [96] B. Derjaguin, L. Landau, *Theory of the stability of strongly charged lyophobic sols and of the adhesion of strongly charged particles in solutions of electrolytes*, *Progress in Surface Science* 43 (1993) 30-59.
- [97] E.J.W. Verwey, J.T.G. Overbeek, K. van Nes, *Theory of the Stability of Lyophobic Colloids: The Interaction of Sol Particles Having an Electric Double Layer*, Elsevier Publishing Company, 1948.
- [98] S. Barcikowski, G. Compagnini, *Advanced nanoparticle generation and excitation by lasers in liquids*, *Phys. Chem. Chem. Phys.* 15 (2013) 3022-3026.
- [99] J.-P. Sylvestre, S. Poulin, A.V. Kabashin, E. Sacher, M. Meunier, H.T. Luong, *Surface Chemistry of Gold Nanoparticles Produced by Laser Ablation in Aqueous Media*, *J. Phys. Chem. B* 108 (2004) 16864-16869.
- [100] D.C. Grahame, *The Electrical Double Layer and the Theory of Electrocapillarity*, *Chemical Reviews* 41 (1947) 441-501.
- [101] A.V. Delgado, F. González-Caballero, R.J. Hunter, L.K. Koopal, J. Lyklema, *Measurement and interpretation of electrokinetic phenomena*, *Journal of Colloid and Interface Science* 309 (2007) 194-224.
- [102] J.N. Israelachvili, *Intermolecular and surface forces*, 3. ed. ed., Elsevier [u.a.], Amsterdam [u.a.], 2011.

- [103] J. Israelachvili, H. Wennerström, *Role of hydration and water structure in biological and colloidal interactions*, Nature 379 (1996) 219.
- [104] H. Schulze, *Schwefelarsen in wässriger Lösung*, Journal für Praktische Chemie 25 (1882) 431-452.
- [105] W.B. Hardy, *A Preliminary Investigation of the Conditions which Determine the Stability of Irreversible Hydrosols*, The Journal of Physical Chemistry 4 (1899) 235-253.
- [106] D.H. Napper, *Flocculation studies of sterically stabilized dispersions*, Journal of Colloid and Interface Science 32 (1970) 106-114.
- [107] J.V. Dawkins, G. Taylor, *Flocculation studies of non-aqueous poly(methyl methacrylate) dispersions stabilized by AB block copolymers of polystyrene and poly(dimethyl siloxane)*, Colloid and Polymer Science 258 (1980) 79-84.
- [108] M.D. Croucher, M.L. Hair, *Effect of free volume on the steric stabilization of nonaqueous latex dispersions*, Journal of Colloid and Interface Science 81 (1981) 257-265.
- [109] P.J. Flory, *Principles of polymer chemistry*, 14. print. H1 - E31 UWA2222 ed., Cornell Univ. Pr., Ithaca [u.a.], 1990.
- [110] S. Asakura, F. Oosawa, *On Interaction between Two Bodies Immersed in a Solution of Macromolecules*, The Journal of Chemical Physics 22 (1954) 1255-1256.
- [111] L.M. Liz-Marzán, *Tailoring Surface Plasmons through the Morphology and Assembly of Metal Nanoparticles*, Langmuir 22 (2006) 32-41.
- [112] P. Mulvaney, *Surface Plasmon Spectroscopy of Nanosized Metal Particles*, Langmuir 12 (1996) 788-800.
- [113] V. Myroshnychenko, J. Rodriguez-Fernandez, I. Pastoriza-Santos, A.M. Funston, C. Novo, P. Mulvaney, L.M. Liz-Marzán, F.J. Garcia de Abajo, *Modelling the optical response of gold nanoparticles*, Chemical Society Reviews 37 (2008) 1792-1805.
- [114] K.A. Willets, R.P. Van Duyne, *Localized Surface Plasmon Resonance Spectroscopy and Sensing*, Annual Review of Physical Chemistry 58 (2007) 267-297.
- [115] P.B. Johnson, R.W. Christy, *Optical Constants of the Noble Metals*, Physical Review B 6 (1972) 4370-4379.
- [116] G. Mie, *Beiträge zur Optik trüber Medien, speziell kolloidaler Metallösungen*, Ann. Phys. 25 (1908) 377-445.
- [117] P.K. Jain, X. Huang, I.H. El-Sayed, M.A. El-Sayed, *Review of Some Interesting Surface Plasmon Resonance-enhanced Properties of Noble Metal Nanoparticles and Their Applications to Biosystems*, Plasmonics 2 (2007) 107-118.
- [118] V. Amendola, M. Meneghetti, *Size Evaluation of Gold Nanoparticles by UV-vis Spectroscopy*, J. Phys. Chem. C 113 (2009) 4277-4285.

- [119] H. Kuwata, H. Tamaru, K. Esumi, K. Miyano, *Resonant light scattering from metal nanoparticles: Practical analysis beyond Rayleigh approximation*, Applied Physics Letters 83 (2003) 4625-4627.
- [120] H.A. Wheeler, *Formulas for the Skin Effect*, Proceedings of the IRE 30 (1942) 412-424.
- [121] U. Kreibig, M. Vollmer, *Optical properties of metal clusters*, Springer, Berlin [u.a.], 1995.
- [122] J. Pérez-Juste, I. Pastoriza-Santos, L.M. Liz-Marzán, P. Mulvaney, *Gold nanorods: Synthesis, characterization and applications*, Coordination Chemistry Reviews 249 (2005) 1870-1901.
- [123] V. Amendola, M. Meneghetti, *Controlled size manipulation of free gold nanoparticles by laser irradiation and their facile bioconjugation*, Journal of Materials Chemistry 17 (2007) 4705-4710.
- [124] H. Wang, A. Pyatenko, K. Kawaguchi, X. Li, Z. Swiatkowska-Warkocka, N. Koshizaki, *Selective Pulsed Heating for the Synthesis of Semiconductor and Metal Submicrometer Spheres*, Angewandte Chemie International Edition 49 (2010) 6361-6364.
- [125] T. Tsuji, T. Yahata, M. Yasutomo, K. Igawa, M. Tsuji, Y. Ishikawa, N. Koshizaki, *Preparation and investigation of the formation mechanism of submicron-sized spherical particles of gold using laser ablation and laser irradiation in liquids*, Physical Chemistry Chemical Physics 15 (2013) 3099-3107.
- [126] F. Mafuné, J.Y. Kohno, Y. Takeda, T. Kondow, H. Sawabe, *Formation and Size Control of Silver Nanoparticles by Laser Ablation in Aqueous Solution*, J. Phys. Chem. B 109(34) (2000) 9111-9117.
- [127] F. Mafuné, J.-y. Kohno, Y. Takeda, T. Kondow, H. Sawabe, *Formation of Gold Nanoparticles by Laser Ablation in Aqueous Solution of Surfactant*, The Journal of Physical Chemistry B 105 (2001) 5114-5120.
- [128] H. Usui, Y. Shimizu, T. Sasaki, N. Koshizaki, *Photoluminescence of ZnO nanoparticles prepared by laser ablation in different surfactant solutions*, J. Phys. Chem. B 109 (1) (2005) 120-124.
- [129] M. Zahid Hussain, R. Khan, R. Ali, Y. Khan, *Optical properties of laser ablated ZnO nanoparticles prepared with Tween-80*, Materials Letters 122 (2014) 147-150.
- [130] R. Singh, R.K. Soni, *Laser synthesis of aluminium nanoparticles in biocompatible polymer solutions*, Applied Physics A 116 (2014) 689-701.
- [131] S. Besner, A.V. Kabashin, F.M. Winnik, M. Meunier, *Synthesis of Size-Tunable Polymer-Protected Gold Nanoparticles by Femtosecond Laser-Based Ablation and Seed Growth*, The Journal of Physical Chemistry C 113 (2009) 9526-9531.
- [132] T. Tsuji, M. Nakanishi, T. Mizuki, S. Ozono, M. Tsuji, Y. Tsuboi, *Preparation and Shape-Modification of Silver Colloids by Laser Ablation in Liquids: A Brief Review*, Sci. Adv. Mater. 4 (2012) 391-400.
- [133] W. Qian, M. Murakami, Y. Ichikawa, Y. Che, *Highly Efficient and Controllable PEGylation of Gold Nanoparticles Prepared by Femtosecond Laser Ablation in Water*, The Journal of Physical Chemistry C 115 (2011) 23293-23298.

- [134] S. Petersen, S. Barcikowski, *In Situ Bioconjugation: Single Step Approach to Tailored Nanoparticle-Bioconjugates by Ultrashort Pulsed Laser Ablation*, *Adv. Funct. Mater.* 19 (2009) 1167-1172.
- [135] R. Zamiri, B.Z. Azmi, M. Darroudi, A.R. Sadrolhosseini, M.S. Husin, A.W. Zaidan, M.A. Mahdi, *Preparation of starch stabilized silver nanoparticles with spatial self-phase modulation properties by laser ablation technique*, *Applied Physics A* 102 (2011) 189-194.
- [136] R. Zamiri, B.Z. Azmi, M.G. Naseri, H.A. Ahangar, M. Darroudi, F.K. Nazarpour, *Laser based fabrication of chitosan mediated silver nanoparticles*, *Applied Physics A* 105 (2011) 255.
- [137] A. Menéndez-Manjón, A. Schwenke, T. Steinke, M. Meyer, U. Giese, P. Wagener, S. Barcikowski, *Ligand-free gold-silver nanoparticle alloy polymer composites generated by picosecond laser ablation in liquid monomer*, *Applied Physics A* 110 (2013) 343-350.
- [138] L.P. Evie, I. Romuald, S. Alice, R. Marina, S.B. Ilker, A. Athanassia, *Nanocomposite fabrication via direct ultra-fast laser ablation of titanium in aqueous monomer solution*, *Laser Physics Letters* 12 (2015) 125601.
- [139] M. Delmée, G. Mertz, J. Bardon, A. Marguier, L. Ploux, V. Roucoules, D. Ruch, *Laser Ablation of Silver in Liquid Organic Monomer: Influence of Experimental Parameters on the Synthesized Silver Nanoparticles/Graphite Colloids*, *The Journal of Physical Chemistry B* 121 (2017) 6646-6654.
- [140] M. Lau, S. Barcikowski, *Quantification of mass-specific laser energy input converted into particle properties during picosecond pulsed laser fragmentation of zinc oxide and boron carbide in liquids*, *Appl. Surf. Sci.* 348 (2015) 22-29.
- [141] D. Amans, C. Malaterre, M. Diouf, C. Mancini, F. Chaput, G. Ledoux, G. Breton, Y. Guillin, C. Dujardin, K. Masenelli-Varlot, P. Perriat, *Synthesis of Oxide Nanoparticles by Pulsed Laser Ablation in Liquids Containing a Complexing Molecule: Impact on Size Distributions and Prepared Phases*, *J. Phys. Chem. C* 115 (2011) 5131-5139.
- [142] G. Marzun, J. Nakamura, X. Zhang, S. Barcikowski, P. Wagener, *Size control and supporting of palladium nanoparticles made by laser ablation in saline solution as a facile route to heterogeneous catalysts*, *Appl. Surf. Sci.* 348 (2015) 75-84.
- [143] K.M. Koczur, S. Mourdikoudis, L. Polavarapu, S.E. Skrabalak, *Polyvinylpyrrolidone (PVP) in nanoparticle synthesis*, *Dalton Transactions* 44 (2015) 17883-17905.
- [144] C. Sajti, A. Barchanski, P. Wagener, S. Klein, S. Barcikowski, *Delay Time and Concentration Effects During Bioconjugation of Nanosecond Laser-Generated Nanoparticles in a Liquid Flow*, *J. Phys. Chem. C* 115 (2011) 5094-5101.
- [145] C.L. Sajti, S. Petersen, A. Menéndez-Manjón, S. Barcikowski, *In-situ bioconjugation in stationary media and in liquid flow by femtosecond laser ablation*, *Appl. Phys. A* 101 (2010) 259-264.
- [146] V. Merk, C. Rehbock, F. Becker, U. Hagemann, H. Nienhaus, S. Barcikowski, *In Situ Non-DLVO Stabilization of Surfactant-Free, Plasmonic Gold Nanoparticles: Effect of Hofmeister's Anions*, *Langmuir* 30 (2014) 4213-4222.
- [147] F. Pfeiffer, M. Bech, O. Bunk, P. Kraft, E.F. Eikenberry, C. Brönnimann, C. Grünzweig, C. David, *Hard-X-ray dark-field imaging using a grating interferometer*, *Nat. Mater.* 7 (2008) 134-137.

- [148] S. Reich, T.d.S. Rolo, A. Letzel, T. Baumbach, A. Plech, *Scalable, large area compound array refractive lens for hard X-rays*, Applied Physics Letters 112 (2018) 151903.
- [149] A. Plech, S. Kürbitz, K.J. Berg, H. Graener, G. Berg, S. Grésillon, M. Kaempfe, J. Feldmann, M. Wulff, G.v. Plessen, *Time-resolved X-ray diffraction on laser-excited metal nanoparticles*, EPL (Europhysics Letters) 61 (2003) 762.
- [150] A. Plech, V. Kotaidis, M. Lorenc, J. Boneberg, *Femtosecond laser near-field ablation from gold nanoparticles*, Nature Physics 2 (2005) 44.
- [151] A. Plech, V. Kotaidis, M. Lorenc, M. Wulff, *Thermal dynamics in laser excited metal nanoparticles*, Chemical Physics Letters 401 (2005) 565-569.
- [152] M. Bremholm, H. Jensen, S.B. Iversen, B.B. Iversen, *Reactor design for in situ X-ray scattering studies of nanoparticle formation in supercritical water syntheses*, The Journal of Supercritical Fluids 44 (2008) 385-390.
- [153] J. Polte, R. Erlen, A.F. Thünemann, S. Sokolov, T.T. Ahner, K. Rademann, F. Emmerling, R. Kraehnert, *Nucleation and Growth of Gold Nanoparticles Studied via in situ Small Angle X-ray Scattering at Millisecond Time Resolution*, ACS Nano 4 (2010) 1076-1082.
- [154] T. Li, A.J. Senesi, B. Lee, *Small Angle X-ray Scattering for Nanoparticle Research*, Chemical Reviews 116 (2016) 11128-11180.
- [155] H.-D. Dörfler, *Grenzflächen und kolloid-disperse Systeme : Physik und Chemie*, Springer, Berlin [u.a.], 2002.
- [156] A. Guinier, G. Fournet, *Small-angle scattering of X-rays*, Wiley, New York, 1955.
- [157] J.S. Pedersen, *Determination of size distribution from small-angle scattering data for systems with effective hard-sphere interactions*, Journal of Applied Crystallography 27 (1994) 595-608.
- [158] M. Harada, K. Kuramitsu, Y. Kimura, K. Saijo, *In situ observation of formation of silver particles in water-in-scCO<sub>2</sub> emulsions*, Colloids and Surfaces A: Physicochemical and Engineering Aspects 327 (2008) 21-33.
- [159] H. Borchert, E.V. Shevchenko, A. Robert, I. Mekis, A. Kornowski, G. Grübel, H. Weller, *Determination of Nanocrystal Sizes: A Comparison of TEM, SAXS, and XRD Studies of Highly Monodisperse CoPt<sub>3</sub> Particles*, Langmuir 21 (2005) 1931-1936.
- [160] A.F. Thünemann, I. Kegel, J. Polte, F. Emmerling, *Superparamagnetic Maghemite Nanorods: Analysis by Coupling Field-Flow Fractionation and Small-Angle X-ray Scattering*, Anal. Chem. 80 (2008) 5905-5911.
- [161] G. Beaucage, *Approximations Leading to a Unified Exponential/Power-Law Approach to Small-Angle Scattering*, J. Appl. Cryst. 28 (1995) 717-728.
- [162] M. Sztucki, T. Narayanan, G. Beaucage, *In situ study of aggregation of soot particles in an acetylene flame by small-angle x-ray scattering* J. Appl. Phys. 101 (2007) 114304.
- [163] G. Beaucage, H.K. Kammler, S.E. Pratsinis, *Particle size distributions from small-angle scattering using global scattering functions*, J. Appl. Cryst. 34 (2004) 532-535.

- [164] B.R. Pauw, J.S. Pedersen, S. Tardif, M. Takata, B.B. Iversen, *Improvements and considerations for size distribution retrieval from small-angle scattering data by Monte Carlo methods*, J. Appl. Cryst. 46 (2013) 365-371.
- [165] I. Bressler, B.R. Pauw, A.F. Thünemann, *McSAS: software for the retrieval of model parameter distributions from scattering patterns*, J. Appl. Cryst. 48 (2015) 962-969.
- [166] O. Kratky, G. Porod, *Zur Kleinwinkelstreuung der Cellulose (Der Lorentzfaktor in seiner Bedeutung für die Streuung parallelepipedischer Körper)*, Zeitschrift für Elektrochemie, Berichte der Bunsengesellschaft für physikalische Chemie 58 (1954) 918-923.
- [167] S. Ibrahimkutty, J. Kim, M. Cammarata, F. Ewald, J. Choi, H. Ihee, A. Plech, *Ultrafast Structural Dynamics of the Photocleavage of Protein Hybrid Nanoparticles*, ACS Nano 5 (2011) 3788-3794.
- [168] A. Lak, A.F. Thünemann, M. Schilling, F. Ludwig, *Resolving particle size modality in bi-modal iron oxide nanoparticle suspensions*, J. Magn. Magn. Mater. 380 (2015) 140-143.
- [169] A. Letzel, B. Gökce, A. Menzel, A. Plech, S. Barcikowski, *Primary particle diameter differentiation and bimodality identification by five analytical methods using gold nanoparticle size distributions synthesized by pulsed laser ablation in liquids*, Appl. Surf. Sci. 435 (2018) 743-751.
- [170] J.L. Heinrich, C.L. Curtis, G.M. Credo, K.L. Kavanagh, M.J. Sailor, *Luminescent colloidal silicon suspensions from porous silicon*, Science 255 (1992) 66-68.
- [171] K.L. Kelly, E. Coronado, L.L. Zhao, G.C. Schatz, *The Optical Properties of Metal Nanoparticles: The Influence of Size, Shape, and Dielectric Environment*, J. Phys. Chem. B 107 (2003) 668-677.
- [172] M. Escobar Castillo, V.V. Shvartsman, D. Gobeljic, Y. Gao, J. Landers, H. Wende, D. Lupascu, *Effect of particle size on ferroelectric and magnetic properties of BiFeO<sub>3</sub> nanopowders*, Nanotechnology 24 (2013) 355701.
- [173] B.R. Saunders, *Hybrid polymer/nanoparticle solar cells: Preparation, principles and challenges*, J. Colloid. Interface Sci. 369 (2012) 1-15.
- [174] T.J. Park, G.C. Papaefthymiou, A.J. Viescas, A.R. Moodenbaugh, S.S. Wong, *Size-Dependent Magnetic Properties of Single-Crystalline Multiferroic BiFeO<sub>3</sub> Nanoparticles*, Nano. Lett. 7 (2007) 766-772.
- [175] A.H. Lu, E.L. Salabas, F. Schüth, *Magnetic nanoparticles: synthesis, protection, functionalization, and application*, Angew. Chem. Int. Ed. 46 (2007) 1222-1244.
- [176] J.D. Blakemore, H.B. Gray, J.R. Winkler, A.M. Müller, *Co<sub>3</sub>O<sub>4</sub> Nanoparticle Water-Oxidation Catalysts Made by Pulsed-Laser Ablation in Liquids*, ACS Catal. 3 (2013) 2479-2500.
- [177] K. Fominykh, P. Chernev, I. Zaharieva, J. Sicklinger, G. Stefanic, M. Dobliger, A. Müller, A. Pokharel, S. Böcklein, C. Scheu, T. Bein, D. Fattakova-Rohlfing, *Iron-Doped Nickel Oxide Nanocrystals as Highly Efficient Electrocatalysts for Alkaline Water Splitting*, ACS Nano 9 (2015) 5180-5188.
- [178] L. Zhang, R. He, H.C. Gu, *Oleic acid coating on the monodisperse magnetite nanoparticles*, Appl. Surf. Sci. 253 (2006) 2611-2617.

- [179] B.A. Korgel, H.G. Monbouquette, *Synthesis of Size-Monodisperse CdS Nanocrystals Using Phosphatidylcholine Vesicles as True Reaction Compartments*, *J. Phys. Chem.* 100 (1996) 346-351.
- [180] A. Taleb, C. Petit, M.P. Pileni, *Synthesis of Highly Monodisperse Silver Nanoparticles from AOT Reverse Micelles: A Way to 2D and 3D Self-Organization*, *Chem. Mater.* 9 (1997) 950-959.
- [181] U. Taylor, D. Tiedemann, C. Rehbock, W.A. Kues, S. Barcikowski, D. Rath, *Influence of Gold, Silver and Gold-Silver Alloy Nanoparticles on Germ Cell Function and Embryo Development*, *Beilstein J. Nanotechnol.* 6 (2015) 651-664.
- [182] T. Baat, A. Al-Kattan, M.-A. Esteve, L. Njim, Y. Ryabchikov, F. Chaspoul, M. Hammami, M. Sentis, A.V. Kabashin, D. Braguer, *Ultrapure Laser-Synthesized Si-Based Nanomaterials for Biomedical Applications of Safety and Biodistribution*, *Sci. Rep.* 6 (2016) 25400.
- [183] K.P. Tamarov, L.A. Osminkina, S.V. Zinoviyev, K.A. Maximova, J.V. Kargina, M.B. Gongalsky, Y. Ryabchikov, A. Al-Kattan, A.P. Sviridov, *Radio Frequency Radiation-Induced Hyperthermia Using Si Nanoparticle-Based Sensitizers for Mild Cancer Therapy*, *Sci. Rep.* 4 (2014) 7034.
- [184] S. Hu, G. Goenaga, C. Melton, T.A. Zawodzinski, D. Mukherjee, *PtCo/CoOx nanocomposites: Bifunctional electrocatalysts for oxygen reduction and evolution reactions synthesized via tandem laser ablation synthesis in solution-galvanic replacement reactions*, *Appl. Catal. B-Environ.* 182 (2016) 286-296.
- [185] S. Gu, J. Kaiser, G. Marzun, A. Ott, Y. Lu, M. Ballauff, A. Zaccone, S. Barcikowski, P. Wagener, *Ligand-free Gold Nanoparticles as a Reference Material for Kinetik Modelling of Catalytic Reduction of 4-Nitrophenol*, *Catal. Lett.* 145 (2015) 1105-1112.
- [186] A. Henglein, *Physicochemical Properties of Small Metal Particles in Solution: "Microelectrode" Reactions, Chemisorption, Composite Metal Particles, and the Atom-to-Metal Transition*, *J. Phys. Chem.* 97 (1993) 5457-5471.
- [187] R. Streubel, G. Bendt, B. Gökce, *Pilot-scale synthesis of metal nanoparticles by high-speed pulsed laser ablation in liquids*, *Nanotechnology* 27 (2016) 205602.
- [188] R. Streubel, S. Barcikowski, B. Gökce, *Continuous multigram nanoparticle synthesis by high-power, high-repetition-rate ultrafast laser ablation in liquids*, *Opt. Lett.* 41 (2016) 1486-1489.
- [189] V. Amendola, P. Riello, M. Meneghetti, *Magnetic Nanoparticles of Iron Carbide, Iron Oxide, Iron@Iron Oxide, and Metal Iron Synthesized by Laser Ablation in Organic Solvents*, *J. Phys. Chem. C* 115 (2011) 5140-5146.
- [190] K.D. Malviya, K. Chattopadhyay, *Synthesis and Mechanism of Composition and Size Dependent Morphology Selection in Nanoparticles of Ag-Cu Alloys Processed by Laser Ablation Under Liquid Medium*, *J. Phys. Chem. C* 118 (2014) 13228-13237.
- [191] D. Zhang, Z. Ma, M. Spasova, A.E. Yelsukowa, S. Lu, M. Farle, U. Wiedwald, B. Gökce, *Formation Mechanism of Laser-Synthesized Iron-Manganese Alloy Nanoparticles, Manganese Oxide Nanosheets and Nanofibers*, *Part. Part. Syst. Charact.* 34 (2016) 1600225.
- [192] A. Letzel, B. Gökce, P. Wagener, S. Ibrahimkutty, A. Menzel, A. Plech, S. Barcikowski, *Size Quenching during Laser Synthesis of Colloids Happens Already in the Vapor Phase of the Cavitation Bubble*, *J. Phys. Chem. C* 121 (2017) 5359-5365.

- [193] H. Lange, *Comparative Test on Methods to Determine Particle Size and Particle Size Distribution in the Submicron Range*, Part. Part. Syst. Charact. 12 (1995) 148-157.
- [194] T.V. Shahbazyan, I.E. Perakis, *Size-Dependent Surface Plasmon Dynamics in Metal Nanoparticles*, Phys. Rev. Lett. 81 (1998) 3120-3123.
- [195] J.P. Sylvestre, S. Poulin, A.V. Kabashin, E. Sacher, M. Meunier, H.T. Luong, *Surface Chemistry of Gold Nanoparticles Produced by Laser Ablation in Aqueous Media*, J. Phys. Chem. B 108 (2004) 16864-16869.
- [196] M. Fischer, J. Hormes, G. Marzun, P. Wagener, U. Hagemann, S. Barcikowski, *In Situ Investigations of Laser-Generated Ligand-Free Platinum Nanoparticles by X-ray Absorption Spectroscopy: How Does the Immediate Environment Influence the Particle Surface?*, Langmuir 32 (2016) 8793-8802.
- [197] T. Zheng, S. Bott, Q. Huo, *Techniques for Accurate Sizing of Gold Nanoparticles Using Dynamic Light Scattering With Particular Application to Chemical and Biological Sensing Based on Aggregate Formation* ACS Appl. Mater. Interfaces 8 (2016) 21585-21594.
- [198] T. Rieker, A. Hanprasopwattana, A. Datye, P. Hubbard, *Particle Size Distribution Inferred from Small-Angle X-ray Scattering and Transmission Electron Microscopy*, Langmuir 15 (1999) 638-641.
- [199] Y. Dieckermann, H. Cölfen, H. Hofmann, A. Petri-Fink, *Particle Size Distribution Measurements of Manganese-Doped ZnS Nanoparticles*, Anal. Chem. 81 (2009) 3889-3895.
- [200] V. Goertz, N. Dingenouts, H. Nirschl, *Comparison of Nanometric Particle Size Distributions as Determined by SAXS, TEM and Analytical Ultracentrifuge*, Part. Part. Syst. Charact. 26 (2009) 17-24.
- [201] S. Pabisch, B. Feichtenschlager, G. Kickelbick, H. Peterlik, *Effect of interparticle interactions on size determination of zirconia and silica based systems – A comparison of SAXS, DLS, BET, XRD and TEM*, Chem. Phys. Lett. 521 (2012) 91-97.
- [202] A. Singh, J. Vihinen, E. Frankberg, L. Hyvärinen, M. Honkanen, E. Levänen, *Pulsed Laser Ablation-Induced Green Synthesis of TiO<sub>2</sub> Nanoparticles and Application of Novel Small Angle X-Ray Scattering Technique for Nanoparticle Size and Size Distribution Analysis*, Nanoscale Res. Lett. (2016) 11:447.
- [203] I. Perevyazko, A. Vollrath, S. Hornig, G.M. Pavlov, U.S. Schubert, *Characterization of poly(methyl methacrylate) nanoparticles prepared by nanoprecipitation using analytical ultracentrifugation, dynamic light scattering, and scanning electron microscopy*, J. Polym. Sci. Pol. Chem. 48 (2010) 3924-3931.
- [204] P. Eaton, P. Quaresma, C. Soares, C. Neves, M.P. de Almeida, E. Pereira, P. West, *A Direct Comparison of Experimental Methods to Measure Dimensions of Synthetic Nanoparticles*, Ultramicroscopy (2017)
- [205] A.F. Thünemann, S. Rolf, P. Knappe, S. Weidner, *In situ analysis of a bimodal size distribution of superparamagnetic nanoparticles*, Anal. Chem. 81 (2009) 296-301.
- [206] Å.K. Jamting, J. Cullen, M. Lawn, J. Hermann, J. Miles, M.J. Ford, *Systematic study of bimodal suspensions of latex nanoparticles using dynamic light scattering*, Adv. Powder Tech. 22 (2011) 290-293.

- [207] R. Bienert, F. Emmerling, A.F. Thünemann, *The size distribution of 'gold standard' nanoparticles*, Anal. Bioanal. Chem. 395 (2009) 1651-1660.
- [208] T. Wagner, M. Wiemann, I. Schmitz, H.G. Lipinski, *A Cluster-Based Method for Improving Analysis of Polydisperse Particle Size Distributions Obtained by Nanoparticle Tracking*, J. Nanoparticles 2013 (2013) 936150.
- [209] V. Kestens, G. Roebben, J. Hermann, Å. Jämting, V. Coleman, C. Minelli, C. Clifford, P.-J. De Temmerman, J. Mast, L. Junjie, F. Babick, H. Cölfen, H. Emons, *Challenges in the size analysis of a silica nanoparticle mixture as candidate certified reference material*, J. Nanopart. Res. 18 (2016) 171.
- [210] I. Bressler, B.R. Pauw, A.F. Thünemann, *SASfit: a tool for small-angle scattering data analysis using a library of analytical expressions*, J. Appl. Cryst. 46 (2015) 962-969.
- [211] T. Schmitz, U. Wiedwald, C. Dubs, B. Gökce, *Ultrasmall yttrium iron garnet nanoparticles with high coercivity at low temperature synthesized by laser ablation and fragmentation of pressed powder*, ChemPhysChem 18 (2017) 1125-1132.
- [212] A. Siems, S.A.L. Weber, J. Boneberg, A. Plech, *Thermodynamics of nanosecond nanobubble formation at laser-excited metal nanoparticles*, New J. Phys. 13 (2011) 043018.
- [213] S.W. Provencher, *Inverse problems in polymer characterization: Direct analysis of polydispersity with photon correlation spectroscopy*, Makromol. Chem. 180 (1979) 201-209.
- [214] S. Eustis, M.A. El-Sayed, *Why gold nanoparticles are more precious than pretty gold: Noble metal surface plasmon resonance and its enhancement of the radiative and nonradiative properties of nanocrystals of different shapes*, Chem. Soc. Rev. 35 (2006) 209-217.
- [215] C.B. Murray, C.R. Kagan, M.G. Bawendi, *Synthesis and Characterization of Monodisperse Nanocrystals and Close-Packed Nanocrystal Assemblies*, Annu. Rev. Mater. Sci. 30 (2000) 545-610.
- [216] W. Haiss, N.T.K. Thanh, J. Aveyard, D.G. Fernig, *Determination of Size and Concentration of Gold Nanoparticles from UV-Vis Spectra*, Anal. Chem. 79 (2007) 4215-4221.
- [217] D. Zhang, J. Liu, P. Li, Z. Tian, C. Liang, *Recent Advances in Surfactant-Free, Surface-Charged, and Defect-Rich Catalysts Developed by Laser Ablation and Processing in Liquids*, ChemNanoMat 3 (2017) 512-533.
- [218] M. Rodio, L. Coluccino, E. Romeo, A. Genovese, A. Diaspro, G. Garau, R. Intartaglia, *Facile fabrication of bioactive ultra-small protein-hydroxyapatite nanoconjugates via liquid-phase laser ablation and their enhanced osteogenic differentiation activity*, Journal of Materials Chemistry B 5 (2017) 279-288.
- [219] M. Muniz-Miranda, C. Gellini, E. Giorgetti, *Surface-Enhanced Raman Scattering from Copper Nanoparticles Obtained by Laser Ablation*, J. Phys. Chem. C 115 (2011) 5021-5027.
- [220] A. De Giacomo, J. Hermann, *Laser-induced plasma emission: from atomic to molecular spectra*, J. Phys. D: Appl. Phys. 50 (2017) 183002.
- [221] T. Tsuji, Y. Tsuboi, N. Kitamura, M. Tsuji, *Microsecond-resolved imaging of laser ablation at solid-liquid interface: investigation of formation process of nano-size metal colloids*, Appl. Surf. Sci. 229 (2004) 365-371.

- [222] P. Wagener, A. Schwenke, B.N. Chichkov, S. Barcikowski, *Pulsed Laser Ablation of Zinc in Tetrahydrofuran: Bypassing the Cavitation Bubble*, J. Phys. Chem. C 114 (2010) 7618-7625.
- [223] A.S. Nikolov, I.I. Balchev, N.N. Nedyalkov, I.K. Kostadinov, D.B. Karashanova, G.B. Atanasova, *Influence of the laser pulse repetition rate and scanning speed on the morphology of Ag nanostructures fabricated by pulsed laser ablation of solid target in water*, Applied Physics A 123 (2017) 719.
- [224] S. Hu, C. Melton, D. Mukherjee, *A facile route for the synthesis of nanostructured oxides and hydroxides of cobalt using laser ablation synthesis in solution (LASIS)*, Physical Chemistry Chemical Physics 16 (2014) 24034-24044.
- [225] S. Kohsakowski, A. Santagata, M. Dell'Aglio, A. de Giacomo, S. Barcikowski, P. Wagener, B. Gökce, *High productive and continuous nanoparticle fabrication by laser ablation of a wire-target in a liquid jet*, Applied Surface Science 403 (2017) 487-499.
- [226] J. Lam, D. Amans, F. Chaput, M. Diouf, G. Ledoux, N. Mary, K. Masenelli-Varlot, V. Motto-Ros, C. Dujardin,  *$\gamma$ -Al<sub>2</sub>O<sub>3</sub> nanoparticles synthesised by pulsed laser ablation in liquids: a plasma analysis*, Phys. Chem. Chem. Phys. 16 (2014) 963-973.
- [227] M.-R. Kalus, N. Bärsch, R. Streubel, E. Gökce, S. Barcikowski, B. Gökce, *How persistent microbubbles shield nanoparticle productivity in laser synthesis of colloids – quantification of their volume, dwell dynamics, and gas composition*, Phys. Chem. Chem. Phys. 19 (2017) 7112-7123.
- [228] A. Baladi, R. Sarraf Mamoori, *Investigation of different liquid media and ablation times on pulsed laser ablation synthesis of aluminum nanoparticles*, Applied Surface Science 256 (2010) 7559-7564.
- [229] R.P. Carney, J.Y. Kim, H. Qian, R. Jin, H. Mehenni, F. Stellacci, O.M. Bakr, *Determination of nanoparticle size distribution together with density or molecular weight by 2D analytical ultracentrifugation*, Nature Communications 2 (2011) 335.
- [230] S. Barcikowski, A. Menendez-Manjon, B. Chichkov, *Generation of nanoparticle colloids by picosecond and femtosecond laser ablations in liquid flow*, Applied Physics Letters 91 (2007) 083113.
- [231] S. Barcikowski, V. Amendola, G. Marzun, C. Rehbock, S. Reichenberger, D. Zhang, B. Gökce, *Handbook of Laser Synthesis of Colloids* DuEPublico, 2016.
- [232] A. De Bonis, T. Lovaglio, A. Galasso, A. Santagata, R. Teghil, *Iron and iron oxide nanoparticles obtained by ultra-short laser ablation in liquid*, Applied Surface Science 353 (2015) 433-438.
- [233] A.V. Kabashin, M. Meunier, *Synthesis of colloidal nanoparticles during femtosecond laser ablation of gold in water*, Journal of Applied Physics 94 (2003) 7941-7943.
- [234] M. Dell'Aglio, A. De Giacomo, S. Kohsakowski, S. Barcikowski, P. Wagener, A. Santagata, *Pulsed laser ablation of wire-shaped target in a thin water jet: effects of plasma features and bubble dynamics on the PLAL process*, J. Phys. D Appl. Phys. 50 (2017) 185204.
- [235] R.-G. Amandine, B. Yann, N. Aotmane En, C. Nouari, *Interaction of a converging laser beam with a Ag colloidal solution during the ablation of a Ag target in water*, Nanotechnology 27 (2016) 215705.

- [236] A. Resano-Garcia, S. Champmartin, Y. Battie, A. Koch, A. En Naciri, A. Ambari, N. Chaoui, *Highly-repeatable generation of very small nanoparticles by pulsed-laser ablation in liquids of a high-speed rotating target*, *Physical Chemistry Chemical Physics* 18 (2016) 32868-32875.
- [237] W.C. Hinds, *Aerosol technology : properties, behavior, and measurement of airborne particles*, 2. ed., Wiley, New York, 1999.
- [238] R. Streubel, S. Barcikowski, B. Gökce, *Continuous multigram nanoparticle synthesis by high-power, high-repetition-rate ultrafast laser ablation in liquids*, *Opt. Lett.* 41 (2016) 1489-1489.
- [239] T.V. Kononenko, V.I. Konov, S.V. Garnov, S.M. Klimentov, F. Dausinger, *Dynamics of Deep Short Pulse Laser Drilling: Ablative Stages and Light Propagation*, *Laser Phys.* 11 (2001) 343-351.
- [240] M. Stafe, C. Negutu, I.M. Popescu, *Theoretical determination of the ablation rate of metals in multiple-nanosecond laser pulses irradiation regime*, *Applied Surface Science* 253 (2007) 6353-6358.
- [241] M. Stafe, C. Negutu, I.M. Popescu, *Combined experimental and theoretical investigation of multiple-nanosecond laser ablation of metals*, 2006.
- [242] C.L. Sajti, R. Sattari, B.N. Chichkov, S. Barcikowski, *Gram Scale Synthesis of Pure Ceramic Nanoparticles by Laser Ablation in Liquid*, *The Journal of Physical Chemistry C* 114 (2010) 2421-2427.
- [243] T.T.P. Nguyen, R. Tanabe, Y. Ito, *Effects of an absorptive coating on the dynamics of underwater laser-induced shock process*, *Applied Physics A* 116 (2014) 1109-1117.
- [244] M.H. Mahdieh, M. Nikbakht, Z. Eghlimi Moghadam, M. Sobhani, *Crater geometry characterization of Al targets irradiated by single pulse and pulse trains of Nd:YAG laser in ambient air and water*, *Applied Surface Science* 256 (2010) 1778-1783.
- [245] M. Dell'Aglio, A. Santagata, G. Valenza, A. De Stradis, A. De Giacomo, *Study of the Effect of Water Pressure on Plasma and Cavitation Bubble Induced by Pulsed Laser Ablation in Liquid of Silver and Missed Variations of Observable Nanoparticle Features*, *ChemPhysChem* 18 (2017) 1165-1174.
- [246] C. Petit, P. Lixon, M.P. Pileni, *In situ synthesis of silver nanocluster in AOT reverse micelles*, *The Journal of Physical Chemistry* 97 (1993) 12974-12983.
- [247] Y. Liu, K. Ai, X. Cheng, L. Huo, L. Lu, *Gold-Nanocluster-Based Fluorescent Sensors for Highly Sensitive and Selective Detection of Cyanide in Water*, *Advanced Functional Materials* 20 (2010) 951-956.
- [248] I. Chakraborty, T. Pradeep, *Atomically Precise Clusters of Noble Metals: Emerging Link between Atoms and Nanoparticles*, *Chemical Reviews* 117 (2017) 8208-8271.
- [249] M. Lau, I. Haxhijaj, P. Wagener, R. Intartaglia, F. Brandi, J. Nakamura, S. Barcikowski, *Ligand-free gold atom clusters adsorbed on graphene nano sheets generated by oxidative laser fragmentation in water*, *Chemical Physics Letters* 610-611 (2014) 256-260.
- [250] T. Nishi, Y. Akimoto, N. Takahasi, K. Kitazumi, S. Kajiyu, Y. Watanabe, *Novel method for Ag colloidal cluster formation by laser ablation at the air-liquid interface*, *Jpn. J. Appl. Phys.* 54 (2015) 095002.

- [251] R.D. Glover, J.M. Miller, J.E. Hutchison, *Generation of Metal Nanoparticles from Silver and Copper Objects: Nanoparticle Dynamics on Surfaces and Potential Sources of Nanoparticles in the Environment*, ACS Nano 5 (2011) 8950-8957.
- [252] N. Lasemi, U. Pacher, L.V. Zhigilei, O. Bomati-Miguel, R. Lahoz, W. Kautek, *Pulsed laser ablation and incubation of nickel, iron and tungsten in liquids and air*, Applied Surface Science 433 (2018) 772-779.
- [253] S. Hashimoto, D. Werner, T. Uwada, *Studies on the interaction of pulsed lasers with plasmonic gold nanoparticles toward light manipulation, heat management, and nanofabrication*, Journal of Photochemistry and Photobiology C: Photochemistry Reviews 13 (2012) 28-54.
- [254] A. Takami, H. Kurita, S. Koda, *Laser-Induced Size Reduction of Noble Metal Particles*, J. Phys. Chem. B 103 (1999) 1226-1232.
- [255] A. Letzel, S. Reich, T. dos Santos Rolo, A. Kanitz, J. Hoppius, A. Rack, M. Olbinado, A. Ostendorf, B. Gökce, A. Plech, S. Barcikowski, *Time and Mechanism of Nanoparticle Functionalization by Macromolecular Ligands during Pulsed Laser Ablation in Liquids*, Langmuir 35 (2019) 3038-3047.
- [256] L. Yang, P.W. May, L. Yin, R. Brown, T.B. Scott, *Direct Growth of Highly Organized Crystalline Carbon Nitride from Liquid-Phase Pulsed Laser Ablation*, Chem. Mater. 18 (2006) 5058-5064.
- [257] H. Zeng, X.W. Du, S.C. Singh, S.A. Kulinich, S. Yang, J. He, W. Cai, *Nanomaterials via Laser Ablation/Irradiation in Liquid: A Review*, Adv. Funct. Mater. 22 (2012) 1333-1353.
- [258] V. Amendola, M. Meneghetti, *What controls the composition and the structure of nanomaterials generated by laser ablation in liquid solution?*, Phys. Chem. Chem. Phys. 15 (2013) 3027-3046.
- [259] Z. Yan, D.B. Chrisey, *Pulsed laser ablation in liquid for micro-/nanostructure generation*, J. Photochem. Photobiol. C 13 (2012) 204-223.
- [260] M. Nath, C.N.R. Rao, R. Albu-Yaron, R. Tenne, *Nanoparticles Produced by Laser Ablation of HfS<sub>3</sub> in Liquid Medium: Inorganic Fullerene-Like Structures of Hf<sub>2</sub>S*, Chem. Mater. 16 (2004) 2238-2243.
- [261] J.P. Sylvestre, A.V. Kabashin, E. Sacher, M. Meunier, J.H.T. Luong, *Stabilization and Size Control of Gold Nanoparticles during Laser Ablation in Aqueous Cyclodextrins*, J. Am. Chem. Soc. 126 (2004) 7176-7177.
- [262] G. Compagnini, A.A. Scalisi, O. Puglisi, C. Spinella, *Synthesis of gold colloids by laser ablation in thiol-alkane solutions*, J. Mater. Res. 19 (2004) 2795-2798.
- [263] S. Petersen, S. Barcikowski, *Conjugation Efficiency of Laser-Based Bioconjugation of Gold Nanoparticles with Nucleic Acids*, J. Phys. Chem. C 113 (2009) 19830-19835.
- [264] A. Barchanski, L. Sajti, C. Sehring, S. Petersen, S. Barcikowski, *Design of Bi-functional Bioconjugated Gold Nanoparticles by Pulsed Laser Ablation with Minimized Degradation*, J. Laser Micro/Nanoeng. 6 (2011) 124-130.
- [265] F. Mafuné, T. Okamoto, M. Ito, *Surfactant-free small Ni nanoparticles trapped on silica nanoparticles prepared by pulsed laser ablation in liquid*, Chem. Phys. Lett. 591 (2014) 193-196.

- [266] S. Hashimoto, T. Uwada, H. Masuhara, T. Asahi, *Fabrication of Gold Nanoparticle-Doped Zeolite L Crystals and Characterization by Optical Microscopy: Laser Ablation- and Crystallization Inclusion-Based Approach*, J. Phys. Chem. C 112 (2008) 15089-15093.
- [267] K. Siuzdak, M. Sawczak, M. Klein, G. Nowaczyk, S. Jurga, A. Cenia, *Preparation of platinum modified titanium dioxide nanoparticles with the use of laser ablation in water*, Phys. Chem. Chem. Phys. 16 (2014) 15199-15206.
- [268] J.G. Walter, S. Petersen, F. Stahl, T. Scheper, S. Barcikowski, *Laser ablation-based one-step generation and bio-functionalization of gold nanoparticles conjugated with aptamers*, J. Nanobiotech. 8 (2010) 21.
- [269] P. Liu, Y.L. Cao, H. Cui, X.Y. Chen, G.W. Yang, *Micro- and Nanocubes of Silicon with Zinc-Blende Structure*, Chem. Mater. 20 (2008) 494-502.
- [270] P. Liu, Y.L. Cao, C.X. Wang, X.Y. Chen, G.W. Yang, *Micro- and Nanocubes of Carbon with C<sub>8</sub>-like and Blue Luminescence*, Nano Lett. 8 (2008) 2570-2575.
- [271] C.H. Bae, S.H. Nam, S.M. Park, *Formation of silver nanoparticles by laser ablation of a silver target in NaCl solution*, Appl. Surf. Sci. 197-198 (2002) 628-634.
- [272] K. Sasaki, N. Takada, *Liquid-phase laser ablation*, Pure Appl. Chem. 82 (2010) 1317-1327.
- [273] K. Sasaki, T. Nakano, W. Soliman, N. Takada, *Effect of Pressurization on the Dynamics of a Cavitation Bubble Induced by Liquid-Phase Laser Ablation*, Appl. Phys. Express 2 (2009) 04651.
- [274] S. Hu, G. Goenaga, C. Melton, T.A. Zawodzinski, D. Mukherjee, *PtCo/CoOx nanocomposites: Bifunctional electrocatalysts for oxygen reduction and evolution reactions synthesized via tandem laser ablation synthesis in solution-galvanic replacement reactions*, Appl. Catal. B; Env. 182 (2016) 286-296.
- [275] S. Hu, M. Tian, E.L. Riberiro, G. Duscher, D. Mukherjee, *Tandem laser ablation synthesis in solution-galvanic replacement reaction (LASIS-GRR) for the production of PtCo nanoalloys as oxygen reduction electrocatalysts*, J. Pow. Sourc. 306 (2016) 413-423.
- [276] N. Dingenouts, J. Bolze, D. Poetschke, M. Ballauff, *Analysis of Polymer Latexes by Small-Angle X-Ray Scattering*, Adc. Polym. Sci. 144 (1999) 1-47.
- [277] L. Lavis, J.L.L. Garrec, L. Hallo, J.M. Jouvard, S. Charles, J. Perez, J.B.A. Mitchell, J. Decloux, M. Girault, V. Potin, H. Andrzejewski, M.C.M.d. Lucas, S. Bourgeois, *In-situ small-angle x-ray scattering study of nanoparticles in the plasma plume induced by pulsed laser irradiation of metallic targets*, Appl. Phys. Lett. 100 (2012) 164103.
- [278] Y. Xiong, S.E. Pratsinis, S.V.R. Mastrangelo, *The effect of ionic additives on aerosol coagulation*, J. Coll. Interf. Sci. 153 (1992) 106-117.
- [279] A. Schwenke, P. Wagener, S. Nolte, S. Barcikowski, *Influence of processing time on nanoparticle generation during picosecond-pulsed fundamental and second harmonic laser ablation of metals in tetrahydrofuran*, Appl. Phys. A 104 (2011) 77-82.
- [280] A. Mendez-Manjón, *Metal nanoparticles formation by laser ablation in liquids*, in, Leibniz University Hannover, 2012.

- [281] R. Tanabe, T.T.P. Nguyen, T. Sugiura, Y. Ito, *Bubble dynamics in metal nanoparticle formation by laser ablation in liquid studied through high-speed laser stroboscopic videography*, Appl. Surf. Sci. 351 (2015) 327-331.
- [282] A. De Giacomo, M. Dell'Aglio, F. Colao, R. Fantoni, *Double pulse laser produced plasma on metallic target in seawater: basic aspects and analytical approach*, Spectrochimica Acta Part B: Atomic Spectroscopy 59 (2004) 1431-1438.
- [283] M.R. Gavrilović, *Impact of the cavitation bubble on a plasma emission following laser ablation in liquid*, Eur. Phys. J. D 71 (2017) 316.
- [284] A. Tamura, T. Sakka, K. Fukami, Y.H. Ogata, *Dynamics of cavitation bubbles generated by multi-pulse laser irradiation of a solid target in water*, Appl. Phys. A 112 (2013) 209-213.
- [285] T. dos Santos Rolo, S. Reich, D. Karpov, S. Gasilov, D. Kunka, E. Fohtung, T. Baumbach, A. Plech, *A Shack-Hartmann Sensor for Single-Shot Multi-Contrast Imaging with Hard X-rays*, Applied Sciences 8 (2018) 737.
- [286] S. Reich, J. Göttlicher, A. Letzel, B. Gökce, S. Barcikowski, T. dos Santos Rolo, T. Baumbach, A. Plech, *X-ray spectroscopic and stroboscopic analysis of pulsed laser ablation of Zn and its oxidation*, Appl. Phys. A 124 (2018) 71.
- [287] F. Spano, A. Massaro, L. Blasi, M. Malerba, R. Cingolani, A. Athanassiou, *In Situ Formation and Size Control of Gold Nanoparticles into Chitosan for Nanocomposite Surfaces with Tailored Wettability*, Langmuir 28 (2012) 3911-3917.
- [288] S. Petersen, J. Jakobi, S. Barcikowski, *In situ bioconjugation - Novel laser based approach to pure nanoparticle conjugates*, Appl. Surf. Sci. 255 (2009) 5435-5438.
- [289] H. Usui, Y. Shimizu, T. Sasaki, N. Koshizaki, *Photoluminescence of ZnO Nanoparticles Prepared by Laser Ablation in Different Surfactant Solutions*, The Journal of Physical Chemistry B 109 (2005) 120-124.
- [290] X. Liu, F. Zhnag, R. Huang, C. Pan, J. Zhu, *Capping Modes in PVP-Directed Silver Nanocrystal Growth: Multi-Twinned Nanorods versus Single-Crystalline Nano-Hexapods*, Cryst. Growth Des. 8 (2008) 1916-1923.
- [291] A. Mezni, T. Dammak, A. Fkiri, A. Mlayah, Y. Abid, L.S. Smiri, *Photochemistry at the Surface of Gold Nanoprisms from Surface-Enhanced Raman Scattering Blinking*, J. Phys. Chem. C 118 (2014) 17956-17967.
- [292] R. Seoudi, A.A. Fouda, Elmenshawy, *Synthesis, characterization and vibrational spectroscopic studies of different particle size of gold nanoparticle capped with polyvinylpyrrolidone*, Physica B 405 (2010) 906-911.
- [293] H.L. Liu, P. Hou, *Low-temperature synthesis and characterization of PVP-capped FeAu nanoparticles*, J. Mater. Res. 26 (2011) 2040-2049.
- [294] P. Abdulkin, T.L. Precht, B.R. Knappett, H.E. Skelton, D.A. Jefferson, A.E.H. Wheatley, *Systematic Control of Size and Morphology in the Synthesis of Gold Nanoparticles*, Part. Part. Syst. Chem. 31 (2014) 571-579.

- [295] D.P. Stankus, S.E. Lohse, J.E. Hutchison, J.A. Nason, *Interactions between Natural Organic Matter and Gold Nanoparticles Stabilized with Different Organic Capping Agents*, Environ. Sci. Technol. 45 (2011) 3238-3244.
- [296] K.I. Requejo, A.V. Liopo, P.J. Derry, E.R. Zubarev, *Accelerating Gold Nanorod Synthesis with Nanomolar Concentrations of Poly(vinylpyrrolidone)*, Langmuir 33 (2017) 12681-12688.
- [297] H.H. Wen, E.E. Bennett, M.M. Hedegus, S.C. Carroll, *Spatial Harmonic Imaging of X-ray Scattering—Initial Results*, IEEE T. Med. Imaging 27 (2008) 997-1002.
- [298] Y. Liu, B. Ahr, A. Linkin, G.J. Diebold, C. Rose-Petruck, *X-ray spatial harmonic imaging of phase objects*, Opt. Lett. 36 (2011) 2209-2211.
- [299] S.K. Lynch, V. Pai, J. Auxier, A.F. Stein, E.E. Bennett, C.K. Kemble, X. Xiao, W.-K. Lee, N.Y. Morgan, H.H. Wen, *Interpretation of dark-field contrast and particle-size selectivity in grating interferometers*, Appl. Opt. 50 (2011) 4310-4319.
- [300] A.F. Stein, J. Ilavsky, R. Kopace, E.E. Bennett, H. Wen, *Selective imaging of nano-particle contrast agents by a single-shot x-ray diffraction technique*, Opt. Express 18 (2010) 13271-13278.
- [301] F.A. Vittoria, M. Endrizzi, P.C. Diemoz, A. Zamir, U.H. Wagner, C. Rau, I.K. Robinson, A. Olivio, *X-ray absorption, phase and dark-field tomography through a beam tracking approach*, Sci. Rep. 5 (2015) 16318.
- [302] G.M. Hale, M.R. Querry, *Optical Constants of Water in the 200-nm to 200- $\mu$ m Wavelength Region*, Applied Optics 12 (1973) 555-563.
- [303] T. Wagner, *thorstenwagner/ij-particlesizer: ParticleSizer 1.0.7*, in, <https://zenodo.org/record/163568#.W0qZWXwiFpg>, 2016.
- [304] H.H. Wen, E.E. Bennett, R. Kopace, A.F. Stein, V. Pai, *Single-shot x-ray differential phase-contrast and diffraction imaging using two-dimensional transmission gratings*, Opt. Lett. 35 (2010) 1932-1934.
- [305] S. Kaepler, F. Bayer, T. Weber, A. Maier, G. Anton, J. Hornegger, M. Beckmann, P.A. Fasching, A. Hartmann, F. Heindl, T. Michel, G. Oezguel, G. Pelzer, C. Rauh, J. Rieger, R. Schulz-Wendtland, M. Uder, D. Wachter, E. Wenkel, C. Riess, *Signal decomposition for X-ray dark-field imaging*, Med. Image. Comput. Assist. Interv. 17 (2014) 170-177.
- [306] G.-R. Zhang, B.-Q. Xu, *Surprisingly strong effect of stabilizer on the properties of Au nanoparticles and Pt<sup>+</sup>Au nanostructures in electrocatalysis*, Nanoscale 2 (2010) 2798-2804.
- [307] H. Tsunoyama, N. Ichikuni, H. Sakurai, T. Tsukuda, *Effect of Electronic Structures of Au Clusters Stabilized by Poly(N-vinyl-2-pyrrolidone) on Aerobic Oxidation Catalysis*, Journal of the American Chemical Society 131 (2009) 7086-7093.
- [308] M. Okumura, Y. Kitagawa, T. Kawakami, M. Haruta, *Theoretical investigation of the hetero-junction effect in PVP-stabilized Au<sub>13</sub> clusters. The role of PVP in their catalytic activities*, Chemical Physics Letters 459 (2008) 133-136.
- [309] H. Wang, X. Qiao, J. Chen, X. Wang, S. Ding, *Mechanisms of PVP in the preparation of silver nanoparticles*, Mater. Chem. Phys. 94 (2005) 449-453.

- [310] P. Wagener, G. Brandes, A. Schwenke, S. Barcikowski, *Impact of in situ polymer coating on particle dispersion into solid laser-generated nanocomposites*, *Physical Chemistry Chemical Physics* 13 (2011) 5120-5126.

## 9 Appendix

Primary particle diameter differentiation and bimodality identification by five analytical methods using gold nanoparticle size distributions synthesized by pulsed laser ablation in liquids

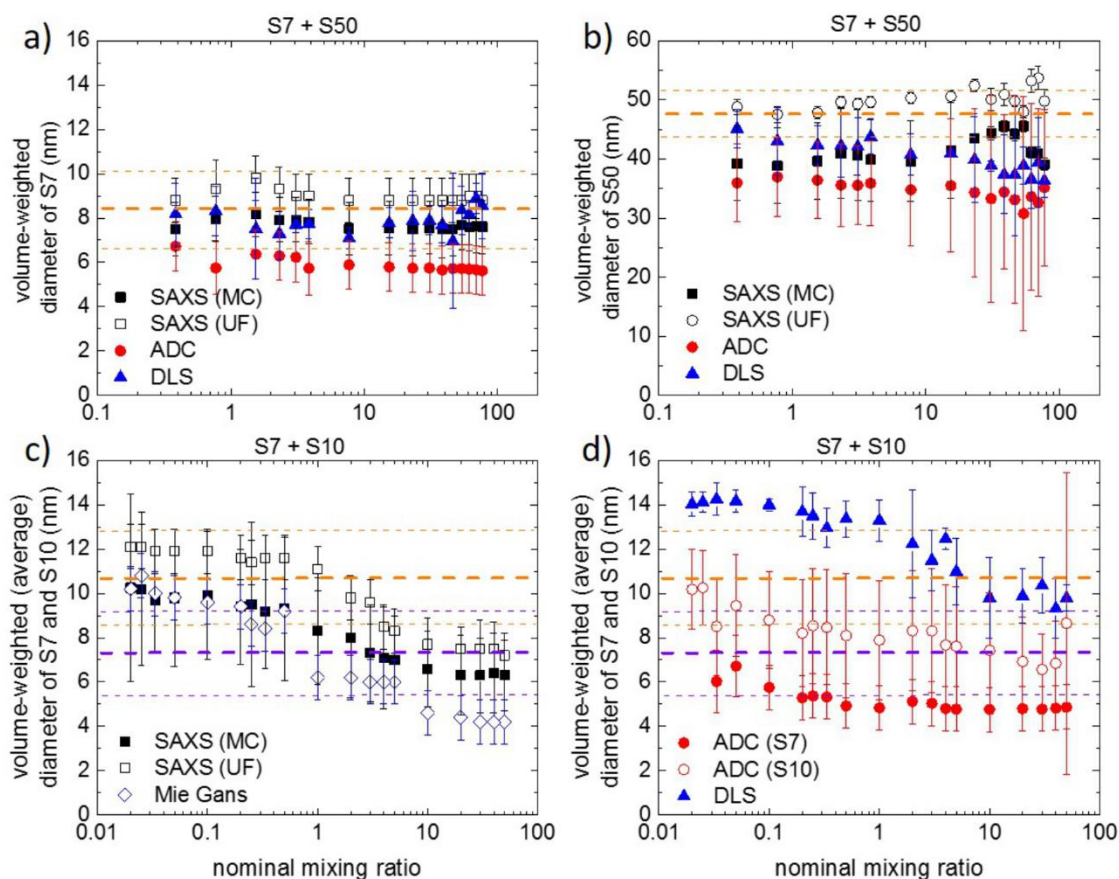


**Figure 38:** Volume-weighted sizes of the underlying fractions of mixtures of S7-S50 (a-b) and S7-S10 (c-d) as function of the nominal mixing ratio. (a) Size evolution of S7 in mixtures of S7-S50. (b) Size evolution of S50 in mixtures of S7-S50. (c) Size evolution of mean particle size in mixtures of S7-S10 (SAXS, Mie-Gans). (d) Size evolution of mean particle size and size fractions in case of ADC in mixtures of S7-S10 (DLS, ADC). The dashed yellow horizontal lines in a-b are guides to the eye and indicate the size obtained of the pure colloids by STEM and their standard deviations. The same accounts for the yellow and purple lines in c-d, which indicate the size of pure S10 (purple) and pure S7 (yellow), respectively.

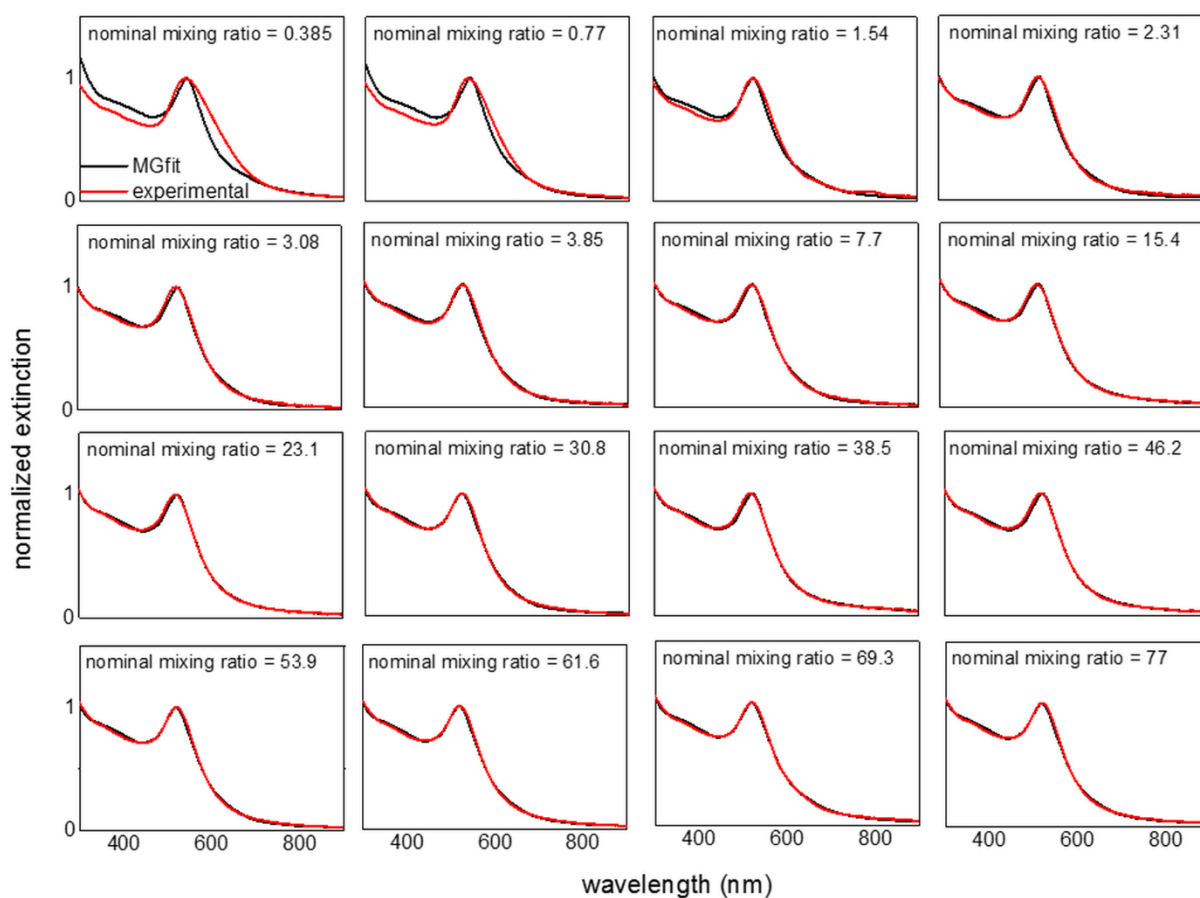


**Figure 39:** UV/Vis spectra of mixtures of S7 and S50 (red lines) and respective fits by Mie-Gans theory (black lines). The corrected nominal mixing ratios are given in every partial diagram. All spectra are normalized to the maximum of the respective surface plasmon resonance peaks.

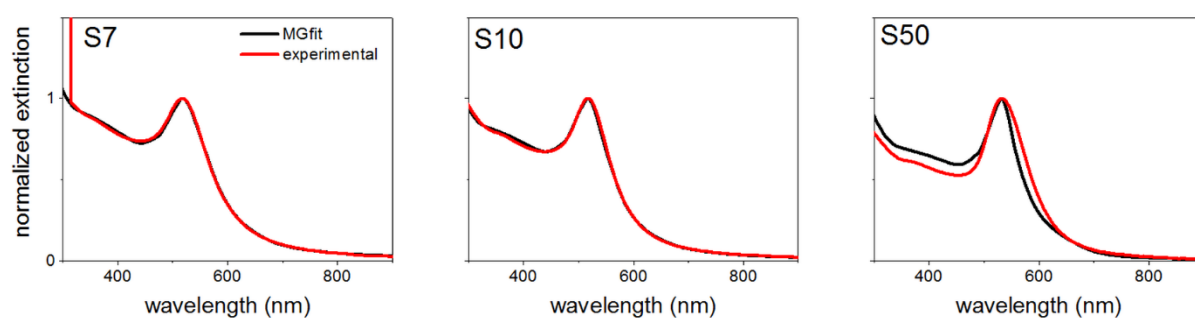


**Figure 40:** UV/Vis spectra of defined colloids S7, S10 and S50 (red lines) and respective fits by Mie-Gans theory (black lines). The corrected nominal mixing ratios are given in every partial diagram. All spectra are normalized to the maximum of the respective surface plasmon resonance peaks.

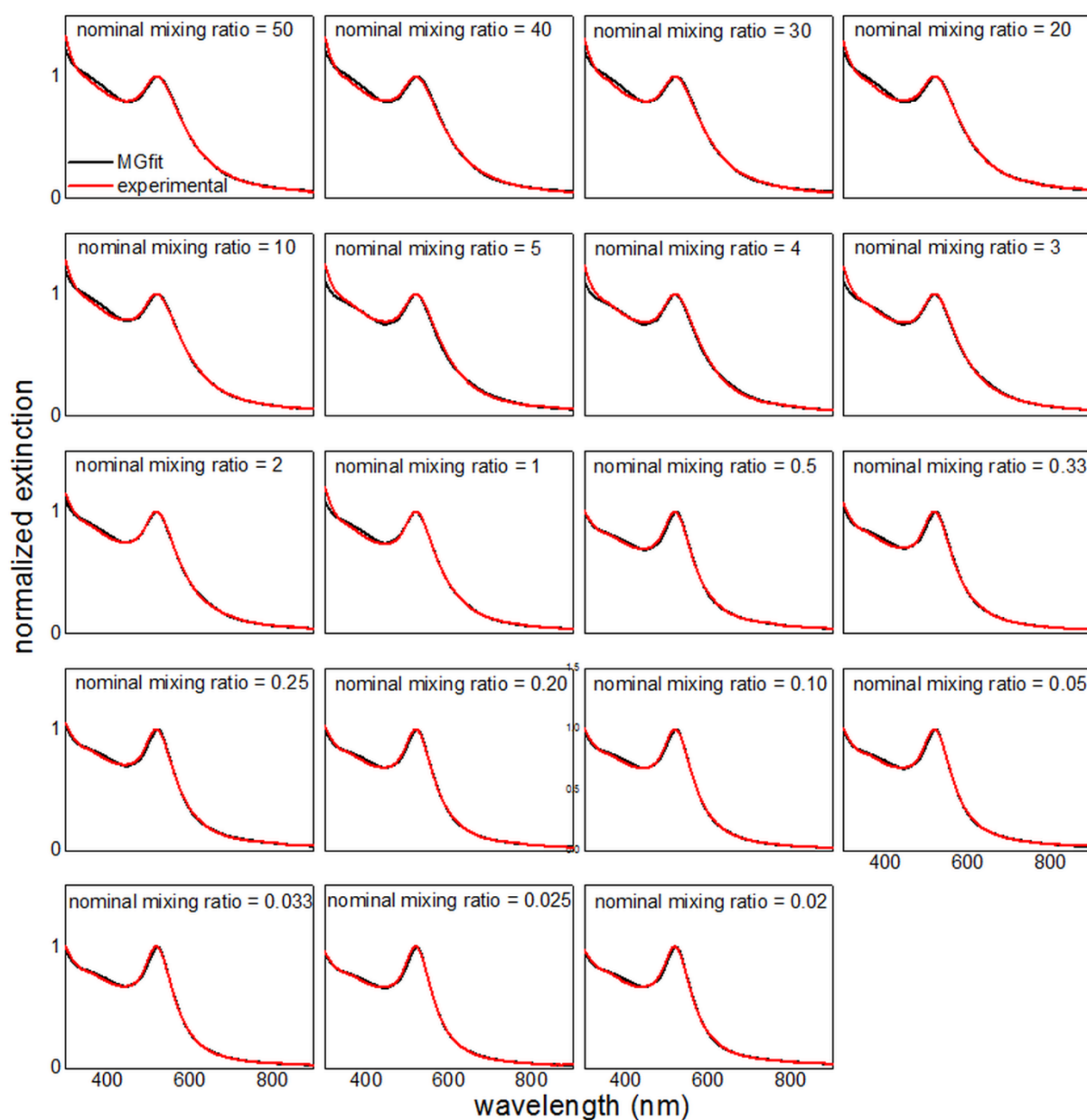


**Figure 41:** UV/Vis spectra of mixtures of S7 and S10 (red lines) and respective fits by Mie-Gans theory (black lines). The corrected nominal mixing ratios are given in every partial diagram. All spectra are normalized to the maximum of the respective surface plasmon resonance peaks.

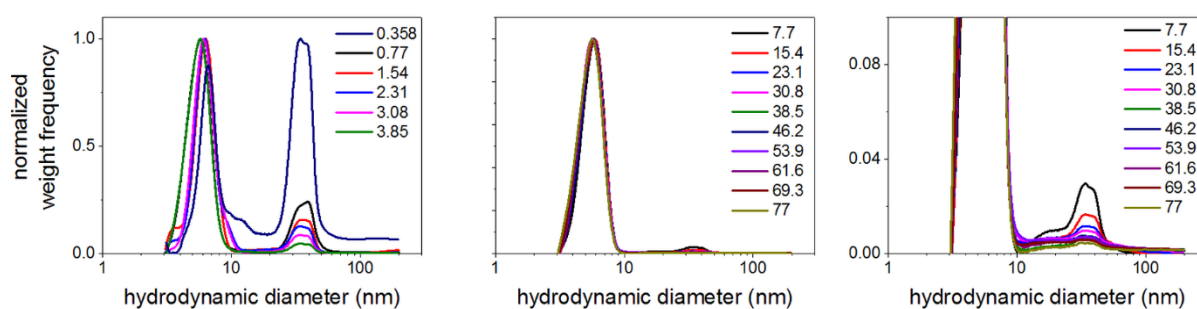


**Figure 42:** Size distributions obtained from analytical disc centrifugation of particle mixtures of S7-S50. All curves are normalized to their maximum. The corrected nominal mixing ratios are given in the caption. The middle and right diagrams show the same data but the mode of S50 is enlarged on the right.

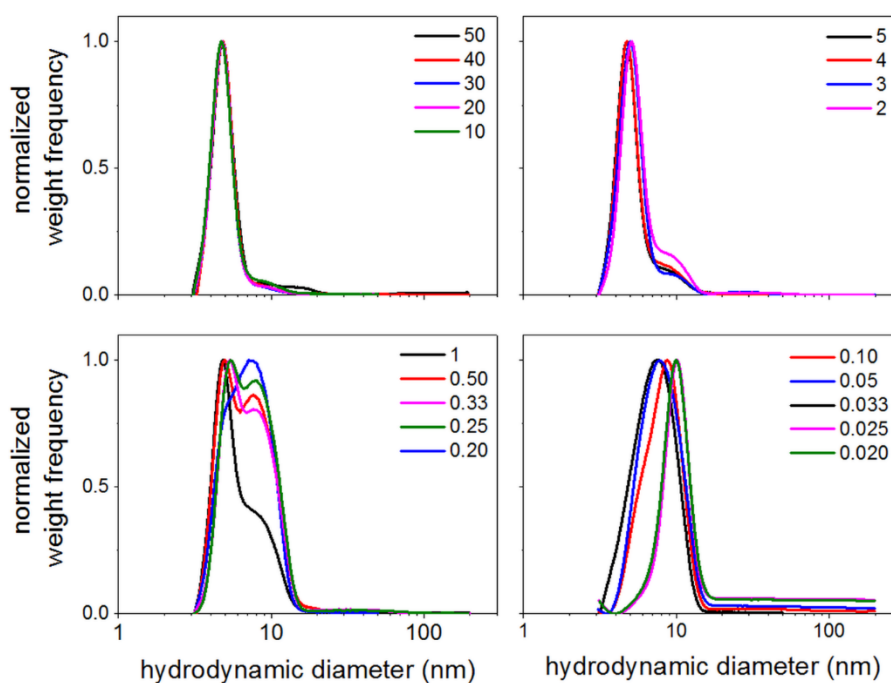


**Figure 43:** Size distributions obtained from analytical disc centrifugation of particle mixtures of S7-S10. All curves are normalized to their maximum. The corrected nominal mixing ratios are given in the caption. This figure highlights the ability of disc centrifugation to distinguish between the peaks of S7 and S10. Hence, peak deconvolution is justified.

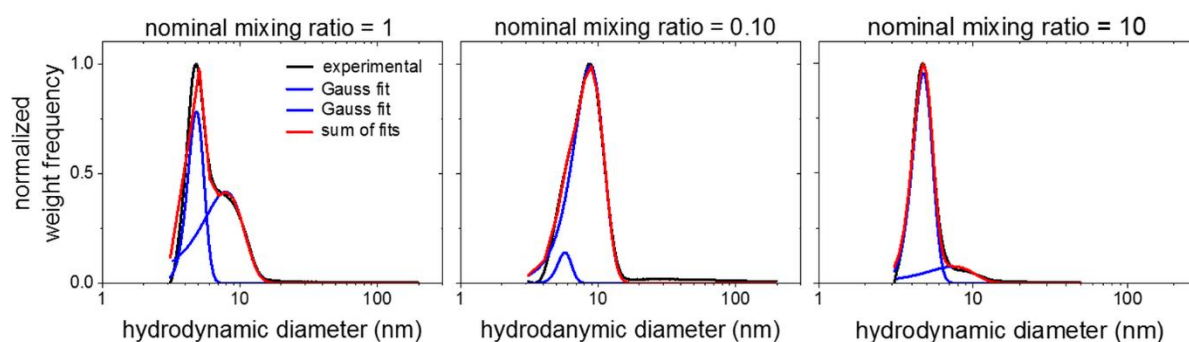


**Figure 44:** Exemplary size distributions obtained from analytical disc centrifugation of particle mixtures of S7-S10 with applied peak deconvolution. All curves are normalized to their maximum.

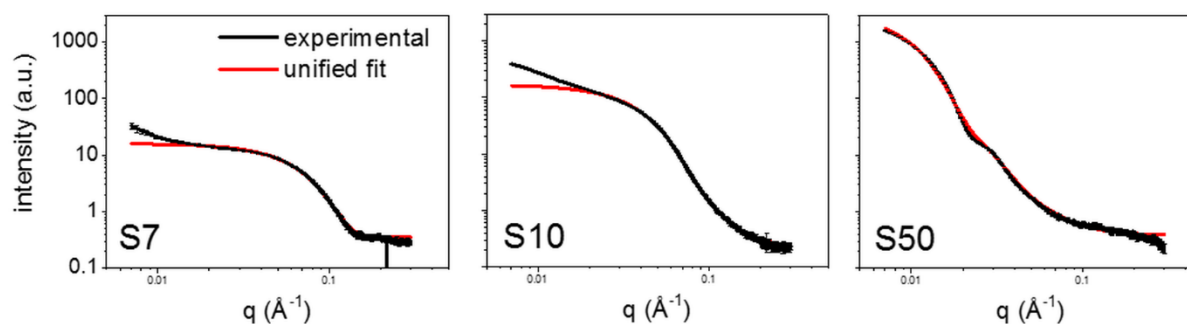


**Figure 45:** SAXS analysis of the colloids S7, S10 and S50. The experimental curves (black lines) are plotted together with fits to the data by the unified fit (red lines).

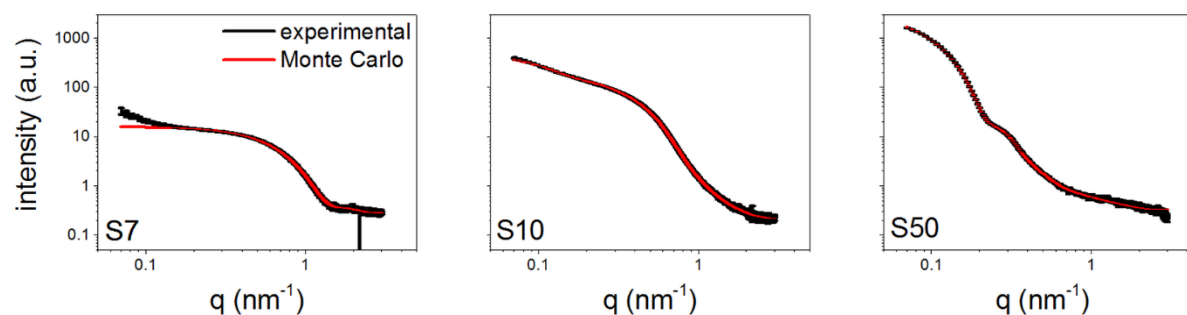


**Figure 46:** SAXS analysis of the colloids S7, S10 and S50. The experimental curves (black lines) are plotted together with fits to the data by the Monte Carlo method (red lines).

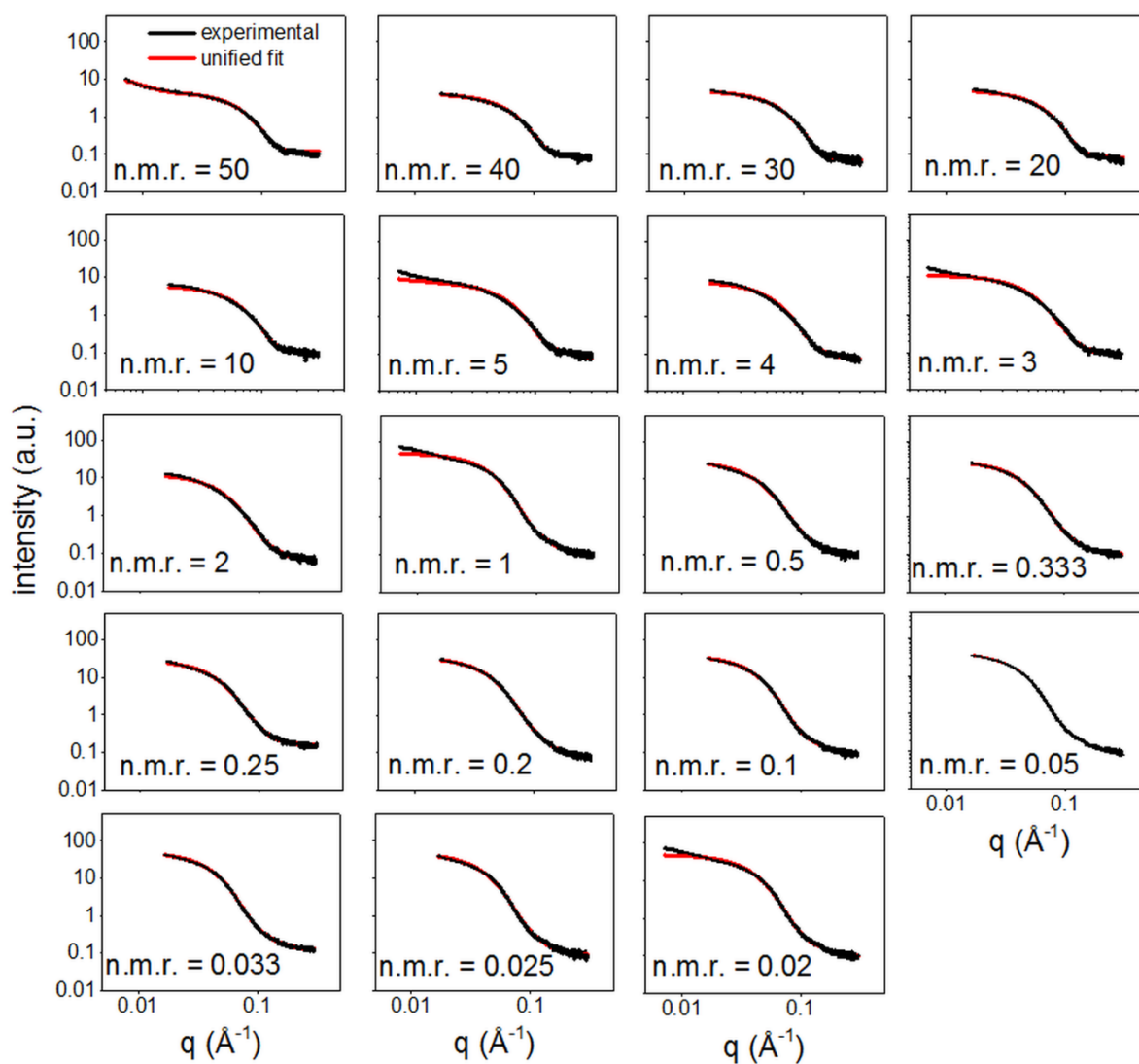


**Figure 47:** SAXS analysis of the mixtures of S7-S10. The experimental curves (black lines) are plotted together with fits to the data by the unified fit (red lines). The nominal mixing ratios (n.m.r.) are given in the individual diagrams.

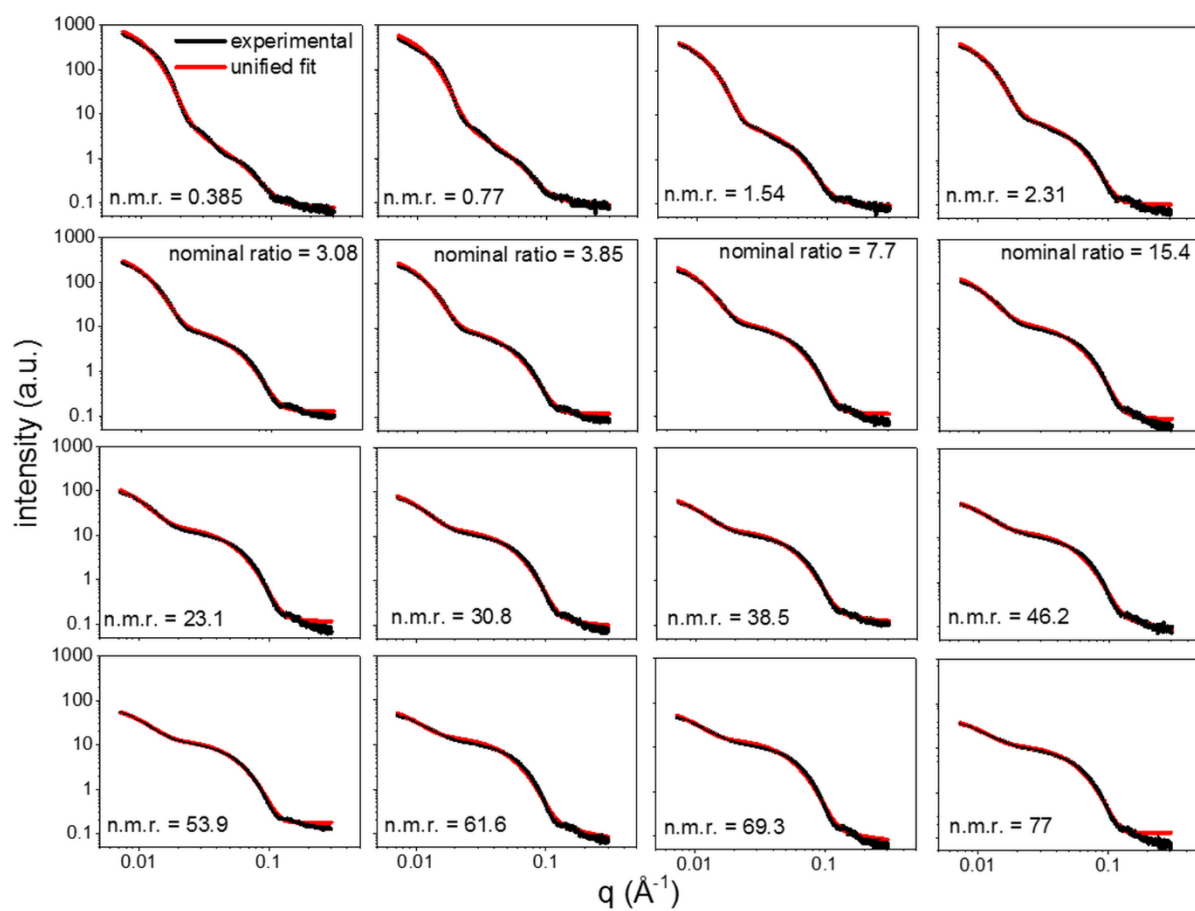


**Figure 48:** SAXS analysis of the mixtures of S7-S50. The experimental curves (black lines) are plotted together with fits to the data by the unified fit (red lines). The corrected nominal mixing ratios (n.m.r.) are given in the individual diagrams.

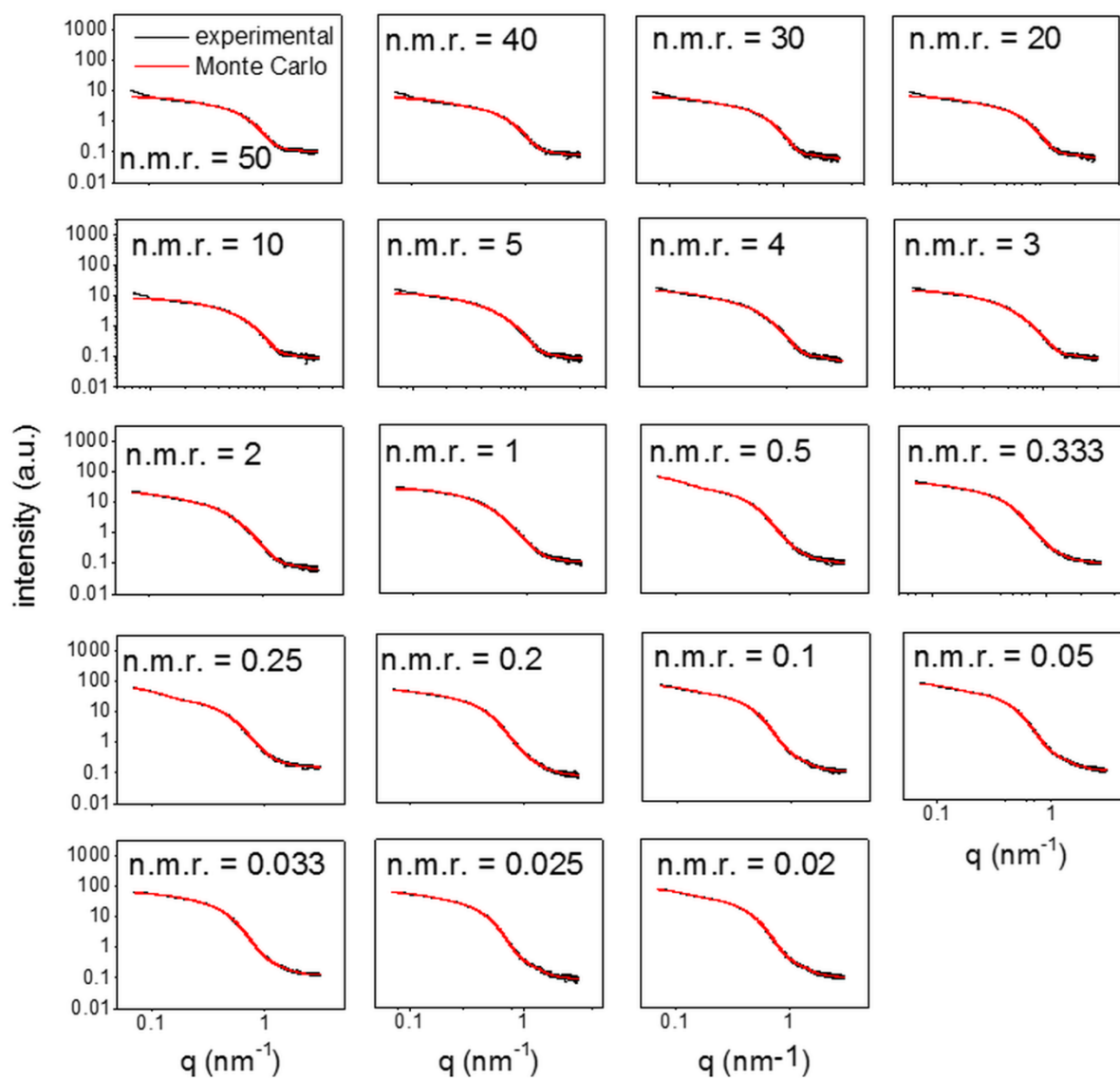


**Figure 49:** SAXS analysis of the mixtures of S7-S10. The experimental curves (black lines) are plotted together with fits to the data by the Monte Carlo method (red lines). The nominal mixing ratios (n.m.r.) are given in the individual diagrams.

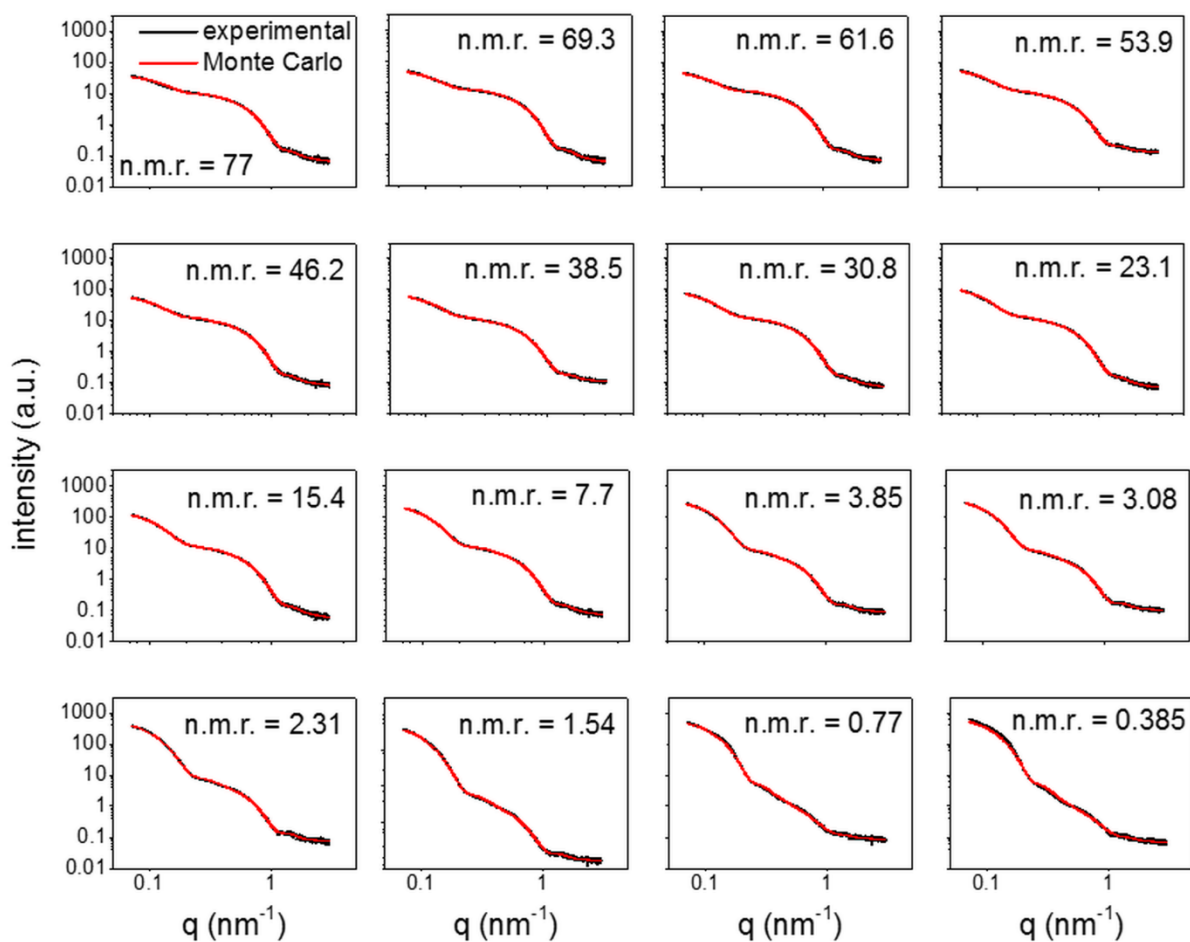


**Figure 50:** SAXS analysis of the mixtures of S7-S50. The experimental curves (black lines) are plotted together with fits to the data by the unified fit (red lines). The corrected nominal mixing ratios (n.m.r.) are given in the individual diagrams.

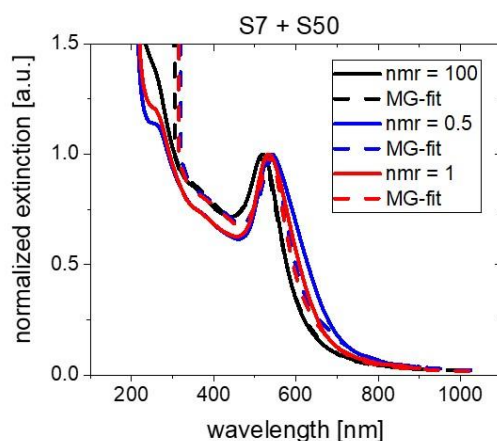


**Figure 51:** Demonstration of the Mie Gans fit quality for mixtures of the samples S7 and S50. For large excess of small nanoparticles ( $n.m.r. = 100$ ) the fit quality is good. When the large particle fraction becomes dominant ( $n.m.r. = 0.5 - 1$ ) the fit does not match the experimental data any more. This is caused by the inability to vary the fitting parameters freely and the design of the algorithm to fit spectra obtained from monodisperse colloids.

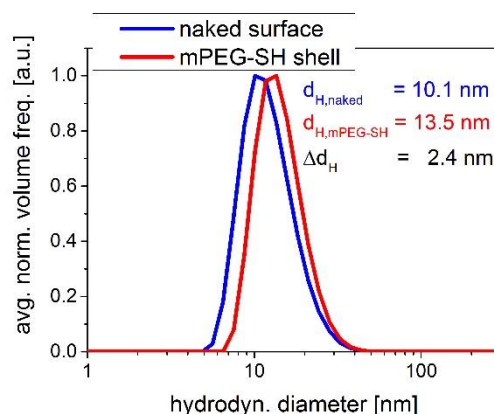


**Figure 52:** Using ligand-free AuNPs would have been preferable for the study. However, it was necessary to sterically stabilize the nanoparticles to prevent agglomeration and aggregation over the entire duration of the study (several months). As shown, DLS from fully stabilized unligated particles returns a smaller hydrodynamic radius and therefore a higher sensitivity on sizes and different fractions in the mixture. The mPEG-SH concentration used to stabilize the colloid was  $10 \mu\text{M}$  in total, which is identical to the concentration for the samples in the manuscript. The ligation provides a well-defined, stabilized state for the suspension to compare the different measurements, also in terms of storage time, transport and final preparation.

### How a re-irradiated ablation target affects cavitation bubble dynamics and nanoparticles properties in laser ablation in liquids

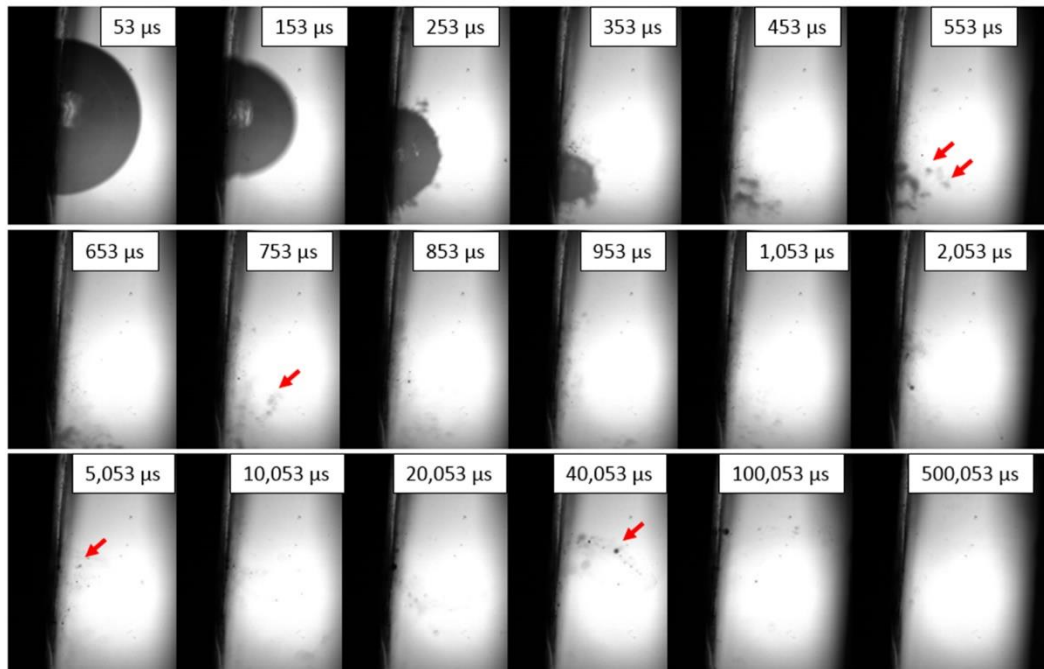


**Figure 53:** Drain of microbubbles from the ablation by a liquid flow: Frames of the interior of the ablation chamber at different delays after laser impact with an applied volume flow of water (11 ml/min) are shown. The cavitation bubble vanished after 500-600  $\mu\text{s}$  but some persistent microbubbles (exemplary marked by arrows) remained present inside the chamber until 100,000  $\mu\text{s}$  (= 0.1 s). As the applied laser repetition rate was 0.2 Hz, equal to one laser pulse each 5 s, the assumption of complete removal of persistent bubbles (and residual nanoparticles) between two laser pulses was validated.

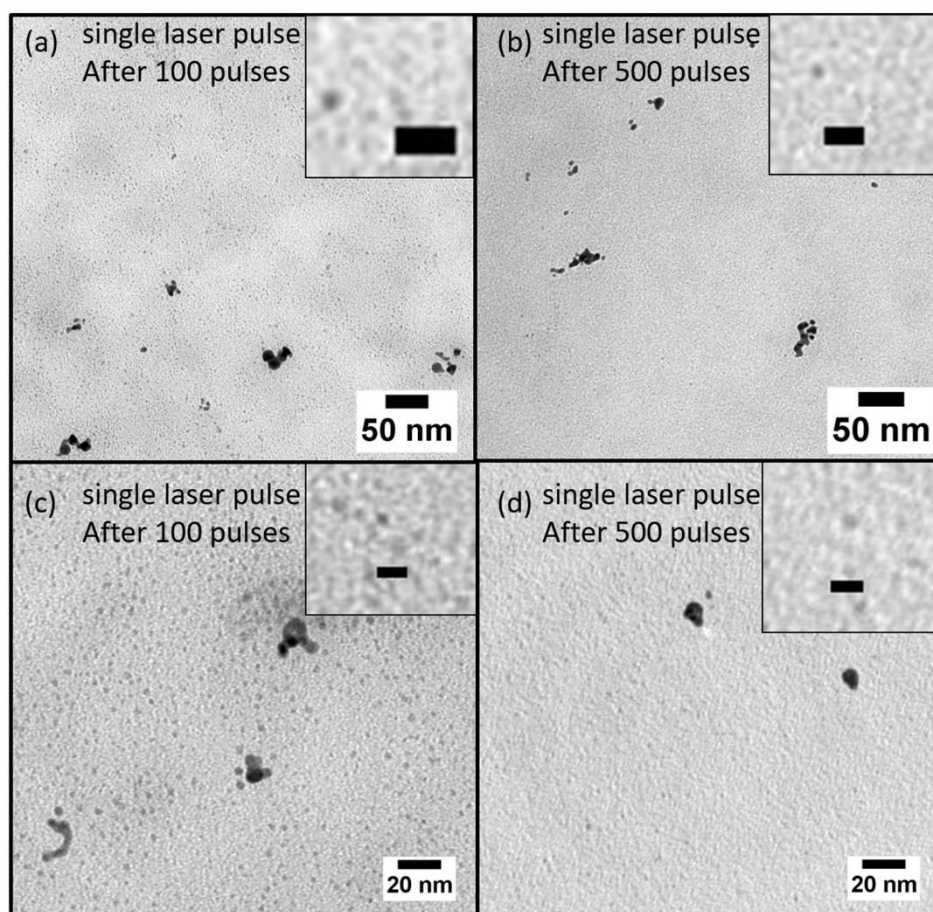


**Figure 54:** Nanoclusters were formed not only during LAL of Ag (see main manuscript) but also during LAL of gold, and even for single laser pulses. The TEM images of gold nanoparticles and nanoclusters obtained by single laser pulses deposited in the craters drilled by 100 (a, c) and 500 (b, d) previous pulses, respectively, are presented. The target thickness was 1.0 nm and the pulse laser pulse energy was 10 mJ. The particle concentration on the grid was increased by drop casting 10-15 drops. The images demonstrate that the nanoclusters were not produced by LFL of nanoparticles in the 10 pulse experiments, and were further not formed on the grid by the dissolution of silver ions. The scale bars in the insets of (a, b) are 10 nm and 5 nm in (c, d).

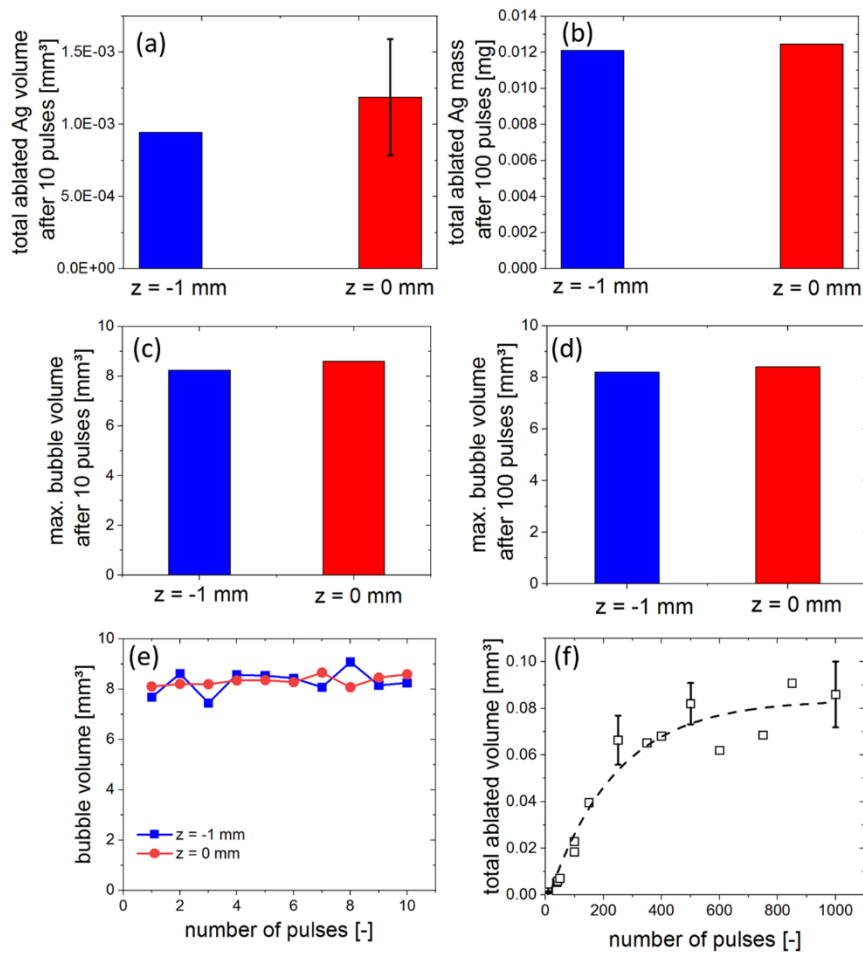


**Figure 55:** Reference experiments excluded large changes of the laser fluence by the crater shape/depth upon drilling a hole in the 1.0 mm thick silver targets. The total ablated silver volume and cavitation bubble volume at maximum extension after 10 and 100 pulses are given in (a, c) and (b, d). The red bars represent fixed focusing conditions as applied in all experiments presented in the main manuscript. The blue bars represent the reference experiments with the position of the focusing lens shifted 1 mm away from the target surface to mimic the fluence at the crater bottom after up to 1,000 pulses (Figure 22, main manuscript). Both the ablation and the bubble volume did not change significantly at  $z = -1$  mm; (e) Comparison of the maximum bubble volume induced by the first 10 laser pulses for  $z = -1$  mm and  $z = 0$  mm; (f) Total ablation volume of Ag as a function of the number of pulses. The volume increased quickly for the first 100-200 pulses but much slower afterward. The final ablated silver volume after 500-1,000 pulses was approximately  $0.08 \text{ mm}^3$  and was hence negligible with respect to the volume  $> 1 \text{ mm}^3$  of the cavitation bubble.

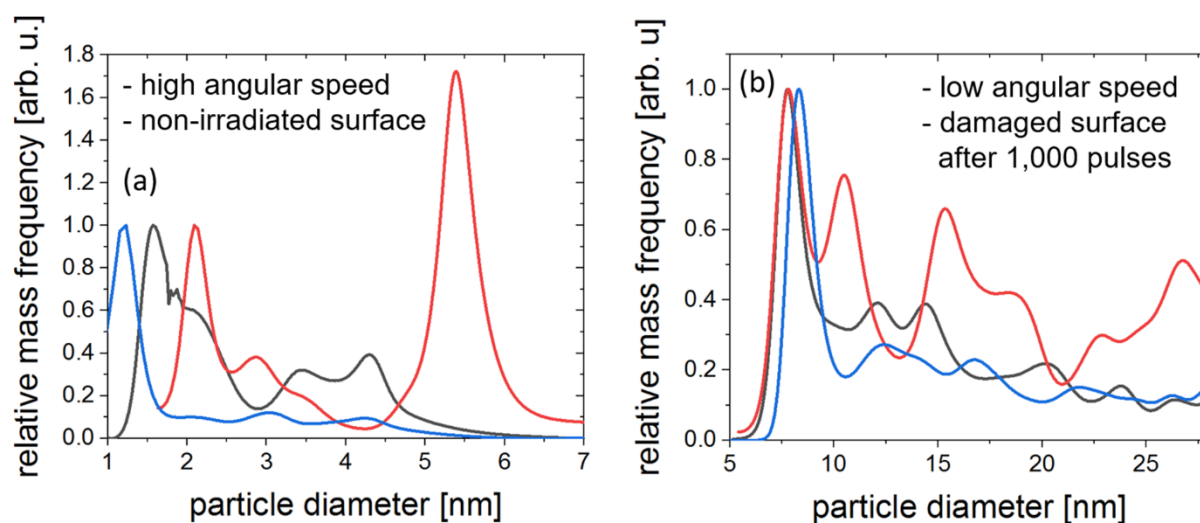


**Figure 56:** Ag particle size distributions of colloids, fabricated under identical conditions, measured by AUZ at angular velocities of 30,000 rpm to detect particles  $\ll 10$  nm (a) and 3,000 rpm to detect particles  $> 5$  nm (b). The distributions were obtained by applying 10 laser pulses on a non-irradiated (a) silver surface and after 1,000 pulses (b). The reproducibility in terms of the peak integrals was low between the individual syntheses. Therefore, no conclusions on the amount of the respective particle size fractions were possible. The pure detection of nanoparticles and nanoclusters size remained unaffected by this issue as no clusters were detected by AUC in pure water. All size distributions were normalized to the respective peak of minimum diameter.

### Size quenching during laser synthesis of colloids happens already in the vapor phase of the cavitation bubble

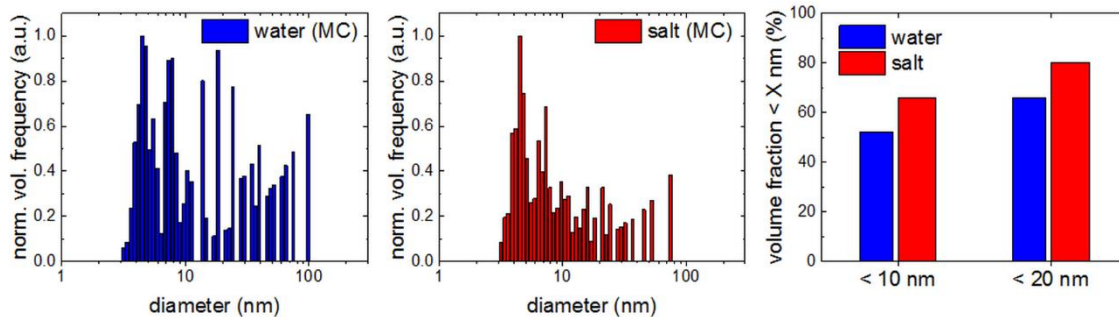


**Figure 57:** Volume-weighted size distributions obtained from Monte Carlo (MC) analysis of *in situ* SAXS data (shown in Figure 28). The size distributions of particles in water (left) and 0.5 mM NaCl solution (middle) differ significantly at sizes above 10 nm. This is clarified by a diagram plotting the volume fraction of particles smaller than 10 nm and 20 nm as function of the ablation medium (right). This fraction of small particles is higher in saline solution.

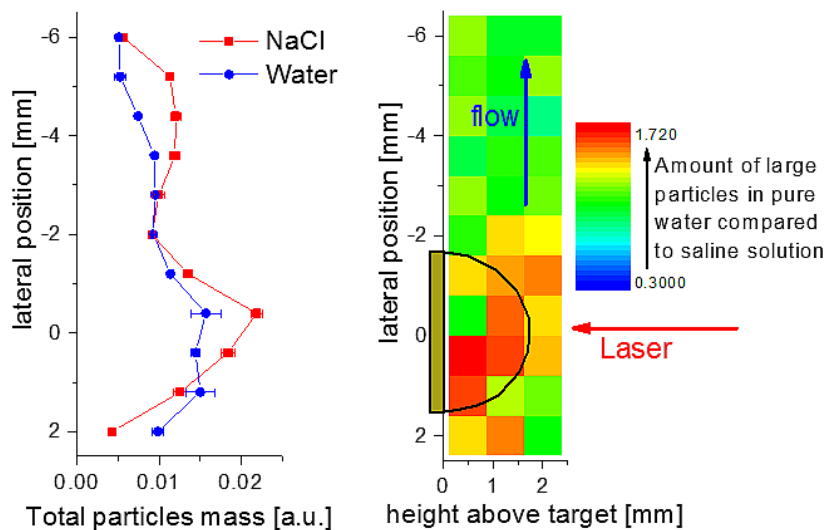


**Figure 58:** Left: Particle mass in dependence of the lateral position inside the ablation chamber volume. Negative lateral positions are representing distinct time delays after the laser impact. The zero position marks the target center. Right: Ratio of large to small particle fraction abundance in pure water compared to micromolar NaCl solution as a function of lateral position and height above target (black hemisphere represents maximum extension of the cavitation bubble). In red areas the amount of large particles in is higher compared to saline solutions.

## Time and mechanism of nanoparticle functionalization by macromolecular ligands during pulsed laser ablation in liquids

### *Influence of the laser fluence during nanoparticle size control by additives*

The laser fluence on the target is a crucial parameter in laser processing and in laser ablation in liquids. As the *in situ* experiments in the main article were conducted at an effective fluence of  $33 \text{ J/cm}^2$  and the *ex situ* LAL at  $27 \text{ J/cm}^2$  a reference experiment is performed to exclude alterations of the particle size by this deviation. Therefore, the fluence was increased above the *in situ* fluence to  $36 \text{ J/cm}^2$  by changing the focusing conditions and LAL was performed under similar conditions compared to the ablations in the main article. The additive concentration was kept constantly at  $0.5 \text{ mM}$  to match the conditions from *in situ* laser ablation. The results from Figure 59 show that in the presence of size and growth quenching additives the effect of the laser fluence is negligible in the given fluence regime.

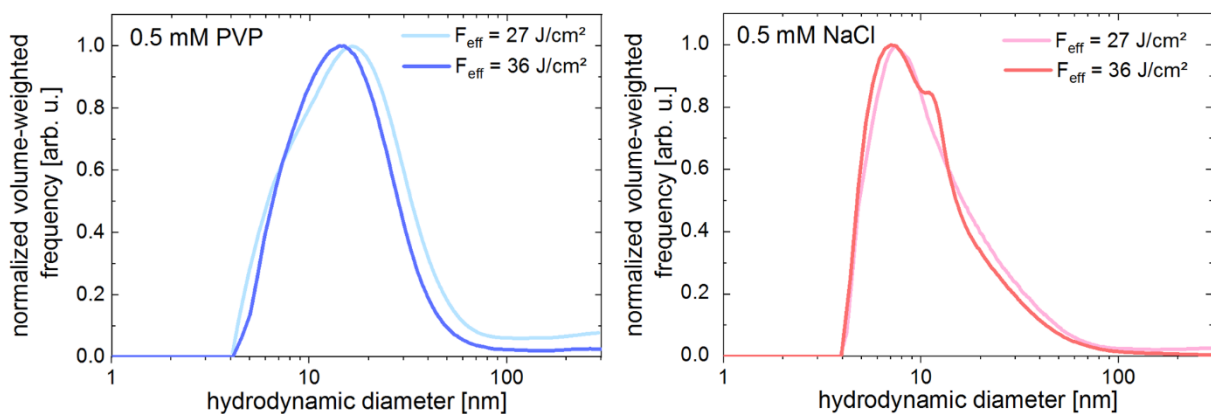


**Figure 59:** Volume-weighted particle size distributions measured by ADC in dependence of the type of additive (left: PVP; right: NaCl) and the effective fluence ( $27 \text{ J/cm}^2$  and  $36 \text{ J/cm}^2$ ). Except for the applied fluence the experimental parameters are the same compared to the *ex situ* ablations in the main article.

## UV/Vis calibration and spectra

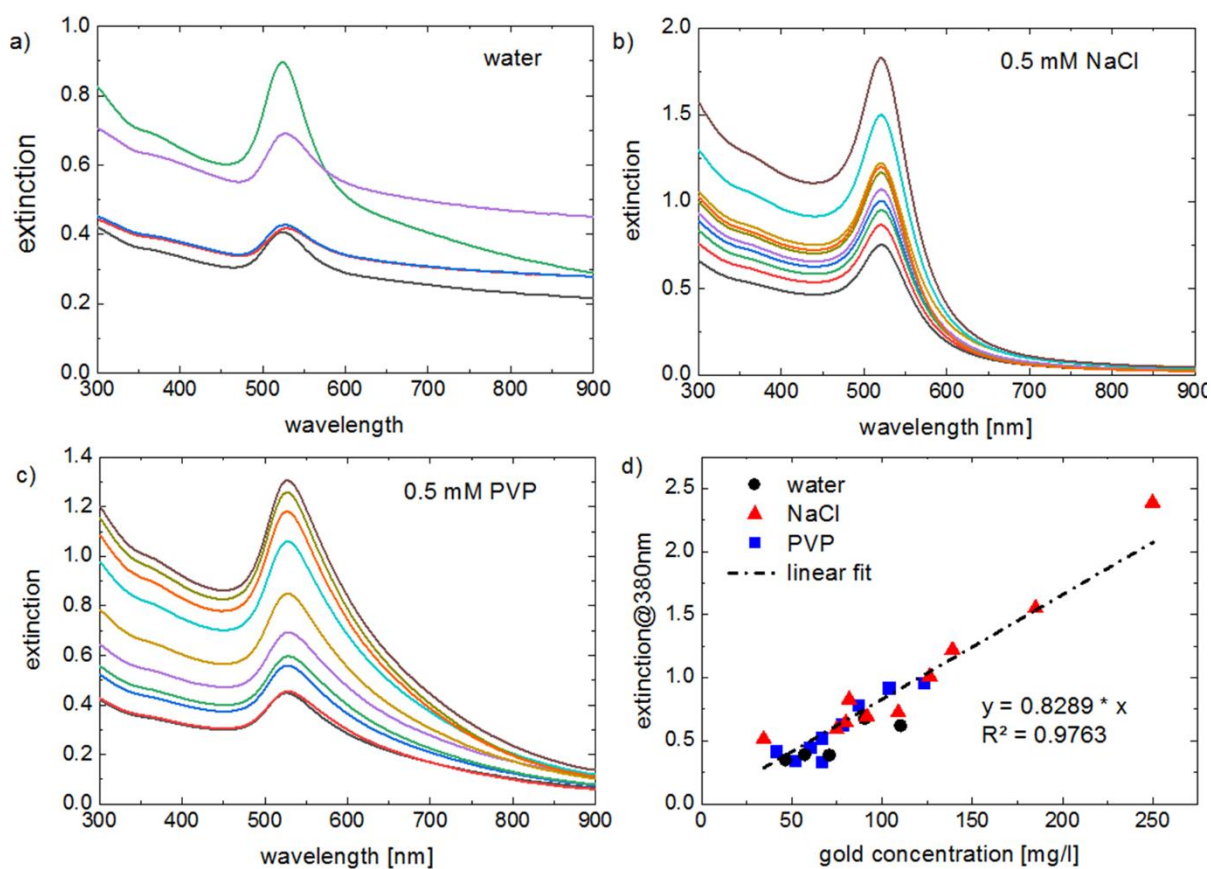


**Figure 60:** UV/Vis extinction spectra of gold nanoparticles synthesized by LAL in pure water (a), 0.5 mM NaCl solution (b), and 0.5 mM PVP solution. The interband absorption at a wavelength of 380 nm was used to obtain a calibration function for the given gold concentration, which was determined by standard gravimetric analysis (d).

### Shadowgraphy

The laser (1064 nm, 9 ns, Innolas Spitlight DPSS-250-100) was operated at 10 mJ pulse energy and focused onto the gold target surface using a lens of 75 mm focal length in air. The effective laser fluence was  $30 \text{ J/cm}^2$ . The camera's (Basler acA1600-60gm, lens: Sill optics correctal T/1,5) gate width was  $10 \mu\text{s}$ . The camera was triggered by the pokes cell's signal of the laser. As the laser travels at the speed of light, the camera was activated after laser impact. Hence, the first  $53 \mu\text{s}$  after impact were not accessible with the presented setup due to the internal delay of the camera. On the other hand, the laser fluence was high enough to record the maximum extension of the laser-induced cavitation bubble and all subsequent bubble states. A LED Lenser L7 flashlight was used as a quasi-continuous light source. For each image one laser pulse was required. By performing LAL in a liquid-flow chamber on usage of a repetition rate as low as 0.2 Hz the exchange of the entire liquid volume inside the chamber is ensured between two laser pulses. The same was done for each of the time-dependent cavitation bubble analysis. The used setup is schematically depicted in Figure 61. The maximum bubble extension was determined at a delay of  $93 \mu\text{s}$  as shown in Figure 62, and the experiment was repeated 10 times for water and PVP solution. For each liquid the entire bubble lifetime was recoded twice. Flat-field correction was applied to remove static artifacts from the images. The recorded image sequences showing the bubble lifetime for LAL in pure water and PVP solution are presented in Figure 63 and 64.

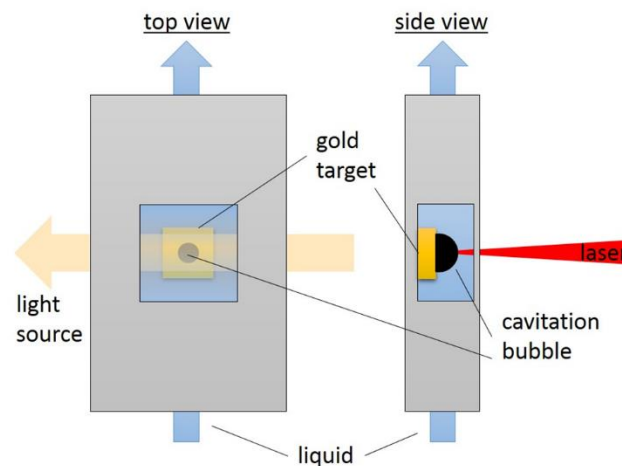


**Figure 61:** Scheme of the 3D-printed liquid flow ablation chamber made of ABS for simultaneous shadowgraphic imaging (top view) of the cavitation bubble during laser ablation (side view).

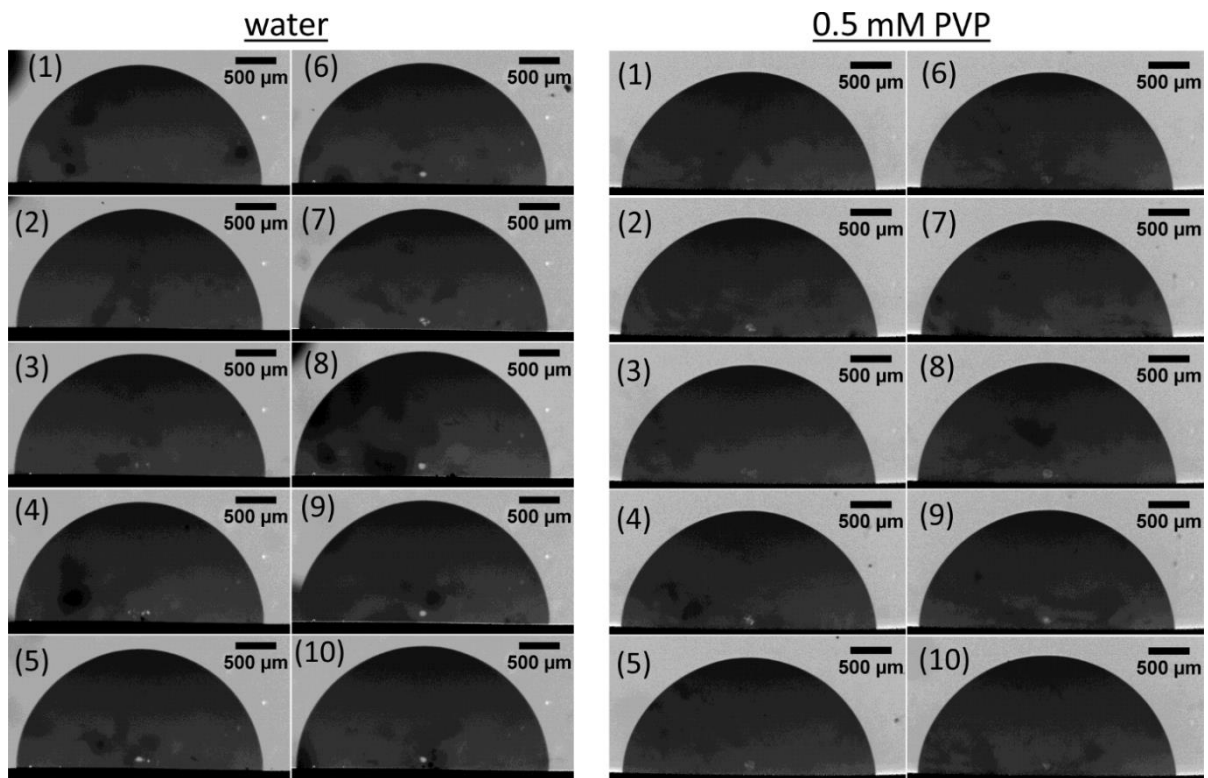


**Figure 62:** Frames from optical shadowgraphy of the laser-induced cavitation bubble at constant delay of  $93 \mu\text{s}$  after laser impact. Each frame represents an individual ablation event with the numbers written in the frames indicating the total number of laser pulses on the same target spot. Left: LAL of gold in pure water. Right: LAL of gold in 0.5 mM PVP solution.

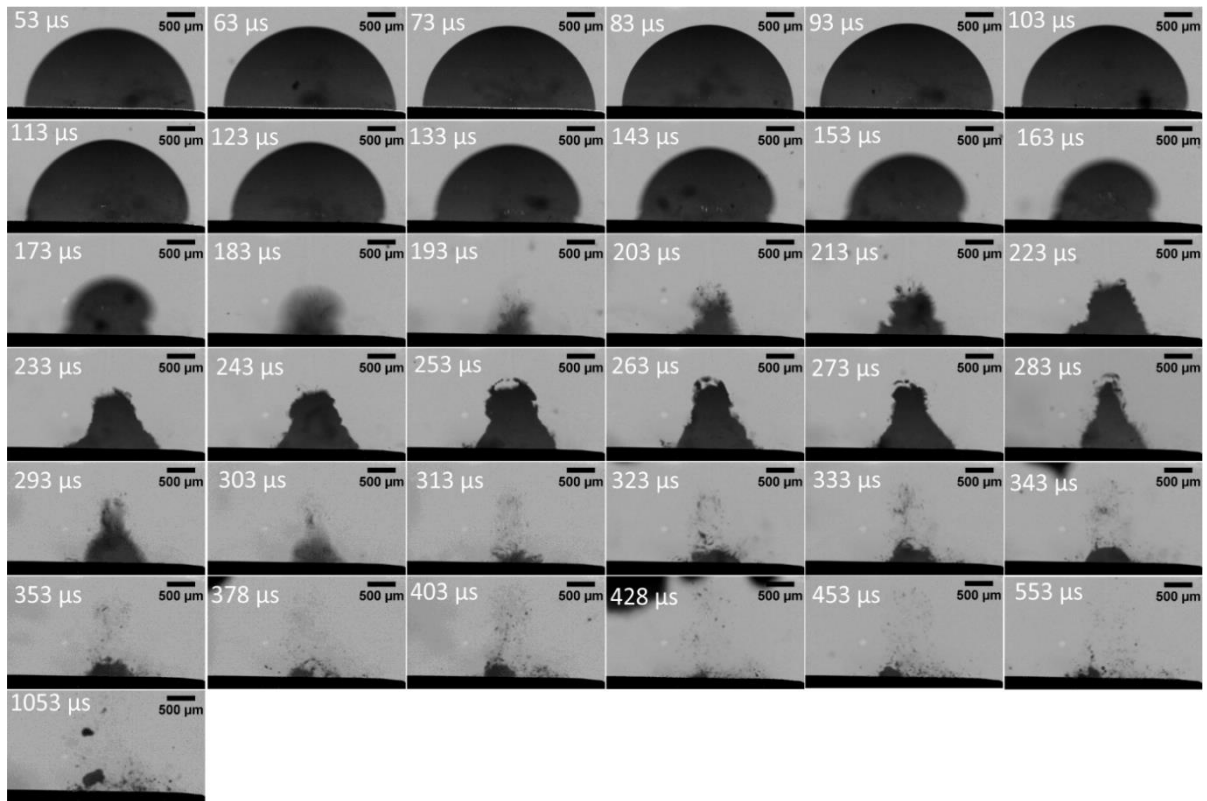


**Figure 63:** Frames from shadowgraphy indicating the cavitation bubble lifetime in pure water. For each frame a new laser pulse was used with constantly increasing camera delay. The target spot was the same for all laser pulses.

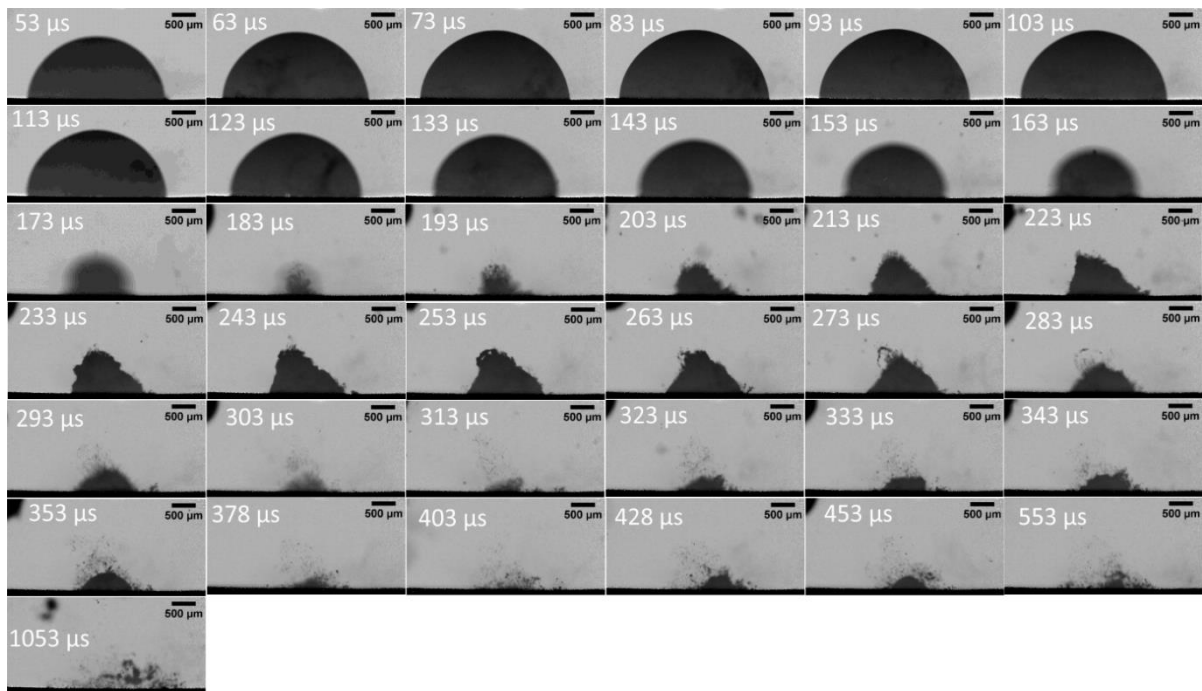


**Figure 64:** Frames from shadowgraphy indicating the cavitation bubble lifetime in 0.5 mM PVP solution. For each frame a new laser pulse was used with constantly increasing camera delay. The target spot was the same for all laser pulses.

*Small-angle X-ray scattering of nanoparticles trapped inside the cavitation bubble*

The experiments were performed at the cSAXS beamline at the Swiss Light Source (PSI Villigen, CH). Further experimental details are published elsewhere [192]. The resolution in Figure 65 is lower compared to the reference because it displays a single measurement, not the statistical mean of several thousand runs.

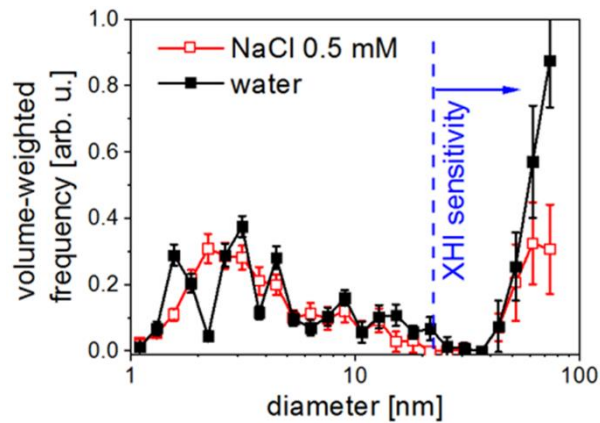


**Figure 65:** Volume-weighted size distributions obtained by in situ SAXS at the maximum extension of the cavitation bubble. While NaCl in the given concentration of 0.5 mM is known to produce smaller primary particles compared to LAL in water, time-resolved SAXS cannot resolve that difference. Changes in large particles size are detected though.

*Laser ablation in solutions of N-vinylpyrrolidone (NVP)*

This section contains additional data on the influence of the different additives used (NVP, PVP, NaCl) on the amount of generated and stabilized nanoparticle surface. Figure 66 shows the hydrodynamic surface-weighted size distributions from ADC analysis for low and high additive concentrations. In 10  $\mu\text{M}$  solutions the polymer PVP is more effective in generating nanoparticles < 10 nm compared to its monomer (NVP) (Figure 66a,c). This trend is maintained from laser ablation in 500  $\mu\text{M}$  solutions of the same additives (Figure 66b,d). While the size distribution in NVP shows a shoulder at 30 nm no such peak is identified in PVP solution. Obviously, both organic molecules physisorb to the gold nanoparticle surface but PVP is able to generate and maintain a higher surface compared to its monomer. Comparing NVA and PVP to the electrolyte NaCl, it is seen that at low (Figure 66e) and at high concentrations (Figure 66f) the ablation in NaCl yields a significant higher share of small particle, weighted by the surface.

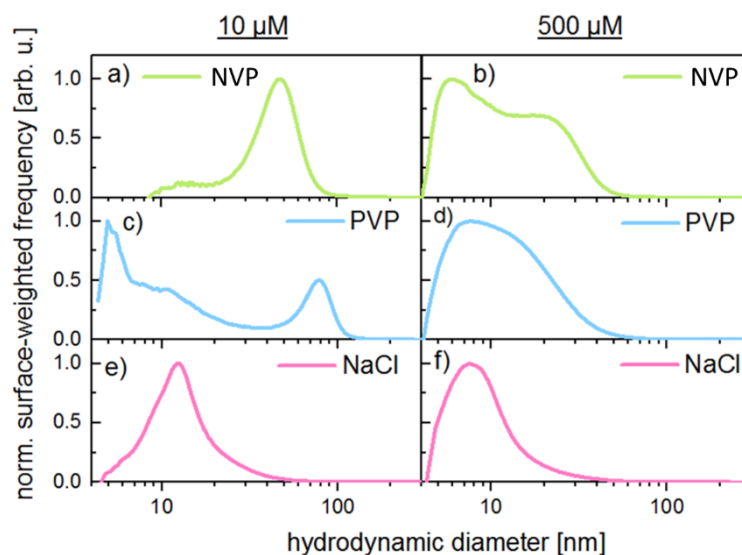


**Figure 66:** Surface-weighted particle size distributions from hydrodynamic ADC analysis. (a,c,e) Colloids in 10  $\mu\text{M}$  solutions of NVP, PVP, and NaCl. (b,d,f) Colloids in 500  $\mu\text{M}$  solutions of the same additives.

TEM images

The TEM images presented here are representatives for the raw data used to determine the size distribution histograms of laser-generated gold nanoparticles as shown in Figure 36 of the main article.

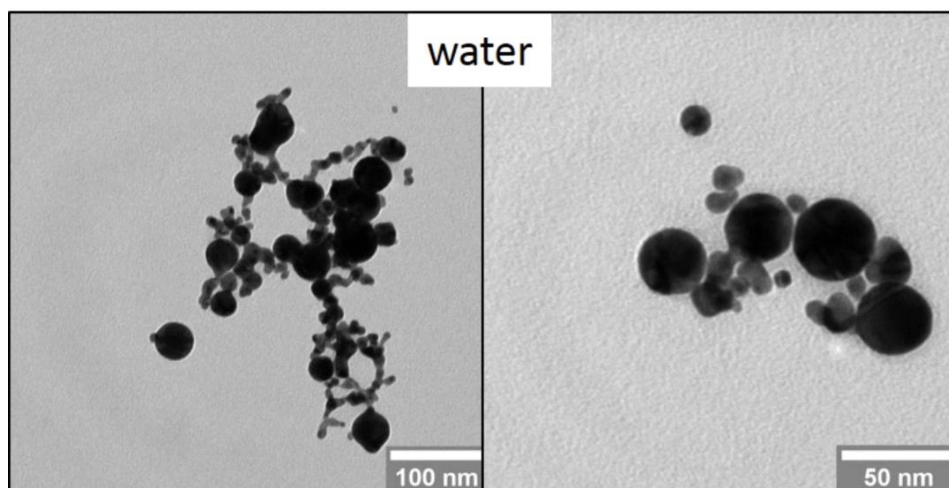


**Figure 67:** TEM images of gold nanoparticles laser ablated in pure water. The calculated number-weighted center of gravity diameter  $X_c$  is 17 nm and the volume-weighted median diameter  $D_{50}$  is 53 nm.

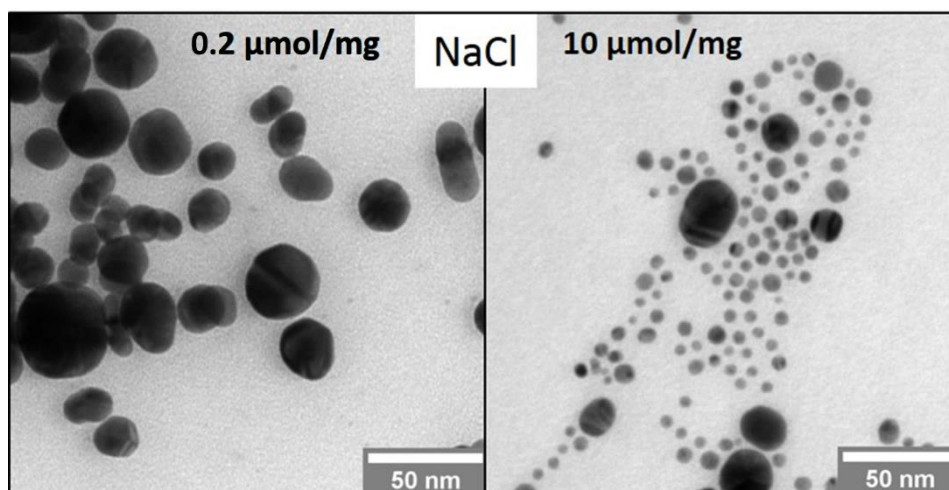


**Figure 68:** TEM images of gold nanoparticles laser ablated in NaCl solution. The images show nanoparticles obtained at AGRs of 0.2  $\mu\text{mol/mg}$  (left,  $X_c = 15$  nm and  $D_{50} = 29$  nm) and 10  $\mu\text{mol/mg}$  (right,  $X_c = 7$  nm and  $D_{50} = 10$  nm).

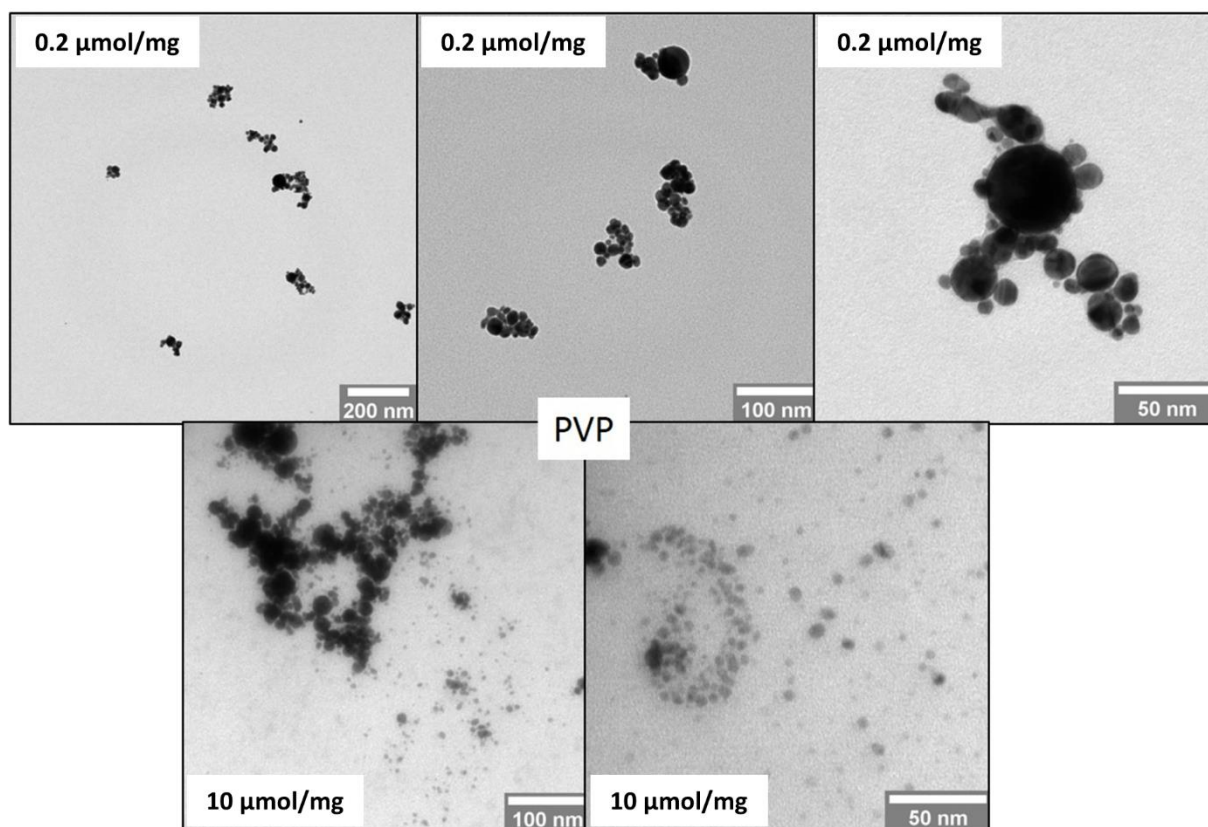


**Figure 69:** TEM images of gold nanoparticles laser ablated in PVP at AGRs of 0.2 μmol/mg (upper row,  $X_c = 13$  nm and  $D_{50} = 32$  nm) and 10 μmol/mg (lower row,  $X_c = 6$  nm and  $D_{50} = 32$  nm).

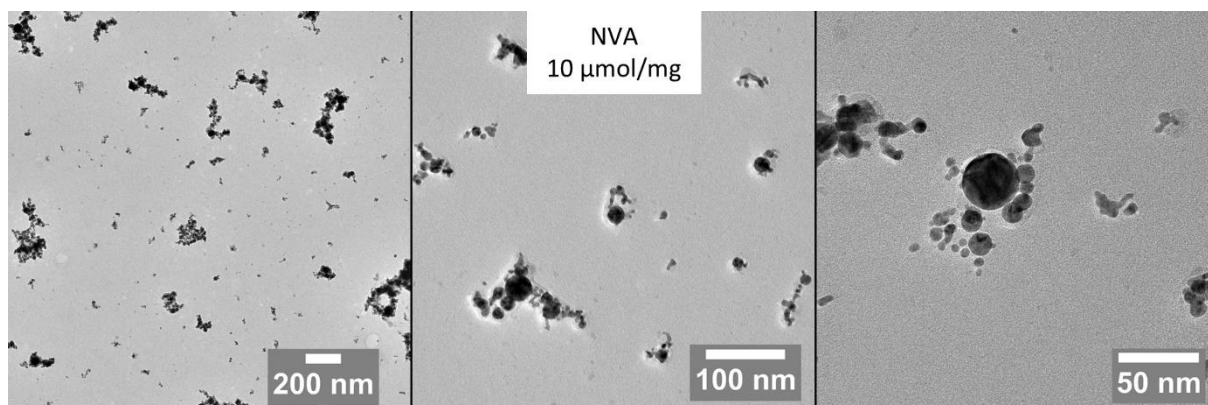


**Figure 70:** TEM images of gold nanoparticles laser ablated in NVA at an AGR of 10 μmol/mg ( $X_c = 8$  nm and  $D_{50} = 32$  nm).

## 9.1 List of figures

- Figure 1:** (a) Dependency of the threshold laser fluence for material ablation on the laser pulse duration. At about 100 ps pulse width the threshold fluence scales with  $F_{th} \sim \tau_p^{1/2}$  [24]. (b) Top: Time-resolved images of the plasma plume above a silver target during PLAL in pure water. The laser pulse width is 6 ns Red color indicates high emission intensity. Bottom: Decay of integrated plasma intensity of the same sample. The plasma lifetime is  $\sim 300$  ns [38]. ..... - 8 -
- Figure 2:** Collage of images that illustrate the fundamental processes occurring during the first millisecond after laser impact during PLAL with nanosecond lasers. (a) Scheme of the different processes and their time dependency [50]. The optically active plasma, which consists of excited species, transfers its energy to the liquid phase within a few microseconds. (b) Cavitation bubble radius as a function of time of laser pulses with 100 mJ and 50 mJ pulse energy. Derived from high-speed imaging of the bubble by shadowgraphy [18]. (c) Example of a laser-induced cavitation bubble at its maximum extension 120  $\mu\text{s}$  after laser impact. The center of the bubble is transparent due to diffusive illumination [29]. (d) High-speed image of the semispherical shockwave emerging away from the target (black vertical line) at different delays. After 1.4  $\mu\text{s}$  additional soundwaves that propagate parallel to the target are observed [18]. ..... - 10 -
- Figure 3:** Maximum bubble volume as a function of laser fluence with nanosecond pulse duration for two target geometries, a flat target (blue squares) and a wire (white squares). The dashed line represents a linear relationship according to a thermal model, with full energy transfer into cavitation bubble formation ( $>50$  J/cm<sup>2</sup>). The dashed-dotted line represents a linear relationship assuming a pure threshold model for ablation and bubble evolution. In the inset, the typical threshold fluence  $F_{th}$  behavior is shown [44]. ..... - 12 -
- Figure 4:** The electrostatic potential of a charged flat surface  $\Psi$  as a function distance  $X$  using the example of a positively charged surface [101]. The potential is a result of the charge density  $\sigma(X)$ . The surface potential is not experimentally accessible. The IHL of specifically adsorbed counterions ends at the IHP ( $\Psi_i$ ;  $X = \beta$ ). The OHL consist of solvated ions, starting at the IHP and ending at the OHP ( $\Psi_o$ ;  $X = d$ ). The OHP marks the beginning of the diffusive layer of counterions which results from the need of electroneutrality of the system. The extension of the diffusive layer can be calculated by linear approximation of the Poisson-Boltzmann differential equation (see Equation (4)). ..... - 19 -
- Figure 5:** Total interaction energy  $W$  as a function of the normalized distance  $\kappa D$  of two charged parallel plates according to the DLVO theory [102]. The repulsive contribution by the electric double layers  $W_R$  and the attractive contribution  $W_A$  by vdW forces are shown as dashed lines. At high surface charge density  $\sigma$ , a secondary minimum at medium distances occurs. It marks reversible agglomeration. At low distances, an energy barrier evolves that hinders the plates from aggregation if it exceeds the thermal energy  $k_B T$  significantly. At even shorter distances of the plates, the vdW attraction becomes superior resulting in irreversible aggregation of particles (primary minimum). - 22 -
- Figure 6:** Schemes of possible polymer mediated interactions between two approaching colloidal particles. (a) Bridging flocculation occurs at low surface coverage of particles with polymers. The polymer must have two active sites to anchor to two particles. (a) Steric stabilization requires full surface coverage of the particles. Interpenetration of the polymer shell is energetically an entropic unfavored. If the shells interpenetrate each other, e.g., because the solvent is at the  $\Theta$ -point, flocculation occurs (e). If on the other hand polymer-polymer interaction in is unfavored compression of the shells occurs when they spatially overlap. A restoring force results and flocculation is prevented (e). (c) Depletion stabilization is an effect of unbound free polymer in solution. At high concentrations, the approaching particles lead to polymer-solvent demixing in the gap. (d) Depletion

- flocculation occurs at medium concentrations of free polymer. The excluded volume around the particles that is not accessible of the polymer is reduced if the particles are in direct contact. The osmotic pressure difference decreases..... - 23 -
- Figure 7:** (a) Bulk dielectric function of gold as a function of the excitation wavelength. The solid curves represent experimental data for the real and imaginary part of the dielectric function taken from [115] by [113]. The dashed lines are derived from Equation (6) [113]. (b) Scheme of the effect of an incident electromagnetic wave on a spherical metal nanoparticle. The induced dipole, indicated by positive and negative signs, oscillates uniform across the nanosphere [114]..... - 26 -
- Figure 8:** (a) Particle diameters obtained by time-resolved SAXS of primary (blue dots) and secondary (here agglomerates) (black squares) particles confined inside the laser-induced cavitation bubble during PLAL as a function of the delay after laser impact (red dashed vertical line). The cavitation bubble was scanned at different heights above the target surface (right ordinate). The dotted vertical line at 150  $\mu\text{s}$  marks the collapse of the first cavitation bubble. [20]. (b) Relative particle fraction mass from SAXS as a function of the delay. The black solid line is the X-ray transmission of the oscillating cavitation bubble [30]. (c) Six individual frames of the third cavitation bubble at 320  $\mu\text{s}$  obtained by X-ray radiography with absorption contrast. The black curved vertical line intersecting the bubbles consist of dense ablated material that is emitted across the gas-liquid interface in a jet-like fashion. The scale bar is 1 mm [30]..... - 33 -
- Figure 9:** Graphical description of the experimental setup for in situ X-ray investigations. The structure of the ablation chamber and the role of the single pieces are described. A continuous gold target (ribbon) is transported upwards across the chamber, perpendicular to the incoming laser beam. The laser is focused on the target by a lens screwed in the outer wall of the chamber. The applied water flow is directed from the bottom to the top. (a) Simplified scheme of the setup. The framework of the chamber and the incoming X-ray beam are neglected. (b) Photograph of the 3D printed ablation chamber as designed and printed at the Karlsruhe Institute of Technology (KIT). The inner channels are visible due to decreased absorption of light at the thin structures. .... - 42 -
- Figure 10:** Sketch of the setup for imaging of the cavitation bubble by optical shadowgraphy. (a) Scheme of the centerpiece of the ablation chamber with the laser entering from the front perpendicular to the target. The side windows allow the visible light to enter the target and the transmitted intensity is recorded by the camera. The liquid flow from the bottom to the top of the chamber, the remaining parts of the chamber, and other equipment are omitted. (b) CAD design of the centerpiece highlighting the geometry of the flow channel and the front and side windows. (c) CAD-view from the side through the chamber. Scale bar accounts for (b) and (c) and is 5 mm..... - 44 -
- Figure 11:** Schemes that illustrate the scientific questions and applied methods that were used to solve them. The upper row (1 and 2) represents the ex situ studies that are presented in the sections 5.1.1 and 5.1.2. The bottom row (3+4) represents the in situ studies that are presented in the sections 5.2.1 and 5.2.2..... - 47 -
- Figure 12:** To reproduce the size distributions from PLAL, monomodal colloids of various sizes are synthesized and mixed in defined nominal mixing ratios (n.m.r.). Left: Scheme of the preparation path of defined bimodal colloids (adapted from reference [169]). In a first step, laser-generated particles are re-irradiated with a laser-wavelength close to the SPR peak of AuNP to fragment the particles and obtain monomodal colloids (top). The 50 nm-sample was obtained commercially. In a second step, the particles are mixed together in defined ratios according to the nanoparticle concentration of the initial colloids (bottom). One series of samples is made of colloids with overlapping size distributions, whereas another series is made of colloids with non-overlapping size distributions. Right: High-resolution TEM of a sample containing nanoparticles from the 7-nm and 50-nm samples in a n.m.r. of one. The inset shows an area of the image with higher magnification. . - 49 -

**Figure 13:** Scheme of the laser-induced cavitation bubble at the delay after laser impact of maximum bubble extension. In the top left, the semispherical bubble on a smooth (= undamaged) target spot is shown. In contrast, after multiple pulses on the same spot, the resulting crater changes the bubble shape to almost spherical, with additional small bubbles surrounding it in the liquid phase. The schematic diagrams in the bottom outline line scans across the target surface. In the case of a smooth surface, no indentations are observed. A re-irradiated target, in contrast, exhibits a distinct ablation crater. .... - 51 -

**Figure 14:** STEM images and resulting number- and volume-weighted size distributions of the pure gold colloids S7 (a–c), S10 (d–f) and S50 (g–i). The left column shows number-weighted size distributions with additional information of cumulative volume-weighted sizes (blue lines). The middle column shows the calculated volume-weighted size distributions. The right column shows representative STEM images of the pure AuNP. (For interpretation of the references to colour in this figure legend, the reader is referred to the web version of this article.) ..... - 59 -

**Figure 15:** Volume-weighted particle size distributions of the pure gold colloids obtained with STEM, SAXS (MC), ADC and DLS. The asterisk indicated that the methods are sensitive to different physical properties of the particles (e. g. hydrodynamic or volume equivalent diameter). All size fractions are fitted with a Gaussian envelope. .... - 61 -

**Figure 16:** Volume-weighted sizes of the underlying fractions of mixtures of S7-S50 (a-b) and S7-S10 (c-d) as function of the nominal mixing ratio. (a) Size evolution of S7 in mixtures of S7-S50. (b) Size evolution of S50 in mixtures of S7-S50. (c) Size evolution of mean particle size in mixtures of S7-S10 (SAXS, Mie-Gans). (d) Size evolution of mean particle size and size fractions in case of ADC in mixtures of S7-S10 (DLS, ADC). The dashed yellow horizontal lines in a-b are guides to the eye and indicate the size obtained of the pure colloids by STEM and their standard deviations. The same accounts for the yellow and purple lines in c-d, which indicate the size of pure S10 (purple) and pure S7 (yellow), respectively. (For interpretation of the references to colour in this figure legend, the reader is referred to the web version of this article.) ..... - 64 -

**Figure 17:** Experimentally obtained mixing ratios of S7-S50 and deviation from nominal mixing ratios. (top) Experimental mixing ratio as function of nominal mining ratio. The dashed diagonal indicates 1 to 1 conformity and serves as guide to the eye. (bottom) Modulus average deviation from nominal mixing ratios as function of applied analytical technique. .... - 66 -

**Figure 18:** Experimental setup used for simultaneous LAL and imaging by shadowgraphy in liquid flow: The self-printed ablation chamber was made of ABS, and it had three glass windows, one perpendicular to the incoming laser beam and two parallel windows that were perpendicular to the optical light source and the camera. MilliQ water was pumped upwards across the ablation chamber by a peristaltic pump to remove persistent gas bubbles and nanoparticles. The pump stroke was removed by coupling a sealed bottle between the pump and ablation chamber. The silver target was fixed by double-sided tape on the back of the chamber, and the laser beam was focused by a 75-mm lens perpendicular to the surface of the target. .... - 73 -

**Figure 19:** (a) Frames of the single laser pulse-induced cavitation bubbles on a 1.0 mm-thick silver target deposited after 1-1,000 preceding pulses on the same spot. Each frame was recorded at a constant delay of 83  $\mu$ s after laser impact with a camera gating time of 10  $\mu$ s. After a single laser pulse, the cavitation bubble was almost hemispherical (sphericity = 1.01), and it exhibited a sharp boundary with the surrounding liquid phase. With the increasing number of pulses on the same target position (0.2 Hz, 20 mJ), the boundary became rougher, exhibited daughter microbubbles, and, finally, the shape of the bubble was transformed to an approximately spherical shape (sphericity = 0.94); (b) Line scans of the craters on the silver target recorded by confocal 3D microscopy. All of the datasets were normalized to the zero position. As the number of laser pulses increased, the

crater became deeper and wider. The latter accounts especially for the first 250 pulses. After 1,000 pulses, the crater approached the target thickness..... - 76 -

**Figure 20:** Evolution of the volume of the cavitation bubble as a function of the delay time after laser impact on the silver target: (a) The grey bar highlights the gating time of the camera (10  $\mu$ s). The maximum size and the total lifetime of the bubble decreased as the number of laser pulses increased because of the damage to the surface of the target, while the lifetime of the first bubble remains unaffected. When comparing the two datasets, it is apparent that the delay in the maximum extension of the bubble remained unaffected; (b) Selected frames of the first cavitation bubble induced on a non-irradiated target surface; (c) Selected frames of the first cavitation bubble induced on a target that experienced 1,000 pulses in advance. .... - 77 -

**Figure 21:** (a) Total ablation mass; (b) ablated mass per pulse (ablation rate); (c) volume of the cavitation bubble; (d) silver mass concentration per cavitation bubble volume (mass concentration). The total ablation mass increases quickly within the first 100 to 200 pulses, after which it increases slower. This is highlighted by the ablation mass per pulse, which follows an exponential decay, which is calculated from the first derivative of the exponential fit (black dashed line in (a)) to the total ablation mass. .... - 79 -

**Figure 22:** (a) Crater depth,  $L$ , crater surface diameter,  $D$ , and aspect ratio,  $L/D$ , as functions of the number of laser pulses. The increase of  $D$  and  $L/D$  shows the ablation of the crater wall with increasing depth of the crater. The target is not eroded all the way through even after 1,000 pulses; (b-e) Selected images obtained from confocal 3D microscopy that were used to analyze the target.... - 81 -

**Figure 23:** Analysis of the silver nanoparticles by AUC (a-c) and scanning HR-TEM (d,e): The AUC size distributions are normalized to the respective minimum peak diameter. (a) Mass-weighted nanoparticle size distributions of colloids obtained from craters drilled by 10, 250, 500, and 1,000 previous pulses. The AUC was operated at 3,000 rpm to detect particles up to several tens of nanometers in diameter. In (e), the colored background highlights the different peaks with the peak diameters plotted versus the number of pulses; (b) Number-weighted frequency of nanoparticles when operating the AUC at 3,000 rpm; (c) Combined normalized size distributions achieved from measurements at high (30,000 rpm, black lines) and low angular speed (3,000 rpm, red lines). High g-force AUC analysis indicated the presence of small nanoclusters < 3 nm as the dominant particle species in all samples; (d) Same data as shown in (c) but weighted by particle number instead of mass. The images from scanning HR-TEM confirmed the presence of nanoclusters (10 pulses in (f), 500 pulses in (g), and 1,000 pulses in (h)). .... - 84 -

**Figure 24:** Principals of bimodality of particle size distributions obtained by PLAL. (a) Laser-generated colloids are made of several size fractions. The smallest fraction, defined as primary particles, consists of small solid spheres ( $d \leq 10$  nm). Larger particles are defined as secondary particles. These can be split into large solid spheres ( $d > 10$  nm) and aggregates ( $d > 100$  nm). (b) Sketch of a typical particle size distribution of gold nanoparticles synthesized by PLAL and obtained from analytical disc centrifugation. The dashed lines show the contribution of primary and secondary nanoparticles to the overall size distribution. .... - 88 -

**Figure 25:** Scheme of the size ranges of scattering objects (nanoparticles) that are accessible by SAXS (blue rectangular area) and XHI (three red curves). The size distribution of a laser-generated colloid is illustrated by the green curve. XHI shows the advantage of easy tunability of the sensitivity maximum to various particle sizes. Sensitivity of XHI is adapted from [255]. .... - 90 -

**Figure 26:** Scheme of the experimental setup of the time-resolved SAXS experiment with a continuously moving gold ribbon target, the supply and exhaust of the water (respectively NaCl solution) from the bottom to the top, and the laser beam entering the chamber from the side

through a sealed lens. The X-ray path intersects the interaction area and is recorded by a photodiode (direct beam) and 2D detector (scattering). ..... - 96 -

**Figure 27:** Relative cavitation bubble radius at 1 mm (black line, bubble top) and 0.5 mm (red line, bubble center) height above the gold target recorded via X-ray transmission. Hatched areas mark the region of interest for particle species analysis at the maximal extension of first bubble, second bubble, and after the final collapse..... - 99 -

**Figure 28:** (top) SAXS curves from in situ measurements in Kratky representation ( $I(q) \cdot q^2$ ) as a function of scattering vector  $q$  at a height of 0.5 mm above target and a delay of 100  $\mu$ s after laser impact and corresponding unified and MC fits. Both fit the experimental data equally well. (bottom) The 5 point weighted moving average of the MC histogram data is plotted vs the corresponding particle diameter. Insets show large solid spheres appearing in ex situ TEM images. .... - 100 -

**Figure 29:** Left: particle size evolution (in situ SAXS) of small/primary and large secondary particles and agglomerates in pure water (full blue symbols) and NaCl solution (open red symbols) as a function of delay after laser impact for two different heights (0.5 mm: squares; 1 mm: circles) above the target. The arrows indicate trends of size change with NaCl addition. The spatial positions are illustrated by an inset scheme. Right: volume ratio between large and primary particle fraction as a function of delay and height above target in pure water (blue bars) and NaCl solution (red bars). - 101 -

**Figure 30:** Ex situ histograms of transmission electron microscopy (gray bars) combined with results from analytical disc centrifugation (water: blue dots; NaCl: red dots) of gold nanoparticles laser-generated in pure water (a) and NaCl solution (c). The asterisk indicates the difference of hydrodynamic  $d_H$  and Feret diameter  $d_F$ . All size distributions are volume-weighted for direct comparison with results from small-angle X-ray scattering. Representative electron microscopic pictures show agglomerated structures for water (b) and stable particles for NaCl (d). Result of subtraction of the TEM histogram of particles in water from that of particles in NaCl (e). The insets exemplify the size reduction of large spherical particles when using NaCl. Comparison of hydrodynamic ( $x_c$  from ADC) and Feret ( $d_{50}$  from TEM) diameter in pure water and NaCl reveals drastic particle size reduction by salt ions of both the hydrodynamic agglomerates and Feret diameter of solid particles (f). ..... - 103 -

**Figure 31:** UV/Vis spectra of gold nanoparticles in water and NaCl solution. The primary particle index (PPI) and  $\zeta$ -potential are given in the table. .... - 105 -

**Figure 32:** Ex situ SAXS curves and MC fits from gold nanoparticles prepared in water and NaCl solution (top). Subtraction of resulting volume weighted size distributions support that in NaCl solution the fraction of small primary particles ( $\sim 9$  nm) is more pronounced compared to water as liquid (bottom). According to this, a larger fraction of large particles (secondary particles and agglomerates  $\sim 40$  nm) are found in water solutions. .... - 106 -

**Figure 33:** Images of the Pt foil acting as a Hartmann mask for in situ experiments obtained by optical microscopy. Front of the mask in reflected (a) and transmitted light mode (b). The laser-drilled holes are funnel-shaped on the front side (side at which the laser beam impinges). Back of the mask in reflected (c) and transmitted light mode (d). Sketch of the XHI approach with the incoming X-ray beam being split into multiple beamlets by the Hartmann mask, and undergoing absorption, differential phase shift (deflection) and diffuse scattering (broadening) when crossing the cavitation bubble and the confined nanoparticles (e). .... - 113 -

**Figure 34:** Scattering sensitivity on nanoparticles as function of the scattering object size for the given setup. The blue dashed-dotted line indicates the size interval above 50 % relative sensitivity (a). Scattering signal as function of the delay after laser impact obtained at the center of the cavitation bubble (inset shows the transmission signal together with the region of interest) (b). Scattering

signals of gold nanoparticles in pure water (black squares), NaCl- (red circles) and PVP-solution (blue triangle) (both 0.5 mM). The shaded curve represents the change in X-ray transmission starting from 1 (0 % intensity change) before laser arrival. Error bars are the standard deviation between several runs..... - 116 -

**Figure 35:** (a) Volume-weighted hydrodynamic median diameter obtained by analytical disc centrifugation and (b) related specific surface area of gold nanoparticles in PVP and NaCl as function of the additive-to-gold ratio (AGR). The dashed-dotted horizontal lines mark the reference experiments from LAL in pure water. Nanoparticle mass concentrations are obtained by optical UV/Vis extinction spectroscopy. (c) Volume-weighted particle size distributions of colloids in low and high additive concentrations derived from ADC analysis. (d) Hydrodynamic size fractions of particles < 20 nm and < 50 nm. The data is derived from the ADC size distributions in (c). The results display the properties of the particles in their nascent hydrodynamic environment..... - 118 -

**Figure 36:** Representative TEM histograms of AuNP in pure water, NaCl and PVP at AGRs of 0.2 and 10  $\mu\text{mol}/\text{mg}$  (left column). The envelopes shown as solid red lines are obtained by lognormal fitting and the center of gravity  $X_c$  is displayed. The middle column shows the calculated volume-weighted histograms of the same samples with corresponding median diameters  $D_{50}$ . In the right column the volume-weighted histograms are further weighted by the XHI sensitivity curve shown in Figure 34a. The plot in the lower right corner sums up the volume-weighted primary particle median diameters as a function of the type and AGR of additive. .... - 122 -

**Figure 37:** (a) Cavitation bubble dynamics as function of the delay from the laser impact. The PVP molecules do not affect the dynamics of the bubble. (b) Results of image analysis of the cavitation bubble at its maximum extension at 93  $\mu\text{s}$  after laser impact on the target showing no difference between pure water and 500  $\mu\text{M}$  PVP solution. (c) UV/Vis extinction spectrum of a 500  $\mu\text{M}$  PVP solution. The solution is transparent at the laser wavelength of 1064 nm. Inset: Dynamic viscosity of pure water and a 0.5 mM PVP solution. .... - 124 -

**Figure 38:** Volume-weighted sizes of the underlying fractions of mixtures of S7-S50 (a-b) and S7-S10 (c-d) as function of the nominal mixing ratio. (a) Size evolution of S7 in mixtures of S7-S50. (b) Size evolution of S50 in mixtures of S7-S50. (c) Size evolution of mean particle size in mixtures of S7-S10 (SAXS, Mie-Gans). (d) Size evolution of mean particle size and size fractions in case of ADC in mixtures of S7-S10 (DLS, ADC). The dashed yellow horizontal lines in a-b are guides to the eye and indicate the size obtained of the pure colloids by STEM and their standard deviations. The same accounts for the yellow and purple lines in c-d, which indicate the size of pure S10 (purple) and pure S7 (yellow), respectively. .... - 154 -

**Figure 39:** UV/Vis spectra of mixtures of S7 and S50 (red lines) and respective fits by Mie-Gans theory (black lines). The corrected nominal mixing ratios are given in every partial diagram. All spectra are normalized to the maximum of the respective surface plasmon resonance peaks. .... - 155 -

**Figure 40:** UV/Vis spectra of defined colloids S7, S10 and S50 (red lines) and respective fits by Mie-Gans theory (black lines). The corrected nominal mixing ratios are given in every partial diagram. All spectra are normalized to the maximum of the respective surface plasmon resonance peaks. .... - 155 -

**Figure 41:** UV/Vis spectra of mixtures of S7 and S10 (red lines) and respective fits by Mie-Gans theory (black lines). The corrected nominal mixing ratios are given in every partial diagram. All spectra are normalized to the maximum of the respective surface plasmon resonance peaks. .... - 156 -

**Figure 42:** Size distributions obtained from analytical disc centrifugation of particle mixtures of S7-S50. All curves are normalized to their maximum. The corrected nominal mixing ratios are given in the caption. The middle and right diagrams show the same data but the mode of S50 is enlarged on the right. .... - 157 -

- Figure 43:** Size distributions obtained from analytical disc centrifugation of particle mixtures of S7-S10. All curves are normalized to their maximum. The corrected nominal mixing ratios are given in the caption. This figure highlights the ability of disc centrifugation to distinguish between the peaks of S7 and S10. Hence, peak deconvolution is justified..... - 157 -
- Figure 44:** Exemplary size distributions obtained from analytical disc centrifugation of particle mixtures of S7-S10 with applied peak deconvolution. All curves are normalized to their maximum..... - 158 -
- Figure 45:** SAXS analysis of the colloids S7, S10 and S50. The experimental curves (black lines) are plotted together with fits to the data by the unified fit (red lines). ..... - 158 -
- Figure 46:** SAXS analysis of the colloids S7, S10 and S50. The experimental curves (black lines) are plotted together with fits to the data by the Monte Carlo method (red lines). ..... - 158 -
- Figure 47:** SAXS analysis of the mixtures of S7-S10. The experimental curves (black lines) are plotted together with fits to the data by the unified fit (red lines). The nominal mixing ratios (n.m.r.) are given in the individual diagrams. .... - 159 -
- Figure 48:** SAXS analysis of the mixtures of S7-S50. The experimental curves (black lines) are plotted together with fits to the data by the unified fit (red lines). The corrected nominal mixing ratios (n.m.r.) are given in the individual diagrams. .... - 160 -
- Figure 49:** SAXS analysis of the mixtures of S7-S10. The experimental curves (black lines) are plotted together with fits to the data by the Monte Carlo method (red lines). The nominal mixing ratios (n.m.r.) are given in the individual diagrams. .... - 161 -
- Figure 50:** SAXS analysis of the mixtures of S7-S50. The experimental curves (black lines) are plotted together with fits to the data by the unified fit (red lines). The corrected nominal mixing ratios (n.m.r.) are given in the individual diagrams. .... - 162 -
- Figure 51:** Demonstration of the Mie Gans fit quality for mixtures of the samples S7 and S50. For large excess of small nanoparticles (n.m.r. = 100) the fit quality is good. When the large particle fraction becomes dominant (n.m.r. = 0.5 - 1) the fit does not match the experimental data any more. This is caused by the inability to vary the fitting parameters freely and the design of the algorithm to fit spectra obtained from monodisperse colloids. .... - 163 -
- Figure 52:** Using ligand-free AuNPs would have been preferable for the study. However, it was necessary to sterically stabilize the nanoparticles to prevent agglomeration and aggregation over the entire duration of the study (several months). As shown, DLS from fully stabilized unligated particles returns a smaller hydrodynamic radius and therefore a higher sensitivity on sizes and different fractions in the mixture. The mPEG-SH concentration used to stabilize the colloid was 10  $\mu\text{M}$  in total, which is identical to the concentration for the samples in the manuscript. The ligation provides a well-defined, stabilized state for the suspension to compare the different measurements, also in terms of storage time, transport and final preparation..... - 163 -
- Figure 53:** Drain of microbubbles from the ablation by a liquid flow: Frames of the interior of the ablation chamber at different delays after laser impact with an applied volume flow of water (11 ml/min) are shown. The cavitation bubble vanished after 500-600  $\mu\text{s}$  but some persistent microbubbles (exemplary marked by arrows) remained present inside the chamber until 100,000  $\mu\text{s}$  (= 0.1 s). As the applied laser repetition rate was 0.2 Hz, equal to one laser pulse each 5 s, the assumption of complete removal of persistent bubbles (and residual nanoparticles) between two laser pulses was validated. .... - 164 -
- Figure 54:** Nanoclusters were formed not only during LAL of Ag (see main manuscript) but also during LAL of gold, and even for single laser pulses. The TEM images of gold nanoparticles and nanoclusters obtained by single laser pulses deposited in the craters drilled by 100 (a, c) and 500 (b, d) previous pulses, respectively, are presented. The target thickness was 1.0  $\mu\text{m}$  and the pulse laser pulse energy

was 10 mJ. The particle concentration on the grid was increased by drop casting 10-15 drops. The images demonstrate that the nanoclusters were not produced by LFL of nanoparticles in the 10 pulse experiments, and were further not formed on the grid by the dissolution of silver ions. The scale bars in the insets of (a, b) are 10 nm and 5 nm in (c, d). ..... - 165 -

**Figure 55:** Reference experiments excluded large changes of the laser fluence by the crater shape/depth upon drilling a hole in the 1.0 mm thick silver targets. The total ablated silver volume and cavitation bubble volume at maximum extension after 10 and 100 pulses are given in (a, c) and (b, d). The red bars represent fixed focusing conditions as applied in all experiments presented in the main manuscript. The blue bars represent the reference experiments with the position of the focusing lens shifted 1 mm away from the target surface to mimic the fluence at the crater bottom after up to 1,000 pulses (Figure 22, main manuscript). Both the ablation and the bubble volume did not change significantly at  $z = -1$  mm; (e) Comparison of the maximum bubble volume induced by the first 10 laser pulses for  $z = -1$  mm and  $z = 0$  mm; (f) Total ablation volume of Ag as a function of the number of pulses. The volume increased quickly for the first 100-200 pulses but much slower afterward. The final ablated silver volume after 500-1,000 pulses was approximately  $0.08 \text{ mm}^3$  and was hence negligible with respect to the volume  $> 1 \text{ mm}^3$  of the cavitation bubble..... - 166 -

**Figure 56:** Ag particle size distributions of colloids, fabricated under identical conditions, measured by AUZ at angular velocities of 30,000 rpm to detect particles  $<< 10$  nm (a) and 3,000 rpm to detect particles  $> 5$  nm (b). The distributions were obtained by applying 10 laser pulses on a non-irradiated (a) silver surface and after 1,000 pulses (b). The reproducibility in terms of the peak integrals was low between the individual syntheses. Therefore, no conclusions on the amount of the respective particle size fractions were possible. The pure detection of nanoparticles and nanoclusters size remained unaffected by this issue as no clusters were detected by AUC in pure water. All size distributions were normalized to the respective peak of minimum diameter. .... - 167 -

**Figure 57:** Volume-weighted size distributions obtained from Monte Carlo (MC) analysis of in situ SAXS data (shown in Figure 28). The size distributions of particles in water (left) and 0.5 mM NaCl solution (middle) differ significantly at sizes above 10 nm. This is clarified by a diagram plotting the volume fraction of particles smaller than 10 nm and 20 nm as function of the ablation medium (right). This fraction of small particles is higher in saline solution. .... - 168 -

**Figure 58:** Left: Particle mass in dependence of the lateral position inside the ablation chamber volume. Negative lateral positions are representing distinct time delays after the laser impact. The zero position marks the target center. Right: Ratio of large to small particle fraction abundance in pure water compared to micromolar NaCl solution as a function of lateral position and height above target (black hemisphere represents maximum extension of the cavitation bubble). In red areas the amount of large particles in is higher compared to saline solutions. .... - 168 -

**Figure 59:** Volume-weighted particle size distributions measured by ADC in dependence of the type of additive (left: PVP; right: NaCl) and the effective fluence ( $27 \text{ J/cm}^2$  and  $36 \text{ J/cm}^2$ ). Except for the applied fluence the experimental parameters are the same compared to the ex situ ablations in the main article..... - 169 -

**Figure 60:** UV/Vis extinction spectra of gold nanoparticles synthesizes by LAL in pure water (a), 0.5 mM NaCl solution (b), and 0.5 mM PVP solution. The interband absorption at a wavelength of 380 nm was used to obtain a calibration function for the given gold concentration, which was determined by standard gravimetric analysis (d). .... - 170 -

**Figure 61:** Scheme of the 3D-printed liquid flow ablation chamber made of ABS for simultaneous shadowgraphic imaging (top view) of the cavitation bubble during laser ablation (side view). .... - 171 -

**Figure 62:** Frames from optical shadowgraphy of the laser-induced cavitation bubble at constant delay of  $93 \mu\text{s}$  after laser impact. Each frame represents an individual ablation event with the numbers

- written in the frames indicating the total number of laser pulses on the same target spot. Left: LAL of gold in pure water. Right: LAL of gold in 0.5 mM PVP solution. .... - 172 -
- Figure 63:** Frames from shadowgraphy indicating the cavitation bubble lifetime in pure water. For each frame a new laser pulse was used with constantly increasing camera delay. The target spot was the same for all laser pulses. .... - 173 -
- Figure 64:** Frames from shadowgraphy indicating the cavitation bubble lifetime in 0.5 mM PVP solution. For each frame a new laser pulse was used with constantly increasing camera delay. The target spot was the same for all laser pulses. .... - 174 -
- Figure 65:** Volume-weighted size distributions obtained by in situ SAXS at the maximum extension of the cavitation bubble. While NaCl in the given concentration of 0.5 mM is known to produce smaller primary particles compared to LAL in water, time-resolved SAXS cannot resolve that difference. Changes in large particles size are detected though..... - 175 -
- Figure 66:** Surface-weighted particle size distributions from hydrodynamic ADC analysis. (a,c,e) Colloids in 10  $\mu$ M solutions of NVP, PVP, and NaCl. (b,d,f) Colloids in 500  $\mu$ M solutions of the same additives. .... - 176 -
- Figure 67:** TEM images of gold nanoparticles laser ablated in pure water. The calculated number-weighted center of gravity diameter  $X_c$  is 17 nm and the volume-weighted median diameter  $D_{50}$  is 53 nm..... - 177 -
- Figure 68:** TEM images of gold nanoparticles laser ablated in NaCl solution. The images show nanoparticles obtained at AGRs of 0.2  $\mu$ mol/mg (left,  $X_c$  = 15 nm and  $D_{50}$  = 29 nm) and 10  $\mu$ mol/mg (right,  $X_c$  = 7 nm and  $D_{50}$  = 10 nm). .... - 177 -
- Figure 69:** TEM images of gold nanoparticles laser ablated in PVP at AGRs of 0.2  $\mu$ mol/mg (upper row,  $X_c$  = 13 nm and  $D_{50}$  = 32 nm) and 10  $\mu$ mol/mg (lower row,  $X_c$  = 6 nm and  $D_{50}$  = 32 nm)..... - 178 -
- Figure 70:** TEM images of gold nanoparticles laser ablated in NVP at an AGR of 10  $\mu$ mol/mg ( $X_c$  = 8 nm and  $D_{50}$  = 32 nm). .... - 178 -

## 9.2 List of tables

<b>Table 1:</b> Summary of the used lasers for nanoparticle synthesis and the applied analytical instruments. ....	- 39 -
<b>Table 2:</b> Specifications of the chemicals used in the experiments. ....	- 41 -
<b>Table 3:</b> <i>Number-weighted mode diameters (<math>d_n</math>) and volume-weighted median (<math>d_{50}</math>) obtained of the pure colloids analyzed by STEM. Median includes information on the entire size distribution and does not require an error bar.</i> .....	- 56 -
<b>Table 4:</b> Summary of the volume-weighted size and volume/mass information obtained from the pure colloids S7, S10 and S50 with all applied methods. In the case of S50 also the volume ratio of the two size fractions was calculated. ....	- 62 -

## **10 Curriculum Vitae**

**„Der Lebenslauf ist in der Online-Version aus Gründen des Datenschutzes nicht enthalten.“**

## **11 Declaration**

Hiermit versichere ich, dass ich die vorliegende Arbeit mit dem Titel

„Size evolution of laser-generated nanoparticles before and after cavitation  
bubble confinement“

selbst verfasst und keine außer den angegebenen Hilfsmitteln und Quellen benutzt habe, und dass die Arbeit in dieser oder ähnlicher Form noch bei keiner anderen Universität eingereicht wurde.

Essen, im Mai 2019

---

Alexander Letzel

## 11.1 Declaration of scientific contributions

The present thesis includes work that has been published in cooperation with co-authors, with my own contributions declared as follows:

### Chapter 5.1.1

Alexander Letzel, Bilal Gökce, Andreas Menzel, Anton Plech, Stephan Barcikowski

*Primary particle diameter differentiation and bimodality identification by five analytical methods using gold nanoparticle size distributions synthesized by pulsed laser ablation in liquids*, Appl. Surf. Sci. 435 (2018) 743-751.

Declaration of own contribution: The experiments, including particle preparation and colloidal analysis, were performed by AL. As an exception, SAXS measurements at the Paul Scherrer Institute were performed by AM, while AL prepared the samples just-in-time. Analysis of 1D-SAXS data was performed by AL. AP contributed to the discussion of the results with a focus on SAXS. The draft and corrections to the manuscript were written by AL. BG and SB supervised the study. The manuscript was revised by BG, AP, and SB.

### Chapter 5.1.2

Alexander Letzel, Marco Santoro, Stefan Reich, Anna Rosa Ziefuß, Julia Frohleiks, Anton Plech, Enza Fazio, B. Gökce, Fortunato Neri, and Stephan Barcikowski

*How the re-irradiation of a single ablation spot affects cavitation bubble dynamics and nanoparticles properties in laser ablation in liquids*, Appl. Surf. Sci. 473 (2018) 828-837.

Declaration of own contribution: The experimental design was done by AL and MS with equal contributions. Preliminary and initial experiments were also performed by AL and MS together. The overall exchange between AL and MS was vast. Final experiments were conducted and analyzed by AL. AZ contributed to the identification of nanoclusters. JF contributed to the surface analysis of the targets. SR and AP contributed by paving the way towards the experimental design by discussion and sharing of expertise. The draft and corrections to the manuscript were done by AL. BG, FN, and SB supervised the study and revised the manuscript.

### Chapter 5.2.1

Alexander Letzel, Bilal Gökce, Philipp Wagener, Shyjumon Ibrahimkutty, Andreas Menzel, Anton Plech, Stephan Barcikowski

*Size quenching during laser synthesis of colloids happens already in the vapor phase of the cavitation bubble*, J. Phys. Chem. C 121 (2017) 5356-5365.

Declaration of own contribution: Initial experiments at the Paul Scherrer Institute were performed by AP, PW, SB, and SI under the supervision and assistance of AM. Data reduction was done by AM and AP. PW prepared several figures and the first draft of the manuscript. Additional experiments at the Paul Scherrer Institute and the University of Duisburg-Essen were done by AL as was the final data analysis, including SAXS data. Restructuring of the manuscript was done by AL as well as the replacement of a significant share of the initial draft. Most figures were done by AL. BG, AP, and SB supervised the work and also revised the manuscript.

### Chapter 5.2.2

Alexander Letzel, Stefan Reich, Tomy dos Santos Rolo, Alexander Kanitz, Jan Hoppius, Alexander Rack, Margie Olbinado, Andreas Ostendorf, Bilal Gökce, Anton Plech, Stephan Barcikowski

*Time and mechanism of nanoparticle functionalization by macromolecular ligands during pulsed laser ablation in liquids*, Langmuir 35 (2019) 3038-3047.

Declaration of own contribution: Experiments at the European Synchrotron Radiation Facility were performed by AP, SR, and AL under the lead of AP. AR and MO contributed as local supervisors and contacts. The collected data were analyzed by SR and are presented as a figure in the manuscript. Preliminary discussions and discussions during data analysis were aided by TdSR. AK, JH, and AO contributed by preparing the perforated foil used as a Hartmann mask. AL performed the preliminary experiments as well as additional experiments. AL prepared most of the figures and prepared the draft of the manuscript. Overall, SR and AL contributed equally to the work. BG, AP, and SB supervised the work and revised the manuscript.

## 12 Publications and conference contributions

During this thesis, several peer-reviewed articles and conference contributions – posters and oral presentations – were published. All contributions are listed below, starting from articles in peer-reviewed journals as the first author, to articles as a co-author, and ending with oral presentations and posters at conferences. The list also includes articles that are in preparation and contributions that have been accepted for upcoming conferences. The presenting author of the oral presentation is highlighted with an asterisk.

### Peer-reviewed journals

A. Letzel, E. Maurer, M. Meixner, R. Poprawe, J. Stollenwerk, S. Hessner, K. Lehmann, B. Gökce, and S. Barcikowski, *Effect of various dispersing agents on the stability of silver microparticle dispersion and the formulation of uniform silver film by laser melting*, J. Laser Appl., 28 (2016) 042004.

A. Letzel, B. Gökce, P. Wagener, S. Ibrahimkutty, A. Menzel, A. Plech, and S. Barcikowski, *Size quenching during laser synthesis of colloids happens already in the vapor phase of the cavitation bubble*, J. Phys. Chem. C, 121 (2017) 5356-5365.

A. Letzel, B. Gökce, A. Menzel, A. Plech, and S. Barcikowski, *Primary particle diameter differentiation and bimodality identification by five analytical methods using gold nanoparticle size distributions synthesized by pulsed laser ablation in liquids*, Appl. Surf. Sci., 435 (2018) 743-751.

A. Letzel, M. Santoro, J. Frohleiks, A. R. Ziefuß, S. Reich, A. Plech, E. Fazio, F. Neri, S. Barcikowski, and B. Gökce, *How the re-irradiation of a single ablation spot affects cavitation bubble dynamics and nanoparticles properties in laser ablation in liquids*, Appl. Surf. Sci. 473 (2018) 828-837.

A. Letzel, S. Reich, T. dos Santos Rolo, A. Kanitz, J. Hoppius, A. Rack, M. Olbinado, A. Ostendorf, B. Gökce, A. Plech, and S. Barcikowski, *Time and mechanism of nanoparticle functionalization by macromolecular ligands during pulsed laser ablation in liquids*, Langmuir 35 (2019) 3037-3047.

S. Reich, P. Schönfeld, P. Wagener, A. Letzel, S. Ibrahimkutty, B. Gökce, S. Barcikowski, A. Menzel, T. dos Santos Rolo, and A. Plech, *Pulsed laser ablation in liquids: Impact of the cavitation bubble on particle formation*, J. Colloid Interface Sci., 489 (2017) 106-113.

S. Reich, P. Schönfeld, [A. Letzel](#), S. Kohsakowski, M. Olbinado, B. Gökce, S. Barcikowski, and A. Plech, *Fluence threshold behaviour on ablation and bubble formation in pulsed laser ablation in liquids*, ChemPhysChem, 18 (2017) 1084-1090.

S. Reich, J. Göttlicher, [A. Letzel](#), B. Gökce, S. Barcikowski, T. dos Santos Rolo, T. Baumbach, and A. Plech, *X-ray spectroscopic and stroboscopic analysis of pulsed-laser ablation of Zn and its oxidation*, Appl. Phys. A, 124 (2018) 71.

C.-Y. Shih, R. Streubel, J. Heberle, [A. Letzel](#), M. V. Shugaev, C. Wu, M. Schmidt, B. Gökce, S. Barcikowski, and L. V. Zhigilei, *Two mechanisms of nanoparticle generation in picosecond laser ablation in liquids: the origin of the bimodal size distribution*, Nanoscale, (2018) DOI: 10.1039/c7nr08614h.

S. Reich, T. dos Santos Rolo, [A. Letzel](#), T. Baumbach, and A. Plech, *Scalable, large area compound array refractive lens for hard X-rays*, Appl. Phys. Lett., 112 (2018), 151903.

## **Conference contributions**

### **Oral presentations with abstract**

[A. Letzel](#)\*, B. Gökce, S. Ibrahimkuty, A. Menzel, A. Plech, and S. Barcikowski, *In situ observation of nanoparticle size reduction by ions during cavitation confinement of laser synthesis in liquids*, 7<sup>th</sup> International Colloids Conference, 06/2017, Sitges, Spain.

[A. Letzel](#)\*, B. Gökce, S. Ibrahimkuty, A. Menzel, A. Plech, and S. Barcikowski, *In situ observation of nanoparticle size reduction by ions during cavitation confinement of laser synthesis in liquids*, 26<sup>th</sup> Annual Meeting of the German Crystallographic Society (DGK), 03/2018, Essen, Germany.

### **Poster presentations with abstract**

[A. Letzel](#)\*, B. Gökce, A. Menzel, A. Plech, and S. Barcikowski, *Particle formation during pulsed laser ablation in liquids: A mechanistic study utilizing X-rays*, Annual celebration of the Center for Nanointegration Duisburg-Essen (CENIDE), 11/2016, Essen, Germany.

[A. Letzel](#)\*, M. Meixner, J. Stollenwerk, I. Kelbassa, B. Gökce, R. Poprawe, and S. Barcikowski, *Prozessadaption von leitfähigen Silberdispersionen an die laserbasierte Herstellung von leitfähigen Strukturen auf organischen Lacken*, Materials for Photonics Symposium, 09/2015, Essen, Germany.

R. Streubel\*, [A. Letzel](#), C.-Y. Shih, J. Heberle, M. V. Shugaev, C. Wu, M. Schmidt, L. V. Zhigilei, S. Barcikowski, and B. Gökce, *Exploring the origin of bimodal size distribution during picosecond laser ablation in liquids*, 5<sup>th</sup> International Conference on Advanced Nanoparticle Generation & Excitation by Lasers in Liquids (ANGEL), 06/2018, Lyon, France.

**Oral presentations with abstract**

[A. Letzel](#), B. Gökce, S. Ibrahimkuty, A. Menzel, A. Plech, and S. Barcikowski\*, *Size quenching during laser synthesis of colloids happens already in the vapor phase of the cavitation bubble*, 5<sup>th</sup> International Conference on Advanced Nanoparticle Generation & Excitation by Lasers in Liquids (ANGEL), 06/2018, Lyon, France.

S. Reich, [A. Letzel](#), T. dos Santos Rolo, P. Schönfeld, B. Gökce, A. Menzel, S. Ibrahimkuty, S. Barcikowski, T. Baumbach, and A. Plech\*, *Disentangling competitive hierarchical processes in pulsed laser ablation in liquids*, 5<sup>th</sup> International Conference on Advanced Nanoparticle Generation & Excitation by Lasers in Liquids (ANGEL), 06/2018, Lyon, France.

S. Reich\*, [A. Letzel](#), T. dos Santos Rolo, B. Gökce, S. Barcikowski, T. Baumbach, M. Olbinado, and A. Plech, *Fast multi-contrast imaging of the ablation process in liquids adding X-ray bright-field and dark-field methods*, 5<sup>th</sup> International Conference on Advanced Nanoparticle Generation & Excitation by Lasers in Liquids (ANGEL), 06/2018, Lyon, France.